Scattering by wave-bearing surfaces under fluid loading

by D. P. Williams

Thesis submitted to the University of Nottingham
for the degree of Doctor of Philosophy, August 1999

Scattering by wave-bearing surfaces under fluid loading

Abstract

Wave-bearing surfaces and compressible fluids are often adjacent, the subsequent interactions are of substantial interest in structural acoustics, acoustic microscopy, seismology and many other fields. Here we take a broad view and discuss a variety of problems, both time harmonic and transient, which are amenable to exact solution. These in turn highlight physical effects and can additionally form the basis of asymptotic solutions.

In structural acoustics the interaction of plate waves with defects is a major source of underwater noise. A model problem of two semi-infinite elastic plates (made of different material) joined in a variety of ways is considered for obliquely incident flexural plate waves. Asymptotic results for 'light' and 'heavy' fluid loading are extracted. In addition reciprocity and power flow relations, besides being of independent interest, provide a useful check on the results.

There are many closely related problems involving a fluid loaded elastic solid. The situation here is somewhat similar, but often more complicated, due to the number of waves that an elastic solid supports, mode conversion at interfaces, and interfacial waves.

We first address the scattering effects of low frequency waves by very small interfacial defects, that is, small relative to a typical wavelength. In this limit, and in related water wave or acoustic work, matched asymptotic expansions are used. An important aspect, that has not been noticed before, is the natural separation that occurs in the inner problem into fluid and solid pieces. A matching argument may now be used to give a useful physical interpretation of these defects and far field directivity patterns show the distinctive beaming that occurs along the Rayleigh angles in the light fluid loading limit.

In many areas of interest embedded defects are imaged by pulses and we therefore require a transient analysis. In this case our problem involves a combination of compressional and shear source loadings beneath a fluid-solid interface. The exact solution is found and a full asymptotic analysis of this solution is performed with an emphasis upon wavefront expansions and leaky waves, and in particular, for 'light' and 'moderate' fluid loading. In some situations, when the sources are near the interface, a pseudo-compressional wavefront is generated and the limit as the loading approaches the interface is investigated. These non-geometric wave arrivals may be important in seismology and elastic wave studies related to the non-destructive evaluation of structures.

This study is generalised to investigate the dynamic stress loading of subsurface cracks in either homogeneous or non-homogeneous media. An iterative method of solution based on physical considerations is developed and quantities of interest such as the scattered displacement fields and the stress intensity factors are determined.

The problems considered here are ideally suited to analysis by transform methods and the Wiener–Hopf and Cagniard–de Hoop techniques.

Acknowledgments

I would like to thank my supervisor Richard Craster for his generous encouragement and expert guidance throughout the duration of my research. Without Richard these pages would still be in the woods. I would also like to thank Richard Tew for many helpful conversations and his part in my supervision, and Neil Balmforth for some contributions.

This work has also benefited from discussions with Ahmos Sansom.

I am grateful to the EPSRC for providing funding via a Research Studentship.

Above all, I thank my parents and my brother whose interest and support have helped to lighten this task.

Nottingham Duncan Williams
August 1999

Summary of contents

Abstract *page* iii

Acknowledgments iv

Summary of contents v

Contents vi

Chapter One
Introduction and overview 1

Chapter Two
Scattering by small defects in the neighbourhood of a fluid-solid interface 10

Chapter Three
Asymptotic representations for transient forcings beneath a fluid-solid interface 35

Chapter Four
Cagniard–de Hoop path perturbations with applications to non-geometric wave arrivals 65

Chapter Five
Pulse scattering by a semi-infinite crack 92

Chapter Six
Diffraction at plate junctions by flexural plate waves 136

Chapter Seven
A reciprocity relation between plane and flexural plate waves scattered by rigid defects 172

Chapter Eight
Concluding remarks 190

References 194

119 references. 72 figures. 2 tables. x + 199 pp.

Contents

Abstract *page* iii

Acknowledgments iv

Summary of contents v

Contents vi

Chapter One
Introduction and overview 1

1.1. Introduction 1

1.1.1. Surface and leaky waves 2

1.1.2. Basic concepts 3

1.2. Overview to the thesis 4

1.3. How to read this thesis 8

References 8

Chapter Two
Scattering by small defects in the neighbourhood of a fluid-solid interface 10

2.1. Introduction 10

2.2. Formulation 11

2.3. A rigid strut 14

2.3.1. The inner problem 15

2.3.2. The outer problem 16

2.3.3. Discussion 18

2.4. An edge crack 21

2.5. A rigid strip 25

2.6. Conclusion 28

References 30

Appendix 2.A. Fourier transformed variables 31

Appendix 2.B. Elastic solutions 32

Appendix 2.C. Numerical method 32

Chapter Three
Asymptotic representations for transient forcings beneath a fluid-solid interface 35

3.1. Introduction 35

3.2. Formulation 37

3.3. Subsurface loadings 40

3.3.1. A subsurface compressional line source 41

3.3.1.1. Exact solution 41

3.3.1.2. The source close to the interface 47

3.3.1.3. Asymptotic analysis 51

3.3.2. A subsurface shear line source 54

3.3.3. Subsurface line force 58

3.4. Conclusion 60

References 62

Appendix 3.A. Fourier and Laplace transformed variables 63

Appendix 3.B. The zeros of $S(\zeta)$ 64

Chapter Four
Cagniard–de Hoop path perturbations with applications to non-geometric wave arrivals 65

4.1. Introduction 65

4.2. A compressional source beneath a fluid-solid interface 68

4.2.1. Exact solution 71

4.2.2. The source close to the interface 74

4.3. A compressional source beneath a thin high velocity layer 78

4.3.1. A fluid layer 79

4.3.2. An elastic layer 83

4.4. Conclusion 86

References 87

Appendix 4.A. Quartic equation 88

Appendix 4.B. The zeros of $s(\zeta)$ 89

Appendix 4.C. Reflection and transmission coefficients 90

Chapter Five
Pulse scattering by a semi-infinite crack 92

5.1. Introduction 92

5.2. Anti-plane loading 95

5.2.1. Exact solution 96

5.2.2. Iterative solution 99

5.2.2.1. First loading 101

5.2.2.2. Reloading by the surface 102

5.2.2.3. Reloading by the interface 105

5.2.3. Comment on fundamental solutions 106

5.3. Invariant integral 106

5.4. Weight functions 114

5.5. In-plane loading 117

5.5.1. Formulation 118

5.5.2. Transform solution 119

5.5.2.1. Reloading by the compressional wave 122

5.5.2.2. Reloadings by other waves 124

5.5.3. Invariant integral 125

5.6. Conclusion 129

References 129

Appendix 5.A. Fourier transform results 131

Appendix 5.B. Product splits 131

Appendix 5.C. Near crack fields 133

Appendix 5.D. Reflection coefficients and Wiener-Hopf notation 134

Chapter Six
Diffraction at plate junctions by flexural plate waves 136

6.1. Introduction 136

6.2. Formulation 137
6.2.1. Non-dimensionalisation 140
6.2.2. Flexural waves and critical angles 140
6.2.3. Radiated acoustic waves 141
6.3. Transform solution 142
6.3.1. The functional equation 144
6.3.2. Reflection, transmission, and diffraction coefficients 148
6.3.3. Power flow 149
6.4. Numerical results for clamped or welded edges 149
6.5. Special cases 155
6.5.1. Rigid plate 155
6.5.2. Soft plate 158
6.5.3. Identical plates 160
6.5.4. Light fluid loading 161
6.5.5. Heavy fluid loading 164
6.6. Concluding remarks 165
References 166
Appendix 6.A. Factorisation: for $K(\xi)$ 167
Appendix 6.B. Edge conditions 170

Chapter Seven
A reciprocity relation between plane and flexural plate waves scattered by rigid defects 172

7.1. Introduction 172
7.2. Basic equations 174
7.2.1. Non-dimensionalisation 175
7.2.2. Incident wave structure 176
7.2.2.1. Flexural waves 176
7.2.2.2. Leaky waves 176
7.2.2.3. Acoustic plane wave 177
7.2.3. Far-field wave structure 178

7.3. The reciprocity relation 180
7.4. Illustrative examples 182
7.4.1. A single line joint 182
7.4.2. A semi-infinite rigid plate 183
7.5. Concluding remarks 187
References 188

Chapter Eight
Concluding remarks 190
8.1. Summary of conclusions 190
8.2. So what happens next ? 191
References 192

References 194

Chapter One

Introduction and overview

1.1. Introduction

Wave-bearing surfaces are often in contact with neighbouring compressible fluids, and the resulting fluid-solid wave interactions are of interest in many practical situations. These include structural acoustics, acoustic microscopy, seismology, and many other branches of geophysics and engineering. In these applications, many solutions exist in the absence of the fluid; fewer exist with the addition of a fluid, which is a complicating feature. The aim of this thesis is to examine the detailed mathematics and physics that emerges for fluid loaded elastic solids, or elastic plates. That is, to investigate several problems that are amenable to exact and asymptotic solutions. Along the way, we place an increasing emphasis on surface and 'leaky' waves and analogous plate waves. Previous problems, with or without the fluid coupling, have not exhausted the interest in fluid loading because the effects are often markedly different in each case.

Several of the problems considered in this thesis are motivated, in part, by an interest in non-destructive testing and seismology. Aspects of interest in seismology are discussed in Ewing *et al.* (1957), Cagniard (1939) and others. However these authors, and also more recent authors (*e.g.* de Hoop & van der Hijden, 1985) have paid less attention to 'leaky' waves than we do here. These waves are particularly important in non-destructive testing techniques, where there is recurrent interest. One such technique is the acoustic microscope which involves imaging an elastic solid with waves incident from an overlying fluid; the experimental technique associated with the acoustic microscope is described in Briggs (1985, 1992). The device is particularly adept at imaging surface breaking (or subsurface) cracks, the book by Briggs (1992) contains several experimental results. In this field, there is particular interest in scattering by very small defects and cracks, see Briggs *et al.* (1990) as these can act as stress concentrators and lead to potentially catastrophic failure of specimens. There has been some recent developments of this technique in medical imaging; Hildebrand & Rugar (1984) is an early example in this blossoming area.

We are also motivated by related problems in structural acoustics. Here, the fluid loading of vibrating structures is important in many other technological or engineering applications. For instance, in marine engineering, mechanical and nuclear engineering, and in physiological process; these areas and many others are described in Crighton (1989). In many contexts it is the diffraction of acoustic and structure-borne waves at

plate junctions that is important; it is this behaviour that is responsible for the sound that is generated in the fluid. Mathematically the fluid loaded elastic solid and elastic plates are naturally similar, and we can investigate potentially important physical results by dealing with the latter as the technical details are easier to deal with. In this vein we investigate obliquely incident waves and material changes for fluid loaded elastic plates.

The fluid loading effects in the above fields are profoundly important. A key aspect, that is often also remarkably subtle, is the emergence of leaky waves. It is this aspect that we aim to illustrate in this thesis in a wide variety of problems.

1.1.1. *Surface and leaky waves*

Elastic solids and plates, in the absence of fluid loading, with planar surfaces support surfaces waves in the form of Rayleigh and flexural plate waves respectively. These unattenuated waves propagate along the surface of material; for an elastic solid there is exponential decay with depth into the elastic material. Leaky waves are perturbations away from these *in vacuo* surface waves. The reason for their name is that, provided the *in vacuo* surface wavespeed is greater than the acoustic wavespeed in the fluid, then the introduction of light fluid loading causes the *in vacuo* wave to be perturbed such that energy is shed into the fluid along a critical angle (Crighton, 1979). This leads to distinctive beaming in the fluid along this angle, together with a response in the angular directivity associated with scattered cylindrical waves, and in the wavefield. We shall see later (Chapter 6) that there are subtleties in this beaming behaviour for plate waves obliquely incident upon defects.

In brief, in a fluid-elastic solid interaction, an unattenuated interfacial wave, the Schölte wave (a Stoneley wave), propagates along the interface; the wave decays exponentially with depth in both materials, it is subsonic relative to the surrounding fluid, and in the light fluid loading limit (where the fluid-solid coupling is weak) the decay is rapid in the solid and weak in the fluid. In the absence of the fluid the corresponding unattenuated surface wave is a Rayleigh wave. Perhaps surprisingly, in the limit as the fluid coupling tends to zero the Schölte wavespeed does not limit to the Rayleigh wavespeed, rather it tends to the compressional fluid wavespeed. Thus if we take an *in vacuo* material and add fluid, the natural question is: Where has the Rayleigh wave gone? In this light fluid loading limit, the Rayleigh wave becomes a leaky wave; it is a perturbation of the usual Rayleigh wave, that is, it is no longer unattenuated, it now decays exponentially with distance along the interface, and energy flows into the fluid along a critical angle.

Similarly for a fluid-elastic plate scenario there is, in the absence of the fluid, an *in vacuo* flexural plate wave that plays the role of the Rayleigh wave. The only difference

is that this wave may, depending upon the frequency, have a wavespeed greater than or less than the acoustic wave speed; that is, it can be either supersonic or subsonic relative to the fluid. In the first case leaky waves emerge. The addition of the fluid leads, analogously to the Schölte wave, to an unattenuated flexural plate wave that is again subsonic relative to the acoustic wavespeed.

Leaky (Rayleigh) waves play a vital role in the acoustic microscope, it is the excitation of the leaky waves caused by a defect that is being observed by the microscope. The wave carries with it detailed information about the elastic properties of the flawed material that leads to an overall picture. The main application of leaky waves has (historically) been in structural acoustics, see for instance Crighton (1989), where the flexural plate waves are perturbed by an overlying fluid. The crucial difference, that the flexural plate wave is frequency dependent however, leads to some mathematical differences.

1.1.2. *Basic concepts*

It is now often suggested in cases when analytical ideas are used that it would be simpler to compute the results using an existing package. In answer, there is firstly, the question of accuracy, but more importantly, careful analysis is essential to delineate the physical processes at hand and to help check and interpret numerical results. The problems described in this thesis are ideally suited to analysis by transform methods and, sometimes, the Wiener–Hopf technique. Some problems are also amenable to the Cagniard–de Hoop inversion method.

The Wiener–Hopf technique is a widely used and valuable mathematical tool. For a detailed description of the method, with an emphasis on some acoustic and electromagnetic applications, see Noble (1958). Often, mixed boundary value problems (examples arising from a semi-infinite geometry are contained in this thesis) are necessarily tackled using Fourier transforms and the Wiener–Hopf technique. The technique is not restricted to being used with Fourier transforms, it can also be used in conjunction with the Mellin transform, see Chapter 2.

The Cagniard–de Hoop method (Cagniard, 1939; de Hoop, 1960) is an excellent method for solving elastic wave interaction problems; it is also referred to as the Lamb–Pekeris method (Lamb, 1904; Pekeris, 1940). The underlying ideas are comprehensively discussed by Miklowitz (1978), Hudson (1980) and others. In essence, the method consists of an elegant transformation that reduces a double transform inversion to an explicit result using a particular time dependence. Along the way, an inversion path is constructed that indirectly captures much of the physical structure of the solution.

1.2. Overview to the thesis

In this thesis we cover various topics in elastic wave propagation in which mathematical analysis may be successfully used to distinguish dominant effects, and in other cases used to aid numerical methods. The plan of the thesis is as follows.

In Chapter 2, the scattering of incident plane elastic waves by a variety of different defects that lie upon a fluid-solid interface is considered in a low frequency limit using matched asymptotic expansions. There are complications due to the interfacial coupling that have apparently dissuaded others from using this route. However, following through the usual philosophy of 'inner' and 'outer' expansions and carefully matching the solutions together progress can be made. This really hinges on one useful aspect, that has not previously been observed: in the limit as $\epsilon \ll 1$ then for the inner problems the fluid and solid pieces uncouple in a particularly convenient manner allowing analytical solutions to be deduced. These inner solutions are then matched with the appropriate outer solutions. An expansion scheme is developed in terms of a parameter ϵ, the ratio of a typical defect length scale to a typical wavelength of the incident field, taken to be small.

Three different canonical situations occur, and these are illustrated via the three specific examples treated here: a rigid strut, an edge crack, and a rigid strip. In each case the leading order matching is performed to identify the leading order contribution of the defect to the acoustic field in the far field. In particular, each defect is identified with a source or dipole response in interfacial stress or displacement; we aim to identify how different defects appear when viewed from afar. Potentially, we are then in a position to model them in a simple manner.

Many practical imaging techniques use pulses to insonify materials. Specifically, cracks and other defects and obstacles are often imaged by pulses (Briggs, 1992) and thus we require a transient analysis; there are also related applications in seismology. Hence to complement the work using time harmonic vibrations, the following three chapters focus on transient wave propagation.

Transient line loadings are first considered in Chapter 3. The loadings are located in an elastic half space that is coupled to an overlying fluid half space. The resulting fluid and solid responses are found exactly in a simple closed form using the Cagniard–de Hoop technique and transform methods. These exact solutions are analysed in detail both for responses upon the interface, and within the fluid. Along the way, we require the numerical identification of the Cagniard paths. A perturbation method is developed when the loading is near the surface to complement these numerical approaches of identifying the Cagniard paths.

There are then three items on our agenda in this chapter. First, a full asymptotic analysis of the solution is performed with an emphasis upon wavefront expansions and leaky waves. These results are used as Green's functions for more complicated spatial and time dependent loadings. Second, we abstract useful information from the exact solution, and the physical structure of the wave responses is revealed. Thirdly, for 'light' and 'moderate' fluid loading, we identify a definite response associated with the leaky Rayleigh pole, and demonstrate how the leaky response emerges.

The asymptotic analysis of the solution is performed via a direct analysis of the transform solution using steepest descents and residue calculus. The forms of the initial wavefronts generated are given exactly, and a wavefront expansion for the disturbance generated by the leaky Rayleigh wave is identified. Close to the interface, Schölte waves contribute to the solution and these too are evaluated. For these waves a residue calculation from the transform solutions is shown to be consistent with the exact analysis. In the limit as the loading approaches the interface, a pseudo-compressional wavefront is generated; this limiting process is also investigated.

All the asymptotic expansions are utilised with the convolution theorem to give asymptotic results valid near the wavefronts for quite general time dependent loadings. This gives quick, and relatively simple, expressions for the full response, thus avoiding time consuming numerical evaluations.

To illustrate the relative importance of 'light' and 'moderate' fluid loading we consider two material combinations, these are typical of metal-water and rock-water combinations.

In Chapter 4 we focus, in more detail, on the near surface fields encountered in the third chapter. These so-called non-geometric wave arrivals are often important in seismology and elastic wave studies related to the non-destructive evaluation of structures. In particular tunnelling signals caused by significant differences in the material parameters, and wavespeeds at interfaces, generate large responses that may often be dominant. This is common in elastic wave propagation, for instance, when a source is close to the interface of a faster medium with a slower medium, the response in the slower medium is dominated by a signal that has 'tunnelled' through the faster medium. Other instances of tunnelling occur when a compressional source is close to a free surface. In this case the compressional to shear wave conversion at the surface, and the mismatch between compressional and shear wavespeeds, leads to a sharp non-geometric shear wave arrival. Equally, thin high velocity layers demonstrate tunnelling effects that are perturbations of the response brought about by a source in a surrounding slower medium. In the above 'close' refers to the viewpoint of an observer some distance away. In all of the instances there is a common feature, namely, each problem contains a ratio of length scales, x/h,

with h either the source depth or layer thickness and x the observer distance; this ratio of length scales characterises the non-geometric responses. Typically, the non-geometric response arises when the current problem is a perturbation away from one where the associated arrival has a direct geometric interpretation.

Such problems are again ideally suited to analysis by the Cagniard-de Hoop technique. Our pitch in this chapter, is that each tunnelling response is identified as a perturbation away from an exact solution; this leads to highly accurate and relatively simple explicit asymptotic solutions. The perturbation scheme is demonstrated here via the solution of two problems: a compressional source placed beneath a fluid-solid interface and placed beneath a thin high velocity layer. The first problem has separate non-geometric responses due to both the material mismatch and the wave conversion at the interface. The thin high velocity layer perturbs the field generated by a compressional source in a slower surrounding medium. In both cases the non-geometric arrivals are analysed in detail.

What seems to be needed now is to give some shape and size to the subsurface defects of the last two chapters. Given the complexity of most fluid-solid problems we first consider non-finite, buried, plates and cracks. In Chapter 5 some complementary techniques are used to investigate the dynamic loading of subsurface cracks in either homogeneous or inhomogeneous media; the quantities of interest such as the scattered fields and the stress intensity factors are determined. For homogeneous media these involve exact solutions utilising transform methods and the Wiener–Hopf technique. In some cases this approach is neither feasible, due to the matrix nature of the problem, nor physically revealing. To ease interpretation an iterative method based on physical considerations is developed. For special loadings invariant integrals are utilised to provide non-trivial extensions of the analysis to inhomogeneous media, at least insofar as the stress intensity factors are concerned.

We firstly illustrate the efficiency and scope of the techniques upon anti-plane subsurface scattering problems. Then we proceed to treat the more complicated and relevant in-plane scattering problems. In both cases we consider a crack that lies in an elastic half space that is coupled to an overlying fluid half space (effectively a vacuum in the first instance). The crack is subjected to a prescribed stress loading on the crack faces. The resulting fluid and solid responses are found exactly by means of an iterative scheme in which successively the Cagniard–de Hoop and Wiener–Hopf techniques are applied.

It is the aim of Chapter 5 to extract the stress and displacement fields, and in addition, the form of the near crack tip fields. These solutions are useful in determining specific

wavefront arrivals that are associated with waves interacting with the crack and interface, and can be used as the basis of asymptotic studies.

Finally, in Chapters 6 and 7, we leave the transient fluid-elastic solid problems of the last three chapters, and return to time-harmonic analysis, but now for fluid-loaded elastic plates. Much of the analysis for fluid-elastic solid problems involves complicated algebra, whereas the fluid-loaded plates are slightly easier and yet physically related. Some problems are not easily amenable to study in the fluid-elastic case, but are approachable for plates. In particular we want to assess how a subsonic (relative to the fluid) surface wave scatters when obliquely incident upon a surface breaking crack, or defect, or change in material properties. This is loosely analogous to flexural plate waves incident obliquely at the junction of two dissimilar, co-planar elastic, fluid-loaded plates, these are the subject of Chapter 6. In particular we want to see if there exists a situation whereby all the wave energy is trapped in a finite region, then this could potentially lead to resonant behaviour.

The oblique aspect of plate wave diffraction has remained relatively unexplored. In this problem, the explicit solution is constructed using Fourier transforms and, the champion of this thesis, the Wiener–Hopf technique for a variety of edge conditions applied at the junction. These solutions illustrate several effects that are specifically associated with oblique incidence, such as cut-off frequencies below which power transmission to infinity in one plate is zero. The solution is presented in a form that neatly connects with limiting cases where one plate is rigid, acoustically soft, or where the two plates have identical material properties. The 'light' and 'heavy' fluid loading limits are briefly examined, and a power flow theorem provides a useful check on the results and information about the distribution of scattered power.

Power-flow, and also reciprocity, relations are often of value in numerical studies involving obstacles and defects in acoustics; they provide a useful check on the results. These reciprocity relations can emerge in many different ways and as a starting point, in Chapter 7, a reciprocity relation between the far-field behaviour of the scattered fields generated by incident waves, either flexural, or acoustic upon rigid defects is derived. These defects are embedded in a thin, elastic, fluid-loaded plate. The reciprocity result is then illustrated upon two model problems for which the explicit solution can be determined and the relation demonstrated. These problems are closely related to those found in Chapter 6.

Finally some concluding remarks are compiled in Chapter 8 together with some discussion of further applications and extensions of this work and our next port of call.

1.3. How to read this thesis

The major thesis chapters (2-7) are presented as completely self contained papers each having its own introduction, discussion and references, and are designed to be read as individual units. Some of the chapters have appeared, or are submitted, in various journals co-authored with R. V. Craster and with R. V. Craster & N. J. Balmforth (6).

Chapter 2 as Scattering by small defects in the neighbourhood of a fluid-solid interface. 1998. *IMA J. Appl. Math.* **61**, 155-177.

Chapter 4 as Cagniard–de Hoop path perturbations with applications to non-geometric wave arrivals. 1999. To appear in *J. Engng. Math.*

Chapter 5 as Pulse scattering by a subsurface semi-infinite crack. 1999. Under consideration in *Int. J. Solids Structures*

Chapter 6 as Diffraction at plate junctions. 1999. Under consideration in *Quart. J. Mech. Appl. Math.*

Chapter 7 as A reciprocity relation for structural acoustics. 1999. Under consideration in *J. Sound Vib.*

References

Briggs, G. A. D., 1985. *An introduction to scanning acoustic microcopy*. Oxford University Press: Royal Microscopical Society.

Briggs, G. A. D., 1992. *Acoustic microscopy*. Monographs on the physics and chemistry of materials: 47, Oxford University Press.

Briggs, G. A. D., Jenkins, P. J. & Hoppe, M., 1990. How fine a surface crack can you see in a scanning acoustic microscope ? *J. Microsc.* **159**, 15–32.

Cagniard, L., 1939. *Réflection et réfraction des ondes séismique progressives*. Gauthiers-Villars, Paris. Trans. and rev. by E. A. Flinn and C. H. Dix, 1962. *Reflection and refraction of progressive seismic waves*. McGraw-Hill, New York.

Crighton, D. G., 1979. The free and forced waves on a fluid–loaded elastic plate. *J. Sound Vib.* **63**, 225–235.

Crighton, D. G., 1989. The 1988 Rayleigh Medal lecture: fluid loading - the interaction between sound and vibration. *J. Sound Vib.* **133**, 1–27.

de Hoop, A. T., 1960. A modification of Cagniard's method for solving seismic pulse problems. *Appl. sci. Res. B* **8**, 349–356.

de Hoop, A. T. & van der Hijden, J. H. M. T., 1985. Seismic waves generated by an impulsive point source in a fluid/solid configuration with a plane boundary. *Geophysics* **50**, 1083–1090.

Ewing, W. M., Jardetzky, W. S. & Press, F., 1957. *Elastic waves in layered media*. McGraw-Hill, New York.

Hildebrand, J. A. & Rugar, D., 1984. Measurement of cellular elastic properties by acoustic microscopy. *J. Microsc.* **134**, 245–260.

Hudson, J. A., 1980. *The excitation and propagation of elastic waves.* Cambridge University Press.

Lamb, H., 1904. On the propagation of tremors over the surface of an elastic solid. *Phil. Trans. R. Soc. Lond. A* **203**, 1–42.

Miklowitz, J., 1978. *The theory of elastic waves and waveguides.* North-Holland.

Noble, B., 1958. *Methods based on the Wiener–Hopf technique.* Pergamon Press.

Pekeris, C. L., 1940. A pathological case in the numerical solution for integral equations. *Proc. Nat. Acad. Sci. USA* **26**, 433–437.

Chapter Two

Scattering by small defects in the neighbourhood of a fluid-solid interface

2.1. Introduction

Scattering effects by small defects at a fluid-solid interface are important in non destructive testing devices such as the acoustic microscope, Briggs (1992). It is therefore useful to have analytical results for scattering by model defects. Unfortunately, due to the complexity of the boundary conditions there are few closed form solutions available even in the case when the fluid is absent. This is due to the inherent mode coupling of compressive, shear, and surface waves at the interface (free surface in the absence of fluid).

There is particular interest in scattering by very small defects, for instance, for very small cracks see Briggs *et al.* (1990). To model these defects we consider the limit when the characteristic length of the defect relative to a typical wavelength is small, and matched asymptotic expansions are used. This approach has been successful in scattering problems in acoustics, Crighton & Leppington (1973), short surface water waves, Leppington (1972), and elastodynamics, Sabina & Willis (1977); a useful review is given by Datta & Sabina (1986). Recent applications of the method have been in water waves-acoustics, McIver & Rawlins (1993), and in elastodynamics, Abrahams & Wickham (1992a, 1992b). There has been no attempt to utilise the technique for coupled media and it is, perhaps, not clear *a priori* that such an approach will simplify matters substantially due to the coupling of the fluid and solid half spaces. However, given the success of the technique elsewhere, it is natural to attempt to extend the analyses above to the coupled fluid-solid situation, with the aim of providing relatively simple analytical results and physical interpretations.

Alternative approaches utilised by Howe (1990), Wickham (1977), and others is to approach problems in this limit using integral equation formulations or an approximate form of a Green's function; this approach is, perhaps, less transparent than the matching procedure.

In essence for each of the problems considered here the outer solutions valid *far* from the defect will be seen to take the form of a source or dipole response whose strength is determined by considering an appropriate inner problem. These outer solutions take the form of interfacial discontinuities in either the normal stress, shear stress, or normal

displacement. There are effectively three different types of surface discontinuity that can arise; the examples chosen here illustrate the occurrence of each type of discontinuity. In each case an inner problem is formulated and the inner solution is valid in the near neighbourhood of the defect. These solutions are found from a static analysis. In this inner limit a natural separation into fluid and solid problems emerges. Each is then solved independently.

Due to the complexity of identifying the inner limit of the outer solution only leading order matching is performed here. To deduce higher order terms, even in the absence of the fluid, proves to be an arduous task, for instance, in the case of the inner limit of a line source near a traction free surface see Brind & Wickham (1991), Datta & El-Akily (1978); whereas identifying the leading order terms can be done directly utilising generalised functions and the evaluation of contour integrals.

2.2. Formulation

In the region $y > 0$ is an isotropic linear elastic material and in $y < 0$ is a compressible fluid. The responses of the two materials are coupled together through continuity conditions along the interface $y = 0$. Time harmonic vibrations of frequency ω are considered, that is, all physical variables are considered to have an $\exp\{-i\omega t\}$ time dependence; this time dependence is considered understood and is suppressed henceforth. A Cartesian coordinate system is adopted with x_1, x_2 corresponding to x, y.

The elastic material has Lamé constants λ, μ, and density ρ. The stresses σ_{ij} in the material are related to the displacements u_i by

$$\sigma_{ij} = \lambda\epsilon_{kk}\delta_{ij} + 2\mu\epsilon_{ij} \text{ where } \epsilon_{ij} = \frac{1}{2}(u_{i,j} + u_{j,i}), \tag{2.2.1}$$

the comma denoting differentiation with respect to x_i. Here it is useful to recognise that the dilatation e, used later, is given by ϵ_{kk}. The compressible fluid in $y < 0$ is effectively an elastic material supporting no shear stresses. Thus

$$\sigma_{ij} = \lambda_f\epsilon_{kk}\delta_{ij}, \tag{2.2.2}$$

where the fluid has density ρ_f and compressional modulus λ_f.

A convenient representation is to adopt the displacement potentials $\phi(x,y)$, $\psi(x,y)$, and $\chi(x,y)$ where the displacement $\mathbf{u}$ is

$$\mathbf{u} = \nabla\phi + \nabla \times \psi\hat{z}, \text{ for } y > 0, \tag{2.2.3}$$

where $\hat{z}$ is the unit vector in the z direction, and

$$\mathbf{u} = \nabla\chi, \text{ for } y < 0. \tag{2.2.4}$$

These potentials satisfy the following Helmholtz equations

$$(\nabla^2 + k_d^2)\phi = 0, \quad (\nabla^2 + k_s^2)\psi = 0, \quad (\nabla^2 + k_o^2)\chi = 0, \tag{2.2.5}$$

where the wavenumbers are defined as $k_d = \omega/c_d$, $k_s = \omega/c_s$, and $k_o = \omega/c_o$. The subscripts d, s, and o denote the variables associated with the dilatational and shear wavespeeds in the solid and the compressional wavespeeds in the fluid, respectively. The wavespeeds c_d, c_s, and c_o are defined as

$$c_d^2 = \frac{\lambda + 2\mu}{\rho}, \quad c_s^2 = \frac{\mu}{\rho}, \quad c_o^2 = \frac{\lambda_f}{\rho_f}. \tag{2.2.6}$$

The assumption that the compressional wavespeed of the fluid is less than the shear wavespeed of the solid implies that $k_o > k_s > k_d$; this is a reasonable assumption for most solid and fluid combinations. The analysis presented here does not rely on this assumption and can easily be generalised to allow $k_s > k_o > k_d$, say.

A coupling parameter $\mathcal{E}$ occurs in the analysis; it is defined as $\mathcal{E} = \rho_f k_d/\rho k_o$ and provides a measure of the fluid loading. The light fluid loading limit is when $\mathcal{E} \ll 1$; this limit is not taken here unless explicitly stated.

Typically we expect the scattered wavefields to consist of body waves in the solid and fluid and interfacial waves. For scattering by a point defect the dominant responses that are generated in the solid are cylindrical shear and compressional body waves together with a leaky Rayleigh wave. The leaky Rayleigh wave is only identified in the light fluid loading limit where it is a perturbation of the Rayleigh wave that would propagate unattenuated along the surface of the elastic solid when in contact with a vacuum. The presence of the fluid causes the wave to leak energy into the fluid. Here the leaky Rayleigh wave decays exponentially with distance along the interface from the source of the waves. In addition an interfacial Stoneley wave, commonly called a Schölte wave is generated. This is an unattenuated wave that decays exponentially with depth in both the fluid and solid materials.

The fluid supports a cylindrical compressional body wave and an exponentially decaying surface wave generated by the leaky Rayleigh wave. There are head waves generated in both the fluid and solid; they decay faster than the cylindrical body waves, and are generated by the cylindrical body waves that cannot satisfy the surface boundary conditions without this correction. If the wavespeed of the fluid is less than the shear wavespeed of the solid then the head waves generated by the acoustic cylindrical wave in the solid are evanescent. A schematic showing the radiated wavefronts for the waves generated by a point defect at a fluid-solid interface with an $\exp\{-i\omega t\}$ dependence suppressed is Figure 2.1. In this figure it is assumed that $k_o > k_s > k_d$.

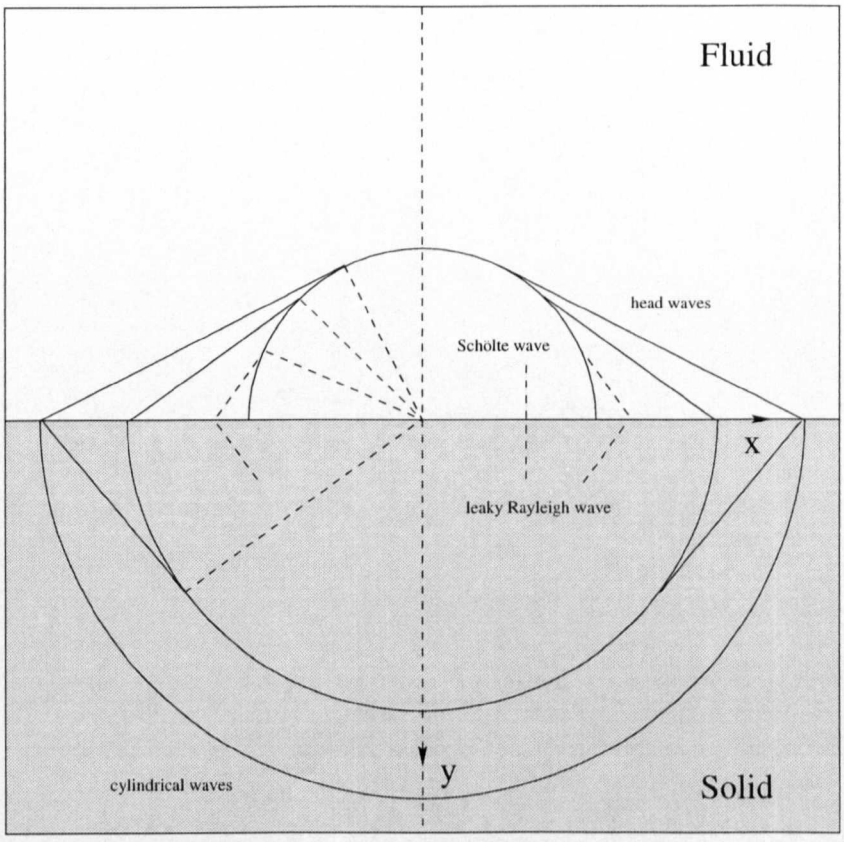

Figure 2.1. A schematic showing the radiated wavefronts for the waves generated by a point defect at a fluid-solid interface with an $\exp\{-i\omega t\}$ dependence suppressed.

Each problem will be expressed in two coordinate systems based on the length scales $1/k_s$ and a in the problem and solved asymptotically by matching. We could have chosen to normalise using either $1/k_o$ or $1/k_d$, but utilise $1/k_s$ for convenience. Each problem has a characteristic length a associated with it. It is assumed that $k_s a = \epsilon \ll 1$.

Use is made of outer and inner coordinate systems. The outer system $(\bar{x}, \bar{y})$, and the inner system (X, Y), are defined as

$$(\bar{x}, \bar{y}) = k_s(x, y), \ (X, Y) = \frac{1}{a}(x, y). \tag{2.2.7}$$

It can be seen that the inner and outer systems are related by $(\bar{x}, \bar{y}) = \epsilon(X, Y)$.

For purposes of matching we take the stresses to be invariant, namely $\sigma_{xy} = \bar{\sigma}_{\bar{x}\bar{y}} = \Sigma_{XY}$ *etc.* This results in the following rescalings for the potentials and displacements:

$$(\bar{u}_{\bar{x}}, \bar{u}_{\bar{y}}) = k_s(u_x, u_y), \ \ (\bar{\phi}, \bar{\psi}, \bar{\chi}) = k_s^2(\phi, \psi, \chi), \tag{2.2.8}$$

in the outer system, and

$$(U_X, U_Y) = \frac{1}{a}(u_x, u_y), \ \ (\Phi, \Psi, \mathcal{X}) = \frac{1}{a^2}(\phi, \psi, \chi), \tag{2.2.9}$$

in the inner system.

There are three types of surface discontinuity that may arise, and each is associated with a specific type of defect. This is demonstrated in the following sections.

2.3. A rigid strut

The first problem we consider can be stated as follows. A plane compressional wave is incident at an angle θ_i from the fluid on the defect at the fluid-solid interface. A rigid strut, length a, is considered normal to the interface; the geometry of the problem is shown in Figure 2.2. The boundary conditions

$$\sigma_{xy} = 0, \quad [\![\sigma_{yy}]\!] = 0, \quad [\![u_y]\!] = 0 \tag{2.3.1}$$

are taken on the interface $y = 0$, where the braces $[\![\ ]\!]$ denote the jump in a quantity across the interface; both the stresses σ_{yy} and the normal displacement u_y are continuous across $y = 0$. The fluid supports no shear stresses and so $\sigma_{xy} = 0$ on $y = 0$. The boundary condition taken on the strut $x = 0$, $-a < y < 0$ is $u_x = 0$. The incident field in the fluid is

$$\chi^{inc}(x, y) = a^2 \exp\left[\mathrm{i}k_o(x\cos\theta_i + y\sin\theta_i)\right], \tag{2.3.2}$$

where the amplitude a^2 is taken for convenience.

In the fluid we take the total wave field to be given by $\chi = \chi^{inc} + \chi^{ref} + \chi^{sc}$, where the superscripts *ref* and *sc* denote the reflected and scattered waves respectively, and formulate a boundary value problem for the scattered field; we take similar expressions for the stresses. The reflected and transmitted fields at a perfect interface are given by Brekhovskikh (1980); in the fluid the reflected field is determined to be

$$\chi^{ref}(x, y) = a^2 R_{ff} \exp\left[\mathrm{i}k_o(x\cos\theta_i - y\sin\theta_i)\right], \tag{2.3.3}$$

where R_{ff} is the reflection coefficient

$$\frac{S^-(k)}{S^+(k)} = \frac{R(k) - E(k)}{R(k) + E(k)}. \tag{2.3.4}$$

In these formulae $k = k_o\cos\theta_i$, $R(k)$ is the standard Rayleigh function, $R(k) = (2k^2 - k_s^2)^2 - 4k^2\gamma_s(k)\gamma_d(k)$, and $E(k) = \mathcal{E}k_s^4 k_o\gamma_d(k)/\gamma_o(k)k_d$. The functions $\gamma_d(k)$, $\gamma_s(k)$, and $\gamma_o(k)$ that appear are defined as $\gamma_q(k) = (k^2 - k_q^2)^{\frac{1}{2}}$ with $q = d,\ s,\ o$.

We construct the problem for the scattered potential $\mathcal{X}^{sc}$, dropping the superscript *sc* for convenience. To achieve this we subtract the solutions for the incident and reflected fields from the total field; the remaining problem is due to any surface defects.

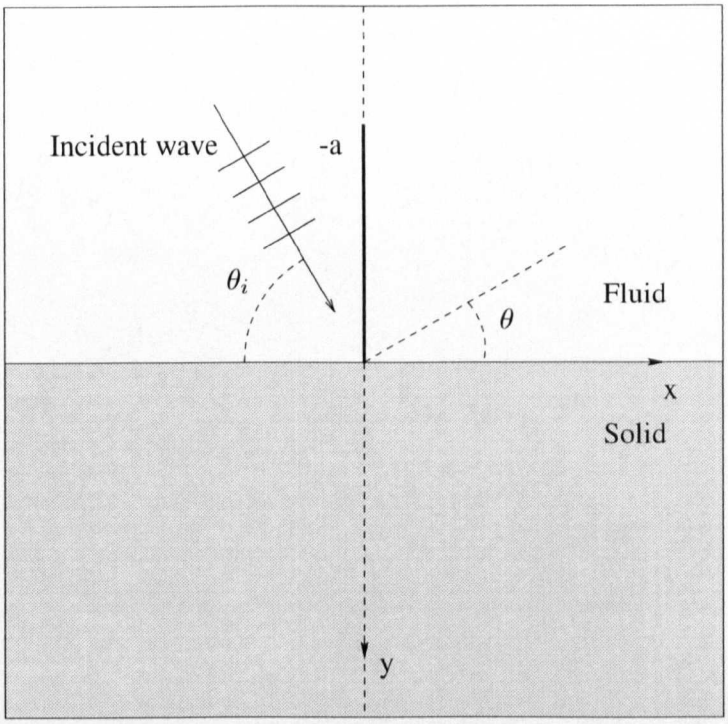

Figure 2.2. The incident wave field: a rigid strut.

2.3.1. *The inner problem*

In the inner coordinate system the Helmholtz equations (2.2.5) become

$$\left(\nabla^2 + \epsilon^2 \frac{k_d^2}{k_s^2}\right) \Phi = 0, \quad (\nabla^2 + \epsilon^2)\Psi = 0, \quad \left(\nabla^2 + \epsilon^2 \frac{k_o^2}{k_s^2}\right) \mathcal{X} = 0, \tag{2.3.5}$$

where $\nabla^2 = \partial^2/\partial X^2 + \partial^2/\partial Y^2$, and we recall that $\epsilon \ll 1$, with the boundary conditions now applicable on $Y = 0$ and $X = 0$, $-1 < Y < 0$.

To analyse the inner problem, and in particular the continuity conditions across $Y = 0$ in this limit, let us consider the stress Σ_{YY} in the fluid, and take suitable expansions in the stresses and displacement, in the form $U_Y = U_{Y\,0} + \epsilon U_{Y\,1} + o(\epsilon^2)$, say. Clearly $\Sigma_{YY} = \lambda_f \nabla^2 \mathcal{X}$ and from (2.3.5) $\nabla^2 \mathcal{X} = O(\epsilon^2)\mathcal{X}$. This implies that the stress induced by the defect is $O(\epsilon^2)\mathcal{X}$ in the fluid and this has important consequences due to the continuity conditions (2.3.1). It suggests that the stress Σ_{YY} at the interface is also $O(\epsilon^2)\mathcal{X}$. Thus to leading order this implies that the solid has traction-free boundary conditions upon the surface and since it is stress-free that we can take $U_Y = 0$ on $Y = 0$. The fluid-solid problems therefore uncouple, and for the leading order problems we are able to treat the fluid and solid half space responses separately. This does not rely upon any light fluid loading limit or similar simplification and is a general property of the equations; this separation allows considerable progress to be made.

By considering the inner limit of the incident and reflected waves we find $\mathcal{X}_0$ to be zero, and construct the order ϵ problem for $\mathcal{X}_1$, dropping the subscript for convenience. The governing equation is now just Laplace's equation $\nabla^2\mathcal{X} = 0$, with the boundary conditions

$$\frac{\partial \mathcal{X}}{\partial Y} = 0 \text{ on } Y = 0, \quad \frac{\partial \mathcal{X}}{\partial X} = -\frac{2ik_oR(k)}{k_sS^+(k)}\cos\theta_i \text{ on } -1 < Y < 0, \ X = 0, \tag{2.3.6}$$

which can be rewritten in polar coordinates with $X = R\cos\theta$, $Y = -R\sin\theta$ to give

$$\frac{\partial \mathcal{X}}{\partial \theta} = 0 \text{ on } \theta = 0, \ \pi, \quad \frac{\partial \mathcal{X}}{\partial \theta} = \frac{2ik_oR(k)}{k_sS^+(k)}R\cos\theta_i \text{ on } \theta = \frac{1}{2}\pi. \tag{2.3.7}$$

The problem is solved using Mellin transforms together with the Wiener–Hopf technique. The Mellin transform in R, and its inverse, are defined as

$$\langle F(s)\rangle = \int_0^\infty F(R)R^{s-1}\mathrm{d}R, \quad F(R) = \frac{1}{2\pi i}\int_{c-\mathrm{i}\infty}^{c+\mathrm{i}\infty}\langle F(s)\rangle R^{-s}\mathrm{d}s, \tag{2.3.8}$$

where s is the transform variable. Here c is chosen from the appropriate analytical properties of the Mellin transform. The solution is now deduced, see for instance Datta (1979), for $0 \le \theta \le \frac{\pi}{2}$, $0 < \mathrm{Re}(c) < 1$ as

$$\mathcal{X}(R,\theta) = -\frac{k_oR(k)}{\pi k_sS^+(k)}\int_{c-\mathrm{i}\infty}^{c+\mathrm{i}\infty}\frac{\Gamma\left(\frac{s}{2}\right)\Gamma\left(\frac{3}{2}-\frac{s}{2}\right)}{\sqrt{\pi}(s^2-1)}\cos\theta_i\cos s\theta R^{-s}\mathrm{d}s, \tag{2.3.9}$$

with $\mathcal{X}(R,\pi-\theta) = -\mathcal{X}(R,\theta)$. The outer limit of $\mathcal{X}(R,\theta)$ is found by closing in the right half plane and is, to leading order,

$$\mathcal{X}(R,\theta) \sim \frac{ik_oR(k)}{k_sS^+(k)}R^{-1}\cos\theta_i\cos\theta, \tag{2.3.10}$$

this is required to match with the inner limit of the outer problem.

2.3.2. *The outer problem*

In the outer coordinate system the strut reduces to $-\epsilon < \bar{y} < 0$, that is, effectively to a point defect. The Helmholtz equations (2.2.5) become

$$\left(\nabla^2 + \frac{k_d^2}{k_s^2}\right)\bar{\phi} = 0, \quad (\nabla^2+1)\bar{\psi} = 0, \quad \left(\nabla^2 + \frac{k_o^2}{k_s^2}\right)\bar{\chi} = 0, \tag{2.3.11}$$

where $\nabla^2 = \partial^2/\partial\bar{x}^2 + \partial^2/\partial\bar{y}^2$. The boundary conditions for the scattered field,

$$\bar{\sigma}_{\bar{x}\bar{y}} = 0, \quad [\![\bar{\sigma}_{\bar{y}\bar{y}}]\!] = 0, \quad [\![\bar{u}_{\bar{y}}]\!] = Q\delta'(\bar{x}), \tag{2.3.12}$$

are taken on the interface $\bar{y} = 0$, where $\delta(\bar{x})$ is the generalised function, the prime $'$ denotes differentiation with respect to the argument, and Q is to be determined.

The boundary conditions can, in general, be simulated in the outer field by expansions of the form $\sigma_{\bar{x}\bar{y}} = a_1\delta(\bar{x}) + a_2\delta'(\bar{x}) + \cdots$, see for instance Sabina & Willis (1977), with similar expressions for the other boundary conditions. In this example only the jump in the normal displacement term contributes at this order, similar expansions could be used in later sections. A slightly different approach is adopted by Abrahams & Wickham (1992a, 1992b) and could be used to generate higher order terms.

The Fourier transform in $\bar{x}$, and its inverse, are defined as

$$f^\star(\xi) = \int_{-\infty}^{\infty} f(\bar{x})e^{\mathrm{i}\xi\bar{x}}\mathrm{d}\bar{x}, \quad f(\bar{x}) = \frac{1}{2\pi}\int_C f^\star(\xi)e^{-\mathrm{i}\xi\bar{x}}\mathrm{d}\xi, \tag{2.3.13}$$

where ξ is the transform variable. The inversion path C runs along the real axis from $-\infty$ to ∞ and is indented to lie below any singularities on the positive real axis and above any that lie on the negative real axis. We now take the Fourier transforms of the governing equations in the scattered potentials and the boundary conditions to give

$$\frac{\mathrm{d}^2\bar{\phi}^\star}{\mathrm{d}\bar{y}^2} - \left(\xi^2 - \frac{k_d^2}{k_s^s}\right)\bar{\phi}^\star = 0, \quad \frac{\mathrm{d}^2\bar{\psi}^\star}{\mathrm{d}\bar{y}^2} - (\xi^2 - 1)\bar{\psi}^\star = 0, \quad \frac{\mathrm{d}^2\bar{\chi}^\star}{\mathrm{d}\bar{y}^2} - \left(\xi^2 - \frac{k_o^2}{k_s^2}\right)\bar{\chi}^\star = 0, \tag{2.3.14}$$

and $\bar{\sigma}^\star_{\bar{x}\bar{y}} = 0$, $[\![\bar{\sigma}^\star_{\bar{y}\bar{y}}]\!] = 0$, $[\![\bar{u}^\star_{\bar{y}}]\!] = -\mathrm{i}\xi Q$, on $\bar{y} = 0$. The appropriate expressions for $\bar{\phi}^\star$, $\bar{\psi}^\star$, and $\bar{\chi}^\star$ are

$$\bar{\phi}^\star(\xi,\bar{y}) = \alpha(\xi)\exp\left\{-\left(\xi^2 - \frac{k_d^2}{k_s^2}\right)^{\frac{1}{2}}\bar{y}\right\}, \tag{2.3.15}$$

$$\bar{\psi}^\star(\xi,\bar{y}) = \beta(\xi)\exp\left\{-\left(\xi^2 - 1\right)^{\frac{1}{2}}\bar{y}\right\}, \tag{2.3.16}$$

$$\bar{\chi}^\star(\xi,\bar{y}) = \zeta(\xi)\exp\left\{\left(\xi^2 - \frac{k_o^2}{k_s^2}\right)^{\frac{1}{2}}\bar{y}\right\}, \tag{2.3.17}$$

where the coefficients α, β, and ζ are to be determined by the boundary conditions.

The representations for the Fourier transformed stresses and displacements are given in Appendix 2.A, and the inverse Fourier transform now yields the following expressions for the scattered potentials

$$\bar{\phi}(\bar{x},\bar{y}) = -\frac{\mathrm{i}}{2\pi}\int_{-\infty}^{\infty}\frac{k_s(2\xi^2-1)\xi E(k_s\xi)}{\gamma_d(k_s\xi)S^+(k_s\xi)}Qe^{-\mathrm{i}\xi\bar{x}-\left(\xi^2-\frac{k_d^2}{k_s^2}\right)^{\frac{1}{2}}\bar{y}}\mathrm{d}\xi, \tag{2.3.18}$$

$$\bar{\psi}(\bar{x},\bar{y}) = -\frac{1}{\pi}\int_{-\infty}^{\infty}\frac{\xi^2 E(k_s\xi)}{S^+(k_s\xi)}Qe^{-\mathrm{i}\xi\bar{x}-(\xi^2-1)^{\frac{1}{2}}\bar{y}}\mathrm{d}\xi, \tag{2.3.19}$$

$$\bar{\chi}(\bar{x},\bar{y}) = \frac{\mathrm{i}}{2\pi}\int_{-\infty}^{\infty} \frac{k_s\xi R(k_s\xi)}{\gamma_o(k_s\xi)S^+(k_s\xi)} Q e^{-\mathrm{i}\xi\bar{x}+\left(\xi^2-\frac{k_o^2}{k_s^2}\right)^{\frac{1}{2}}\bar{y}}\mathrm{d}\xi. \tag{2.3.20}$$

The limit as $|\xi| \to \infty$ in the transform space corresponds to the limit as $x \to 0$ in the physical domain, thus taking this inner limit, and evaluating the resulting transform, gives

$$\bar{\chi}(\bar{r},\theta) \sim \frac{1}{\pi\bar{r}} Q\cos\theta \tag{2.3.21}$$

to within an arbitrary constant.

This is now matched to the outer limit of the inner solution (2.3.10), writing both limits in the original coordinate system, this gives

$$Q = \epsilon^2 a^2 \pi \mathrm{i} k_o k_s \frac{R(k)}{S^+(k)}\cos\theta_i. \tag{2.3.22}$$

Note that we have retained the amplitude a^2 we introduced in (2.3.3) in the expression (2.3.22).

2.3.3. *Discussion*

Thus to order ϵ^2, we have the total wave field

$$\begin{aligned}\chi(x,y) = \chi^{inc}(x,y) + \chi^{ref}(x,y) \\ - \epsilon^2 a^2 \frac{k_o}{2k_s^2}\int_{-\infty}^{\infty} \frac{\xi R(k)R(\xi)}{\gamma_o(\xi)S^+(k)S^+(\xi)}\cos\theta_i e^{-\mathrm{i}\xi x+\gamma_o(\xi)y}\mathrm{d}\xi,\end{aligned} \tag{2.3.23}$$

where χ^{inc} and χ^{ref} are given by (2.3.2) and (2.3.3) respectively, and we have the following expression for the jump in the normal displacement u_y,

$$[\![u_y]\!] = \epsilon^2 a^2 \pi \mathrm{i}\frac{k_o}{k_s^2}\frac{R(k)}{S^+(k)}\cos\theta_i \delta'(x). \tag{2.3.24}$$

It is at first sight unclear that by matching the fields in the fluid that we have automatically matched in the solid as well. Thus as a consistency check upon our analysis we use the solution found within the fluid to drive the solid response. Here it is useful to repose the problem and match the dilatation in the solid. The dilatation e is defined to be $u_{i,i}$ and in the outer problem the dilatation reduces to $e = \nabla^2\bar{\phi} = -k_d^2/k_s^2\bar{\phi}$. Thus from our transform analysis and by a similar argument to the previous section the inner limit as $|\xi| \to \infty$, is

$$e \sim \frac{k_d k_o}{\pi(k_d^2 - k_s^2)}\mathcal{E}Q\bar{r}^{-1}\cos\theta, \tag{2.3.25}$$

to within an arbitrary constant, where we have utilised the limit $R(k_s\xi) \to 2(k_d^2 - k_s^2)k_s^2\xi^2$.

In the inner problem, the dilatation can be written as the stress combination

$$\Sigma_{RR} + \Sigma_{\theta\theta} = 2(\lambda+\mu)e. \tag{2.3.26}$$

We now form the complex stress combination $R^2(\Sigma_{R\theta} + \mathrm{i}\Sigma_{\theta\theta})$ and take the Mellin transform, Hein & Erdogan (1971), to obtain

$$\left\langle R^2(\Sigma_{R\theta} + i\Sigma_{\theta\theta})\right\rangle = (s+1)\left(\frac{\mathrm{d}}{\mathrm{d}\theta} + \mathrm{i}s\right)\langle \mathcal{A}i\rangle \tag{2.3.27}$$

in terms of the transformed Airy stress function, $\langle \mathcal{A}i\rangle = Ae^{\mathrm{i}s\theta} + \bar{A}e^{-\mathrm{i}s\theta} + Be^{\mathrm{i}(s+2)\theta} + \bar{B}e^{-\mathrm{i}(s+2)\theta}$. The stress boundary conditions on the surface are taken to be those forced by the inner solution (2.3.9) deduced in the fluid. The boundary conditions are

$$\Sigma_{R\theta} + \mathrm{i}\Sigma_{\theta\theta} = \pm \mathrm{i}\sigma R^{-1} \text{ on } \theta = 0,\ \pi, \text{ respectively for } R > 1, \tag{2.3.28}$$

where $\sigma = -\epsilon a^2 \mathrm{i}\mu k_o^2 R(k)\mathcal{E}\cos\theta_i / k_s k_d S^+(k)$. As we are interested in the outer limit of the inner problem we have simply taken the stress to be zero for $R < 1$ on $\theta = 0, \pi$.

We can determine $\mathcal{A}i$ to yield the inverse Mellin transform

$$2(\lambda+\mu)e = \frac{1}{2\pi\mathrm{i}}\int_{c-\mathrm{i}\infty}^{c+\mathrm{i}\infty} \frac{2\sigma}{(s+1)\sin\frac{1}{2}s\pi}\sin\left[(s+2)\theta - \frac{1}{2}s\pi\right] R^{-(s+2)}\mathrm{d}s \tag{2.3.29}$$

where the outer limit is to leading order,

$$2(\lambda+\mu)e \sim 2\sigma R^{-1}\cos\theta \tag{2.3.30}$$

found by closing in the left half plane. This expression for the dilatation e matches with (2.3.25) when Q is written explicitly. This suggests that both the uncoupling of the inner problems is correct and that it is sufficient, to this order, to match within the fluid (or in later sections in the solid); further verification follows from evaluating the inner limit of σ_{yy} in the solid, found as $\sigma_{yy} = -\mathrm{i}2\epsilon^3\mu\mathcal{E}k_o^2 R(k)\cos\theta_i\cos\theta/k_d k_s S^+(k)R$, that is, it is clearly $O(\epsilon^2)$ times (2.3.10).

The far-field scattered cylindrical wave structure is extracted from (2.3.23) using the saddle point method,

$$\chi(r,\theta) \sim \mathrm{i}\epsilon^2 a^2 \frac{k_o^2}{k_s^2}\left(\frac{\pi}{2k_o r}\right)^{\frac{1}{2}} \frac{\cos\theta R(k)R(k_o\cos\theta)}{S^+(k)S^+(k_o\cos\theta)}\cos\theta_i e^{\mathrm{i}k_o r - \frac{1}{4}\mathrm{i}\pi} \tag{2.3.31}$$

for $k_o r \gg 1$. This potential may be written as $D(\theta)e^{\mathrm{i}k_o r}/(k_o r)^{1/2}$ where $D(\theta)$ is the directivity associated with the wave. For comparative purposes the angular dependence of a typical directivity shape given by $|\cos\theta R(k_o\cos\theta)/S^+(k_o\cos\theta)|$ is shown for two sets of material parameters, in Figures 2.3a, 2.3b.

The first set of material parameters taken, $k_d = \frac{1}{2}k_s = \frac{1}{6}k_o$, is typical of metal-water combinations; solids with relatively high densities and wavespeeds relative to the fluid. The Rayleigh wavespeed is $k_r = 1.07236k_s$, and the Schölte wavespeed, with $\mathcal{E} = 0.08$,

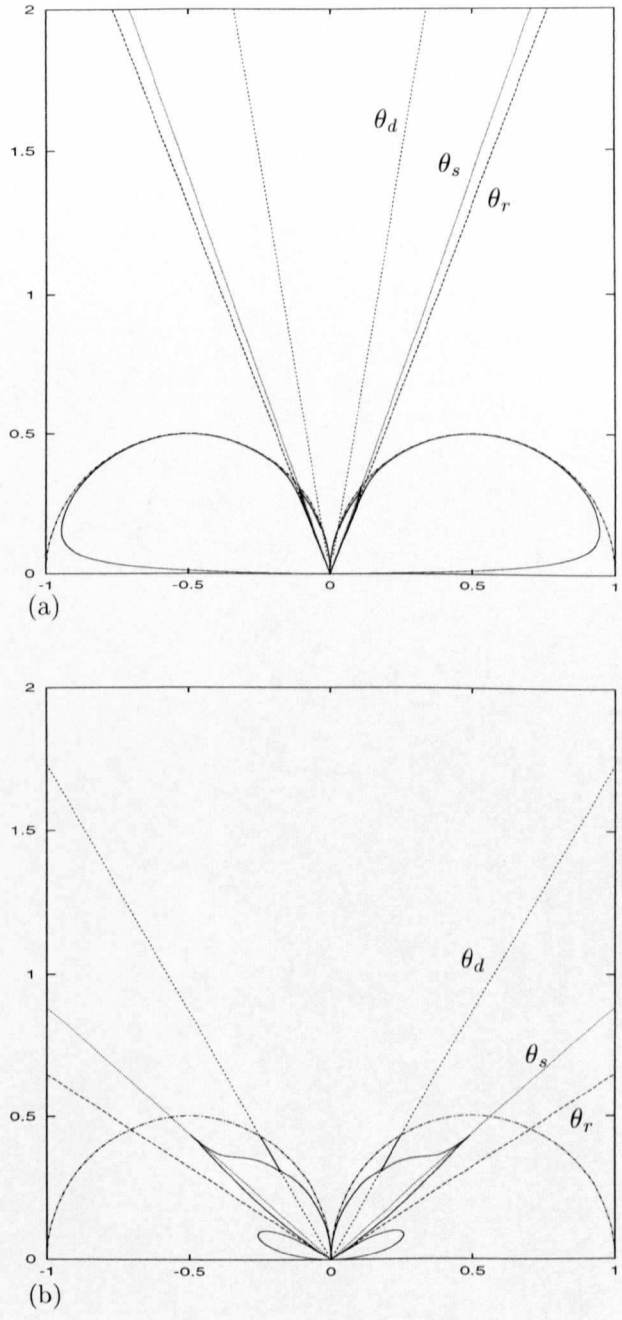

Figure 2.3. A typical directivity shape for scattering by a rigid strut. (a) $\mathcal{E} = 0.08$. (b) $\mathcal{E} = 0.32$.

is $k_{sch} = 1.00075k_o$. The second set of material parameters taken, $k_d = \frac{2}{3}k_s = \frac{1}{2}k_o$, with $\mathcal{E} = 0.32$, is more typical of rock-water combinations. Here the Poisson's ratio is small, that is, $\nu = 0.1$.

In the following discussion the critical angles θ_d, θ_s, and θ_r are defined as θ_q =

$\cos^{-1}(k_q/k_o)$ with $q = d,\ s,\ r$; k_r is the wavenumber associated with the Rayleigh wave that would exist in the absence of fluid. The assumption that the compressional wavespeed of the fluid is less than the shear wavespeed of the solid implies that $\theta_d > \theta_s > \theta_r$. The critical angles θ_d and θ_s are where the head waves meet the cylindrical wave, and θ_r is the angle along which the leaky Rayleigh wave sheds energy into the fluid; these are important to the dominant features of the directivity patterns. The angles are shown in Figures 2.3a, 2.3b by the dashed lines. The limiting case $\mathcal{E} = 0$ that corresponds to a rigid strut on a rigid plate and an acoustic dipole response is shown by the dotted-dashed line.

The beam formations along θ_d and θ_s are generated by interaction with shear and compressional waves in the solid. This response becomes more evident for low Poisson's ratio, Figure 2.3b. In contrast to the cases we consider in the next two sections, the directivity vanishes along the Rayleigh angle θ_r. This brings about the distinctive lobes in $0 \leq \theta \leq \theta_r$ in Figures 2.3a, 2.3b. The lobes are shortened as θ_r decreases; this corresponds to k_r approaching k_o, Figure 2.3b.

2.4. An edge crack

Surface breaking cracks are of particular importance with regard to acoustic microscopy and that device has been particularly adept at imaging cracks in a variety of situations, the book by Briggs (1992) contains several examples. The problem we now consider can be stated as follows. A plane compressional wave is incident normally from the fluid on the defect at the fluid-solid interface. An edge crack, length a, is considered normal to the interface as shown in Figure 2.4.

The continuity conditions (2.3.1) are taken on the interface $y = 0$. The boundary conditions taken on the crack $x = 0,\ 0 < y < a$, are $\sigma_{xx} = 0,\quad \sigma_{yx} = 0$; the crack is stress free. The crack faces are assumed not to interact with each other; this is a viable assumption if we are modelling an open crack of finite width. The incident field in the fluid is taken in the form

$$\chi^{inc}(x, y) = a^2 \exp(\mathrm{i}k_o y), \tag{2.4.1}$$

and the transmitted field at a perfect interface (Brekhovskikh, 1980) is determined to be

$$\phi^{tr}(x, y) = 2a^2 \frac{k_o}{k_d} \frac{\mathcal{E}}{1 + \mathcal{E}} \exp(\mathrm{i}k_d y), \quad \psi^{tr}(x, y) = 0. \tag{2.4.2}$$

In contrast to the incident field (2.3.2) in Section 2.3, the normally incident wave has no x dependence.

These fields are subtracted out to leave a boundary value problem for the scattered

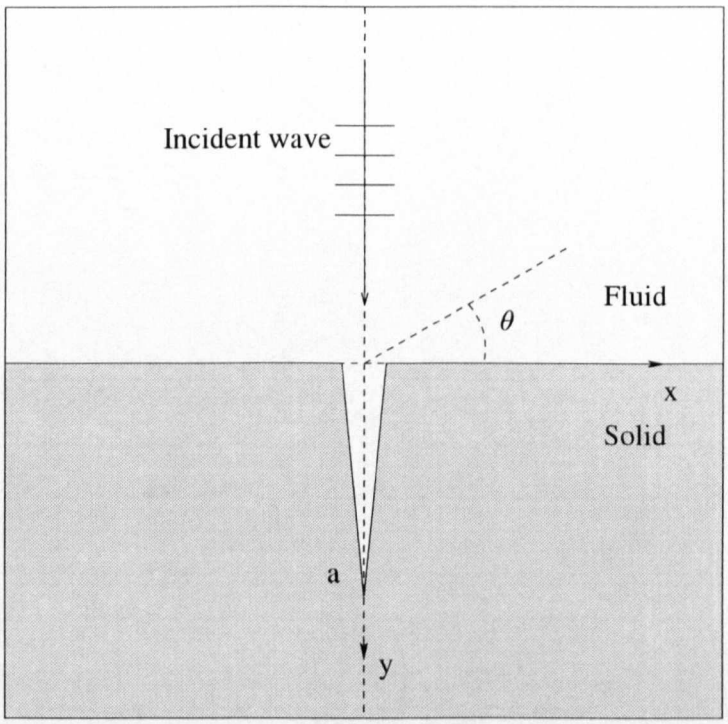

Figure 2.4. The incident wave field: an edge crack.

field. Taking a suitable expansion in the stresses and displacement, and by a similar argument to the above, it can be seen that the fluid-solid problems uncouple in the inner problem and we treat the fluid and solid half space responses separately. Here it is convenient to match the dilatation in the solid. The boundary conditions for the scattered field in this inner region become

$$\Sigma_{R\vartheta} + \mathrm{i}\Sigma_{\vartheta\vartheta} = 0 \text{ on } \vartheta = \frac{1}{2}\pi, \ -\frac{1}{2}\pi, \tag{2.4.3}$$

$$\Sigma_{R\vartheta} + \mathrm{i}\Sigma_{\vartheta\vartheta} = -\mathrm{i}\sigma \text{ on } \vartheta = 0, \text{ for } R < 1, \tag{2.4.4}$$

where $\vartheta = \theta + \frac{1}{2}\pi$ and $\sigma \sim -2a^2\lambda k_o k_d \mathcal{E}/(1+\mathcal{E})$.

Symmetry is used to break this into a problem defined in the quadrant $0 \leq \vartheta \leq \frac{1}{2}\pi$ and is formulated in terms of the Mellin transform. This can then be solved using the Wiener–Hopf technique as in Stallybrass (1970). The outer limit of the dilatation given by this solution is deduced as

$$2(\lambda+\mu)e = 2\sigma h_-(-2)h_+(0)R^{-2}\cos 2\vartheta, \tag{2.4.5}$$

where the functions

$$\log h_-(-2) = \log h_+(0) = -\frac{1}{\pi}\int_0^\infty \log\left(1 - \frac{\eta^2}{\sinh^2 \frac{1}{2}\pi\eta}\right)\frac{\mathrm{d}\eta}{\eta^2+1} \sim 0.114687 \tag{2.4.6}$$

are deduced from the Wiener–Hopf analysis.

Following the construction of the problem in the outer coordinate system of the rigid strut we have the same governing equations together with the boundary conditions for the scattered field,

$$\bar{\sigma}_{\bar{x}\bar{y}} = Q\delta'(\bar{x}),\ [\![\bar{\sigma}_{\bar{y}\bar{y}}]\!] = 0,\ [\![\bar{u}_{\bar{y}}]\!] = 0, \tag{2.4.7}$$

taken on the interface $\bar{y} = 0$, where Q is to be determined. This choice proves to be sufficient for the matching procedure. Now taking the Fourier transform gives $\bar{\sigma}^{\star}_{\bar{x}\bar{y}} = -\mathrm{i}\xi Q$, $[\![\bar{\sigma}^{\star}_{\bar{y}\bar{y}}]\!] = 0$, $[\![\bar{u}^{\star}_{\bar{y}}]\!] = 0$, on $\bar{y} = 0$, and Fourier transforms yield an expression for the scattered potential as

$$\bar{\phi}(\bar{x},\bar{y}) = \frac{1}{2\pi}\int_{-\infty}^{\infty} \frac{k_s\xi^2\left[2k_s^2\gamma_s(k_s\xi)\gamma_d(k_s\xi) - E(k_s\xi)\right]}{\gamma_d(k_s\xi)S^+(k_s\xi)\mu} Q e^{-\mathrm{i}\xi\bar{x} - \left(\xi^2 - \frac{k_d^2}{k_s^2}\right)^{\frac{1}{2}}\bar{y}}\,\mathrm{d}\xi, \tag{2.4.8}$$

with similar expressions for $\bar{\psi}$ and $\bar{\chi}$.

It can be seen as in (2.3.25) that taking the inner limit as $|\xi| \to \infty$ the dilatation reduces to

$$e \sim \frac{k_d^2}{\pi(k_d^2 - k_s^2)\mu} Q\bar{r}^{-2}\cos 2\theta \tag{2.4.9}$$

to leading order. Matching now gives Q explicitly as

$$Q = \epsilon^2\pi\sigma h_+^2(0). \tag{2.4.10}$$

Thus to order ϵ^2, we have the following expression for the shear stresses σ_{xy} on the interface,

$$\sigma_{xy} = \epsilon^2 a^2\pi\lambda\frac{k_o k_d}{k_s^2}\frac{\mathcal{E}}{1+\mathcal{E}}h_+^2(0)\delta'(x). \tag{2.4.11}$$

The inner limit of σ_{yy} in the fluid is consistent with our results, and this suggests that our separation argument in the inner problem is correct.

The far field scattered cylindrical wave structure is extracted from an inverse Fourier transform representation for the fluid potential $\chi(x,y)$, see for instance (2.3.23), using the saddle point method,

$$\chi(r,\theta) \sim \mathrm{i}\frac{k_o^2}{k_s^2}\frac{Q}{\mu(2\pi k_o r)^{\frac{1}{2}}}\frac{\cos^2\theta\left[2k_o^2\cos^2\theta - k_s^2 - 2\gamma_s(k_o\cos\theta)\gamma_d(k_o\cos\theta)\right]}{S^+(k_o\cos\theta)}e^{\mathrm{i}k_o r - \frac{1}{4}\mathrm{i}\pi} \tag{2.4.12}$$

for $k_o r \gg 1$, where Q is given by (2.4.10). The angular dependence of a typical directivity shape given by $|\cos^2\theta[2k_o^2\cos^2\theta - k_s^2 - 2\gamma_s(k_o\cos\theta)\gamma_d(k_o\cos\theta)]/S^+(k_o\cos\theta)|$ is shown for the material parameters and critical angles described above, in Figures 2.5a, 2.5b.

Note the strong beam formation along θ_r, in Figure 2.5a, consistent with the leaky

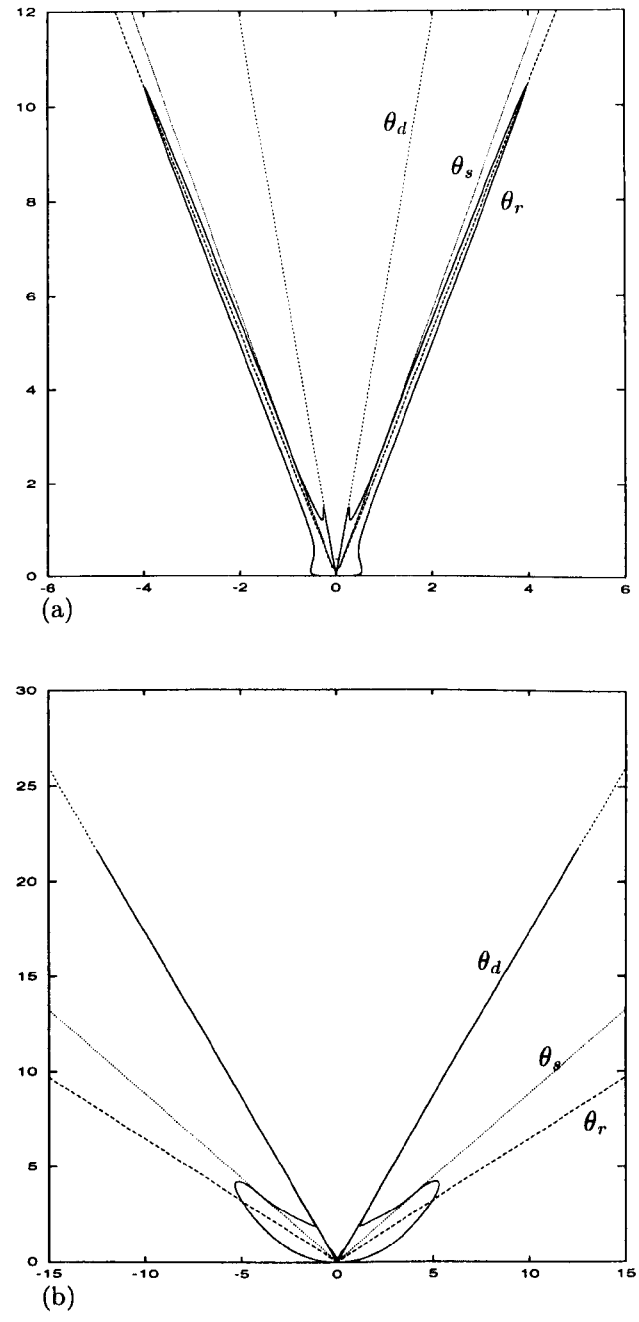

Figure 2.5. A typical directivity shape for scattering by an edge crack. (a) $\mathcal{E} = 0.08$. (b) $\mathcal{E} = 0.32$.

Rayleigh wave that occurs in this light fluid loading limit. The response becomes less evident as $\mathcal{E}$ increases. The lesser peaks in Figure 2.5a form along θ_d where the angular dependence of the directivity reduces to $|k_d^2/k_o^2(2k_d^2 - k_s^2)|$. Thus for low Poisson's

ratio, such as the material parameters chosen in Figure 2.5b; this response can become dominant.

2.5. A rigid strip

Perhaps surprisingly the representation of a defect by a jump in the normal stress has not, thus far, arisen; particularly as this is sometimes taken to be a model for surface breaking cracks. To illustrate how this representation occurs we consider a plane compressional wave, harmonic in time with frequency w, incident at an angle θ_i from the fluid on the defect at the fluid-solid interface. A rigid strip, length $2a$, is considered lying along the interface as shown in Figure 2.6.

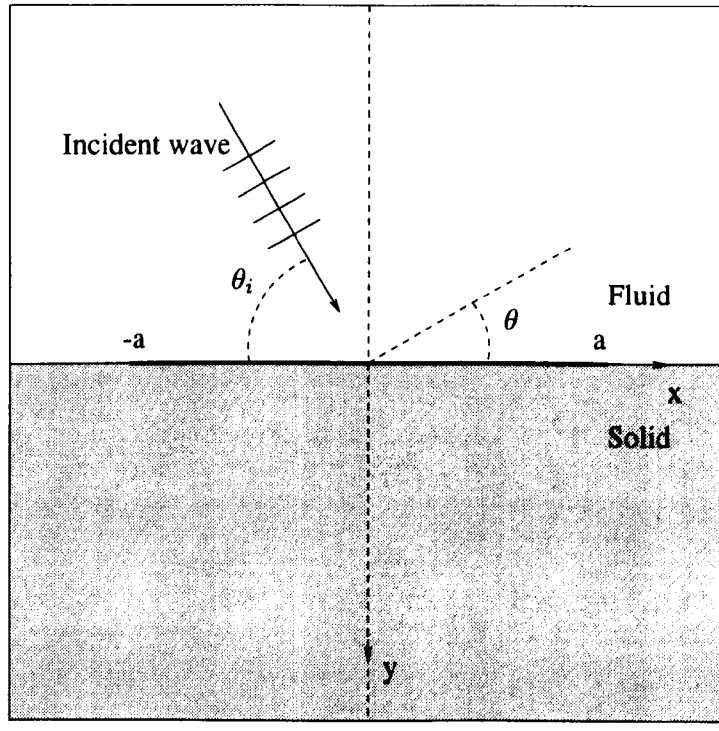

Figure 2.6. The incident wave field: a rigid strip.

The continuity conditions (2.3.1) are taken on the interface $y = 0$, $|x| > a$. The boundary conditions taken on the strip $y = 0$, $|x| < a$, are $\sigma_{xy} = 0$, $u_y = 0$; for simplicity the rigid strip is smoothly bonded to the solid. The incident field in the fluid is

$$\chi^{inc}(x, y) = \mathrm{i}a^2 \exp\left[\mathrm{i}k_o(x \cos\theta_i + y \sin\theta_i)\right]. \tag{2.5.1}$$

The introduction of the imaginary amplitude is to accommodate the complex variable method of Muskhelishvili (1953); this assumes that the stresses and displacements are

real. The reflected field at a perfect interface (Brekhovskikh, 1980) is

$$\chi^{ref}(x,y) = \mathrm{i}a^2 R_{ff} \exp\left[\mathrm{i}k_o(x\cos\theta_i - y\sin\theta_i)\right]. \tag{2.5.2}$$

These fields are subtracted out to leave a boundary value problem for the scattered fields and this is now solved using matched asymptotic expansions on the interface $y = 0$. The fluid-solid problems uncouple once again in the inner problem and we treat the fluid and solid half space responses separately. In this section it is required that the normal displacements in the solid are matched; matching the dilatation is no longer sufficient. As an aside this example demonstrates that it is not, as suggested by Abrahams & Wickham (1992b), always sufficient in elastodynamic half space problems to just match the dilatation.

Without loss of generality matching is performed in this example on the plane $Y = 0$. Treating the leading order boundary value problem that occurs in the solid we find that in the inner coordinate system the boundary conditions for the scattered field are

$$U_Y = q, \quad \Sigma_{XY} = 0 \text{ on } Y = 0, \text{ for } |X| < 1, \tag{2.5.3}$$

$$\Sigma_{YY} - \mathrm{i}\Sigma_{XY} = 0 \text{ on } Y = 0, \text{ for } |X| > 1, \tag{2.5.4}$$

where $q \sim 2ak_oE(k)\sin\theta_i/S^+(k)$.

The problem is solved by formulating it in terms of a harmonic function $\Omega(z)$ where $z = X + \mathrm{i}Y$; the representations for the stresses and displacements in terms of $\Omega(z)$ are given in Appendix 2.B (Muskhelishvili, 1953). The solution is deduced, England (1971), as

$$U_Y(X,0) = \frac{k_s^2}{2\pi(k_d^2 - k_s^2)\mu} F \log\left[|X| + (X^2-1)^{\frac{1}{2}}\right] + q, \text{ for } |X| > 1, \tag{2.5.5}$$

where F is the unknown resultant force and q is the known displacement. The outer limit of $U_Y(X,0)$ is

$$U_Y(X,0) = \frac{k_s^2}{2\pi(k_d^2 - k_s^2)\mu} F \log 2|X| + q. \tag{2.5.6}$$

To match with this outer limit we take the boundary conditions for the outer problem as

$$\bar{\sigma}_{\bar{x}\bar{y}} = 0, \ [\![\bar{\sigma}_{\bar{y}\bar{y}}]\!] = Q\delta(\bar{x}), \ [\![\bar{u}_{\bar{y}}]\!] = 0, \tag{2.5.7}$$

on the interface $\bar{y} = 0$, where Q is to be determined. Taking the Fourier transform gives $\bar{\sigma}^\star_{\bar{x}\bar{y}} = 0$, $[\![\bar{\sigma}^\star_{\bar{y}\bar{y}}]\!] = Q$, $[\![\bar{u}^\star_{\bar{y}}]\!] = 0$, on $\bar{y} = 0$, and after solving the transformed field equation and taking the inverse Fourier transform, yields an expression for the normal displacement as

$$\bar{u}_{\bar{y}}(\bar{x},0) = \frac{1}{2\pi}\int_{-\infty}^{\infty} \frac{k_s^3\gamma_d(k_s\xi)}{\mu S^+(k_s\xi)} Q e^{-\mathrm{i}\xi\bar{x}}\mathrm{d}\xi. \tag{2.5.8}$$

The inner limit is found by taking the limit as $|\xi| \to \infty$,

$$\bar{u}_{\bar{y}}(\bar{x},0) \sim \frac{k_s^2}{2\pi(k_s^2-k_d^2)\mu} Q \log\frac{|\bar{x}|}{2} + \frac{Q}{\mu}\alpha \tag{2.5.9}$$

where α is a constant to be determined from the integral (2.5.8) by a numerical method. The representation for the integral, in terms of the integration variable $k_s\xi$, is given in Appendix 2.C. This limit (2.5.9) is matched with (2.5.6) above to give

$$Q = -\epsilon F. \tag{2.5.10}$$

To determine F we need to match the terms like ϵ^0, namely F is determined from

$$F\left(\alpha + \frac{k_s^2}{2\pi(k_s^2-k_d^2)}\log\frac{\epsilon}{4}\right) + \mu q = 0. \tag{2.5.11}$$

Here we have adopted the matching procedure described in Crighton & Leppington (1973), that is, the $\log\epsilon$ terms are grouped with the constant terms; terms are ordered algebraically only.

Thus the rigid strip is approximated by the following expression for the jump in the normal stresses σ_{yy},

$$[\![\sigma_{yy}]\!] = \frac{2a^2\mu k_o \dfrac{E(k)}{S^+(k)}\sin\theta_i}{\alpha + \dfrac{k_s^2}{2\pi(k_s^2-k_d^2)}\log\dfrac{\epsilon}{4}}\delta(x). \tag{2.5.12}$$

Similarly consistency checks to those performed in the previous sections can be utilised to validate the separation approach.

The boundary value problem can alternatively be formulated in terms of integral equations; in the absence of the fluid see Wickham (1977). The displacement boundary condition q is used to reduce the problem to an integral equation of the first kind,

$$q(p,0) = \int_{-a}^{a} \frac{\sigma_{yy}(x,0)}{\mu}\mathcal{L}(|x-p|)\mathrm{d}x, \text{ for } |p| \le a \tag{2.5.13}$$

where the kernel is the inverse Fourier transform

$$\mathcal{L}(|x-p|) = \frac{k_s^2}{2\pi}\int_{-\infty}^{\infty}\frac{\gamma_d(\xi)}{S^+(\xi)}e^{-i\xi|x-p|}\mathrm{d}\xi. \tag{2.5.14}$$

This equation can be shown to be equivalent to a certain integral equation of the second kind with a kernel which is small in the low frequency limit. In the absence of the fluid the iterative solution of the integral equation of the second kind is given by Wickham (1977) who gives an explicit asymptotic formula for the normal stresses in terms of the

prescribed displacement, Poisson's ratio, and the parameter ϵ. To leading order this agrees with the results here.

Once again the far field scattered cylindrical wave structure is extracted from an inverse Fourier transform representation for the fluid potential $\chi(x,y)$,

$$\chi(r,\theta) \sim \mathrm{i}ak_s^2 \frac{F}{\mu(2\pi k_o r)^{\frac{1}{2}}} \frac{\gamma_d(k_o\cos\theta)}{S^+(k_o\cos\theta)} e^{\mathrm{i}k_o r - \frac{1}{4}\mathrm{i}\pi} \tag{2.5.15}$$

for $k_o r \gg 1$, where F is given by (2.5.11). The angular dependence of a typical directivity shape given by $|\gamma_d(k_o\cos\theta)\ /S^+(k_o\cos\theta)|$ is shown in Figures 2.7a, 2.7b. The dominant features driven by the leaky Rayleigh wave have already been discussed in Section 2.4, in this example it is important to note that the directivity vanishes along θ_d and the associated peaks form in the neighbourhood of θ_d only.

There are also interesting non-uniformities for $\mathcal{E} \ll 1$ in the acoustic far field behaviour given by the evaluation of integrals like (2.5.8). The far field directivities in the fluid such as (2.5.15) are strictly valid for $k_o r \gg 1/\mathcal{E}^2$. On an intermediate length scale $1/\mathcal{E}^2 \gg k_o r \gg 1$ there is detailed structure associated with the beaming along the Rayleigh angles. Integrals of this type have been much studied by for instance Crighton (1979) in structural acoustics and Tew (1992) in the fluid-solid context.

2.6. Conclusion

Matched asymptotic expansions have been used to examine three model scattering problems. In each case, we have identified the defect with a specific interfacial discontinuity and have obtained explicit leading order expressions for the jump in interfacial stress or displacement. A particularly useful aspect, that has not been noticed before, is the natural separation that occurs in the inner problem into fluid and solid responses. This enables elastostatic analysis to be utilised for the inner problems. In the text this is shown to be consistent with our outer problems by checking that in the inner limit we do recover the separation.

Given the complexity of the full fluid-solid problems it is useful to have physical interpretations such as those exposed by the matching arguments for these model defects. The results will also be useful as analytic checks upon numerical work.

This chapter demonstrates that matched asymptotic expansions may now be applied in a routine manner to coupled fluid-solid media. The technique may be extended to examine, say, defects within the solid, for instance for subsurface inclusions and cavities in the absence of the fluid see Datta & El-Akily (1978). Further extensions could take advantage of the light fluid loading limit. The solutions found by Sabina & Willis (1977)

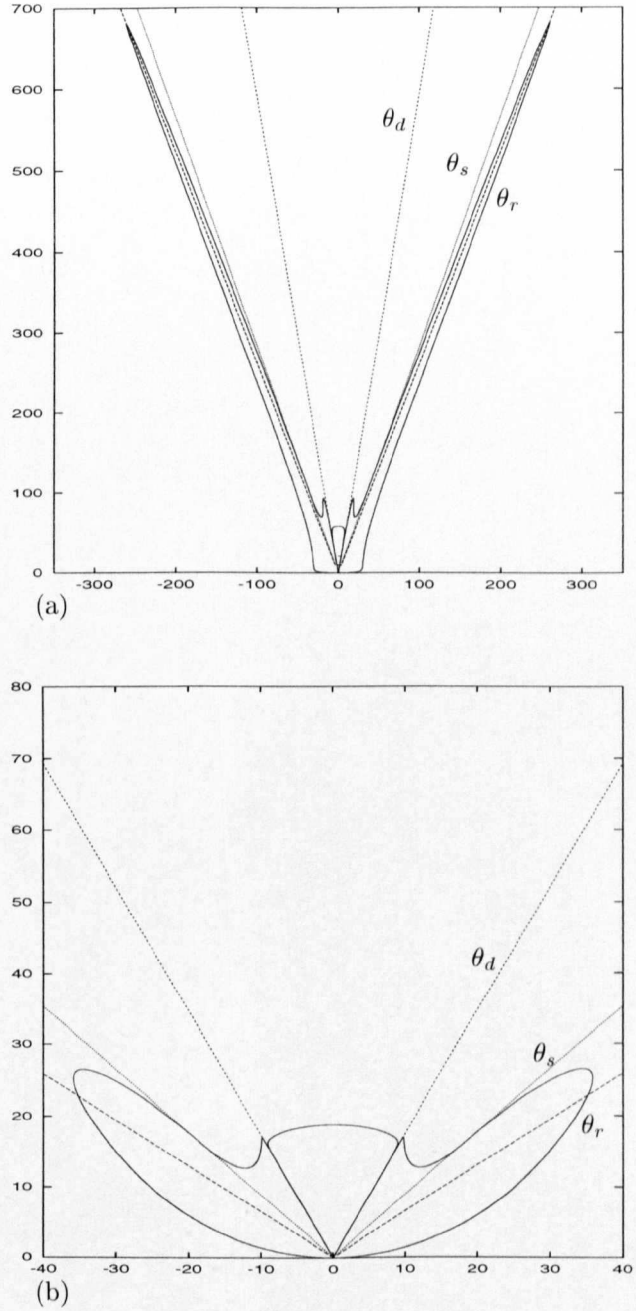

Figure 2.7. A typical directivity shape for scattering by a rigid strip. (a) $\mathcal{E} = 0.08$. (b) $\mathcal{E} = 0.32$.

and Abrahams & Wickham (1992a, 1992b) for Rayleigh wave incidence on defects at a traction free surface may be adapted for use in the analysis here if required, and could be directly utilised in the light fluid loading limit where a further separation occurs, Craster (1997).

Typical far field directivity patterns are shown demonstrating, for small $\mathcal{E}$, the dis-

tinctive beaming that occurs along the Rayleigh angles. This is to be expected and is the dominant response usually detected experimentally. However it is interesting to note that for one class of obstacles, namely the rigid strut, there is no response along that angle. The dominant features that form along the critical angles associated with the head waves are distinctive in each case and are affected by particular combinations of the material parameters. In particular as the fluid coupling increases the beaming along the Rayleigh angles decreases, and for relatively low values of Poisson's ratio then large responses may occur along the critical angles associated with the head waves.

References

Abrahams, I. D. & Wickham, G. R., 1992a. Scattering of elastic waves by a small inclined surface breaking crack. *J. Mech. Phys. Solids* **40**, 1707–1733.

Abrahams, I. D. & Wickham, G. R., 1992b. Scattering of elastic waves by an arbitrary small imperfection in the surface of a half-space. *op. cit.* 1683–1706.

Brekhovskikh, L. M., 1980. *Waves in layered media*. Academic Press, New York, Second edition.

Briggs, G. A. D., 1992. *Acoustic microscopy*. Monographs on the physics and chemistry of materials: 47, Oxford University Press.

Briggs, G. A. D., Jenkins, P. J. & Hoppe, M., 1990. How fine a surface crack can you see in a scanning acoustic microscope? *J. Microsc.* **159**, 15–32.

Brind, R. J. & Wickham, G. R., 1991. Near-field behaviour of the fundamental elastodynamic solutions for a semi-infinite homogeneous isotropic elastic solid. *Proc. R. Soc. Lond. A* **433**, 101–120.

Craster, R. V., 1997. The light fluid loading limit for fluid/solid interactions. *Euro. J. Appl. Math.* **8**, 485–505.

Crighton, D. G., 1979. The free and forced waves on a fluid-loaded elastic plate. *J. Sound Vib.* **63**, 225–235.

Crighton, D. G. & Leppington, F. G., 1973. Singular perturbation methods in acoustics: diffraction by a plate of finite thickness. *Proc. R. Soc. Lond. A* **335**, 313–339.

Datta, S. K., 1979. Diffraction of SH-waves by an edge crack. *J. Appl. Mech.* **46**, 101–106.

Datta, S. K. & El-Akily, N., 1978. Diffraction of elastic waves in a half-space I: Integral representation and matched asymptotic expansions. In *Proc. IUTAM symposium on modern problems in elastic wave propagation*, ed. by J. Miklowitz & J. D. Achenbach, 197-218.

Datta, S. K. & Sabina, F. J., 1986. Matched asymptotic expansions applied to diffraction of elastic waves. In *Low and high frequency asymptotics*, ed. by V. K. Varadan & V. V. Varadan, 71-264.

England, A. H., 1971. *Complex variable methods in elasticity*. Wiley.

Hein, V. L. & Erdogan, F., 1971. Stress singularities in a two-material wedge. *Int. Journ. of Fracture Mech.* **7**, 317–330.

Howe, M. S., 1990. Diffraction of sound by a surface scratch on an elastic solid. *Euro. J. Appl.*

Math. **1**, 353–369.

Leppington, F. G., 1972. On the radiation and scattering of short surface waves. Part 1. *J. Fluid Mech.* **56**, 101–119.

McIver, P. & Rawlins, A. D., 1993. Two-dimensional wave-scattering problems involving parallel-walled ducts. *Quart. J. Mech. Appl. Math.* **46**, 89–116.

Muskhelishvili, N. I., 1953. *Some basic problems of the mathematical theory of elasticity.* P. Noordhoff Ltd., Groningen, Holland, Third edition.

Sabina, F. J. & Willis, J. R., 1977. Scattering of Rayleigh waves by a ridge. *J. Geophys.* **43**, 401–419.

Stallybrass, M. P., 1970. A crack perpendicular to an elastic half-plane. *Int. J. Engng Sci.* **8**, 351–362.

Tew, R. H., 1992. Diffraction of sound by a surface inhomogeneity at a fluid-solid interface. *Euro. J. Appl. Math.* **3**, 115–145.

Wickham, G. R., 1977. The forced two dimensional oscillations of a rigid strip in smooth contact with a semi-infinite elastic solid. *Proc. Camb. Phil. Soc.* **81**, 291–311.

Appendix 2.A. Fourier transformed variables

In $\bar{y} > 0$, the material is elastic and the Fourier transformed displacements and stresses are

$$\bar{u}_{\bar{x}}^{\star}(\xi,\bar{y}) = -\mathrm{i}\xi\alpha(\xi)e^{-\left(\xi^2-\frac{k_d^2}{k_s^2}\right)^{\frac{1}{2}}\bar{y}} - \frac{\gamma_s(k_s\xi)}{k_s}\beta(\xi)e^{-(\xi^2-1)^{\frac{1}{2}}\bar{y}}, \tag{2.A 1}$$

$$\bar{u}_{\bar{y}}^{\star}(\xi,\bar{y}) = -\frac{\gamma_d(k_s\xi)}{k_s}\alpha(\xi)e^{-\left(\xi^2-\frac{k_d^2}{k_s^2}\right)^{\frac{1}{2}}\bar{y}} + \mathrm{i}\xi\beta(\xi)e^{-(\xi^2-1)^{\frac{1}{2}}\bar{y}}, \tag{2.A 2}$$

$$\bar{\sigma}_{\bar{x}\bar{y}}^{\star}(\xi,\bar{y}) = \mu\left[2\mathrm{i}\xi\frac{\gamma_d(k_s\xi)}{k_s}\alpha(\xi)e^{-\left(\xi^2-\frac{k_d^2}{k_s^2}\right)^{\frac{1}{2}}\bar{y}} + (2\xi^2-1)\beta(\xi)e^{-(\xi^2-1)^{\frac{1}{2}}\bar{y}}\right], \tag{2.A 3}$$

$$\bar{\sigma}_{\bar{y}\bar{y}}^{\star}(\xi,\bar{y}) = \mu\left[(2\xi^2-1)\alpha(\xi)e^{-\left(\xi^2-\frac{k_d^2}{k_s^2}\right)^{\frac{1}{2}}\bar{y}} - 2\mathrm{i}\xi\frac{\gamma_s(k_s\xi)}{k_s}\beta(\xi)e^{-(\xi^2-1)^{\frac{1}{2}}\bar{y}}\right], \tag{2.A 4}$$

and in the fluid region $\bar{y} < 0$, the relevant Fourier transformed variables are

$$\bar{u}_{\bar{y}}^{\star}(\xi,\bar{y}) = \frac{\gamma_o(k_s\xi)}{k_s}\zeta(\xi)e^{\left(\xi^2-\frac{k_o^2}{k_s^2}\right)^{\frac{1}{2}}\bar{y}}, \tag{2.A 5}$$

$$\bar{\sigma}_{\bar{y}\bar{y}}^{\star}(\xi,\bar{y}) = -\mu\frac{\rho_f}{\rho}\zeta(\xi)e^{\left(\xi^2-\frac{k_o^2}{k_s^2}\right)^{\frac{1}{2}}\bar{y}}, \tag{2.A 6}$$

where the coefficients α, β, and ζ are to be determined by the boundary conditions.

Appendix 2.B. Elastic solutions

Following the complex variable notation of Muskhelishvili (1953) and England (1971), for a static elastic material with Poisson ratio ν, the field variables can, utilising a stress continuation across $Y = 0$, be written in terms of one harmonic function $\Omega(z)$ where $z = X + \mathrm{i}Y$ and $\kappa = 3 - 4\nu$

$$2\mu(U_X + \mathrm{i}U_Y) = \kappa\Omega(z) + \Omega(\overline{z}) + (\overline{z} - z)\overline{\Omega'(z)}, \tag{2.B 1}$$

$$\Sigma_{XX} + \Sigma_{YY} = 2(\Omega'(z) + \overline{\Omega'(z)}), \tag{2.B 2}$$

$$\Sigma_{YY} - \mathrm{i}\Sigma_{XY} = \Omega'(z) - \Omega'(\overline{z}) + (z - \overline{z})\overline{\Omega''(z)}; \tag{2.B 3}$$

the overbar denotes the complex conjugate.

Appendix 2.C. Numerical method

The denominator that appears within the integrand is the Schölte wave function $S^+(\xi)$ rather than the Rayleigh wave function $R(\xi)$ that typically occurs in the absence of the fluid. The former contains six branch points and either two or four zeros depending upon the precise choice of branch cuts. The latter has four branch points and two real zeros.

In the limit as $x \to 0$,

$$\frac{1}{2\pi}\int_{-\infty}^{\infty} \frac{k_s^2\gamma_d(\xi)}{S^+(\xi)} e^{-\mathrm{i}\xi x}\mathrm{d}\xi \sim \frac{k_s^2}{2\pi(k_s^2 - k_d^2)} \log\frac{k_s|x|}{2} + \alpha. \tag{2.C 1}$$

The constant α is unknown and the purpose of this appendix is to detail how it is found.

Here the choice of branch cuts for the functions $\gamma_q(\xi) = (\xi^2 - k_q^2)^{\frac{1}{2}}$, $q = d,\ s,\ o$, in the upper half of the complex ξ-plane is taken such that they run from 0 to $+k_q$ along the real axis and from 0 to $+\mathrm{i}\infty$ along the imaginary axis, Figure 2.8. By deforming the branch cuts from the conventional choice of straight lines from $+k_q$ to $+k_q + \mathrm{i}\infty$ the zeros at $\pm k_l$, corresponding to leaky Rayleigh waves, are crossed and move onto the lower Riemann sheet; they play no role here.

The Schölte wave speed, k_{sch}, is

$$k_{sch} = k_s^2\left(\frac{1+\mathcal{E}}{2(k_s^2 - k_d^2)}\right)^{\frac{1}{2}} \exp\left(\frac{1}{2\pi}\int_{k_d}^{k_s} \tan^{-1}\phi_1 \frac{2\mathrm{d}\tau}{\tau} + \frac{1}{2\pi}\int_{k_s}^{k_o} \tan^{-1}\phi_2 \frac{2\mathrm{d}\tau}{\tau}\right). \tag{2.C 2}$$

The functions ϕ_1 and ϕ_2 are

$$\phi_1 = \frac{4\tau^2(\tau^2 - k_d^2)^{\frac{1}{2}}(k_s^2 - \tau^2)^{\frac{1}{2}} + \mathcal{E}k_s^4 \dfrac{k_o(\tau^2 - k_d^2)^{\frac{1}{2}}}{k_d(k_o^2 - \tau^2)^{\frac{1}{2}}}}{(2\tau^2 - k_s^2)^2}, \tag{2.C 3}$$

$$\phi_2 = \frac{\mathcal{E}k_s^4 k_o(\tau^2 - k_d^2)^{\frac{1}{2}}}{k_d(k_o^2 - \tau^2)^{\frac{1}{2}}[(2\tau^2 - k_s^2)^2 - 4\tau^2(\tau^2 - k_d^2)^{\frac{1}{2}}(\tau^2 - k_s^2)^{\frac{1}{2}}]}, \tag{2.C 4}$$

and the branch of the inverse tangent is chosen such that $0 \le \tan^{-1}\phi \le \pi$. The Schölte wavespeed

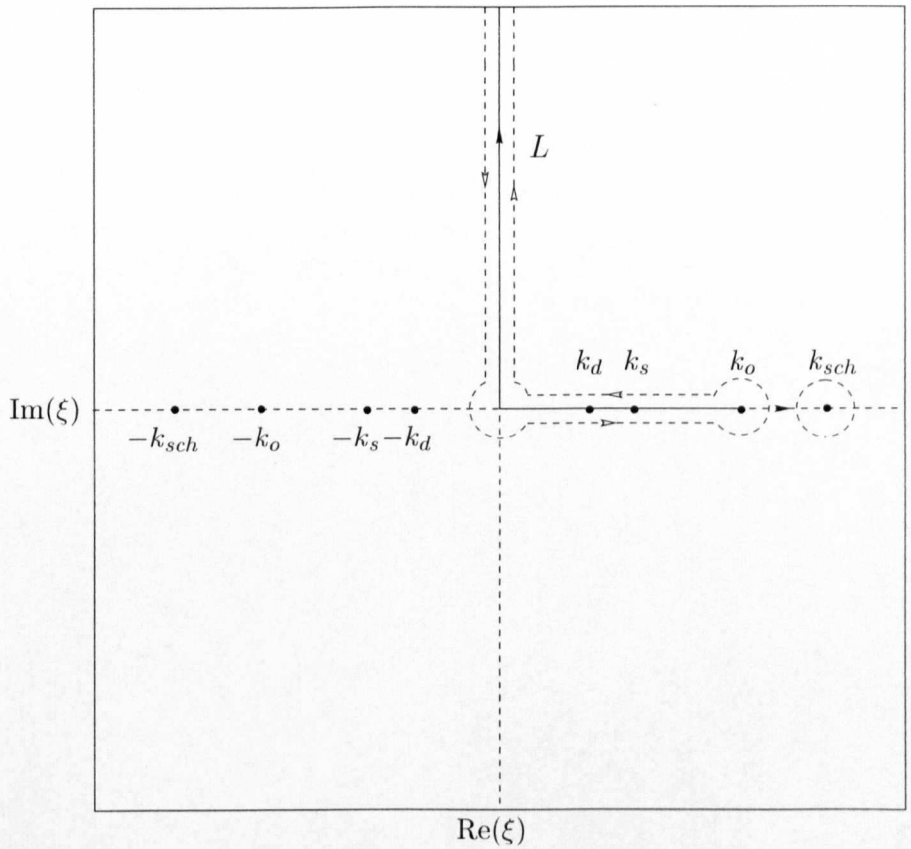

Figure 2.8. The position of the poles and branch cuts, together with the contour L, here shown explicitly by the broken line, in the upper half of the complex ξ-plane; the branch cut is shown by the solid line.

is not related to the Rayleigh wavespeed, indeed for $\mathcal{E} \ll 1$ it is marginally less than the compressional wavespeed of the fluid.

We now subtract the well known Hankel function representation from the integral (2.C 1) in the limit as $x \to 0$, in the form

$$\frac{1}{4\pi}\int_{-\infty}^{\infty} \frac{k_s^2}{(k_s^2-k_d^2)\gamma_s(\xi)} e^{-\mathrm{i}\xi x}\mathrm{d}\xi \sim \frac{k_s^2}{2\pi(k_d^2-k_s^2)} \log\frac{k_s|x|}{2} + \frac{k_s^2}{k_d^2-k_s^2}\left(\frac{\gamma}{2\pi}-\frac{\mathrm{i}}{4}\right), \tag{2.C 5}$$

where γ is Euler's constant, to remove the logarithmic term explicitly. Setting $x = 0$ without loss of generality,

$$\frac{1}{2\pi}\int_{-\infty}^{\infty}\left(\frac{k_s^2\gamma_d(\xi)}{S^+(\xi)} - \frac{k_s^2}{2(k_d^2-k_s^2)\gamma_s(\xi)}\right)\mathrm{d}\xi = \alpha + \frac{k_s^2}{k_d^2-k_s^2}\left(\frac{\gamma}{2\pi}-\frac{\mathrm{i}}{4}\right). \tag{2.C 6}$$

This produces a representation for α.

The remaining integrand is manipulated around the integration contour L, in the ξ-plane, Figure 2.8; combining the integral along the two sides of the branch cuts from 0 to $+k_q$ and from 0 to $+\mathrm{i}\infty$. The contribution due to the Schölte wavenumber is calculated explicitly by the

theory of residues. Now standard numerical techniques, here Gaussian quadrature, yield fast and accurate results.

It can be shown that the integral (2.C 6) is entirely real, and we can express the imaginary part of α simply by the term,

$$\mathrm{Im}(\alpha) = \frac{k_s^2}{4(k_d^2 - k_s^2)}. \tag{2.C 7}$$

Chapter Three

Asymptotic representations for transient forcings beneath a fluid-solid interface

3.1. Introduction

The coupled dynamics of a fluid overlying a solid are of fundamental importance in several different branches of geophysics, applied mathematics and engineering. The principal applications are to seismology and to non-destructive testing techniques. One of the primary aims of non-destructive testing is to identify the presence of any defects. The testing of a solid to detect such defects is often undertaken with the solid immersed in a fluid. The solid is usually imaged by waves incident from the fluid. One such testing device is the acoustic microscope; the experimental technique associated with the acoustic microscope is described in Briggs (1992). In other experimental devices the theoretical results can be used as an aid to determining the material parameters of the solid, and the geometry of any subsurface structures. In particular, this approach is used in vertical seismic profiling, see for instance de Hoop & van der Hijden (1985).

In marine seismology the coupled dynamics of the ocean and sedimentary layers are of considerable interest; shallow explosive sources are a key ingredient in oil exploration. The analysis here of a compressional source beneath a fluid-solid interface, in the limit as the source depth tends to zero, is of relevance in that context.

The aim here is to examine the exact solutions for some model problems in detail and extract as much analytical information as possible. The fluid and solid responses are found exactly in a simple closed form using the Cagniard–de Hoop (Cagniard, 1939; de Hoop, 1960) technique. Asymptotic analyses for special time dependent loadings are used to determine the form of the wavefronts. Once these expansions are obtained asymptotic solutions to general time dependent forcings are easily found, thus providing an accurate and versatile method of analysis avoiding long numerical calculations. We model subsurface defects as line force loadings which due to the complexity of the wavefronts generated are split into compressional and shear source terms and these are analysed separately. In the future we aim to utilise these Green's function solutions, and their associated asymptotics, to model more complex subsurface defects.

Leaky waves will feature heavily in the analysis and they principally occur when fluid, or other, coupling perturbs an interfacial wave that would in the absence of the coupling be unattenuated. Typically this causes leakage of energy from that wave into the fluid,

leading to attenuation. Their principal application has been in structural acoustics, see for instance Crighton (1989), where flexural plate waves are perturbed by an overlying fluid. The situation for a fluid loaded elastic solid is somewhat similar, but more complicated, due to the number of waves that an elastic solid sustains and their interactions at interfaces. Also here we are interested in the transient response.

In the absence of the fluid an unattenuated surface wave, the Rayleigh wave, propagates along the surface. With the addition of a fluid loading the unattenuated interfacial wave is a Stoneley wave, often called the Schölte wave. Perhaps surprisingly, in the limit as the fluid coupling tends to zero the Schölte wave does not tend to the Rayleigh wave; it tends to the compressional wave in the fluid, thus this limit is non-uniform. With a small amount of fluid loading the Rayleigh wave becomes a leaky wave; it is a perturbation of the usual Rayleigh wave, that is, it is no longer unattenuated, and energy now flows into the fluid along a critical angle. For situations when the fluid loading is significant, the leaky wave looses its significance and it is more difficult to attribute a direct response to it. This is typically the case in rock-water combinations, nonetheless the asymptotic solutions we find later still perform well in this limit.

In the absence of the fluid Chapman (1972) has presented a detailed treatment of the responses to subsurface loadings, Lamb's problem (Lamb, 1904), with particular attention to the leaky waves that may occur for specific ranges of Poisson's ratio. These leaky waves are not the same as those that occur due to fluid loading, and arise in a different context, they are related to small pulse arrivals near to the head wave arrivals. Nevertheless the treatment is instructive, and our treatment of the leaky Rayleigh wave is similar in approach.

In addition to the Schölte and, possibly, leaky Rayleigh waves the fluid will also carry waves generated by the interaction of elastic body waves, either compressional or shear, with the interface.

In the limit as the line loading tends to the surface, that is $h/x \to 0$, a sharp response becomes evident in a certain region. This is the precursor of the cylindrical compressional wavefront in the fluid created when the source is on the surface; this limiting situation is also treated.

Similar configurations have been treated by several authors, for instance Roever *et al.* (1959) and in a series of papers by de Hoop & van der Hijden (1983, 1984, 1985). They considered several problems involving sources either in the fluid, or within the solid. Their approach differs from ours in several respects, with a different interpretation of the leaky Rayleigh pole that does not lead to quantitative asymptotic representations, nor lend itself easily to generalisations to more complicated situations. There is also a

less detailed analysis of the solution. In particular the light fluid limit is not explored in detail, nor is the limit as the source tends to the surface discussed. Typically in previous papers the primary results are numerical, and are limited to the interfacial responses. In this investigation, the exact solution is presented for the full field in the fluid, together with a detailed analysis of all the salient responses. We also make generalisations to find the asymptotic responses for more general time dependence.

It is emphasised here that the Cagniard–de Hoop technique has considerable numerical and analytical advantages over alternative approaches such as using, say, Fourier transforms for harmonic sources, and then using superposition to generate more general time dependence. In particular most of our solutions are explicit and not limited to far field evaluations, they are in real time, and involve minimal numerical work. Further applications of the method to anisotropy and layered materials are to be found in van der Hijden (1987).

3.2. Formulation

In the region $y > 0$ is an isotropic linear elastic material and in $y < 0$ is a compressible fluid. The problem is two dimensional and typical configurations to be considered are shown in Figure 3.1 and Figure 3.2; the wavefronts are described in detail later. The responses of the two half spaces are coupled together through the continuity boundary conditions along the interface $y = 0$, these are discussed following (3.2.6).

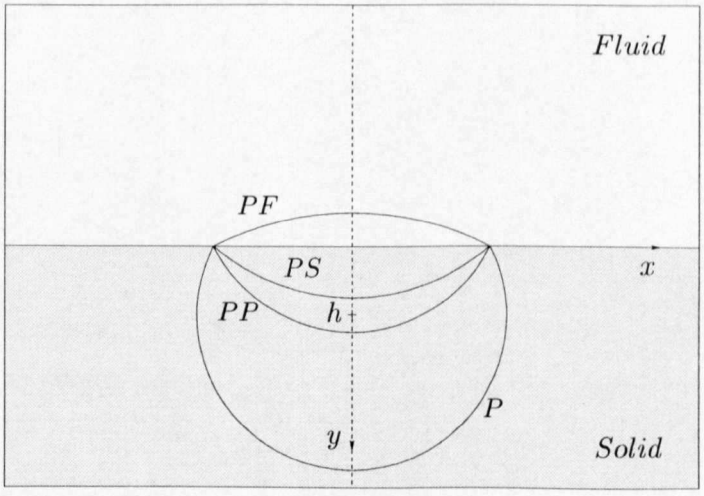

Figure 3.1. A schematic showing the radiated wavefronts for the waves generated by a line compressional source a distance h beneath a fluid-solid interface.

A Cartesian coordinate system is adopted with x_1, x_2 corresponding to x, y.

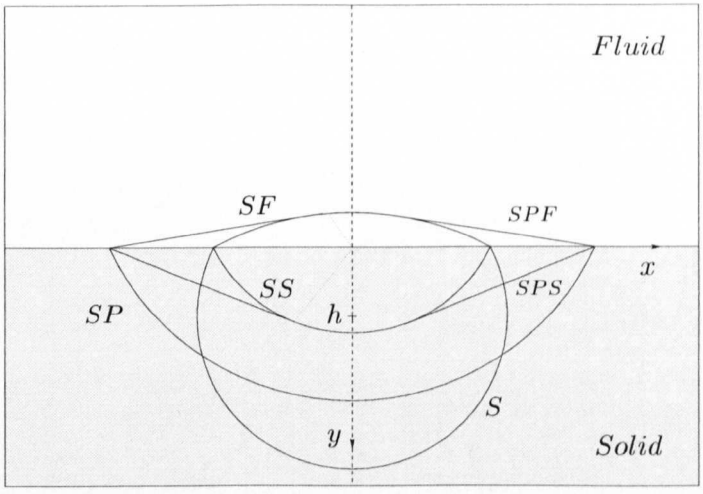

Figure 3.2. A schematic showing the radiated wavefronts for the waves generated by a line shear source a distance h beneath a fluid-solid interface.

The elastic material has Lamé constants λ, μ, and density ρ. The stresses σ_{ij} in the material are related to the displacements u_i by

$$\sigma_{ij} = \lambda \epsilon_{kk} \delta_{ij} + 2\mu \epsilon_{ij} \text{ where } \epsilon_{ij} = \frac{1}{2}(u_{i,j} + u_{j,i}), \tag{3.2.1}$$

the comma denoting differentiation with respect to x_i. The governing equations are the equilibrium equations $\sigma_{ij,j} = \rho \ddot{u}_i$, where the notation $\ddot{}$ denotes double partial differentiation with respect to time.

It is convenient to adopt displacement potentials ϕ and ψ where the displacement $\mathbf{u}$ is $\mathbf{u} = \nabla\phi + \nabla \times \psi\hat{z}$, where $\hat{z}$ is the unit vector in the z direction, that satisfy the wave equations

$$\nabla^2\phi = \ddot{\phi}/c_d^2, \ \nabla^2\psi = \ddot{\psi}/c_s^2. \tag{3.2.2}$$

The displacement potentials ϕ and ψ are related to the compressional (or dilatational) and shear disturbances respectively, thus we utilise these when generating compressional and shear sources. The wave speeds c_d, c_s are defined in terms of the material parameters as

$$c_d^2 = \frac{\lambda + 2\mu}{\rho}, \ c_s^2 = \frac{\mu}{\rho}. \tag{3.2.3}$$

The subscripts d and s denote the variables associated with the dilatational and shear waves respectively.

The compressible fluid in $y < 0$ is effectively an elastic material that supports no shear stresses, thus

$$\sigma_{ij} = \lambda_f \epsilon_{kk} \delta_{ij}, \tag{3.2.4}$$

where the fluid has density ρ_f and compressional modulus λ_f. The governing equations

are $\sigma_{ij,j} = \rho\ddot{u}_i$ again, and we introduce a third displacement potential χ such that the displacement $\mathbf{u}$ is $\mathbf{u} = \nabla\chi$; this potential satisfies

$$\nabla^2\chi = \ddot{\chi}/c_o^2. \tag{3.2.5}$$

The compressional wavespeed of the fluid is defined as $c_o^2 = \lambda_f/\rho_f$.

The continuity boundary conditions

$$[\![\sigma_{yy}(x,0,t)]\!] = 0,\ \sigma_{xy} = 0,\ [\![u_y(x,0,t)]\!] = 0 \tag{3.2.6}$$

are taken on the interface $y = 0$, where the braces $[\![\ ]\!]$ denote the jump in a quantity across the interface; both the stresses σ_{yy} and the normal displacement u_y are continuous across $y = 0$. The fluid supports no shear stresses, thus $\sigma_{xy} = 0$ on $y = 0$.

A coupling parameter ϵ occurs throughout the analysis; it is defined as $\epsilon = \rho_f c_o/\rho c_d$. The coupling parameter is physically interpreted as the ratio of the fluid and solid impedances relative to the compressional waves, and gives a frequency independent measure of the fluid-solid coupling. The light fluid loading limit is when $\epsilon \ll 1$; this specific limit is not taken here unless explicitly stated, although the metal-water results are for $\epsilon \sim 0.086$. The set of material parameters usually taken for the figures is typical of either metal-water or rock-water combinations. Metals have relatively high densities and wavespeeds relative to the fluid. For aluminium-water the solid density is 2700kg/m^3 with compressional and shear wavespeeds 6374m/s and 3111m/s respectively. The fluid density is 1000kg/m^3 with wavespeed 1480m/s. The Rayleigh and Schölte wavespeeds are 2906m/s and 1477m/s respectively; here $\epsilon = 0.086$. A second set of material parameters typical of rock-water combinations (sandstone-water) is taken for comparative purposes, now c_d and c_s are 2920m/s and 1840m/s respectively; the parameters demonstrate the effects of increasing the fluid coupling, ϵ, and reducing the mismatch between a 'fast' solid and 'slow' fluid. In particular for this case the Rayleigh and Schölte wavespeeds are 1667m/s and 1358m/s respectively, and $\epsilon = 0.201$. The reduced mismatch between solid and fluid wavespeeds and increased fluid coupling leads to different behaviour from the metal-water case. The material parameters are primarily taken from Briggs (1992) and are compiled in Table 3.1.

The assumption that the compressional wavespeed of the fluid is less than the shear wavespeed of the solid is taken so that $c_d > c_s > c_o$; this is a reasonable assumption for most solid and fluid combinations. The analysis presented here does not rely on this assumption, and is easily generalised to allow $c_d > c_o > c_s$, say, which would be typical of perspex-water combinations.

The analysis is performed using Fourier and Laplace transforms in space and time

	ρ	c_d	c_s	c_o	ϵ (water)	c_r	c_{sch}
Aluminium	2700	6374	3111	...	0.086	2906	1477
Sandstone	2440	2920	1840	...	0.201	1667	1358
Water	1000	...	...	1480	...	...	...
	kg/m^3	m/s	m/s	m/s		m/s	m/s

Table 3.1. Material parameters (Briggs, 1992).

respectively: the Laplace transform in t, and its inverse, are defined as

$$\overline{f}(p) = \int_0^\infty f(t)e^{-pt}\mathrm{d}t, \; f(t) = \frac{1}{2\pi\mathrm{i}}\int_{c-\mathrm{i}\infty}^{c+\mathrm{i}\infty}\overline{f}(p)e^{pt}\mathrm{d}p, \text{ for } \mathrm{Re}(c) > 0 \tag{3.2.7}$$

where p is the transform variable, and the Fourier transform in x, and its inverse, are defined as

$$\widetilde{f}(\xi) = \int_{-\infty}^{\infty} f(x)e^{\mathrm{i}\xi x}\mathrm{d}x, \; f(x) = \frac{1}{2\pi}\int_C \widetilde{f}(\xi)e^{-\mathrm{i}\xi x}\mathrm{d}\xi, \tag{3.2.8}$$

where ξ is the transform variable. The inversion path C runs along the real axis from $-\infty$ to ∞ and, if necessary, is indented to lie below any singularities on the positive real axis and above any that lie on the negative real axis. We also utilise the Cagniard–de Hoop method; it is often stated that p *must* be real and positive but this is unnecessary, see the discussion in Section 5.1.

The representations for the Fourier and Laplace transformed stresses and displacements are given in Appendix 3.A. A brief description of the functions that occur during the analysis is also given.

3.3. Subsurface loadings

In this section we solve three canonical problems exactly, these are the responses generated by compressional and shear sources within the solid, and by a line force within the solid. The line force is given by a combination of the source results. These problems, once solved, open the way to considering a wide range of scattering problems. For instance more realistic fluid-solid problems involving specific geometries that are so far out of analytical reach. Perhaps most importantly, the physical structure of the results is revealed; we consider the fields in the fluid in detail. We demonstrate that, in the light fluid coupling case, a definite response is associated with the leaky Rayleigh pole; this is done by using an alternative choice of branch cuts from that usually adopted to move

the pole from the lower to upper Riemann sheet and then using a residue calculation. In addition wavefront expansions are deduced and it is illustrated that these expansions can be used together with the convolution theorem to deduce asymptotic results valid for general loadings.

To avoid any notational confusion the pressure in the fluid will be described as the negative of the stress σ_{yy}. The results presented in the text describe the field generated by source interactions with the interface.

3.3.1. *A subsurface compressional line source*

Consider a line compressional source a distance h beneath the interface; the geometry of the problem is shown in Figure 3.1 together with a schematic of the primary wavefronts generated. The notation that appears has been adopted from geometrical ray theory. The letters P, S, and F are used to denote the compressional and shear waves in the solid, and the compressional wave in the fluid, respectively. The field generated by interaction with the interface is denoted by a combination of two or more letters; the final letter denotes the type of wave and the letters preceding it denote the source type. For instance, in the following discussion, PP, PS, and PF denote the compressional and shear responses in the solid, and the compressional wave in the fluid, generated by a compressional source loading, respectively. As we only show the fields in the fluid we only discuss the PF wave. The conventional Figure 3.2, omits several 'wavefronts' that, as we shall see, are significant. The missing responses are those due to the interfacial Schölte wave, the leaky Rayleigh wave and, in the limit as $h \to 0$, the response due to a pseudo-compressional wave in the fluid.

The plan of this section is that we solve the source problems exactly, both for displacements and pressures; the asymptotic analysis then follows in Section 3.3.1.3.

The continuity boundary conditions (3.2.6) are taken on the interface $y = 0$. The total field in the solid consists of the superposition of two fields. The first is the solution to $\nabla^2\phi - \ddot{\phi}/c_d^2 = F(t)\delta(x)\delta(y-h)$, in an infinite elastic material, where $F(t)$ is the pulse shape and $\delta(\ )$ is the generalised function. The second field is the response generated by the interfacial boundary conditions; all figures show this second field.

3.3.1.1. *Exact solution*

Using the integral representations for the quantities of interest in Appendix 3.A the solutions are derived. In the fluid the Laplace transform of the normal displacement is

$$\overline{u}_y(x,y,p) = -\frac{1}{2\pi}\int_{-\infty}^{\infty} \frac{k^2}{c_d}\frac{p\overline{F}(p)(2\zeta^2+k^2)}{S(\zeta)} e^{-p(\gamma_d'(\zeta)h-\gamma_o'(\zeta)y+i\zeta x)/c_d} d\zeta, \qquad (3.3.1)$$

where $\overline{F}(p)$ is the Laplace transform of $F(t)$ given by (3.2.7). We have introduced the rescaling $\xi = p\zeta/c_d$ for convenience, see Appendix 3.A. In this formula k and k' are defined to be the ratios c_d/c_s and c_d/c_o respectively.

The fluid pressure is given by the Laplace transform

$$\overline{\sigma}_{yy}(x,y,p) = -\frac{1}{2\pi}\int_{-\infty}^{\infty} \rho_f k^2 \frac{p^2\overline{F}(p)(2\zeta^2+k^2)}{\gamma_o'(\zeta)S(\zeta)} e^{-p(\gamma_d'(\zeta)h-\gamma_o'(\zeta)y+\mathrm{i}\zeta x)/c_d}\mathrm{d}\zeta. \tag{3.3.2}$$

The Schölte function $S(\zeta)$ is vital to the analysis and is defined as $S(\zeta) = R(\zeta) + \epsilon k^4 k'(\zeta^2+1)^{\frac{1}{2}}/(\zeta^2+k'^2)^{\frac{1}{2}}$. It contains six branch points at $\pm\mathrm{i}$, $\pm\mathrm{i}k$, $\pm\mathrm{i}k'$, and either two or four zeros depending upon the precise choice of branch cuts. If $\epsilon = 0$, that is, if the fluid is decoupled from the solid, the Schölte function is truncated to the function $R(\zeta)$. This is the standard Rayleigh function, $R(\zeta) = (2\zeta^2+k^2)^2 - 4\zeta^2(\zeta^2+1)^{\frac{1}{2}}(\zeta^2+k^2)^{\frac{1}{2}}$; this function has four branch points at $\pm\mathrm{i}$, $\pm\mathrm{i}k$, and two zeros at $\pm\mathrm{i}k_r$ where $k_r = c_d/c_r$ and c_r is the Rayleigh wavespeed ($k < k_r < k'$).

The functions $\gamma_d'(\xi,p)$, $\gamma_s'(\xi,p)$, and $\gamma_o'(\xi,p)$ that appear are defined as $\gamma_q'(\zeta) = (\zeta^2 + k_q^2)^{\frac{1}{2}}$, with $q = d,\ s,\ o$, see Appendix 3.A. Here, unless stated, the choice of branch cuts for the functions $\gamma_q'(\zeta)$ in the complex ζ-plane is taken such that they run from $\pm\mathrm{i}k_q$ to $\pm\mathrm{i}\infty$ along the imaginary axis. With this choice of branch cuts the zeros of the Schölte function corresponding to leaky Rayleigh waves in the physical domain then occur on the lower Riemann sheet, and play no explicit role in the exact solution. However the effect of these zeros is observed experimentally, Roever *et al.* (1959), as in the case for some of the materials discussed below and we later extract these responses asymptotically. Given the choice of branch cuts above the Schölte function has only two zeros at $\pm\mathrm{i}k_{sch}$ where $k_{sch} = c_d/c_{sch}$ and c_{sch} is the Schölte wavespeed ($k_{sch} > k'$). This wavespeed is not related to the Rayleigh wavespeed, indeed for $\epsilon \ll 1$ it is marginally less than the compressional wavespeed of the fluid in this limit. An asymptotic representation when $\epsilon \ll 1$ is

$$\mathrm{i}k_{sch} \sim \mathrm{i}k'\left(1 + \frac{\epsilon^2(k'^2-1)k^8}{2R^2(\mathrm{i}k')}\right) = \mathrm{i}k'\left(1+\frac{1}{2}\epsilon^2 u^2\right), \tag{3.3.3}$$

and in general the root is found numerically.

The case $F(t) = H(t)$, where $H(t)$ is the Heaviside step function, is considered in detail for the displacements and is denoted by $u_y^H(x,y,t)$; for more general $F(t)$ the convolution theorem gives

$$u_y(x,y,t) = \int_0^t F'(t-\tau)u_y^H(x,y,\tau)\mathrm{d}\tau \tag{3.3.4}$$

provided $F(0) = 0$. The $H(t)$ loading is convenient as a loading for the displacements as explicit solutions are easily found. We shall consider general loadings later and demonstrate the routine manner in which they are treated. In addition we show that wavefront

expansions under general $F(t)$ can be obtained by a convolution using the asymptotic solutions. In a similar manner the loading $tH(t)$ is convenient for obtaining the exact solution for the pressure, and general loadings are found using a convolution; the superscript tH is used to denote the loading.

The full solution is found using the Cagniard–de Hoop method, see for instance Miklowitz (1978). The inversion contour is chosen so that

$$c_d t = (\zeta^2 + 1)^{\frac{1}{2}} h - (\zeta^2 + k'^2)^{\frac{1}{2}} y + \mathrm{i}\zeta x \tag{3.3.5}$$

and this then places the integral (3.3.1) in the form of a Laplace transform. This amounts to a transformation of the Fourier integration path. As we ultimately require the inverse Laplace transform of this integral our solution in real time is found immediately by inspection. We adopt polar coordinates based upon the defect such that $y - h = -r\cos\theta$ and $x = r\sin\theta$.

On the interface, $y = 0$, the Cagniard path for $\zeta(t)$ can be found explicitly; the situation for $y < 0$ is more complicated and the path is found either numerically, or for $h \ll x$ via a perturbation analysis (the details of which are in Section 3.3.1.2). For responses in the fluid, $y < 0$, both γ_d' and γ_o' are present in the exponential term of (3.3.2). This complicates the analysis as a convenient analytic form, valid for all x, y, and h, for $\zeta(t)$ is not forthcoming. From the formulation of a quartic algebraic equation (see for instance Appendix 4.A) or via a Newton–Raphson algorithm, the Cagniard path $\zeta(t)$ is found numerically as the root of equation (3.3.5) with positive real part. Using symmetry properties of the integrand it is sufficient to only consider the path in the fourth quadrant and this is given by taking the branch of $\zeta(t)$ with the positive square root.

Three typical paths are shown in Figure 3.3. For $y = 0$ the integration path, shown in Figure 3.3, is given by

$$\zeta(t) = -\mathrm{i}\frac{c_d t}{r}\sin\theta \pm \left[\left(\frac{c_d t}{r}\right)^2 - 1\right]^{\frac{1}{2}} \cos\theta, \text{ for } \frac{r}{c_d} \leq t < \infty, \tag{3.3.6}$$

where $r^2 = x^2 + h^2$ and $\tan\theta = x/h$; r is the distance of a point on the interface from the source. For this explicit case the path cuts the imaginary axis at $\zeta = -\mathrm{i}\sin\theta$ so the path does not intersect the branch cuts of the functions appearing in the transforms. The time at which the path cuts the imaginary axis is the arrival time for the PF wave, t_{pf}. The path is hyperbolic and approaches the asymptote $\mathrm{Im}(\zeta)/\mathrm{Re}(\zeta) = \pm\tan\theta$. For h, $y \neq 0$ the Cagniard path, in the lower plane, cuts the negative axis between $-\mathrm{i}$ and 0. As the source approaches to the surface, in the limit as $h \to 0$, the point at which it cuts the axis tends to $-\mathrm{i}$ and the path $\zeta(t)$ tightens around the branch cut originating at $\zeta = -\mathrm{i}$; this is treated separately in 3.3.1.2. Thus in the general case the situation is

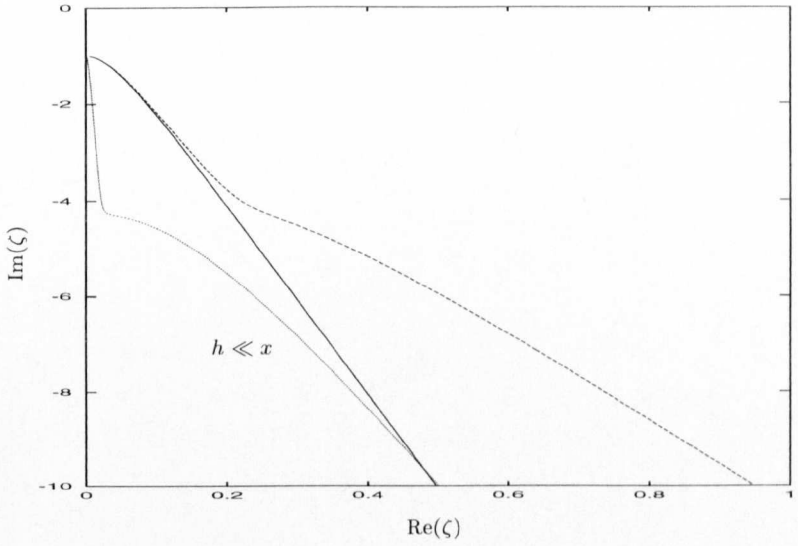

Figure 3.3. Three typical Cagniard paths; $y = 0$ solid line, $y < 0$ dashed lines. The path when $h \ll x$ is labelled.

similar to that when $y = 0$, except that we usually have to find both the path and t_{pf} numerically.

The exact solution for the vertical displacement in $y \leq 0$, written as a function of t, is simply

$$u_y^H(x, y, t) = -\frac{k^2}{\pi c_d} H(t - t_{pf}) \mathrm{Re}\left(\frac{(2\zeta^2(t) + k^2)}{S(\zeta(t))} \frac{\mathrm{d}\zeta(t)}{\mathrm{d}t} \right), \tag{3.3.7}$$

where t_{pf} ($= r/c_d$ when $y = 0$) corresponds to the arrival of the PF wave and $\zeta(t)$ is the path described above. The wavefront arrivals are shown for $\pi c_d u_y^H(x, y, t)/k^2$ versus t for the rock-water case in Figures 3.4, 3.5 for typical values of x, y, and h. The ratios x/h and y/h determine the shape of the response; we have avoided rescaling each figure by h for convenience. The plots for the metal-water case are also shown in Figures 3.6, 3.7. Also shown on these figures are asymptotic representations for the dominant responses; these are derived in the next section. The lines denoted by t_{pf}, t_l, and t_{sch} are the arrival times associated with the PF, leaky Rayleigh, and Schölte waves respectively. The differences in material parameters lead to different dominant responses in each case. For the rock-water cases the Schölte response is very dominant with a rather weak, but nonetheless distinctive leaky Rayleigh response.

An additional compressional response is visible for very small h see Figures 3.9, 3.10 and the discussion of Section 3.3.1.2.

The metal-water case has very large leaky Rayleigh responses whilst the Schölte wave, once we are off the interface, is typically rather small. From looking at the Cagniard

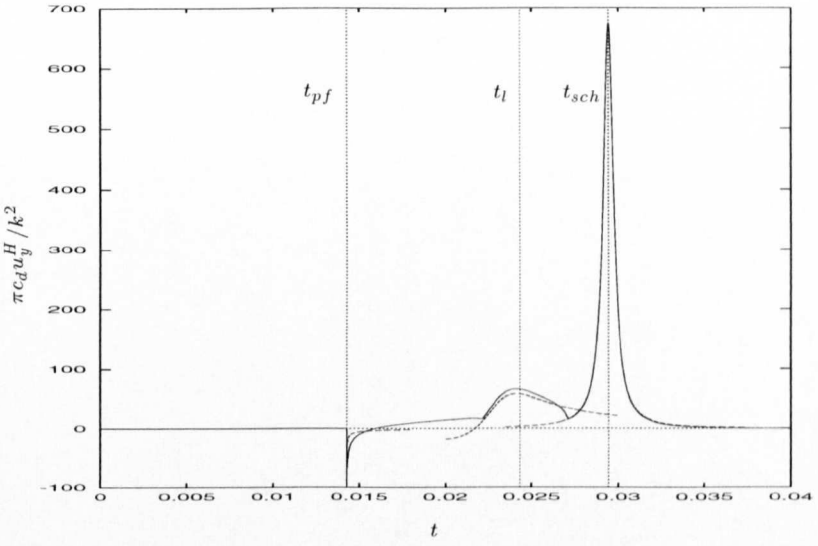

Figure 3.4. A plot of $\pi c_d u_y^H / k^2$ versus t for material parameters typical of rock-water combinations; $x = 40$, $y = -1$, $h = 0.1$.

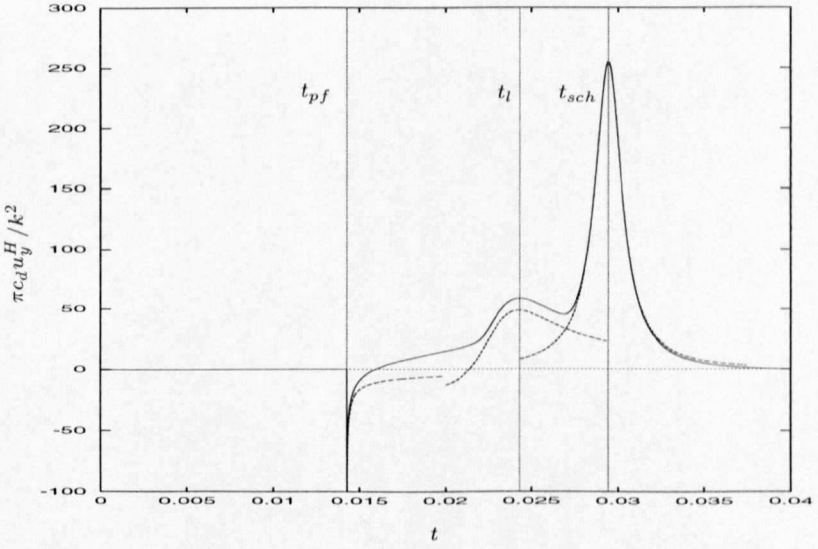

Figure 3.5. A plot of $\pi c_d u_y^H / k^2$ versus t for material parameters typical of rock-water combinations; $x = 40$, $y = -1$, $h = 1$.

path one can deduce that the Schölte wave only becomes fully developed when $x/h > 1/\epsilon^2 k' u^2$, where u is defined in (3.3.3). In addition the Schölte response is confined to the neighbourhood of the interface.

In both cases the first arrival is the compressional wave in the fluid, which is singular, and this arrives at $t = t_{pf}$. The large distinctive peak at $t = t_l$ in these plots is the response due to the presence of the leaky Rayleigh wave, and is one of the dominant

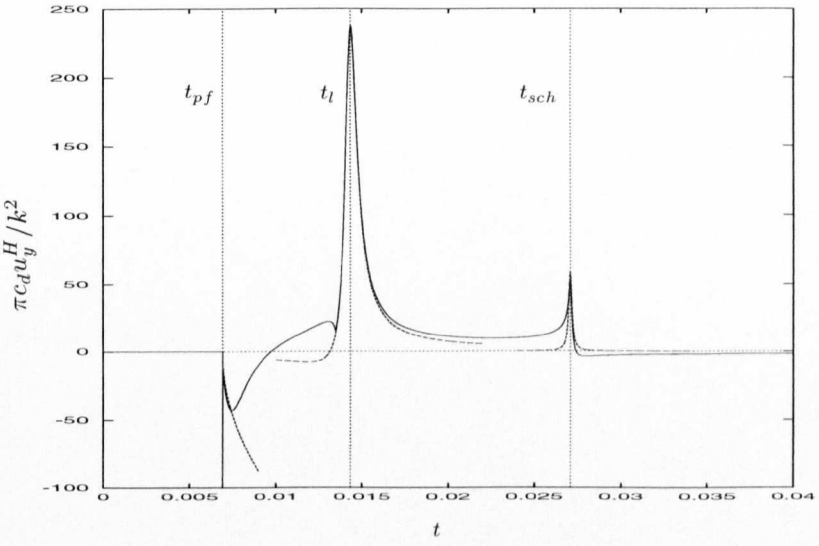

Figure 3.6. A plot of $\pi c_d u_y^H / k^2$ versus t for material parameters typical of metal-water combinations; $x = 40$, $y = -1$, $h = 0.1$.

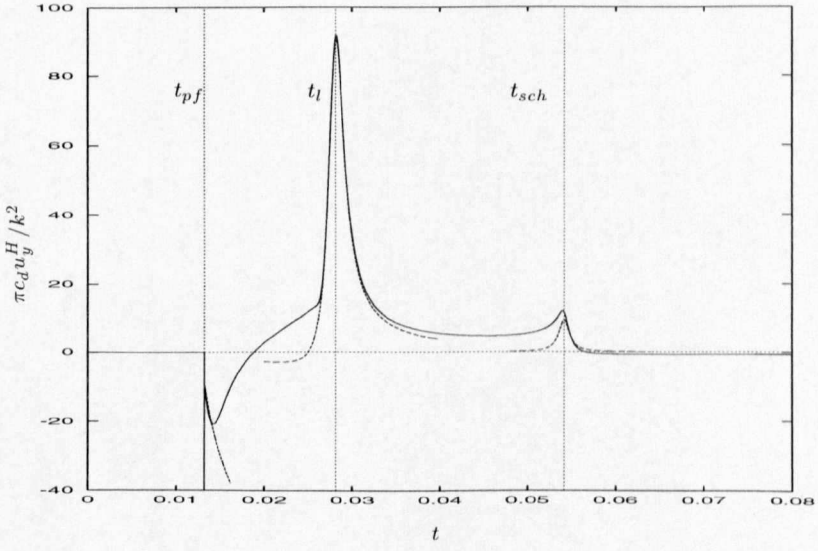

Figure 3.7. A plot of $\pi c_d u_y^H / k^2$ versus t for material parameters typical of metal-water combinations; $x = 40$, $y = -1$, $h = 1$.

responses for $\epsilon \ll 1$. It only exists in the angular region defined by $t_l \geq t_{pf}$; the angle θ_r, in polar coordinates based at the origin $x = r \sin\theta, y = -r\cos\theta$, is $\sin^{-1}(c_o/c_r)$ when $h = 0$. The arrival time t_l of the leaky Rayleigh wave is defined in equation (3.3.15). As ϵ increases this peak decreases in size. Increasing the coupling, as in the rock-water cases, leads to a large distinctive peak forming at $t = t_{sch} = x/c_{sch}$, that is due to the Schölte wave. Increasing h decreases the magnitude of the responses.

The pressure in the fluid is given as

$$\sigma_{yy}^{tH}(x,y,t) = -\frac{\rho_f k^2}{\pi} H(t-t_{pf}) \mathrm{Re}\left(\frac{2\zeta^2(t)+k^2}{\gamma_o'(\zeta(t))S(\zeta(t))}\frac{\mathrm{d}\zeta(t)}{\mathrm{d}t}\right). \tag{3.3.8}$$

This differs from the displacement only in the γ_o' term, this alters the response by magnifying the pseudo-compressional response when $h \ll x$. Apart from that the responses are qualitatively similar to those found for the displacements, and the asymptotics are of similar accuracy.

In Figure 3.8 we show the pressures with increasing x. This corresponds to increasing the receiver distance along the interface, and the magnitude of the responses decrease and the arrivals become more separated in time. The situation when $\epsilon = 0$ and $\epsilon = 0.086$ is shown; by simply setting $\epsilon = 0$ in equation (3.3.8) we have not removed the effect of the fluid that emerges through the γ_o' term so strictly we are not *in vacuo*. This can be seen as a small bump in both panels of Figure 3.8 after the (leaky) Rayleigh wave arrival; some further examples are shown in later figures. Nevertheless, when the fluid decouples from the solid such that $\epsilon = 0$ then the *in vacuo* results of Garvin (1956) are replicated, at least insofar as the Rayleigh wave is concerned.

In this figure the dimensionless time τ is the ratio of the real time to r/c_d, the time that would be required by the incident pulse to reach a point if travelling at c_d. An increase in $x/(h-y)$ corresponds to a contraction of the real time scale. In the absence of the fluid the Rayleigh wave grows until it takes on the strongly peaked form described by Garvin (1956). For $\epsilon = 0$ Figure 3.8 demonstrates the birth of the Rayleigh wave as we move away from the source. The shape of the pulse remains essentially unchanged in shape beyond $x/(h-y) = 20.0$. With the fluid loading, the leakage of energy causes the wave to die away, and we witness the decay and finally the death of the leaky wave. The Schölte wave is unattenuated and grows to take on a peaked form; this is slightly obscured in the figure as its amplitude is $O(\epsilon)$.

3.3.1.2. *The source close to the interface*

In Figure 3.3 a typical path for $h \ll x$ is shown and is labelled, this is distinctly different from the other two paths. The different shape is interpreted via considering the case when the source is actually on the surface, that is, $h = 0$. Here the situation $h = 0$ is non-physical for the compressional source loading as it does not satisfy the interfacial conditions correctly. Nevertheless, in this case the path, $\zeta(t)$, then consists of a piece running directly along the branch cuts from $\zeta = -\mathrm{i}$ to $\zeta = -\mathrm{i}k'\sin\theta$ together with an almost hyperbolic path; the appropriate expressions are in Craster (1996b). The angle is defined in polar coordinates based at the origin, that is, $x = r\sin\theta$, $y = -r\cos\theta$.

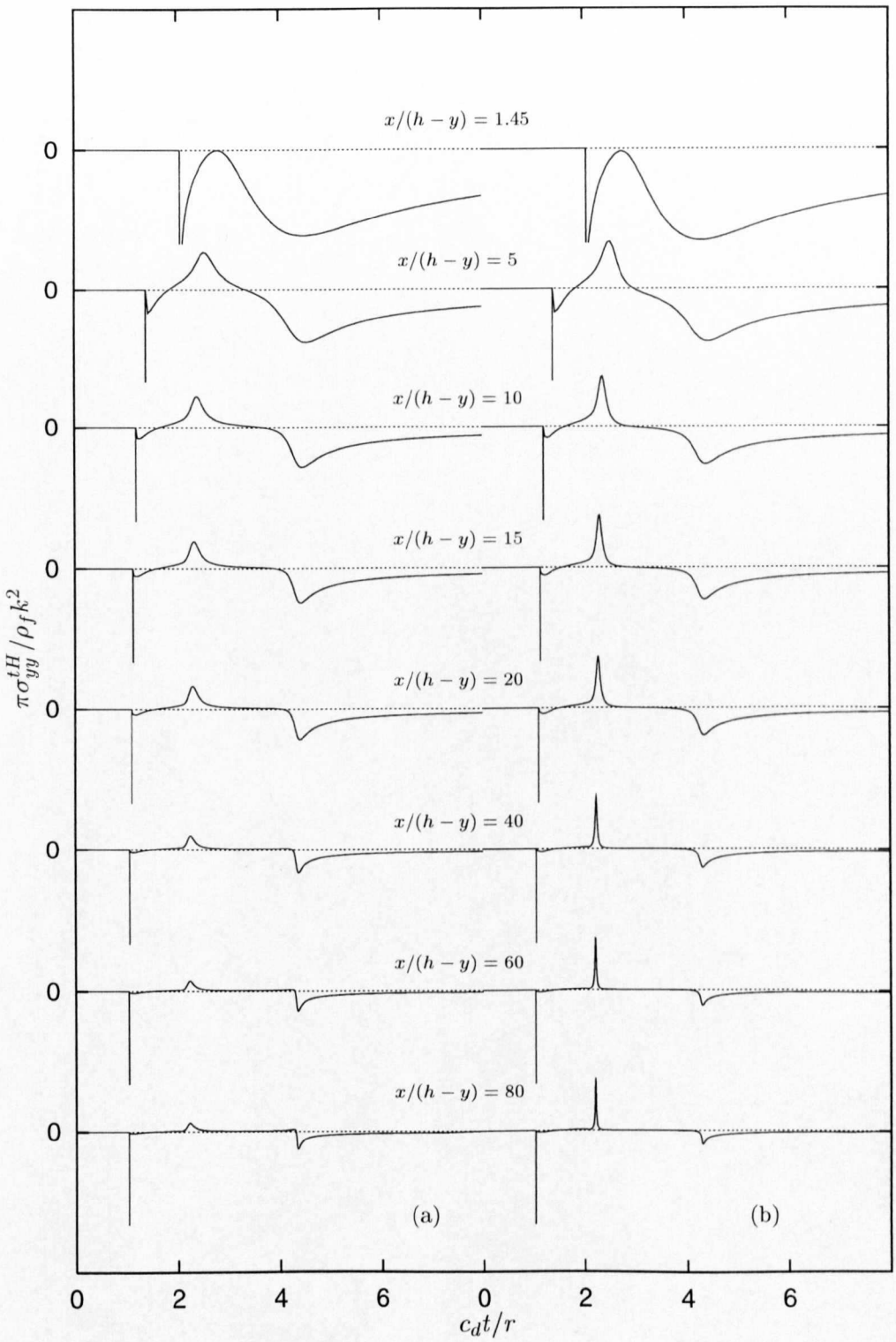

Figure 3.8. A plot of $\pi\sigma_{yy}^{tH}/\rho_f k^2$ versus $c_d t/r$ for increments of $x/(h-y)$. The birth and death of the leaky Rayleigh wave can be seen in panel (a), and it is compared to the case with no fluid loading shown in panel (b).

In essence the integrals along the branch cuts give head wave contributions. If $h = 0$ the point $\zeta = -ik' \sin\theta$ is the saddle point in a steepest descents analysis and gives wavefronts travelling with wavespeed c_o due to a compressional wave generated within the fluid. In the context of the schematic 3.1 it then forms a semicircular arc in the fluid. For $0 \leq \theta < \sin^{-1}(c_o/c_d)$ this is the same as the PF wavefront. However for $\theta \geq \sin^{-1}(c_o/c_d)$ this is not shown in the schematic and elements of this response emerge quite strongly when $h \ll x$. When $h \ll x$ the path runs from $-i\zeta_{pf}$ very close to the branch cuts before turning away at approximately $\zeta \sim -ik' \sin\theta$. This point generates a distinctive response in the fluid when $t \sim r/c_o = t_o$. The importance of points like this in the Cagniard path in different situations have been recognised previously by, for instance Hong & Helmberger (1977), Drijkoningen & Chapman (1988), but either not analysed in detail, or investigated in simpler situations. This regime is discussed in detail in Chapter 4.

Here, in general, the path must be found numerically, but noticing the similarity with the $h = 0$ path suggests a perturbation approach. A useful asymptotic representation for the path when h is small is thus found by perturbing away from the $h = 0$ path. That is, we consider $\zeta_p(t) = \zeta^{(0)}(t) + h\zeta^{(1)}(t)$ where $\zeta^{(0)}(t)$ is simply

$$\zeta^{(0)}(t) = -i\frac{c_d t}{r}\sin\theta + ik'\left[1 - \left(\frac{c_o t}{r}\right)^2\right]^{\frac{1}{2}}\cos\theta \tag{3.3.9}$$

for $t_{pf} < t < r/c_o$ and its analytic continuation for $t > r/c_o$, where $t_{pf} = (x - y(k'^2 - 1)^{\frac{1}{2}})/c_d$. In this formula $r^2 = x^2 + y^2$ and $\tan\theta = -x/y$. The perturbation $\zeta^{(1)}(t)$ is

$$\zeta^{(1)}(t) = \frac{-(\zeta^{(0)2} + 1)^{\frac{1}{2}}}{ix - y\zeta^{(0)}(\zeta^{(0)2} + k'^2)^{-\frac{1}{2}}}; \tag{3.3.10}$$

a measure of the error in t is easily found by substituting this back into (3.3.5), whence the error is $\zeta^{(1)}\zeta^{(0)}/(\zeta^{(0)2} + k'^2)^{\frac{1}{2}}$.

Both the path and the solutions for the displacements and stresses found using this approximation are indistinguishable from the numerical solution provided $h \ll x$, thus to all intents and purposes the solutions for the stresses and displacements in this regime are completely explicit. The expressions are somewhat lengthy, so are omitted from the text. Nonetheless this perturbed path is useful as asymptotic expressions for the limit $h/x \to 0$ can be awkward to evaluate. In particular when $h \ll x$, and we are not in the close neighbourhood of the interface, the Schölte response is small and the compressional response at $t \sim r/c_o = t_o$ begins to emerge. The pressure in the neighbourhood of t_o is then given as

$$\sigma_{yy}^{tH}(x, y, t) \sim -\frac{\rho_f k^2}{\pi}\mathrm{Re}\left(\frac{2\zeta^2(t) + k^2}{\gamma_o'(\zeta(t))S(\zeta(t))}\Big|_{\zeta=-ik'\sin\theta}\frac{\mathrm{d}\zeta_p(t)}{\mathrm{d}t}\right), \tag{3.3.11}$$

where $\zeta_p(t)$ is given above. Two typical pressure plots are shown in Figures 3.9, 3.10, the solid line is the exact solution and the dashed lines are the asymptotic expressions; those around $t = t_l$, t_{pf} are given in the next section.

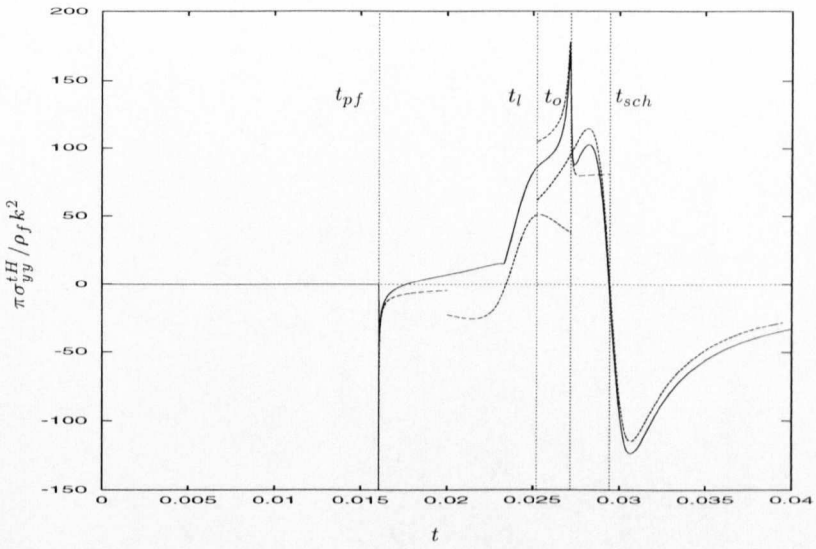

Figure 3.9. A plot of $\pi\sigma_{yy}^{tH}/\rho_f k^2$ versus t for material parameters typical of rock-water combinations; $x = 40$, $y = -4$, $h = 0.1$.

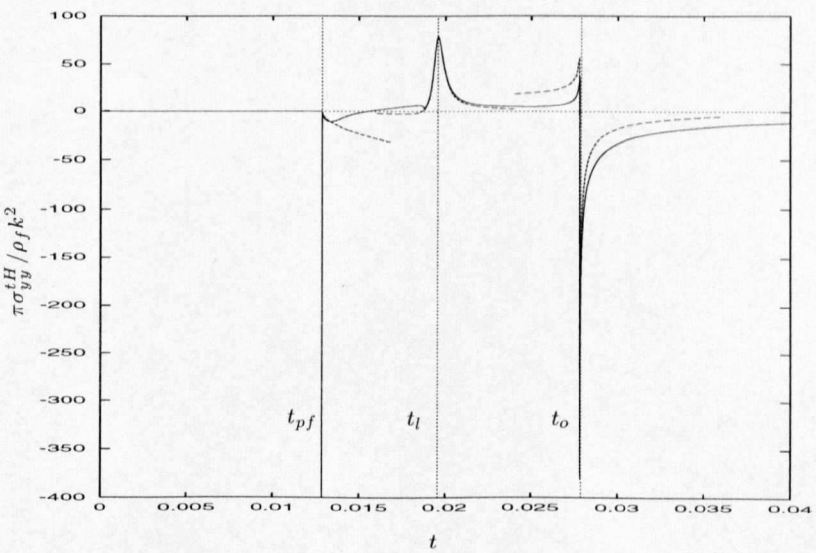

Figure 3.10. A plot of $\pi\sigma_{yy}^{tH}/\rho_f k^2$ versus t for material parameters typical of metal-water combinations; $x = 40$, $y = -10$, $h = 0.01$.

As we increase y the wavefronts move closer, more evidently for the rock-water case, nonetheless the asymptotics are still accurate. The only response masked somewhat is

that for leaky Rayleigh wave. In the metal-water case the Schölte response disappears once we are sufficiently far from the interface.

3.3.1.3. *Asymptotic analysis*

It is clear there are distinctive responses within the fluid associated with various wavefronts, we now wish to extract these explicitly. The previous section dealt with the emergence of the compressional response at $t \sim (x^2+y^2)^{\frac{1}{2}}/c_o$ as $h/x \to 0$; this section is concerned with the asymptotic forms of the other responses.

The Cagniard–de Hoop solution is intimately connected with the method of steepest descents, Knopoff & Gilbert (1959), in particular the saddle point is the point at which the Cagniard path cuts the imaginary axis. In the situation considered in this section this identifies the first arrival at $t = t_{pf}$. Thus one can explore the asymptotic behaviour of the solution either from the explicit solutions (3.3.8,3.3.2), or via an analysis of the Fourier transform and subsequent Laplace inversion. Since the path $\zeta(t)$ has often to be found numerically we use the later route as this leads to explicit results.

The inverse Fourier transform of (3.3.2) can be reduced to the sum of residue contributions and line integrals, however with the choice of branch cuts used above the poles either lie upon the cuts or on the lower Riemann sheet. For this calculation it is therefore convenient to change the orientation of the branch cuts, that is, we now take the cuts for $(\zeta^2+k^2)^{\frac{1}{2}}$, in the lower half plane, to run from $-ik$ to $-ik-\infty$, with similar definitions when k is replaced by k', 1. With our original choice of branch cuts the leaky Rayleigh pole lay on the lower Riemann sheet, thus we could not ascribe any response explicitly to it. However with this new choice of cuts the leaky pole is exposed, as is the Schölte pole; the leaky pole now lies upon the upper Riemann sheet. A convenient way of visualising a function like $S(\zeta)$ and the various associated cuts and zeros, Chapman (1972), is to consider the natural logarithm of the modulus of the Schölte function. For $S(\zeta)$ this is shown contoured on the upper Riemann sheet, and the features in the lower half of the complex ζ-plane are shown in Figure 3.11; the zeros are labelled $-ik_l$ and $-ik_{sch}$, and the branch cuts are shown by the bold solid lines. The Schölte zero is very close to the branch point at $-ik'$. Using this choice of cuts the asymptotic behaviour of the wavefronts is identified.

We examine each wave response in turn, beginning with the first arrival at $t = t_{pf}$. The wavefront is given by the limit as $\zeta \sim -i\zeta_{pf}$ in the exact solution (or using this as the saddle point in a steepest descents approach), where $\zeta(t_{pf}) = -i\zeta_{pf}$. Thus

$$\sigma_{yy}^{tH}(x,y,t) = -\frac{\rho_f k^2}{\pi}\frac{(k^2-2\zeta_{pf}^2)}{(k'^2-\zeta_{pf}^2)^{\frac{1}{2}}S(-i\zeta_{pf})[2\alpha_{pf}(t-t_{pf})]^{\frac{1}{2}}}, \tag{3.3.12}$$

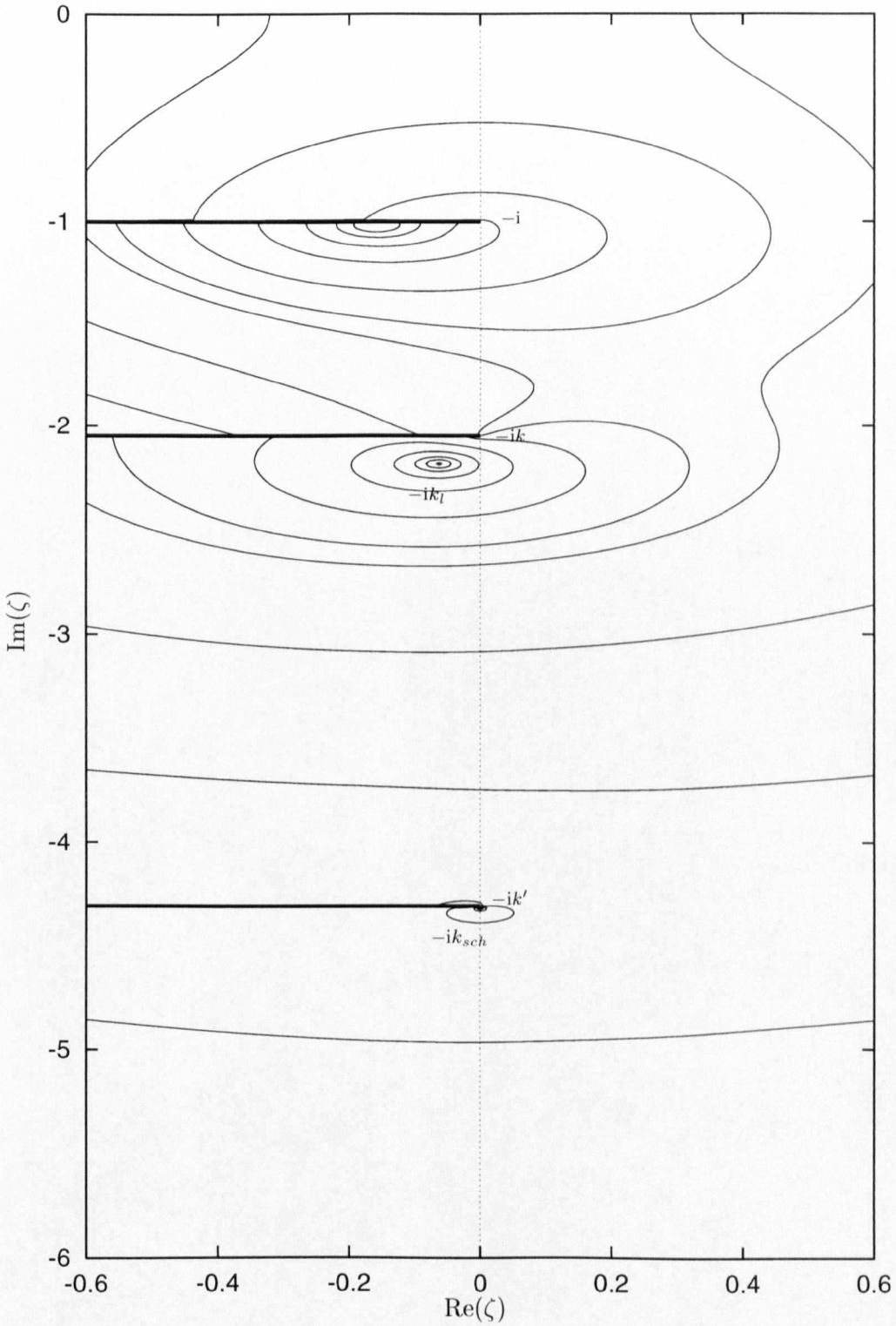

Figure 3.11. The natural logarithm of the modulus of the Schölte function contoured on the physical Riemann sheet, shown in the lower half of the complex ζ-plane. The zeros are labelled $-\mathrm{i}k_l$ and $-\mathrm{i}k_{sch}$ and the branch cuts are shown by the bold solid lines.

where $\alpha_{pf} = [h/(1-\zeta_{pf}^2)^{\frac{3}{2}} - k'^2 y/(k'^2-\zeta_{pf}^2)^{\frac{3}{2}}]/c_d$ and $S(-\mathrm{i}\zeta_{pf})$ is real. This is a one-sided disturbance for $t > t_{pf}$. This captures the singularity at $t = t_{pf}$, but if $h \ll 1$ there is a small, but distinctive peak that follows this singularity which is not captured by (3.3.12), see Figure 3.6. When $h \ll 1$ the Cagniard path becomes closer to the branch cuts and the saddle point $\zeta = -\mathrm{i}\zeta_{pf}$ approaches the branch point at $\zeta = -\mathrm{i}$, thus further terms are required and the asymptotic response is represented by

$$\sigma_{yy}^{tH}(x,y,t) \sim -\frac{\rho_f k^2}{\pi(k'^2-1)^{\frac{1}{2}}(k^2-2)}\left[\frac{1}{(2\alpha_{pf}(t-t_{pf}))^{\frac{1}{2}}} - \frac{4c_d}{h\zeta_{pf}(k^2-2)^2}\left(\frac{2(t-t_{pf})(k^2-1)}{\alpha_{pf}}\right)^{\frac{1}{2}}\right]. \tag{3.3.13}$$

The next response in time is due to the leaky Rayleigh wave; from the figures this clearly generates a large distinctive response in the fluid. As the choice of branch cuts above exposes the Rayleigh pole we calculate the leaky Rayleigh response via residues. The precise position of the pole is deduced using a simple numerical scheme described in detail in Appendix 3.B. Typical results are that, for aluminium-water, $\pm\mathrm{i}k_l = \pm 0.06336 \pm$ i2.18398, and for sandstone-water, $\pm\mathrm{i}k_l = \pm 0.15201 \pm$i1.64787. An asymptotic expression for k_l is

$$-\mathrm{i}k_l \sim -\mathrm{i}k_r + \frac{\mathrm{i}\epsilon k^4 k'(k_r^2-1)^{\frac{1}{2}}}{(k'^2-k_r^2)^{\frac{1}{2}}R'(-\mathrm{i}k_r)} \tag{3.3.14}$$

recalling that $R'(-\mathrm{i}k_r)$ is imaginary we rewrite this for convenience as $-\mathrm{i}k_l = -\mathrm{i}k_r - \epsilon k_c$. Thus one deduces an approximate arrival time for the leaky wave as

$$c_d t_l \sim k_r x - (k'^2 - k_r^2)^{\frac{1}{2}} y - \frac{\epsilon h k_r k_c}{(k_r^2-1)^{\frac{1}{2}}}, \tag{3.3.15}$$

and crucially this contains a source depth correction to the arrival time one deduces via geometrical ray theory.

The residue from the leaky pole is

$$\overline{\sigma}_{yy}^{tH}(x,y,p) = -\rho_f k^2 \mathrm{Re}\left[\frac{\mathrm{i}(k^2-2k_l^2)}{\gamma_o'(-\mathrm{i}k_l)S'(-\mathrm{i}k_l)} e^{-p(\gamma_d'(-\mathrm{i}k_l)h - \gamma_o'(-\mathrm{i}k_l)y + k_l x)/c_d}\right], \tag{3.3.16}$$

and upon taking the inverse Laplace transformation, we obtain

$$\sigma_{yy}^{tH}(x,y,t) = -\frac{\rho_f k^2}{\pi}\mathrm{Re}\left[\frac{(k^2-2k_l^2)}{\gamma_o'(-\mathrm{i}k_l)S'(-\mathrm{i}k_l)[t-(\gamma_d'(-\mathrm{i}k_l)h - \gamma_o'(-\mathrm{i}k_l)y + k_l x)/c_d]}\right], \tag{3.3.17}$$

together with terms of less significance; we have employed well known properties of the exponential integral in the above.

The expression (3.3.17), or the corresponding formula for the displacement, is plotted versus the exact solution in Figures 3.4, 3.5, 3.6, 3.7; (3.3.17) is the dotted line in the neighbourhood of t_l. Thus it is clear that equation (3.3.17) correctly predicts the position and magnitude of the peak associated with the leaky Rayleigh wave both for light and moderate fluid loading. It is perhaps surprising that the result still performs well even when ϵ is relatively large, as in rock-water, and this demonstrates the persistence of the leaky Rayleigh response even in this regime.

It is clear from the exact solution that there is an additional, sometimes significant, response. This is identified with either the Schölte wave, when $y \ll x$, or a compressional wave in the fluid, for $h \ll x$ see Section 3.3.1.2; or a combination of the two.

When the Schölte response is fully developed, as in Figure 3.4, a residue calculation yields the appropriate expression near t_{sch} for the Schölte wave as,

$$\sigma_{yy}^{tH}(x,y,t) = -\frac{\rho_f k^2}{\pi} \frac{(2k_{sch}^2 - k^2)(t - t_{sch})}{(k_{sch}^2 - k'^2)^{\frac{1}{2}}((t - t_{sch})^2 + \Lambda_1^2)\mathrm{i}S'(-\mathrm{i}k_{sch})} \tag{3.3.18}$$

where $\Lambda_1 = [y(k_{sch}^2 - k'^2)^{\frac{1}{2}} - h(k_{sch}^2 - 1)^{\frac{1}{2}}]/c_d$, and $S'(-\mathrm{i}k_{sch})$ is imaginary. Once again this asymptotic formula, or the corresponding result for the displacements, is highly accurate. It is shown as the dotted line in the neighbourhood of t_{sch} in the figures.

If both $h \ll x$ and $y \ll x$ both the Schölte and compressional fluid responses found in Section 3.3.1.2 are evident. If we are dealing with the metal-water case the Schölte pole is very close to the branch point at $-\mathrm{i}k'$ and this complicates the asymptotics deduced via transforms, however the analysis in 3.3.1.2 using the perturbed path allows the asymptotic forms to be extracted.

3.3.2. *A subsurface shear line source*

In an analogous manner to the above the transform solutions to the normal displacement and fluid pressure can be found; we will only treat the pressure here. The field consists of two pieces, the first is taken to be the solution of $\nabla^2\psi - \ddot{\psi}/c_s^2 = F(t)\delta(x)\delta(y-h)$ in an infinite elastic material, and the total field in the solid then consists of the superposition of this infinite body solution and the scattered field generated by the interface. We investigate the scattered field in detail. Figure 3.2 shows the geometry of the problem together with a schematic of the wavefronts generated.

Using the integral representations for the quantities of interest in Appendix 3.A the solutions are derived. In the fluid the Laplace transform of the fluid pressure is given by the Laplace transform

$$\overline{\sigma}_{yy}(x,y,p) = \frac{1}{2\pi}\int_{-\infty}^{\infty} \rho_f k^2 \frac{p^2\overline{F}(p)2\mathrm{i}\zeta\gamma_d'(\zeta)}{\gamma_o'(\zeta)S(\zeta)} e^{-p(\gamma_s'(\zeta)h - \gamma_o'(\zeta)y + \mathrm{i}\zeta x)/c_d}\mathrm{d}\zeta; \tag{3.3.19}$$

the inversion contour $\zeta(t)$ is chosen so that $c_d t = (\zeta^2 + k^2)^{\frac{1}{2}} h - (\zeta^2 + k'^2)^{\frac{1}{2}} y + \mathrm{i}\zeta x$. This might appear only trivially different from the path in the previous section, however this path can now intersect the branch cuts, and this leads to additional effects.

If, for simplicity, we initially restrict ourselves to results on the surface by setting $y = 0$ the integration path is given by

$$\zeta(t) = -\mathrm{i}\frac{c_d t}{r}\sin\theta \pm k\left[\left(\frac{c_s t}{r}\right)^2 - 1\right]^{\frac{1}{2}}\cos\theta, \text{ for } \frac{r}{c_s} \leq t < \infty, \tag{3.3.20}$$

where $r^2 = x^2 + h^2$ and $\tan\theta = x/h$. The path now cuts the imaginary axis at $\zeta = -\mathrm{i}k\sin\theta$ and does not intersect the branch cuts provided that $0 \leq \theta < \sin^{-1} c_s/c_d$. If however $\sin^{-1} c_s/c_d \leq \theta \leq \pi/2$ then the path must be supplemented by integrals taken along the branch cuts; these paths are defined as

$$\zeta_c(t) = -\mathrm{i}\frac{c_d t}{r}\sin\theta \pm \mathrm{i}k\left[1 - \left(\frac{c_s t}{r}\right)^2\right]^{\frac{1}{2}}\cos\theta, \text{ for } t \leq \frac{r}{c_s}. \tag{3.3.21}$$

In essence the integrals along the branch cuts give the head wave, SPF, contributions and an asymptotic analysis near the branch points yields the wavefront behaviour, described below for $y < 0$.

For $y < 0$ the Cagniard path $\zeta(t)$ is, as in the previous section, found numerically, or for $h \ll x$ via a perturbation from the $h = 0$ solution. Three typical paths are shown in Figure 3.12. These differ from the path found for the compressional source as the point where the path meets the imaginary axis $\zeta(t_{sf}) = -\mathrm{i}\zeta_{sf}$ (t_{sf} is the arrival time of the SF wave) can intersect the branch cuts, that is, $\zeta_{sf} > 1$. In this case the path is supplemented by an additional piece $\zeta_c(t)$ that runs along the branch cut from $\zeta = -\mathrm{i}$ to $\zeta = -\mathrm{i}\zeta_{sf}$. The function $\zeta_c(t)$ is also typically found numerically.

The pressure is

$$\begin{aligned}\sigma_{yy}^{tH}(x,y,t) = \frac{\rho_f k^2}{\pi}\Bigg[&H(t - t_{sf})\mathrm{Re}\left(\frac{2\mathrm{i}\zeta(t)\gamma_d'(\zeta(t))}{\gamma_o'(\zeta(t))S(\zeta(t))}\frac{\mathrm{d}\zeta(t)}{\mathrm{d}t}\right)\\ &+(H(t - t_{spf}) - H(t - t_{sf}))\mathrm{Re}\left(\frac{2\mathrm{i}\zeta_c(t)\gamma_d'(\zeta_c(t))}{\gamma_o'(\zeta_c(t))S(\zeta_c(t))}\frac{\mathrm{d}\zeta_c(t)}{\mathrm{d}t}\right)\Bigg],\end{aligned} \tag{3.3.22}$$

and two typical plots of $\pi\sigma_{yy}^{tH}(x,y,t)/\rho_f k^2$ versus t are shown in Figures 3.13, 3.14. The second term in 3.3.22 uses the supplementary path ζ_c and only occurs for $\theta \geq \theta_{spf}$ where $\theta_{spf} = \tan^{-1}[(k^2 - 1)^{-1/2} - (k'^2 - 1)^{-1/2} y/h]/[1 - (y/h)]$. In this case the first arrival is the head wave generated by the compressional wave in the solid and this occurs at $t_{spf} = [(k^2 - 1)^{\frac{1}{2}} h - (k'^2 - 1)^{\frac{1}{2}} y + x]/c_d$.

The pressure is singular at the arrival of the wave SF that is at $t = t_{sf}$. In the interval

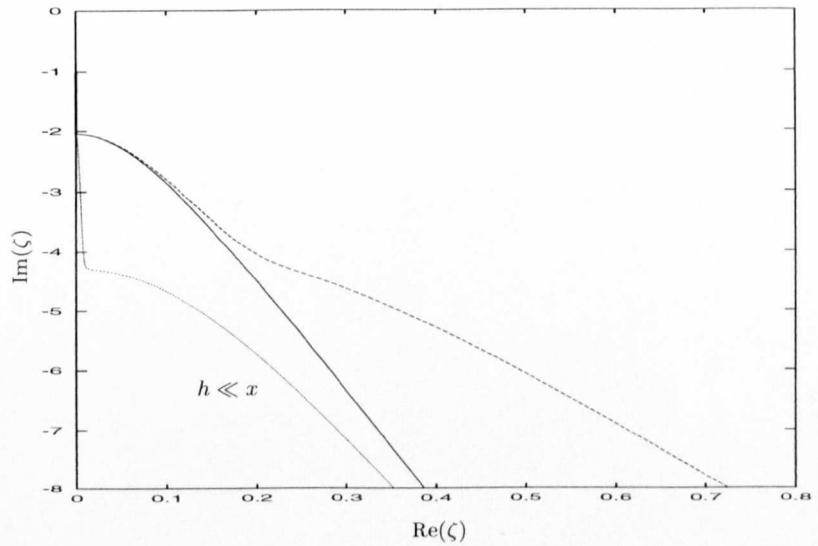

Figure 3.12. Three typical Cagniard paths; $y = 0$ solid line, $y < 0$ dashed lines.

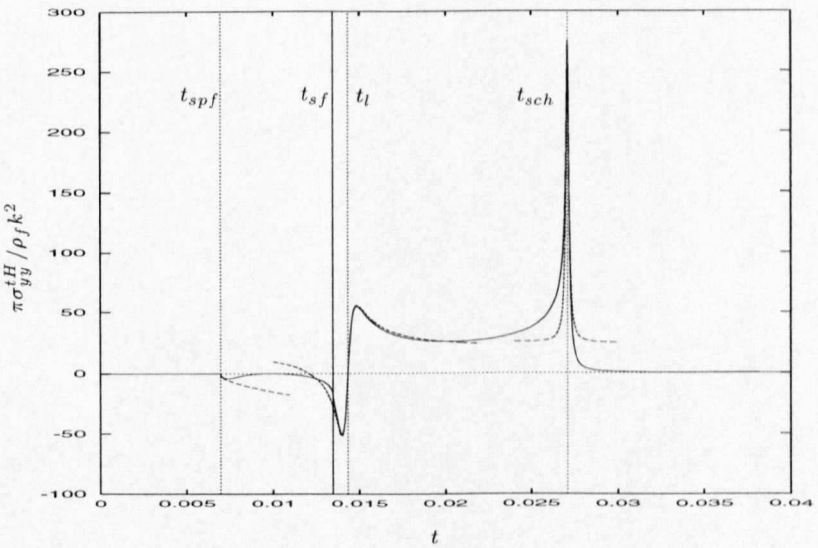

Figure 3.13. A plot of $\pi\sigma_{yy}^{tH}/\rho_f k^2$ versus t for material parameters typical of metal-water combinations; $x = 40$, $y = -1$, $h = 0.1$.

between t_{spf} and t_{sf} the pressure has a zero with zero slope; the zero arrives at time $t = (k(x+h) - (2k'^2 - k^2)^{\frac{1}{2}}y)/\sqrt{2}c_d$. The point of zero pressure travels along the interface with a horizontal velocity equal to $\sqrt{2}$ times the shear wavespeed of the solid, thus it is independent of both the fluid and the compressional wavespeed of the solid. A similar phenomenon occurs in the problem discussed by Roever *et al.* (1959). The pressure is

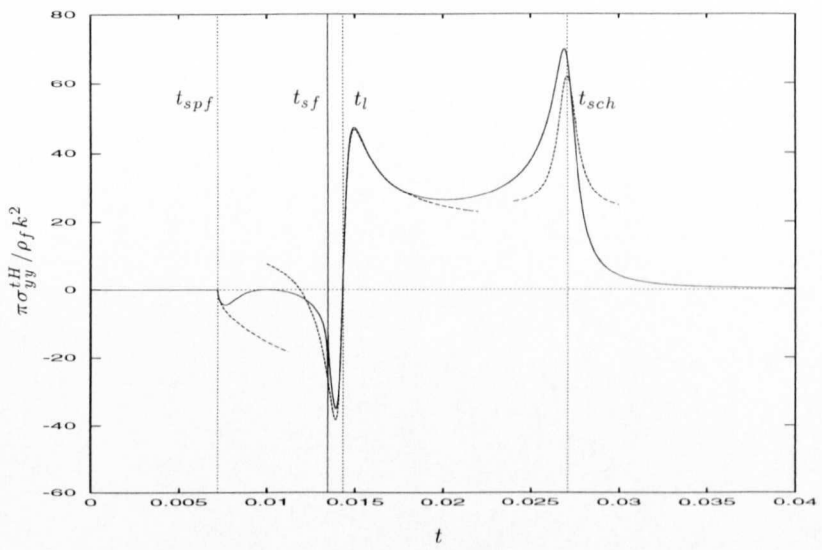

Figure 3.14. A plot of $\pi\sigma_{yy}^{tH}/\rho_f k^2$ versus t for material parameters typical of metal-water combinations; $x = 40$, $y = -1$, $h = 1$.

zero at the arrival time of the leaky Rayleigh wave, t_l where

$$c_d t_l \sim k_r x - (k'^2 - k_r^2)^{\frac{1}{2}} y - \frac{\epsilon h k_r k_c}{(k_r^2 - k^2)^{\frac{1}{2}}} \tag{3.3.23}$$

with two large distinctive peaks either side of t_l. The Schölte response follows at $t = t_{sch}$, and we have a similar situation to that of Section 3.3.1.2 when $h \ll 1$ with the emergence of a sharp compressional response at $t = t_o$.

The asymptotic behaviour in the neighbourhood of each wavefront arrival is shown by the dashed lines. They are deduced in a similar manner to those of the previous section.

The form of the head wave generated by the compressional wave in the solid is found from the exact solution in the limit as $\zeta \sim -\mathrm{i}$ and it is

$$\sigma_{yy}^{tH}(x, y, t) = -\frac{\rho_f k^2}{\pi} \frac{2(2(t - t_{spf}))^{\frac{1}{2}}}{(k'^2 - 1)^{\frac{1}{2}}(k^2 - 2)^2 \alpha_{spf}^{3/2}}, \tag{3.3.24}$$

where $\alpha_{spf} = (x + y/(k'^2 - 1)^{\frac{1}{2}} - h/(k^2 - 1)^{\frac{1}{2}})$. This is a one-sided disturbance for $t > t_{spf}$. In the neighbourhood of the point, $\theta = \theta_{spf}$, where it meets the compressional wave the above approximation fails and we recover the approximation to the compressional wave below. This is a two-sided disturbance and near its wavefront $\zeta \sim -\mathrm{i}\zeta_{sf}$

$$\sigma_{yy}^{tH}(x, y, t) = -\frac{\rho_f k^2}{\pi} \frac{2\zeta_{sf}(\zeta_{sf}^2 - 1)^{\frac{1}{2}} \delta_1}{(k'^2 - \zeta_{sf}^2)^{\frac{1}{2}}(\delta_1^2 + \delta_2^2)(2\alpha_{sf}(t_{sf} - t))^{\frac{1}{2}}}, \tag{3.3.25}$$

and $\zeta \sim -\mathrm{i}\zeta_{sf_+}$

$$\sigma_{yy}^{tH}(x,y,t) = \frac{\rho_f k^2}{\pi} \frac{2\zeta_{sf}(\zeta_{sf}^2-1)^{\frac{1}{2}}\delta_2}{(k'^2-\zeta_{sf}^2)^{\frac{1}{2}}(\delta_1^2+\delta_2^2)(2\alpha_{sf}(t-t_{sf}))^{\frac{1}{2}}}. \tag{3.3.26}$$

In these formulae $\delta_1 = (k^2-2\zeta_{sf}^2)^2$, $\delta_2 = 4\zeta_{sf}^2(\zeta_{sf}^2-1)^{\frac{1}{2}}(k^2-\zeta_{sf}^2)^{\frac{1}{2}} + \epsilon k^4 k'(\zeta_{sf}^2-1)^{\frac{1}{2}}/(k'^2-\zeta_{sf}^2)^{\frac{1}{2}}$, and $\alpha_{sf} = (k^2 h/(k^2-\zeta_{sf}^2)^{\frac{3}{2}} - k'^2 y/(k'^2-\zeta_{sf}^2)^{\frac{3}{2}})/c_d$. The plus and minus signs for $\zeta_{sf_\pm}$ denote the direction from which we approach. Note this exchanges a spatial singularity for one in time.

Once again we find the response due to the leaky Rayleigh wave by changing the orientation of the branch cuts, as discussed in the previous section, and use the residue contribution from the leaky Rayleigh pole this gives

$$\sigma_{yy}^{tH}(x,y,t) = \frac{\rho_f k^2}{\pi}\mathrm{Re}\left[\frac{2\mathrm{i}k_l\gamma_d'(-\mathrm{i}k_l)}{\gamma_o'(-\mathrm{i}k_l)S'(-\mathrm{i}k_l)}\left(\frac{1}{[t-(\gamma_s'(-\mathrm{i}k_l)h-\gamma_o'(-\mathrm{i}k_l)y+k_l x)/c_d]} - \frac{1}{[t_l-(\gamma_s'(-\mathrm{i}k_l)h-\gamma_o'(-\mathrm{i}k_l)y+k_l x)/c_d]}\right)\right], \tag{3.3.27}$$

where we have utilised the asymptotic form of the Laplace transform of the exponential function, and for additional accuracy we have incorporated the next term in the expansion. Equation (3.3.27) correctly predicts the position and magnitude of the peaks either side of the arrival time t_l, and confirms that they are due to the presence of the leaky Rayleigh pole; one could be misinterpreted as being due to the arrival of the SF wave.

Taking the residue due to the pole at $\zeta = -\mathrm{i}k_{sch}$ yields the appropriate expression for the Schölte wave, that is,

$$\sigma_{yy}^{tH}(x,y,t) = -\frac{\rho_f k^2}{\pi} \frac{2k_{sch}(k_{sch}^2-1)\Lambda_k}{c_d(k_{sch}^2-k'^2)^{\frac{1}{2}}((t-t_{sch})^2+\Lambda_k^2)\mathrm{i}S'(-\mathrm{i}k_{sch})} \tag{3.3.28}$$

where $\Lambda_k = [y(k_{sch}^2-k'^2)^{\frac{1}{2}} - h(k_{sch}-k^2)^{\frac{1}{2}}]/c_d$.

When $h \ll x$ a perturbation from the $h = 0$ path similar to that adopted in 3.3.1.2 is used, and this gives a strong response near t_o; this is shown in Figure 3.13.

3.3.3. *Subsurface line force*

Now we consider a vertical line force a distance h beneath the interface; the geometry of the problem together with a schematic of the wavefronts generated is borrowed from a superposition of Figures 3.1, 3.2. The field generated by the interaction of the line force with the interface is equivalent to the two-dimensional field generated by a plane pulse, with the wavefront parallel to the interface, incident upon an elastic solid containing a

small cylindrical void. Thus this example has a practical interpretation. The line force is also useful as a Green's solution for integral equation formulations.

The line force is characterised by $\rho\underline{F} = F(t)\delta(x)\delta(y-h)\hat{y}$ where $\hat{y}$ is the unit vector in the y direction. The fluid pressure is

$$\overline{\sigma}_{yy}(x,y,p) = \frac{1}{2\pi}\int_{-\infty}^{\infty} \frac{\epsilon k'k^2}{c_d}\frac{p\overline{F}(p)\gamma_d'(\zeta)}{\gamma_o'(\zeta)S(\zeta)}\Big[(2\zeta^2+k^2)e^{-p(\gamma_d'(\zeta)h-\gamma_o'(\zeta)y)/c_d} - 2\zeta^2 e^{-p(\gamma_s'(\zeta)h-\gamma_o'(\zeta)y)/c_d}\Big]e^{-ip\zeta x/c_d}\mathrm{d}\zeta; \tag{3.3.29}$$

this is closely related to the compressional and shear line sources. Equation (3.3.29) is the sum of compressional and shear terms that are distinguished by the subscripts d, s in the exponential terms. Thus in each piece we utilise the analysis of the previous sections. In particular the Cagniard paths described in the previous sections are used for the compressional and shear pieces, plots of $\pi c_d\sigma_{yy}^H(x,y,t)/\epsilon k'k^2$ versus t are shown in Figure 3.15 together with the asymptotic wavefronts. The first arrival is the compressional fluid wave generated by the compressional wave in the solid and this arrives at $t = t_{pf}$. This is immediately followed by the head wave generated by the shear wave in the solid. The compressional fluid wave generated by the shear wave in the solid arrives at $t = t_{sf}$. The asymptotic forms of the wavefronts follow by a minor adjustment of those in the earlier sections, and are not given here. The arrival time of the leaky response is slightly different for the compressional and shear pieces, however the difference is not noticeable in this figure. If the line force lies on the surface, $h = 0$, then the fluid pressure for a surface line force in Craster (1996b) is recovered.

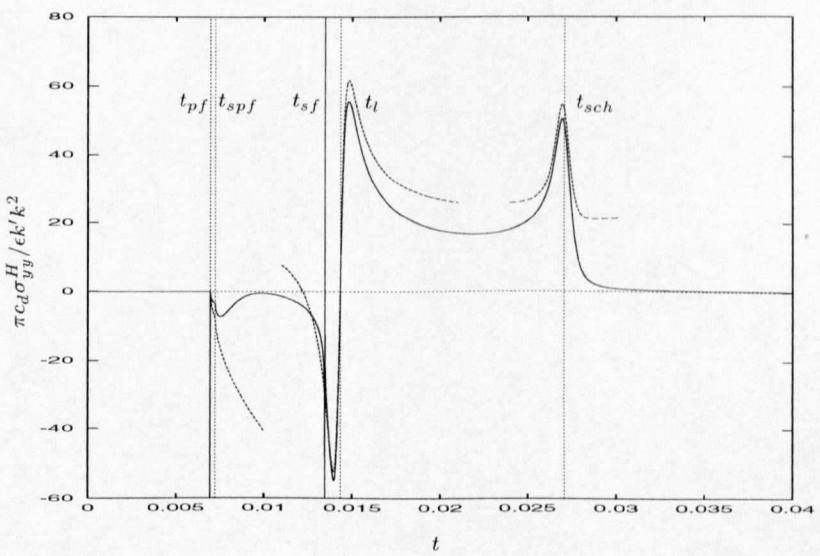

Figure 3.15. A plot of $\pi c_d\sigma_{yy}^H/\epsilon k'k^2$ versus t for material parameters typical of metal-water combinations; $x = 40$, $y = -1$, $h = 1$.

To demonstrate the ease by which more general loadings are incorporated we take the pulse shape of the source to be the four-point optimum Blackman window function, Harris (1978), i.e.,

$$F(t) = \begin{cases} 0 & \text{when } -\infty < t < 0 \\ \sum_{n=0}^{3} b_n \cos\left(\frac{2\pi n t}{T}\right) & \text{when } 0 < t < T \\ 0 & \text{when } T < t < \infty \end{cases} \tag{3.3.30}$$

in which the constants b_n are given by $b_0 = 0.35869$, $b_1 = -0.48829$, $b_2 = 0.14128$, and $b_3 = -0.01168$. This pulse shows similarity with the classical Ricker wavelet often used in seismology, de Hoop & van der Hijden (1985). To get the numerical form of the pressure response we convolve the pressures found for the special time dependence used in previous sections, that is, equations (3.3.8,3.3.22) and, if required, the analogous normal displacements, with the second and first derivative of this function, respectively. The pulse duration is taken to be $T = 0.01$ and the results are shown in Figures 3.16, 3.17. The response in the interior of the fluid is presented; the wavefront arrivals are clearly visible in the synthetic seismograms shown. The wavefront expansions for these more general cases are obtained by convolving the explicit expressions following equations (3.3.8) and (3.3.22) with the second and first derivative of (3.3.30), respectively. The expansions could be directly obtained via an asymptotic analysis of the transform solutions. However, it is an useful feature of our analysis that we generate these representations by a simple convolution.

Figures 3.16, 3.17 shows the wavefront expansions versus the exact solution and the agreement is reasonable.

3.4. Conclusion

The Cagniard–de Hoop technique has been used to examine three canonical problems, each of which is essentially a Green's function in space and time. In each case the exact solution is found in a simple closed form requiring minimal numerical work, and we are able to identify asymptotic representations for each wavefront arrival. When the sources are close to the surface an asymptotic representation of the Cagniard path is found, thus explicit solutions when $h \ll x$ are obtained. The perturbation approach of generating Cagniard paths should be useful in a range of related problems. This is explored further in Chapter 4. In addition we have identified the response due to the leaky Rayleigh wave, and in many circumstances this is the dominant disturbance. The origin of the leaky Rayleigh wave from a pole on the lower Riemann sheet demonstrates the importance of

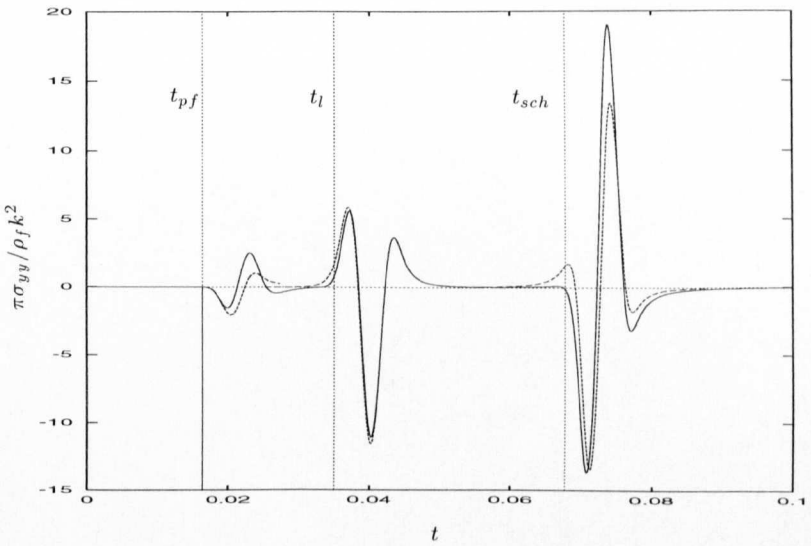

Figure 3.16. A plot of $\pi\sigma_{yy}/\rho_f k^2$ versus t for the four-point optimum Blackman window function under compressional source loading for material parameters typical of metal-water combinations; $x = 100$, $y = -1$, $h = 1$.

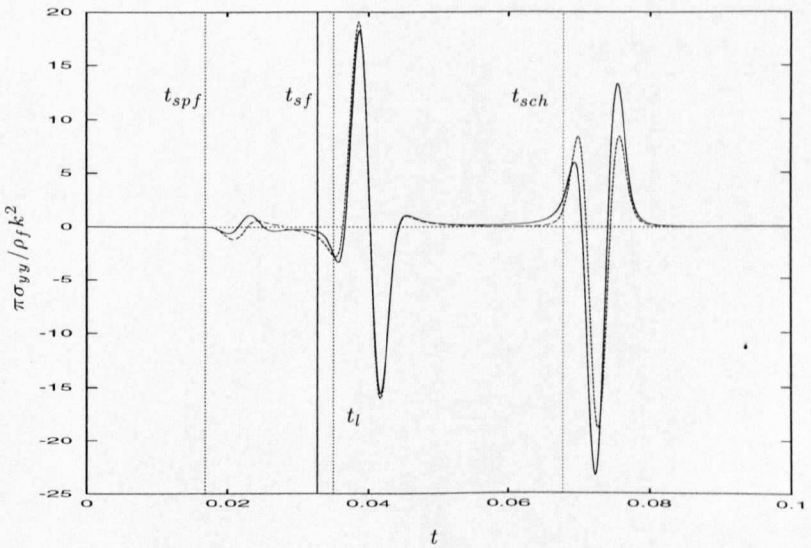

Figure 3.17. A plot of $\pi\sigma_{yy}/\rho_f k^2$ versus t for the four-point optimum Blackman window function under shear source loading for material parameters typical of metal-water combinations; $x = 100$, $y = -1$, $h = 1$.

the contribution of complex poles on lower Riemann sheets to the full solution. The effect of these poles is often ignored, or it is incorrectly stated that they cannot be utilised.

A particularly useful aspect of our asymptotic analysis is that general time dependent forcings are easily treated. That is we can construct the asymptotic form of the wavefront

arrivals for a general forcing utilising the wavefront expansions found for simpler Green's function forcings; these are considerably simpler to use than the full solution. They are also considerably faster to evaluate than the full convolution solution; this will become even more noticeable when similar methods are used in more complicated geometries.

Similar methods can be used to find the wavefronts in the solid, and moreover, the asymptotic fields in the solid for any forcing. It is felt that these results are of less practical importance, and therefore the results are not presented here. One other aspect not treated here is the asymptotics of very light fluid loading, $\epsilon \ll 1$. As described in Craster (1997) one can perturb away from the *in vacuo* elastic solution and obtain relatively simple and accurate approximations.

The above results will be useful in formulating more realistic fluid-solid interaction problems. The treatment may be routinely extended to examine the equivalent three dimensional problems as well as extensions to layered media and anisotropic elastic materials.

References

Briggs, G. A. D., 1992. *Acoustic microscopy.* Monographs on the physics and chemistry of materials: 47, Oxford University Press.

Cagniard, L., 1939. *Réflection et réfraction des ondes séismique progressives.* Gauthiers-Villars, Paris. Trans. and rev. by E. A. Flinn and C. H. Dix, 1962. *Reflection and refraction of progressive seismic waves.* McGraw-Hill, New York.

Chapman, C. H., 1972. Lamb's problem and comments on the paper 'On Leaking Modes' by Usha Gupta. *Pure Appl. Geophys.* **94**, 233–247.

Craster, R. V., 1996a. A canonical problem for fluid-solid interfacial wave coupling. *Proc. R. Soc. Lond. A* **452**, 1695–1711.

Craster, R. V., 1996b. Wavefront expansions for pulse scattering by a surface inhomogeneity. *Quart. J. Mech. Appl. Math.* **49**, 657–674.

Craster, R. V., 1997. The light fluid loading limit for fluid/solid interactions. *Euro. J. Appl. Math* **8**, 405–505.

Crighton, D. G., 1989. The 1988 Rayleigh Medal lecture: fluid loading - the interaction between sound and vibration. *J. Sound Vib.* **133**, 1–27.

de Hoop, A. T., 1960. A modification of Cagniard's method for solving seismic pulse problems. *Appl. sci. Res. B* **8**, 349–356.

de Hoop, A. T. & van der Hijden, J. H. M. T., 1983. Generation of acoustic waves by an impulsive line source in a fluid/solid configuration with a plane boundary. *J. Acoust. Soc. Am.* **74**, 333–342.

de Hoop, A. T. & van der Hijden, J. H. M. T., 1984. Generation of acoustic waves by an impulsive point source in a fluid/solid configuration with a plane boundary. *J. Acoust. Soc. Am.* **75**,

1709–1715.

de Hoop, A. T. & van der Hijden, J. H. M. T., 1985. Seismic waves generated by an impulsive point source in a fluid/solid configuration with a plane boundary. *Geophysics* **50**, 1083–1090.

Drijkoningen, G. G. & Chapman, C. H., 1988. Tunneling rays using the Cagniard de Hoop method. *Bull. Seism. Soc. Am.* **78**, 898–907.

Garvin, W. W., 1956. Exact transient solution of the buried line source problem. *Proc. R. Soc. Lond. A* **234**, 528–541.

Harris, F. J., 1978. On the use of windows for harmonic analysis with the discrete Fourier transform. *Proc. Inst. Elect. and Electron. Eng.* **66**, 51–83.

Hong, T. L. & Helmberger, D. V., 1977. Generalized ray theory for dipping structure. *Bull. Seism. Soc. Am.* **67**, 995–1008.

Knopoff, L. & Gilbert, F., 1959. First motion methods in theoretical seismology. *J. Acoust. Soc. Am.* **31**, 1161–1168.

Lamb, H., 1904. On the propagation of tremors over the surface of an elastic solid. *Phil. Trans. R. Soc. Lond. A* **203**, 1–42.

Miklowitz, J., 1978. *The theory of elastic waves and waveguides*. North-Holland.

Roever, W. L., Vining, T. F. & Strick, E., 1959. Propagation of elastic wave motion from an impulsive source along a fluid/solid interface. *Phil. Trans. R. Soc. Lond. A* **251**, 455–523.

van der Hijden, J. H. M. T., 1987. *Propagation of transient elastic waves in stratified anisotropic media*. North-Holland series in applied mathematics and mechanics: vol. 32.

Appendix 3.A. Fourier and Laplace transformed variables

In $y > 0$ the material is elastic and the Fourier and Laplace transformed displacements and stresses are

$$\widetilde{\widetilde{u}}_x(\xi,y,p) = -\mathrm{i}\xi A(\xi,p)e^{-\gamma_d(\xi,p)y} - \gamma_s(\xi,p)B(\xi,p)e^{-\gamma_s(\xi,p)y}, \tag{3.A 1}$$

$$\widetilde{\widetilde{u}}_y(\xi,y,p) = -\gamma_d(\xi,p)A(\xi,p)e^{-\gamma_d(\xi,p)y} + \mathrm{i}\xi B(\xi,p)e^{-\gamma_s(\xi,p)y}, \tag{3.A 2}$$

$$\widetilde{\widetilde{\sigma}}_{xy}(\xi,y,p) = \mu\left[2\mathrm{i}\xi\gamma_d(\xi,p)A(\xi,p)e^{-\gamma_d(\xi,p)y} + B(\xi,p)\left(2\xi^2 + \frac{p^2}{c_s^2}\right)e^{-\gamma_s(\xi,p)y}\right], \tag{3.A 3}$$

$$\widetilde{\widetilde{\sigma}}_{yy}(\xi,y,p) = \mu\left[\left(2\xi^2 + \frac{p^2}{c_s^2}\right)A(\xi,p)e^{-\gamma_d(\xi,p)y} - 2\mathrm{i}\xi\gamma_s(\xi,p)B(\xi,p)e^{-\gamma_s(\xi,p)y}\right], \tag{3.A 4}$$

and in the fluid region $y < 0$ the relevant Fourier and Laplace transformed variables are

$$\widetilde{\widetilde{u}}_y(\xi,y,p) = \gamma_o(\xi,p)C(\xi,p)e^{\gamma_o(\xi,p)y}, \tag{3.A 5}$$

$$\widetilde{\widetilde{\sigma}}_{yy}(\xi,y,p) = \rho_f p^2 C(\xi,p)e^{\gamma_o(\xi,p)y}, \tag{3.A 6}$$

where the functions $A(\xi,p)$, $B(\xi,p)$, and $C(\xi,p)$ are presently unknown functions of ξ and p.

The functions $\gamma_d(\xi,p)$, $\gamma_s(\xi,p)$, and $\gamma_o(\xi,p)$ that appear are defined as $\gamma_q(\xi,p) = (\xi^2 + p^2/c_q^2)^{\frac{1}{2}}$ with $q = d,\ s,\ o$; the functions have branch cuts from $\pm\mathrm{i}p/c_q$ to $\pm\mathrm{i}\infty$. We introduce a rescaling $\xi = p\zeta/c_d$ in the text, such that the functions are now given by $\gamma'_q(\zeta) = (\zeta^2 + k_q^2)^{\frac{1}{2}}$, with $q = d,\ s,\ o$; the factor p/c_d is extracted explicitly. In this formula $k_d = 1, k_s = k = c_d/c_s$ and $k_o = k' = c_d/c_o$.

Appendix 3.B. The zeros of $S(\zeta)$

The purpose of this appendix is to obtain the position of the leaky Rayleigh zero of the Schölte function $S(\zeta)$, this is required in the text. As noted earlier the zeros are usually on the lower Riemann sheet and have no explicit influence, however we can choose the branch cuts appropriately to move them onto the upper Riemann sheet. The leaky poles are then utilised in the residue calculation. In this appendix the branch cuts for the function γ_q' are taken to be the straight lines from $\pm \mathrm{i}k_q$ to $\pm \mathrm{i}k_q \pm \infty$; this choice of branch cuts differs from that adopted in Appendix 3.A, and the additional zeros now move back to the upper Riemann sheet. The two leaky poles are at $\pm \mathrm{i}k_l$; for simplicity only the upper half plane is considered here. The position of the zero at $\mathrm{i}k_l$ is found using a simple numerical scheme outlined in Craster (1996a).

Given an analytic function $f(z)$ that has a simple zero inside the closed domain D, then the integral

$$\int_{\partial D} \frac{z f'(z)}{f(z)} \mathrm{d}z, \tag{3.B 1}$$

around a positively orientated contour along the boundary of D, extracts its position explicitly. This integral is performed numerically around a rectangle whose longer sides run along the edges of the branch cuts for $(\zeta - \mathrm{i}k)^{\frac{1}{2}}$ and $(\zeta - \mathrm{i}k')^{\frac{1}{2}}$ and shorter sides are parallel to the imaginary axis; the part of the imaginary axis between $\mathrm{i}k$ and $\mathrm{i}k'$ is enclosed by the rectangle. It can be demonstrated using the argument principle that a zero lies in this region.

The root is found to an accuracy of 10^{-5} using a standard numerical quadrature routine. Typical results are that, for aluminium-water, $\pm \mathrm{i}k_l = \pm 0.06336 \pm \mathrm{i}2.18398$, and for sandstone-water, $\pm \mathrm{i}k_l = \pm 0.15201 \pm \mathrm{i}1.64787$. Hence, the position of the leaky zero is considered known when it is used in the text.

The numerical scheme can equally be used to find the Schölte zero at $\pm \mathrm{i}k_{sch}$; the rectangle is now positioned above the branch cut at $\mathrm{i}k'$ in the upper half plane.

Chapter Four

Cagniard–de Hoop path perturbations with applications to non-geometric wave arrivals

4.1. Introduction

The Cagniard–de Hoop technique, Cagniard (1939), de Hoop (1960), provides an excellent method for solving and investigating various elastic wave interaction problems. Indeed, many model problems can be analysed in detail, and both the physical structure and the importance of the responses determined. In particular, the interactions between source excitations, interfaces and layers are revealed, and explicit solutions found; this, together with a useful asymptotic scheme, is the aim of the current chapter.

In seismology and seismic exploration many cases exist where tunnelling is important; this contribution is sometimes overlooked. One major area where this response is relevant is in oil exploration where shallow explosive sources generate these signals due to mode conversion at the free surface. The responses may also be evident in acoustic microscopy when dealing with scattering by shallow sub-surface cracks.

The method itself is discussed in considerable detail by Aki & Richards (1980), Miklowitz (1978), and others. In essence, the solution is given in terms of a path (or several paths) $\zeta(x,y,t)$ that, in general, depends on a parameter, h, that is either the source depth, or the layer thickness. Using a particular time dependence the Cagniard–de Hoop method consists of an elegant transformation that reduces a double transform inversion to an explicit result; more general time dependence is then easily incorporated using convolution theorems.

In brief, we utilise Fourier and Laplace transforms in space and time respectively: the Laplace transform in time t, and its inverse, are defined as

$$\overline{f}(p) = \int_0^\infty f(t)e^{-pt}\mathrm{d}t, \quad f(t) = \frac{1}{2\pi\mathrm{i}}\int_{c-\mathrm{i}\infty}^{c+\mathrm{i}\infty}\overline{f}(p)e^{pt}\mathrm{d}p, \quad \text{for } \mathrm{Re}(c) > 0 \tag{4.1.1}$$

where p is the Laplace transform variable, and the Fourier transform in x, and its inverse, are defined as

$$\widetilde{f}(\xi) = \int_{-\infty}^{\infty} f(x)e^{\mathrm{i}\xi x}\mathrm{d}x, \quad f(x) = \frac{1}{2\pi}\int_C \widetilde{f}(\xi)e^{-\mathrm{i}\xi x}\mathrm{d}\xi, \tag{4.1.2}$$

where ξ is the Fourier transform variable. The inversion path C runs along the real axis from $-\infty$ to ∞. Using transformations of the governing equations, to be discussed in

Section 4.2, and a rescaling of the transform variable, typically $\xi = p\zeta$, we obtain

$$f(x,y,t) = \frac{1}{2\pi \mathrm{i}} \int_{c-\mathrm{i}\infty}^{c+\mathrm{i}\infty} \frac{1}{2\pi} \int_{-\infty}^{\infty} g(\zeta) e^{-pz(\zeta)} \mathrm{d}\zeta e^{pt} \mathrm{d}p. \tag{4.1.3}$$

Both the functions $g(\zeta)$ and $z(\zeta)$ are usually rather complicated, containing branch points and poles. Typically, as in the case we consider in Section 4.2, the function $z(\zeta)$ takes the form

$$z(\zeta) = \gamma_d(\zeta)h + \gamma_s(\zeta)y + \mathrm{i}\zeta x. \tag{4.1.4}$$

The functions γ_q that appear are defined as $\gamma_d(\zeta) = (\zeta^2 + 1)^{\frac{1}{2}}$, $\gamma_s(\zeta) = (\zeta^2 + k^2)^{\frac{1}{2}}$, where the branch cuts are taken running along the imaginary axes from $\pm\mathrm{i}$ to $\pm\mathrm{i}\infty$ and $\pm\mathrm{i}k$ to $\pm\mathrm{i}\infty$ respectively. The Cagniard–de Hoop technique now involves defining a Fourier inversion path $\zeta(x,y,t)$ such that it is the solution of the transcendental equation $z(\zeta) = t$, namely

$$t = \gamma_d(\zeta)h + \gamma_s(\zeta)y + \mathrm{i}\zeta x, \tag{4.1.5}$$

with $t > t_{critical}$ say. Once such a path is found the double transform above becomes the inverse Laplace transform of a Laplace transform, thus the explicit answer is clear by inspection.

In simple cases when, say $h = 0$, equation (4.1.5) is solvable explicitly and this then yields much useful information. In particular we can study the wavefront arrivals and their asymptotic forms explicitly. These can then be used in conjunction with a convolution theorem to generate fast and accurate artificial seismograms.

The limit as the ratio $h/x \to 0$ is of interest in many applications. This perturbation away from $h = 0$ smooths out the sharp wavefront arrivals that were, when $h = 0$, associated with saddle points in the transform domain, or equivalently specific points on the Cagniard paths where the path left the branch cuts. Once the parameter h is non-zero the analysis becomes more difficult since the path $\zeta(t)$ must now be found numerically. A quartic equation may be formulated and solved explicitly; the analysis is relegated to Appendix 4.A. However in the limit as $h/x \to 0$ this is not particularly revealing. In this case we expect the asymptotics of the wavefronts to be less obvious; this occurs for many model problems. For instance the path in (4.1.5) is required if we are interested in studying the $S^\star$ arrival, Hron & Mikhailenko (1981), that has been given much attention and which we describe in Section 4.2. In the limit as the source tends to the interface, $h \to 0$, the Cagniard path has a noticeable sharp bend; this has been noticed before by Hron & Mikhailenko (1981). This dramatic bend occurs near to the point at which the path would have left the branch cuts when $h = 0$, thus it is natural to investigate perturbing away from the $h = 0$ solutions.

In the case of a thin fast fluid layer sandwiched between larger fluid layers, Mellman &

Helmberger (1974) also noticed a sharp bend in one of the Cagniard paths for a generalised ray and drew attention to the connection with the non-geometric transmitted wavefront. Later Drijkoningen & Chapman (1988) and Drijkoningen (1991) suggested that this bend in the Cagniard path was generic for many wave arrivals of this type, and that the Cagniard technique was the natural way to study these phenomena. The problems treated in Drijkoningen & Chapman (1988) concentrate upon fluid half spaces for which the Cagniard paths are known explicitly, the current chapter is an extension of this approach in that the elastic counterparts are treated. More generally the perturbation scheme we use easily leads to asymptotic results in the more complicated cases when the Cagniard path must be found numerically.

One detail that appears to have been overlooked, but is rather useful, is that in the limit as the ratio h/x tends to zero we can use the explicit path found when $h = 0$ to generate an accurate asymptotic representation for $\zeta(t)$ outside some close neighbourhood of t_{s^*}, that we discuss and determine in Section 4.2. In itself this is already faster than finding $\zeta(t)$ numerically but crucially any further manipulations are much less time-consuming, particularly if we then wish to look at quite general time dependent sources, or consider extensions to three dimensions. It also indicates that the approach might be equally rewarding in anisotropic media. More importantly it also allows a thorough asymptotic analysis of the underlying physical problems to be examined.

In this chapter we consider a compressional source beneath a fluid-solid interface. This problem illustrates tunnelling effects within a 'slow' material (the fluid) due to a source in a 'fast' material, and also tunnelling in the 'fast' material due to the coupling between a 'fast' compressional wave and a 'slow' shear wave.

To demonstrate the wider applicability of the approach used here we also consider a thin fast layer and use generalised ray theory to analyse this in detail. In this case we pick out the paths relating to the non-geometric arrivals, and these are then treated using the asymptotic approach.

Several alternative approaches to similar problems have been considered in the literature, but the explicit effect of the non-geometric waves is often hard to extract. Treating time harmonic dependence, several authors have identified high frequency, far field responses, see for instance Abramovici *et al.* (1989), Gutowski *et al.* (1984), Daley & Hron (1983); the analysis then involves steepest descents and follows, say, Brekhovskikh (1980); the equivalent responses are evanescent waves. Complex ray theory could also be employed since the arrivals have complex phase, see for instance Einziger & Felsen (1982), Babich & Kiselev (1989), or numerical modelling, see for instance Hron & Mikhailenko (1981), Stephen & Bolmer (1985). However, the Cagniard-de Hoop approach is very

direct, particularly revealing, and explicit solutions in all space and time are deduced; the time harmonic results, if required, are then a subset of these solutions.

4.2. A compressional source beneath a fluid-solid interface

In this section we solve the problem of a compressional source beneath a fluid-solid interface. We demonstrate that, in the limit as the ratio $h/x \to 0$, a definite response occurs in the solid associated with the prominent $S^\star$ arrival. The $S^\star$ response is a non-geometric arrival that is formed by the reflected shear wave at the interface. Moreover, we identify the part of the Cagniard path that contributes to this response, namely the bend in the path that is close to the branch cuts. In order to appreciate the characteristics of the pseudo-shear wave a wavefront expansion is deduced using a perturbation of the Cagniard path that may be found explicitly when the source depth $h = 0$. This approach will open the way to considering a wide range of problems that contain a characteristic length scale h that effects non-geometric responses. In the next section we consider a thin fast layer; this configuration often occurs in model problems. The non-geometric response in the fluid is not treated here.

The fluid-solid configuration to be considered is shown in Figures 4.1 and 4.2 with the y-axis pointing downwards. The depth, h, of the line compressional source is not shown; it is taken to be $0 < h/x \ll 1$. In addition a schematic of the primary geometric wavefronts generated in each case, $h/x \to 0$ and $h = 0$, is shown in Figure 4.1 and Figure 4.2 respectively. Here the situation $h = 0$ is non-physical for the compressional source loading as it does not satisfy the interfacial conditions correctly. Nevertheless, the physical effects are relevant when this problem is perturbed; we are interested in this limiting case.

The notation that appears in the two schematics has been adopted from geometrical ray theory. The letters PP, PS, and PF are used to denote the compressional and shear waves in the solid, and the compressional wave in the fluid, generated by the direct compressional field from the source respectively. In the case $h = 0$ both the PS and PF responses take the shape of head waves.

The starred letters $F^\star$, $S^\star$, and $SF^\star$ are used to denote the compressional wave in the fluid, the shear wave in the solid, and the head wave in the fluid generated by the shear wave respectively, in Figure 4.1. That is, these are the waves generated by interaction with the interface. These waves are the precursors to the unstarred field in Figure 4.2, and are investigated in the current chapter. As h is sufficiently increased the starred fields loose their prominence. In addition, the figures omit the wavefronts due to the

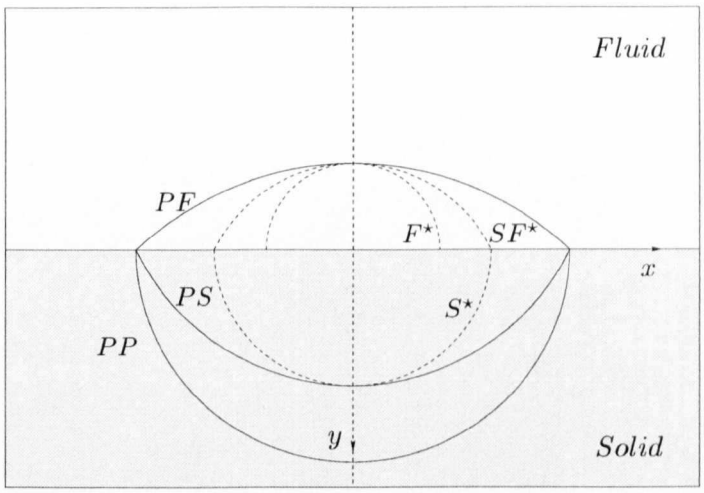

Figure 4.1. A schematic showing the radiated wavefronts for the waves generated by a line compressional source in the limit as the ratio $h/x \to 0$.

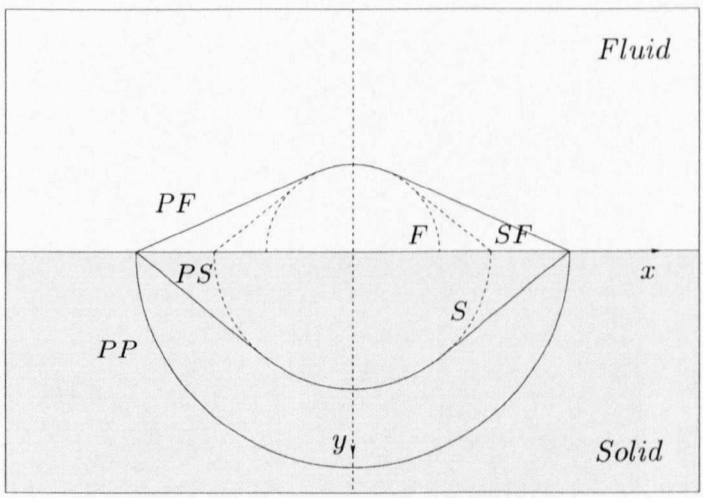

Figure 4.2. A schematic showing the radiated wavefronts for the waves generated by a line force at a fluid-solid interface; $h = 0$.

interfacial Schölte wave and, for light fluid loading, the leaky Rayleigh wave, and the direct compressional wave from the source.

The configuration consists of an isotropic linear elastic material in $y > 0$ and a compressible fluid in $y < 0$. The responses of the two half spaces are coupled together through the continuity boundary conditions along the interface $y = 0$, these are discussed following (4.2.1). A Cartesian coordinate system is adopted with x_1, x_2 corresponding to x, y.

In the usual way, the elastic material has Lamé constants λ, μ, and density ρ. The stresses σ_{ij} in the material are related to the displacements u_i via $\sigma_{ij} = \lambda\epsilon_{kk}\delta_{ij} + 2\mu\epsilon_{ij}$

where $\epsilon_{ij} = \frac{1}{2}(u_{i,j} + u_{j,i})$, the comma denoting differentiation with respect to x_i. The governing equations in the elastic material are the equilibrium equations $\sigma_{ij,j} = \rho\ddot{u}_i$, where the notation $\ddot{}$ denotes double partial differentiation with respect to time.

The compressible fluid in $y < 0$ is effectively an elastic material that supports no shear stresses. Thus $\sigma_{ij} = \lambda_f \epsilon_{kk}\delta_{ij}$, where the fluid has density ρ_f and compressional modulus λ_f. The governing equations are $\sigma_{ij,j} = \rho_f \ddot{u}_i$ again.

We utilise the displacement potentials ϕ, ψ, and χ where the displacements are $\mathbf{u} = \nabla\phi + \nabla \times \psi\hat{z}$ (where $\hat{z}$ is the unit vector in the z direction) in $y > 0$ and $\mathbf{u} = \nabla\chi$ in $y < 0$. The displacement potentials ϕ and ψ are related to the compressional and shear disturbances respectively, thus we utilise these when generating compressional sources. The following wave speeds c_d, c_s, and c_o are defined in terms of the material parameters as $c_d^2 = (\lambda + 2\mu)/\rho$, $c_s^2 = \mu/\rho$, and $c_o^2 = \lambda_f/\rho_f$.

The assumption that the compressional wavespeed of the fluid is less than the shear wavespeed of the solid is taken so that $c_d > c_s > c_o$; this is a reasonable assumption for most solid and fluid combinations. The analysis presented here does not rely on this assumption, and is easily generalised to allow $c_d > c_o > c_s$, say, which would be typical of perspex-water combinations. A coupling parameter ϵ occurs in the analysis; it is defined as $\epsilon = \rho_f c_o/\rho c_d$, and gives a measure of the fluid-solid coupling. The light fluid loading limit is when $\epsilon \ll 1$; this specific limit is not taken here unless explicitly stated.

The continuity boundary conditions

$$[\![\sigma_{yy}(x,0,t)]\!] = 0, \ \sigma_{xy} = 0, \ [\![u_y(x,0,t)]\!] = 0 \tag{4.2.1}$$

are taken on the interface $y = 0$, where the braces $[\![\ ]\!]$ denote the jump in a quantity across the interface; both the stresses σ_{yy} and the normal displacement u_y are continuous across $y = 0$. The fluid supports no shear stresses, thus $\sigma_{xy} = 0$ on $y = 0$. The total field in the solid consists of the superposition of two fields. The first is the solution to the source problem $\nabla^2\phi - \ddot{\phi}/c_d^2 = F(t)\delta(x)\delta(y-h)$, in an infinite elastic material, where $F(t)$ gives the time dependence of the source and $\delta(\ )$ denotes the delta function. The second field is the response generated by the interfacial boundary conditions; all figures show this second field.

The analysis is performed using the Fourier and Laplace transforms defined by equations (4.1.1) and (4.1.2) respectively. The representations for the Fourier and Laplace transformed stresses and displacements are given in Appendix 3.A; they are not repeated here.

The plan of this section is that we solve the source problems exactly, both for displacements and stresses; the asymptotic analysis is then developed as in Section 3.3.1.3. In this

chapter we concentrate solely upon the asymptotics associated with the non-geometric effect; the asymptotics for the other responses are shown in the figures, but the expressions are not given explicitly here. We concentrate upon the $S^\star$ response in the solid; the $F^\star$ response in the fluid is treated more briefly in Section 3.3.1.2.

4.2.1. *Exact solution*

Using the appropriate integral representations the solutions are derived. In the solid the Laplace transform of the normal displacement is

$$\begin{aligned}\overline{u}_y(x,y,p) = &-\frac{1}{2\pi}\int_{-\infty}^{\infty}\frac{1}{2c_d}\frac{p\overline{F}(p)s(\zeta)}{S(\zeta)}e^{-p(\gamma_d(\zeta)(h+y)+\mathrm{i}\zeta x)/c_d}\mathrm{d}\zeta \\ &+\frac{1}{2\pi}\int_{-\infty}^{\infty}\frac{2}{c_d}\frac{p\overline{F}(p)\zeta^2(2\zeta^2+k^2)}{S(\zeta)}e^{-p(\gamma_d(\zeta)h+\gamma_s(\zeta)y+\mathrm{i}\zeta x)/c_d}\mathrm{d}\zeta,\end{aligned} \tag{4.2.2}$$

where $\overline{F}(p)$ is the Laplace transform of $F(t)$ given by (4.1.2). The stress $\overline{\sigma}_{yy}$ in the solid is given by a similar Laplace transform:

$$\begin{aligned}\overline{\sigma}_{yy}(x,y,p) = &\frac{1}{2\pi}\int_{-\infty}^{\infty}\frac{\mu}{2c_d^2}\frac{p^2\overline{F}(p)s(\zeta)(2\zeta^2+k^2)}{\gamma_d(\zeta)S(\zeta)}e^{-p(\gamma_d(\zeta)(h+y)+\mathrm{i}\zeta x)/c_d}\mathrm{d}\zeta \\ &-\frac{1}{2\pi}\int_{-\infty}^{\infty}\frac{4\mu}{c_d^2}\frac{p^2\overline{F}(p)\zeta^2(2\zeta^2+k^2)\gamma_s(\zeta)}{S(\zeta)}e^{-p(\gamma_d(\zeta)h+\gamma_s(\zeta)y+\mathrm{i}\zeta x)/c_d}\mathrm{d}\zeta.\end{aligned} \tag{4.2.3}$$

The plan is to discuss the response due to the normal displacement and identify asymptotic representations with particular attention to the non-geometric wavefront $S^\star$. The pressure in the fluid and stresses can then be similarly treated, but for brevity we exclude them here.

The Schölte function $S(\zeta)$ appears in both formulae, and is vital to the analysis; it is defined as $S(\zeta) = R(\zeta) + \epsilon k^4 k'(\zeta^2+1)^{\frac{1}{2}}/(\zeta^2+k'^2)^{\frac{1}{2}}$. In this formula k and k' are defined to be the ratios c_d/c_s and c_d/c_o respectively. The Schölte function contains six branch points at $\pm\mathrm{i}, \pm\mathrm{i}k, \pm\mathrm{i}k'$, and either two or four zeros depending upon the precise choice of branch cuts. If $\epsilon = 0$, that is, if the fluid is decoupled from the solid, the Schölte function is truncated to the function $R(\zeta)$. This is the standard Rayleigh function, $R(\zeta) = (2\zeta^2+k^2)^2 - 4\zeta^2(\zeta^2+1)^{\frac{1}{2}}(\zeta^2+k^2)^{\frac{1}{2}}$; this function has four branch points at $\pm\mathrm{i}, \pm\mathrm{i}k$, and two zeros at $\pm\mathrm{i}k_r$ where $k_r = c_d/c_r$ and c_r is the Rayleigh wavespeed ($k < k_r < k'$). The complement function $s(\zeta)$ defined as $s(\zeta) = r(\zeta) - \epsilon k^4 k'(\zeta^2+1)^{\frac{1}{2}}/(\zeta^2+k'^2)^{\frac{1}{2}}$, where $r(\zeta) = (2\zeta^2+k^2)^2 + 4\zeta^2(\zeta^2+1)^{\frac{1}{2}}(\zeta^2+k^2)^{\frac{1}{2}}$, is also required and is described in Appendix 4.B.

The functions $\gamma_d(\zeta)$ that occur are defined as $\gamma_q(\zeta) = (\zeta^2+k_q^2)^{\frac{1}{2}}$, with $q = d,\ s,\ o$; $k_d = 1$, $k_s = k$, $k_o = k'$. Here the choice of branch cuts for the functions $\gamma_q(\zeta)$ in the complex ζ-plane is taken such that they run from $\pm\mathrm{i}k_q$ to $\pm\mathrm{i}\infty$ along the imaginary axis. With this choice of branch cuts the zeros of the Schölte function corresponding to

leaky Rayleigh waves in the physical domain then occur on the lower Riemann sheet, and play no explicit role in the exact solution. Given the choice of branch cuts above, the Schölte function has only two zeros at $\pm ik_{sch}$ where $k_{sch} = c_d/c_{sch}$ and c_{sch} is the Schölte wavespeed ($k_{sch} > k'$). This wavespeed is not related to the Rayleigh wavespeed, indeed for $\epsilon \ll 1$ it is marginally less than the compressional wavespeed of the fluid in this limit. The *migratory* behaviour of the zeros of $s(\zeta)$ from the imaginary axis, Roever *et al.* (1959), is found to be important and a full description is given in Appendix 4.B. In essence, for low values of the Poisson's ratio both zeros of $s(\zeta)$ lie on the imaginary axis, the second zero lies close to the branch point at $-\mathrm{i}$. As the Poisson's ratio is increased the zeros approach each other, intersect, and, typically at $0.28 < \nu < 0.3$, migrate from imaginary axis and form conjugate pairs. Typical results are that, for aluminium-water, $\pm ik_p = \mp 0.15979 \pm \mathrm{i}1.01638$, and for sandstone-water, $\pm ik_p = \pm \mathrm{i}0.99912$, $\pm \mathrm{i}0.638995$.

The loading $F(t) = H(t)$, where $H(t)$ is the Heaviside step function, now reduces the integral equations to the form (4.1.3). This case is now considered in detail for the displacements for convenience, and is denoted by $u_y^H(x, y, t)$. To incorporate more general loadings, $F(t)$, we may utilise the following convolution theorem,

$$u_y(x, y, t) = \int_0^t F'(t - \tau) u_y^H(x, y, \tau) \mathrm{d}\tau \tag{4.2.4}$$

provided $F(0) = 0$.

The explicit solution is found using the Cagniard–de Hoop method, see for instance Miklowitz (1978). The displacement has been written above, in equation (4.2.2), as the sum of two integrals, that is, in the form $\int g_1(\zeta) e^{-pz_1(\zeta)} \mathrm{d}\zeta + \int g_2(\zeta) e^{-pz_2(\zeta)} \mathrm{d}\zeta$ where the two functions z_1 and z_2 differ only by the function multiplying y. Two inversion contours are chosen so that $z_1(\zeta) = t$ and $z_2(\zeta) = t$, namely,

$$c_d t = (\zeta^{(P)^2} + 1)^{\frac{1}{2}}(h + y) + \mathrm{i}\zeta^{(P)} x \tag{4.2.5}$$

$$\text{and } c_d t = (\zeta^{(S)^2} + 1)^{\frac{1}{2}} h + (\zeta^{(S)^2} + k^2)^{\frac{1}{2}} y + \mathrm{i}\zeta^{(S)} x. \tag{4.2.6}$$

These contours are used in turn in the integrals appearing in (4.2.2,4.2.3) to place each integral in the form of a Laplace transform. This amounts to a transformation of the Fourier integration path. As we ultimately require the inverse Laplace transform of this integral, our solution in real time is found immediately by inspection. The superscripts (P) and (S) relate to the compressional and shear disturbances respectively.

For the response in the solid the first Cagniard path (4.2.5), $\zeta^{(P)}(x, y, t)$, is found explicitly. The integration path is given by

$$\zeta^{(P)}(t) = -\mathrm{i}\frac{c_d t}{r} \sin\theta + \left[\left(\frac{c_d t}{r}\right)^2 - 1\right]^{\frac{1}{2}} \cos\theta, \text{ for } t_{pp} \leq t < \infty, \tag{4.2.7}$$

where $t_{pp} = r/c_d$, $r^2 = x^2 + (h+y)^2$, and $\tan\theta = x/(h+y)$. This path is of less interest with regard to the asymptotic procedure. The situation for $y > 0$ is more complicated for the second Cagniard path (4.2.6), $\zeta^{(S)}(x, y, t)$, and the path is found numerically, or for either $h \ll x$ or $y \ll x$ via a perturbation analysis (the details are given in Section 4.2.2). From the formulation of a quartic algebraic equation, the full details are given in Appendix 4.A, or via a Newton–Raphson algorithm, the Cagniard path $\zeta^{(S)}(t)$ is found numerically as the root of equation (4.2.6) with positive real part. Using symmetry properties of the integrand it is sufficient to only consider the path in the fourth quadrant and this is given by taking the branch of $\zeta^{(S)}(t)$ with the positive square root. When $y = 0$ the integration path is already given explicitly by (4.2.7) where $r^2 = x^2 + h^2$ and $\tan\theta = x/h$.

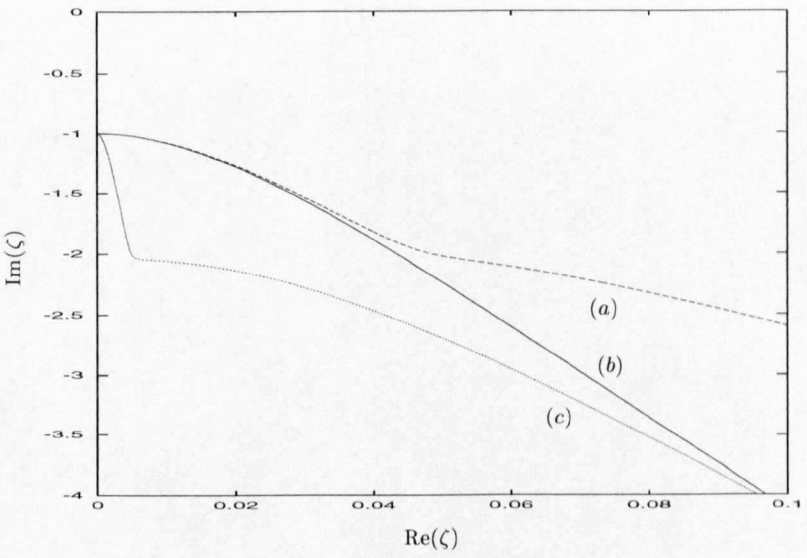

Figure 4.3. Three typical Cagniard paths for $\zeta^{(S)}(t)$. (*a*) $x/h = 40$, $y/h = 1$. (*b*) $x/h = 40$, $y/h = 0$. (*c*) $x/h = 400$, $y/h = 10$. Note the sharp bend in (*c*).

In each case the Cagniard path, in the lower half plane, cuts the negative imaginary axis between 0 and -1. For particular choices of x/h and y/h the path departs from the axis very close to $-\mathrm{i}$; this can be seen in Figure 4.3 and in the next section in Figures 4.8 and 4.11. In Figure 4.3 a typical path for $h \ll x$ is shown and is labelled (*c*), this is distinctly different to the other two paths. In this limit the path approaches the branch point at $-\mathrm{i}$ and tightens around the branch cuts along the negative imaginary axis. In particular the path has a dramatic bend away from the axis near the saddle point that would exist at $-\mathrm{i}k\sin\theta$ in the case $h = 0$; in this case it is associated with the direct reflected shear arrival. Thus in the general case the situation is similar to that when $y = 0$, except that we usually have to find both the path and t_{ps} $(= t_{critical})$ numerically.

The exact solution for the vertical displacement in $y > 0$, written as a function of t, is simply

$$u_y^H(x,y,t) = -\frac{1}{2\pi c_d} H(t-t_{pp}) \mathrm{Re}\left(\frac{s(\zeta^{(P)})}{S(\zeta^{(P)})}\frac{\mathrm{d}\zeta^{(P)}(t)}{\mathrm{d}t}\right) + \frac{2}{\pi c_d} H(t-t_{ps}) \mathrm{Re}\left(\frac{\zeta^{(S)^2}(2\zeta^{(S)^2}+k^2)}{S(\zeta^{(S)})}\frac{\mathrm{d}\zeta^{(S)}(t)}{\mathrm{d}t}\right), \tag{4.2.8}$$

where t_{pp} and t_{ps} ($= r/c_d$ when $y = 0$) correspond to the arrival of the PP and PS waves respectively and $\zeta^{(P)}(t)$, $\zeta^{(S)}(t)$ are the paths described above.

The wavefront arrivals are shown for $\pi c_d u_y^H(x,y,t)$ versus t in Figure 4.4 for typical values of x, y, and h. The ratios x/h and y/h determine the shape of the response; we have avoided rescaling each figure by h for convenience. The material parameters (Briggs, 1992; Table 3.1) are taken to be typical of sandstone-water configuration; c_d and c_s are 2920m/s and 1840m/s respectively, and c_o is 1480m/s, the solid and fluid densities are 2440kg/m^3 and 1000kg/m^3 respectively. Also shown on these figures are asymptotic representations for the dominant responses; the expressions are not given here, but are found following Section 3.3.1.3. The lines denoted by t_{pp}, t_{ps}, t_l, and t_{sch} are the arrival times associated with the PP, PS, leaky Rayleigh, and Schölte waves respectively. The non-geometric $S^\star$ arrival is denoted by an arrival time $t_{s^\star}$.

In Figure 4.4 the compressional wave in the solid arrives first at $t = t_{pp}$, and this is shortly followed by the shear wave at $t = t_{ps}$. The shape of these arrivals is brought about in each case by the branch points or poles that lie close to the path. The Schölte wave generates a distinctive response that dominates the leaky wave that precedes it; nevertheless the leaky wave has a definite shape that here persists, away from a light fluid loading limit. The piece of the Cagniard path that gives the contribution leading to the compressional wavefront arrival is often close to a zero of the Schölte complement function $s(\zeta)$. The importance of the zeros of this function are that the sign of the singularity associated with this response may change, this phenomenon is not illustrated.

An additional shear response, that is $S^\star$, is visible for small h, see the discussion of Section 4.2.2. This response is shown in detail in Figure 4.5, together with an asymptotic representation.

4.2.2. *The source close to the interface*

In this section we investigate directly the signals associated with non-geometric arrivals. These arrivals only give large responses when the source is close to the interface, that is, when h is small. As h increases their effect is diminished. We have already observed that in the limit $h/x \to 0$ the Cagniard path is distinctly different to the typical path,

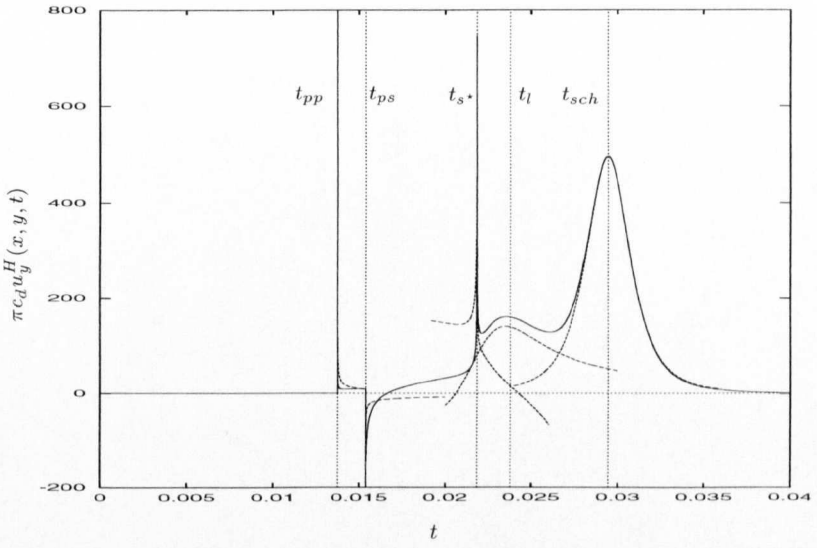

Figure 4.4. A plot of $\pi c_d u_y^H(x, y, t)$ versus t for material parameters typical of sandstone-water; $x = 40$, $y = 4$, $h = 0.01$. The asymptotic results are the dashed lines.

see Figure 4.3(a, b) and (c). This motivates us to examine the Cagniard path, and we crucially identify the $S^\star$ arrival with the sharp bend in the path in the limit $h/x \to 0$; in Figure 4.3(c). The physical significance of the bend in the path has also been observed by Hron & Mikhailenko (1981).

In the limiting case $h = 0$, corresponding to the source on the interface, the path, $\zeta^{(S)}(t)$, consists of a piece running directly along the branch cuts from $\zeta^{(S)} = -\mathrm{i}$ to $\zeta^{(S)} = -\mathrm{i}k\sin\theta$ together with a hyperbolic path; in these formulae, $x = r\sin\theta$, $y = r\cos\theta$. The point $\zeta^{(S)} = -\mathrm{i}k\sin\theta$, where the path leaves the imaginary axis, is the saddle point in a steepest descents analysis and gives wavefronts travelling with wavespeed c_s due to a shear wave, S, generated within the solid. This is shown in Figure 4.2. When $h \ll x$ the path runs from $-\mathrm{i}\zeta_{ps}$ very close to the branch cuts before turning away dramatically at approximately $\zeta^{(S)} \sim -\mathrm{i}k\sin\theta$. This point generates the distinctive response $S^\star$ in the solid when $t \sim r/c_s = t_{s^\star}$. The Cagniard–de Hoop technique identifies this response; it is useful to analyse the structure of the response by constructing an asymptotic representation.

As an alternative to finding the Cagniard path numerically we find a useful asymptotic representation for the path, when h is small, by perturbing away from the $h = 0$ path. That is, we consider the path

$$\zeta_p^{(S)}(t) = \zeta_{h0}(t) + h\zeta_{h1}(t) \tag{4.2.9}$$

where $\zeta_{h0}(t)$ is simply the solution to $c_d t = (\zeta_{h0}^2 + k^2)^{\frac{1}{2}} y + \mathrm{i}\zeta_{h0} x$. This is found explicitly

as

$$\zeta_{h0}(t) = \begin{cases} -\mathrm{i}\dfrac{c_d t}{r}\sin\theta + \mathrm{i}k\left[1-\left(\dfrac{c_s t}{r}\right)^2\right]^{\frac{1}{2}}\cos\theta & \text{when } t_{h0} \le t < \dfrac{r}{c_s} \\ -\mathrm{i}\dfrac{c_d t}{r}\sin\theta + k\left[\left(\dfrac{c_s t}{r}\right)^2 - 1\right]^{\frac{1}{2}}\cos\theta & \text{when } \dfrac{r}{c_s} \le t < \infty \end{cases} \tag{4.2.10}$$

where $t_{h0} = (x + y(k^2-1)^{\frac{1}{2}})/c_d$. In this formula $r^2 = x^2 + y^2$ and $\tan\theta = x/y$. Utilising the path (4.2.9) in the transcendental equation (4.2.6), the perturbation term $\zeta_{h1}(t)$ is found to be

$$\zeta_{h1}(t) = -\zeta_{h0}(\zeta_{h0}^2+1)^{\frac{1}{2}}\left(c_d t - \frac{k^2 y}{(\zeta_{h0}^2+k^2)^{\frac{1}{2}}}\right)^{-1}, \tag{4.2.11}$$

but crucially the denominator in expression (4.2.11) is zero at $\mathrm{d}t(\zeta_{h0})/\mathrm{d}\zeta_{h0} = 0$ and this occurs when $\zeta_{h0} = -\mathrm{i}k\sin\theta$ at arrival time t_{s^*}. It follows that the representation (4.2.9) is only valid outside some close interval of t_{s^*}. It is an unfortunate consequence of perturbing away from the explicit zero path that the perturbed path we find is invalid for $|t - t_{s^*}| < t_\epsilon = O(h/c_d)$. This non-uniformity is because the part of the zero path that sharply departs from the imaginary axis leads to a large change in (4.2.11). The exact path found numerically contains a smoothing term of order $\mathrm{i}h$.

In addition, we may construct a similar expression for the derivative of the path via a direct differentiation of equation (4.2.9) or expanding an expression for the path in the derivative of the path (4.2.6); this is a vital part of the explicit solution:

$$\frac{\mathrm{d}\zeta_p^{(S)}}{\mathrm{d}t} \sim \frac{\mathrm{d}\zeta_{h0}}{\mathrm{d}t} - h\frac{\left(c_d t - k^2 y(\zeta_{h0}^2+k^2+\zeta_{h0}^2+1)(\zeta_{h0}^2+k^2)^{-\frac{3}{2}}\right)}{c_d^2(\zeta_{h0}^2+1)^{\frac{1}{2}}}\left(\frac{\mathrm{d}\zeta_{h0}}{\mathrm{d}t}\right)^3, \tag{4.2.12}$$

where

$$\frac{\mathrm{d}\zeta_{h0}}{\mathrm{d}t} = c_d\zeta_{h0}\left(c_d t - \frac{k^2 y}{(\zeta_{h0}^2+k^2)^{\frac{1}{2}}}\right)^{-1}. \tag{4.2.13}$$

There is some interest in near surface responses, that is, when the receiver depth y is also small. We construct an asymptotic representation for the Cagniard path when y is small by following the approach described above, and now perturbing away from the explicit $y = 0$ path. Once again, we consider $\zeta_p^{(S)}(t) = \zeta_{y0}(t) + y\zeta_{y1}(t)$ where the perturbation $\zeta_{y1}(t)$ is

$$\zeta_{y1}(t) = -\zeta_{y0}(\zeta_{y0}^2+k^2)^{\frac{1}{2}}\left(c_d t - \frac{y}{(\zeta_{y0}^2+1)^{\frac{1}{2}}}\right)^{-1}. \tag{4.2.14}$$

The smooth behaviour of the $y = 0$ path, see Figure 4.3(b), avoids any difficulty close

to $t_{s^\star}$. In Figure 4.6 we show an approximation to the $S^\star$ arrival in the restricted case $h \ll y \ll x$.

From the discussion above we see that when $h \ll x$ the response associated with the $S^\star$ wave at $t_{s^\star} \sim r/c_s$ begins to emerge. The displacement in the neighbourhood of $t_{s^\star}$ is then given as

$$u_y^H(x,y,t) \sim -\frac{1}{2\pi c_d}\mathrm{Re}\left(\frac{s(\zeta^{(P)})}{S(\zeta^{(P)})}\frac{\mathrm{d}\zeta^{(P)}(t)}{\mathrm{d}t}\right) + \frac{2}{\pi c_d}\mathrm{Re}\left(\frac{\zeta^2(2\zeta^2+k^2)}{S(\zeta)}\Big|_{\zeta=-\mathrm{i}k\sin\theta}\frac{\mathrm{d}\zeta_p^{(S)}(t)}{\mathrm{d}t}\right), \tag{4.2.15}$$

where $\zeta^{(P)}(t)$ and $\zeta_p^{(S)}(t)$ are given by equations (4.2.7) and (4.2.9, 4.2.10, 4.2.11) respectively.

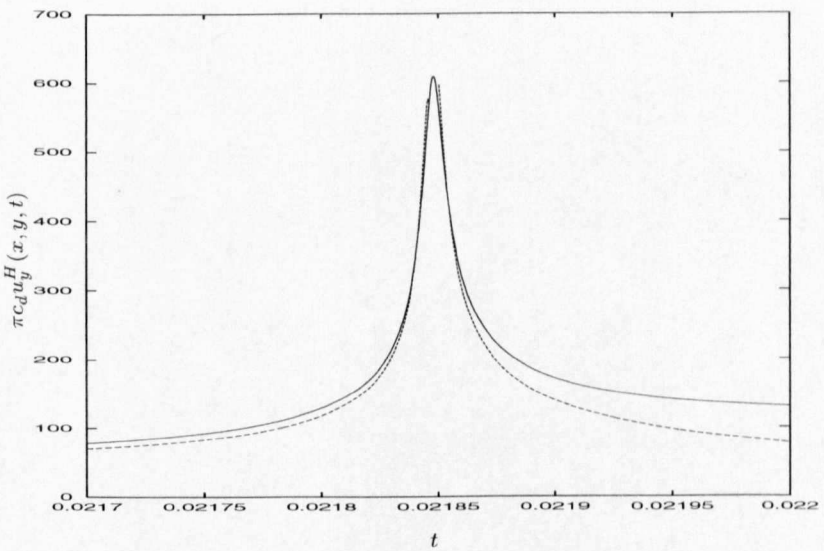

Figure 4.5. The exact and asymptotic expressions for $\pi c_d u_y^H(x,y,t)$ versus t in the region near $t_{s^\star}$ in Figure 4.4; $x = 40$, $y = 4$, $h = 0.01$. Material parameters are sandstone-water.

In Figure 4.5 we compare the exact and asymptotic solutions for the normal displacement. The basic features of the $S^\star$ arrival have been preserved. The position and shape of the response is well predicted before and after $t_{s^\star}$. The asymptotic representation for the displacement when we are in the close neighbourhood of the interface so that $h \ll y \ll x$ is shown in Figure 4.6. Now the shape of the response is well matched almost everywhere. There can, however, be a reasonable difference in the size and position of the exact and approximate responses. This is principally due to the interference of nearby wavefronts.

As we increase y the wavefronts move closer, particularly in this rock-water case,

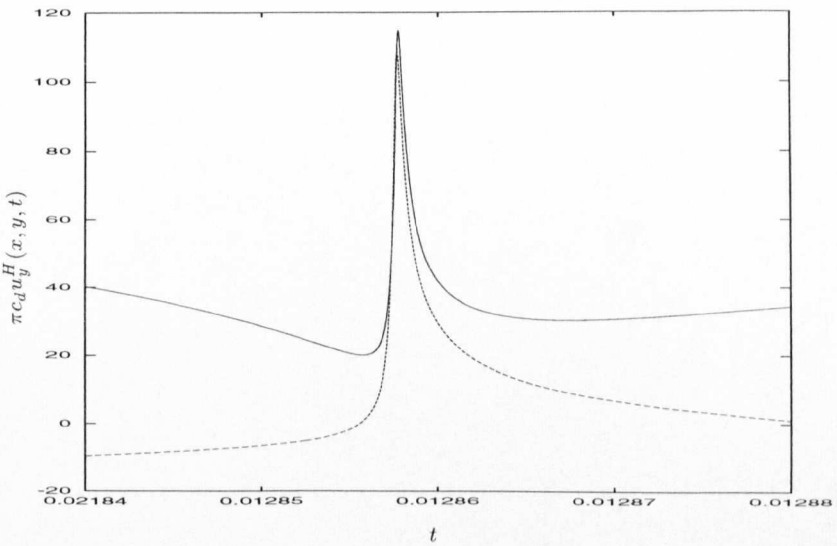

Figure 4.6. The exact and asymptotic expressions for $\pi c_d u_y^H(x, y, t)$ versus t in the region near t_s. in the case $h \ll y \ll x$; $x = 40$, $y = 0.1$, $h = 0.0008$. Material parameters are aluminium-water.

nonetheless the asymptotics are still accurate. The leaky Rayleigh response may be masked and interfere with the non-geometric shear arrival that dominates.

The arrival time of the PS wave, t_{ps}, is the first arrival and is typically found numerically. Often it is a useful characteristic and we determine its approximate form, when $h \ll x$, be seeking a solution to $\mathrm{d}t(\zeta_{ps})/\mathrm{d}\zeta_{ps} = 0$ in the form $\zeta_{ps} = -\mathrm{i} + \mathrm{i}\zeta_{ps}^{\epsilon}$ where $\zeta_{ps}^{\epsilon} \ll 1$. Thus we find that

$$c_d t_{ps} \sim x + y(k^2 - 1)^{\frac{1}{2}} + h^2 \left(x - \frac{y}{(k^2 - 1)^{\frac{1}{2}}} \right)^{-1} . \tag{4.2.16}$$

For $h/x \ll 1$ this provides the small curvature correction from the straight head wave wavefront found when $h = 0$. The head waves are confined to the region defined by $c_s t \leq r \leq c_d t(\sin\theta + (k^2 - 1)^{\frac{1}{2}} \cos\theta)^{-1}$ and $\sin^{-1} c_s/c_d \leq \theta \leq \pi/2$. In these formulae $x = r\cos\theta$, $y = r\sin\theta$.

4.3. A compressional source beneath a thin high velocity layer

The previous section described the tunnelling effects in dissimilar material half spaces due to either material mismatch, or wave coupling at the interface. Another example of tunnelling occurs when a thin, high velocity layer lies embedded within a slow surrounding material. For illustrative purposes we first consider a source above a fluid layer, see for instance Mellman & Helmberger (1974), Drijkoningen & Chapman (1988), and use generalised ray theory to identify the explicit solution for the wavefronts transmitted

through the layer. We then move on to treat the more relevant elastic problem. The tunnelling response is the perturbation caused to the cylindrical wavefront that would, in the absence of the layer, be seen. Instead of a sharp, singular, wavefront some smoothing that is dependent upon the layer thickness occurs, and we aim to find this dependence.

It turns out that under certain conditions on the source depth and layer thickness only one generalised ray contributes to the tunnelling response. We may then analyse this path in a similar manner to the previous section. This avoids having to consider the complete generalised ray expansion and we are able to neatly pick out the non-geometric response. Importantly, we are able to identify these conditions and further make a prediction when a second ray becomes important.

When we proceed to treat the more complicated elastic analogue, that is, a compressional source and an elastic layer between two elastic half spaces, and look at the transmitted compressional wavefront, a similar simplification can be employed thus avoiding rather complicated sums of rays.

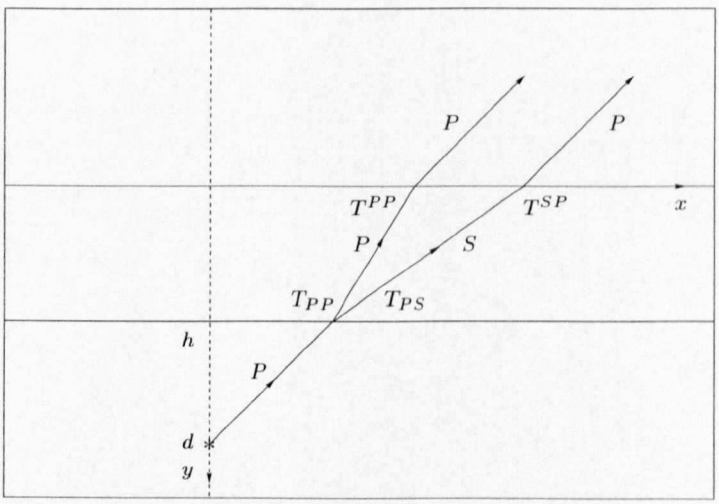

Figure 4.7. The geometry of a typical configuration considered in the text. The layer occupies $0 < y < h$ and the semi-infinite space $y > h$ contains a source at depth d. The paths of the generalised rays are shown to illustrate the tunnelling response; the letters P and S denote the wave type and the transmission coefficients are included at the interfaces.

4.3.1. *A fluid layer*

As a brief illustrative example of the generalised theory and our perturbation scheme on the leading generalised ray we first treat the equivalent fluid problem, that is, the shear ray path is absent from the schematic in Figure 4.7. The fluid is again assumed to be compressible, and has density ρ_1 and wavespeed c_1, apart from the layer in $0 < y < h$,

that has density ρ_2 and wavespeed c_2 ($c_2 > c_1$). The governing equations follow those outlined in Section 4.2 and the equivalent source equation is given following equation (4.2.1).

We employ the method of generalised rays, see for instance Pao & Gajewski (1977), to derive the solution. In essence the multiply reflected and refracted waves in the solution are represented by a series of ray integrals. Each integral is then evaluated exactly using the Cagniard–de Hoop method and the exact solution is then found up to the arrival of the next ray.

In the fluid for $y < 0$ the Laplace transform of the normal displacement is

$$\overline{u}_y(x,y,p) = \frac{1}{2\pi}\int_{-\infty}^{\infty} \frac{1}{2c_2} p\overline{F}(p) T_{PP}(\zeta) T^{PP}(\zeta) \sum_{m=0}^{\infty} \Big(R_{PP}(\zeta) R^{PP}(\zeta)\Big)^m e^{-pZ_m(\zeta)} \mathrm{d}\zeta \tag{4.3.1}$$

where $Z_m(\zeta) = (\gamma_1(\zeta)(d-h-y) + (2m+1)\gamma_2(\zeta)h + \mathrm{i}\zeta x)/c_2$. The reflection and transmission coefficients, which are usually given as functions of angle of incidence, Ewing *et al.* (1957), are expressed in terms of ζ in Appendix 4.C. The ratios of the transmitted and reflected waves to the incident waves are denoted by the letters T and R respectively. We have introduced the rescaling $\xi = p\zeta/c_2$ for convenience. In this formula ρ is defined to be the ratio ρ_2/ρ_1 and $\overline{F}(p)$ is the Laplace transform of $F(t)$ given by (4.1.2). The functions $\gamma_1(\zeta)$, $\gamma_2(\zeta)$ that appear are defined as $(\zeta^2 + k^2)^{\frac{1}{2}}$ ($k = c_2/c_1$) and $(\zeta^2 + 1)^{\frac{1}{2}}$ respectively.

To calculate the exact solution utilising the Cagniard–de Hoop method, a Cagniard path for each of the generalised rays is determined by setting $Z_m(\zeta) = t$, that is

$$c_2 t = \gamma_1(\zeta_m)(d - y - h) + (2m+1)\gamma_2(\zeta_m)h + \mathrm{i}\zeta_m x \tag{4.3.2}$$

so that $\zeta_m(t)$ is the root of this equation typically found numerically. In Figure 4.8 typical Cagniard paths are shown. The path departs from the negative imaginary axis at $-\mathrm{i}\zeta_m$, between 0 and $-\mathrm{i}$ at time t_m. Using (4.3.2) t_m, the arrival time of the direct geometrical wave, is determined by the condition $\mathrm{d}t(\zeta_m)/\mathrm{d}\zeta_m = 0$. This corresponds to a combined contribution of a geometric and a head wave type arrival. The other, and more important, feature of the path is the bend; this is the part of the path that we are interested in since it gives us the tunnelling ray.

First consider the behaviour of the first path ($m = 0$). This path runs close to the imaginary axis before sharply bending away near $-\mathrm{i}k\sin\theta$ at $t \sim r/c_1 = t_{p^*}$ ($x = r\sin\theta$, $d - y = r\sin\theta$). This sharp bend has been observed by Drijkoningen (1991). The change in the shape of the path typically becomes less pronounced as h is increased,

and in particular, the bend is less prominent. When $h = 0$ the Cagniard paths are all equivalent. Otherwise the paths are separate, however when h is *very* small, several paths now have a significant bend. The bend in each of these paths now contribute to the tunnelling signal, and our analysis then requires modification.

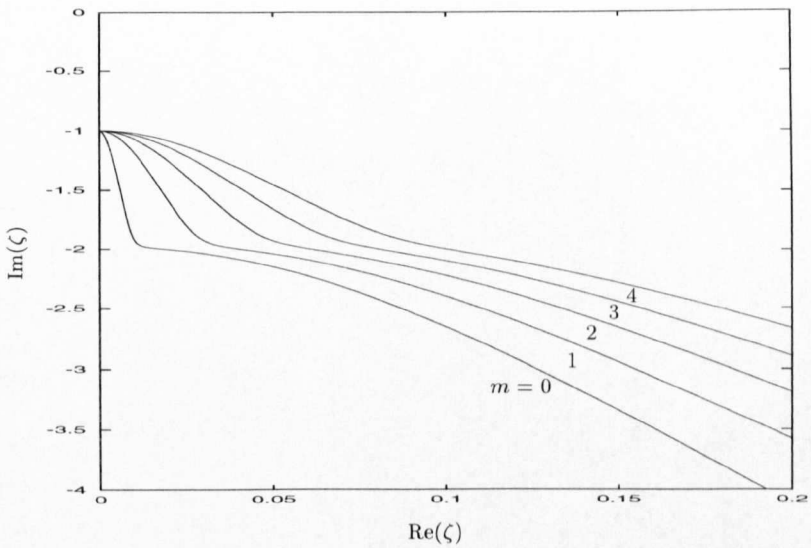

Figure 4.8. Typical Cagniard paths, $\zeta_m(t)$, for values of $m = 0, 4$ as labelled.

A useful asymptotic representation for the path when h is small is found following the scheme described in Section 4.2.2, that is, by perturbing away from the $h = 0$ path. We consider $\zeta_{m,p}(t) = \zeta_{h0}(t) + h\zeta_{m,h1}(t)$ where $\zeta_{h0}(t)$ is for all values of m simply the solution to $c_2 t = (\zeta_{h0}^2 + k^2)^{\frac{1}{2}}(d - y) + \mathrm{i}\zeta_{h0}x$. Now the perturbation $\zeta_{m,h1}(t)$ is

$$\zeta_{m,h1}(t) = \zeta_{h0}\left[(\zeta_{h0}^2 + k^2)^{\frac{1}{2}} - (2m+1)(\zeta_{h0}^2 + 1)^{\frac{1}{2}}\right]\left(c_2 t - \frac{k^2(d-y)}{(\zeta_{h0}^2 + k^2)^{\frac{1}{2}}}\right)^{-1}. \tag{4.3.3}$$

This approximation to the path is identical to the path found numerically outside some small interval of t_{p^*} as discussed in Section 4.2.2. Indeed, equation (4.3.3) performs well for greater values of h, and is not exclusive to the first path ($m = 0$).

In addition we determine an approximate form for t_m be seeking a solution to (4.3.2) of the form $\zeta_m = -\mathrm{i} + \mathrm{i}\zeta_m^\epsilon$ where $\zeta_m^\epsilon \ll 1$;

$$c_2 t_m = x + (d - y - h)(k^2 - 1)^{\frac{1}{2}} + (2m+1)^2 h^2 \left(x - \frac{(d-y-h)}{(k^2-1)^{\frac{1}{2}}}\right)^{-1}. \tag{4.3.4}$$

The following numerical results are calculated for the loading $F(t) = H(t)$. Other loadings may be incorporated as described in Section 4.2. In Figure 4.9 the exact response $\pi c_2 u_y^H(x, y, t)/2\rho$ is plotted against t for $c_2/c_1 = 2$ and $\rho_2/\rho_1 = 1.4$, together with an

asymptotic representation for the tunnelling wave and the first solution ($m = 0$). The total (added) solution is described by the summed response in the figures, and is taken for values of m up to $m = 24$. There are a succession of square root singularities associated with the geometrical wave; the singularities appear very close together in the figures shown. In the added response the different rays interfere. The head wave arrivals are altered when we include many multiples. The shape of the first response has almost completely disappeared, see for instance Mellman & Helmberger (1974), where similar behaviour is discussed. The waves that have been multiply reflected in the layer interfere with the size of the tunnelling wave and can cause a reasonable offset, however, the shape of the arrival is not very different from the response due to the tunnelling only once. This direct tunnelling signal is completely captured by the first path in this case. We identify a wavefront expansion for the tunnelling signal in a similar manner to equation (4.2.15) in Section 4.2.2.

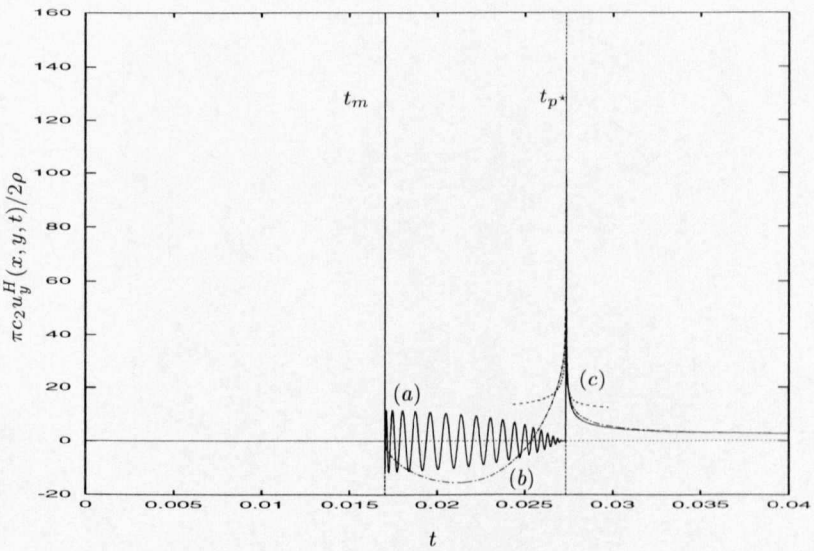

Figure 4.9. A plot of $\pi c_2 u_y^H(x, y, t)/2\rho$ versus t in $y < 0$; $x = 40$, $y = -4$, $h = 0.004$, $d = 2$. (a) Summed response up to $m = 24$. (b) Exact response $m = 0$. (c) Approximation $m = 0$.

The displacement in the neighbourhood of t_{p^*} is given as

$$u_y^H(x, y, t) = \frac{2\rho}{\pi c_2} \mathrm{Re}\left(\frac{\gamma_1(\zeta)\gamma_2(\zeta)}{(\gamma_2(\zeta) + \rho\gamma_2(\zeta))^2}\Big|_{\zeta=-ik\sin\theta} \frac{\mathrm{d}\zeta_{0,p}(t)}{\mathrm{d}t} \right). \tag{4.3.5}$$

The last term can be written in a more explicit form using (4.3.3). In Figure 4.10 we compare the exact response with the approximate response. The basic features of the tunnelling signal have been preserved, and both the shape and size of the leading solution are well matched. The multiply reflected arrivals can cause a considerable size difference to exist between the exact and approximate solutions. Nonetheless the direct tunnelling

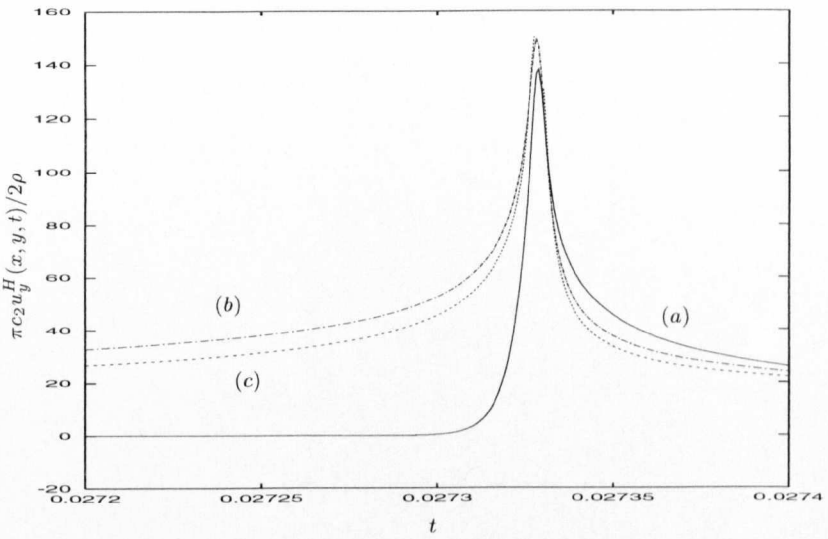

Figure 4.10. The exact and asymptotic expressions for $\pi c_2 u_y^H(x,y,t)/2\rho$ versus t in the region near t_{p^*} in Figure 4.9. (*a*) Summed response up to $m = 24$. (*b*) Exact response $m = 0$. (*c*) Approximation $m = 0$.

wave, a key feature in the wave field, is itself well predicted. In other cases when h becomes very small, we need a second generalised ray to fully capture the wavefront that has tunnelled through the layer, and then expect to represent this wavefront by a sum of expressions like (4.3.5), involving $\zeta_{m,p}$ for $m = 0, 1, \ldots$

4.3.2. *An elastic layer*

We now proceed to treat the more relevant elastic layer problem. As shown in Section 4.3.1 the generalised ray theory yields the exact solution to the model problem up to the arrival of the next ray. Moreover, this approach directly constructs the ray integrals, thus avoiding any laborious matrix determination, see for instance the discussion in Kennett (1983). This enables us to pick out the main features associated with the leading arrivals directly with a minimum of work.

Now consider a line compressional source at $y = d$ beneath an elastic layer, thickness h; the geometry is shown in Figure 4.7. The elastic material has density ρ_1 and compressional and shear wavespeeds c_{d1} and c_{s1}, apart from the layer in $0 < y < h$, that has density ρ_2 and wavespeeds c_{d2}, c_{s2}; we assume that $c_{d2} > c_{d1} > c_{s2} > c_{s1}$. The governing equations follow those outlined in Section 4.2 and the equivalent source equation is given following equation (4.2.1).

We now proceed to derive the solution. At each of the interfaces $y = 0$ and $y = h$ we have to satisfy four continuity conditions: the continuity of the stresses σ_{yy} and σ_{xy}, and

the continuity of the displacements u_x and u_y. Instead of determining the coefficients from a system of eight simultaneous equations and then constructing the ray integrals we prefer to employ the method of generalised rays, see for instance Pao & Gajewski (1977) and the discussion of Section 4.3.1.

We have already observed, when treating the fluid layer, that the shape of the wavefronts in the summed solution closely resembles the response given only by the leading generalised ray. The equivalent physical approximation leads us to consider only the transmitted waves in the layer; the multiply reflected and refracted waves are omitted. The compressional part of the transmitted wave in the layer is obtained by superimposing all transmitted P waves, together with the source function:

$$\overline{u}_y(x,y,p) = -\frac{1}{2\pi}\int_{-\infty}^{\infty} \frac{1}{2c_{d2}} p\overline{F}(p)\left(T_{PP}T^{PP}e^{p\gamma_{s2}h/c_{d2}} + T_{PS}T^{SP}e^{p\gamma_{d2}h/c_{d2}}\right) \times e^{-p((\gamma_{d2}+\gamma_{s2})h+\gamma_{d1}(d-h-y)+\mathrm{i}\zeta x)/c_{d2}}\,\mathrm{d}\zeta. \tag{4.3.6}$$

The reflection and transmission coefficients in this formula are expressed in terms of ζ in Appendix 4.C together with a brief description of the notation. In addition the functions γ_{d2}, γ_{s2}, γ_{d1}, and γ_{s1} that appear are defined. We have introduced the following wavespeed ratios: $k_{d2} = 1$, $k_{s2} = c_{d2}/c_{s2}$, $k_{d1} = c_{d2}/c_{d1}$, and $k_{s1} = c_{d2}/c_{s1}$.

A generalised ray path has been constructed to connect the source and receiver for each transmitted waves, see Figure 4.7. The path describes the vertical distance travelled by each mode of waves in each layer, the total horizontal distance, and the direction of propagation. The two Cagniard paths in this case are now found by identifying the ray paths with t, that is, setting

$$c_{d2}t = \gamma_{d1}(\zeta_1)(d-h-y) + \gamma_{d2}(\zeta_1)h + \mathrm{i}\zeta_1 x, \tag{4.3.7}$$

$$c_{d2}t = \gamma_{d1}(\zeta_2)(d-h-y) + \gamma_{s2}(\zeta_2)h + \mathrm{i}\zeta_2 x. \tag{4.3.8}$$

The subscripts 1 and 2 on ζ have been introduced to describe the first and second paths. Note that when $h = 0$ the two paths are equivalent. Both Cagniard paths $\zeta_1(t)$ and $\zeta_2(t)$ are again found numerically and are shown in Figure 4.11. As we have already observed the paths have two main features. First the path leaves the negative axis. For the first path this occurs at $-\mathrm{i}\zeta_p$ $(0 < \zeta_p < 1)$, the second path has a piece lying along the negative axis from $-\mathrm{i}$ to $-\mathrm{i}\zeta_s$ $(1 < \zeta_s < k_{d1})$. In both cases the intersection occurs at $\mathrm{d}t(\zeta)/\mathrm{d}\zeta = 0$ and this corresponds to the direct geometrical arrival. The branch point at $-\mathrm{i}$ causes a head wave in the second path. The second and more interesting feature is the sharp bend in the path, that we have previously identified with the non-geometric and tunnelling signals; the two paths bend away at approximately $-\mathrm{i}k_{d1}\sin\theta$ and $-\mathrm{i}k_{s2}\sin\theta$.

The exact solution for the direct transmitted compressional part of the normal displace-

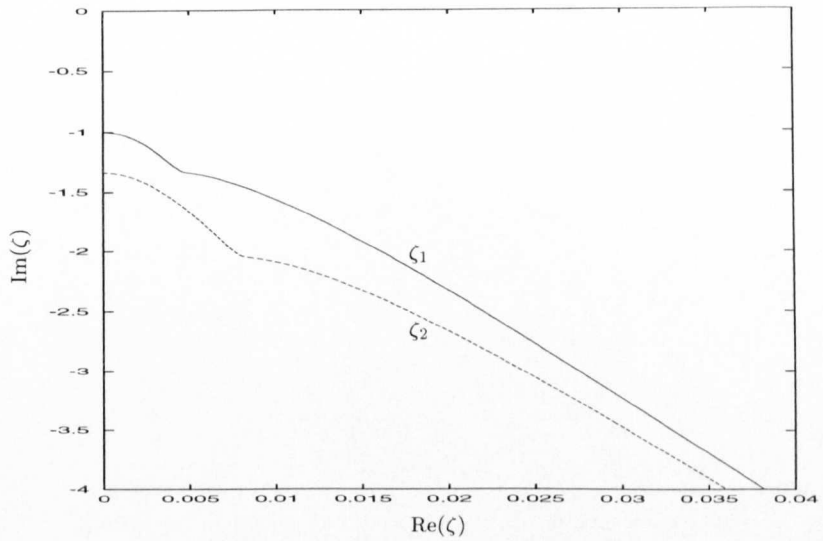

Figure 4.11. The Cagniard paths $\zeta_1(t)$ and $\zeta_2(t)$ for $x/h = 200$ and $(d-y)/h = 2$.

ment in $y < 0$ may now be extracted utilising the Cagniard method; it is not included here. Moreover, we may employ our perturbation scheme to find a further asymptotic representation for the ζ_1 path when h is small. Thus $\zeta_{1,p}(t) = \zeta_{h0}(t) + h\zeta_{1,h1}(t)$, where $\zeta_{h0}(t)$ is again the explicit zero path and the perturbation $\zeta_{1,h1}(t)$ is

$$\zeta_{1,h1}(t) = \zeta_{h0}\left[(\zeta_{h0}^2 + k_{d1}^2)^{\frac{1}{2}} - (\zeta_{h0}^2 + 1)^{\frac{1}{2}}\right]\left(c_{d2}t - \frac{k_{d1}^2(d-y)}{(\zeta_{h0}^2 + k_{d1}^2)^{\frac{1}{2}}}\right)^{-1}. \tag{4.3.9}$$

The ζ_2 path is well predicted by the zero path since t_{sp} is close to $t_{p^\star} = r/c_{d1}$, and leaves the imaginary axis at $\zeta_{sp} - \delta$ for some $\delta \ll 1$; the second bend in the path occurs near $t = r/c_{s2}$.

In Figure 4.12 the leading compressional response $2\pi c_{d2} u_y^H$ is plotted against t. To demonstrate the tunnelling signal, the material parameters of aluminium and copper, typical of a fast and slow material are utilised. The density of copper is 8933kg/m^3 with compressional and shear wavespeeds 4759m/s and 2325m/s respectively, and aluminium density is 2700kg/m^3 with compressional and shear wavespeeds 6374m/s and 3111m/s respectively. The material parameters are taken from Briggs (1992) and Bradfield (1964).

In the figure the geometric wave, SP generated by the shear wave in the layer arrives at t_{sp}. Immediately prior to this arrival is the sharp non-geometrical wavefront that we identify as $P^\star$, the cylindrical wave in the case $h = 0$. The asymptotic expression performs well and correctly matches the position and shape of the tunnelling signal. This is particularly useful, since other asymptotic approaches are awkward to evaluate, particularly close to a direct geometric arrival.

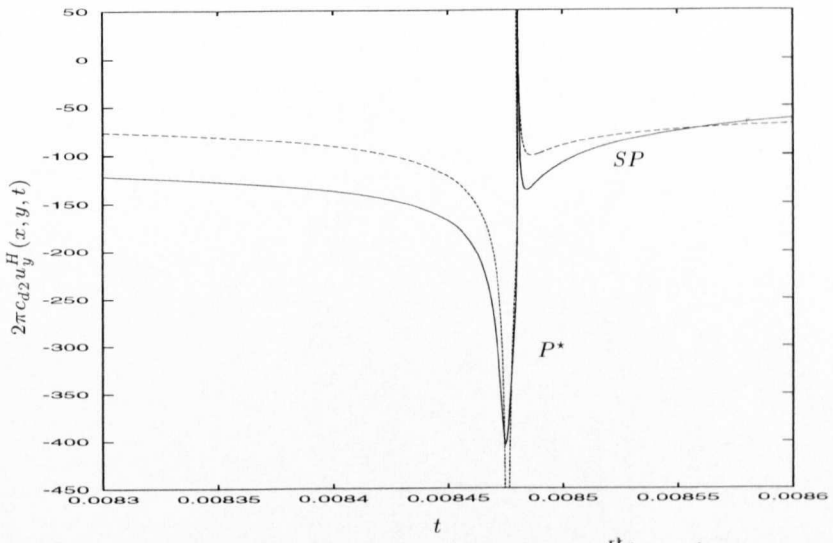

Figure 4.12. The exact and asymptotic expressions for $2\pi c_{d2} u_y^H(x, y, t)$ versus t in the region near $t_{p^\star} = r/c_{d1}$ and t_{sp} . (*a*) Tunnelling wave. (*b*) Direct compressional wave SP.

4.4. Conclusion

Tunnelling rays in dissimilar and layered materials are ideally suited to analysis via the Cagniard–de Hoop method, and we examine two canonical problems. In each case an asymptotic representation of the Cagniard path is found, thus explicit and highly accurate solutions when $h/x \to 0$ are obtained. This perturbation approach of generating Cagniard paths bypasses any numerical work, and should be useful in the asymptotic study of a range of related problems.

In each case we approximate the exact response and obtain simple expressions for the tunnelling signal. A particularly useful aspect is that the approximation to the tunnelling signal does not rely on an explicit expression for the contour.

In the example of a thin high velocity layer we have obtained the tunnelling ray using generalised ray theory.

The results presented here will be valuable in formulating more realistic fluid-solid interaction problems. The treatment may be routinely extended to examine the equivalent three dimensional problems as well as to dipping structures, see for instance Hong & Helmberger (1977), Pao *et al.* (1989). Since one is freed from the numerical calculation of many Cagniard paths, one can consider more complicated scenarios and further extensions may be to examine fluid-layered elastic, anisotropic media and model problems involving cracks beneath interfaces and multiple reflections.

References

Abramovici, F., Lawrence, H. T. L. & Kanasewich, E. R., 1989. The evanescent wave in Cagniard's problem for a line source generating SH waves. *Bull. Seism. Soc. Am.* **79**, 1941–1955.

Abramowitz, M. & Stegun, I. A., 1972. *Handbook of Mathematical Functions*. Dover.

Aki, K. & Richards, P. G., 1980. *Quantitative seismology: theory and methods*. W.H. Freeman and Co., San Francisco.

Babich, V. M. & Kiselev, A. P., 1989. Non-geometrical waves - are there any? An asymptotic description of some 'non-geometrical' phenomena in seismic wave propagation. *Geophys. J. Int.* **99**, 415–420.

Bradfield, G., 1964. Notes on applied science No. 30 *Use in industry of elasticity measurements in metals with the help of mechanical vibrations*. H.M.S.O, London.

Brekhovskikh, L. M., 1980. *Waves in layered media*. Academic Press, New York, Second edition.

Briggs, G. A. D., 1992. *Acoustic microscopy*. Monographs on the physics and chemistry of materials: 47, Oxford University Press.

Cagniard, L., 1939. *Réflection et réfraction des ondes séismique progressives*. Gauthiers-Villars, Paris. Trans. and rev. by E. A. Flinn & C. H. Dix, 1962. *Reflection and refraction of progressive seismic waves*. McGraw-Hill, New York.

Daley, P. F. & Hron, F., 1983. High-frequency approximation to the nongeometrical S^* arrival. *Bull. Seism. Soc. Am.* **73**, 109–123.

de Hoop, A. T., 1960. A modification of Cagniard's method for solving seismic pulse problems. *Appl. sci. Res. B* **8**, 349–356.

Drijkoningen, G. G., 1991. Tunneling and the generalized ray method in piecewise homogeneous media. *Geophysical Prospecting* **39**, 757–781.

Drijkoningen, G. G. & Chapman, C. H., 1988. Tunneling rays using the Cagniard–de Hoop method. *Bull. Seism. Soc. Am.* **78**, 898–907.

Einziger, P. D. & Felsen, L. B., 1982. Evanescent waves and complex rays. *IEEE Trans. Antennas Propagat.* **AP-30**, 594–605.

Ewing, W. M., Jardetzky, W. S. & Press, F., 1957. *Elastic waves in layered media*. McGraw-Hill, New York.

Gutowski, P. R., Hron, F., Wagner, D. E. & Treitel, S., 1984. S^*. *Bull. Seism. Soc. Am.* **74**, 61–78.

Hong, T. L. & Helmberger, D. V., 1977. Generalized ray theory for dipping structure. *Bull. Seism. Soc. Am.* **67**, 995–1008.

Hron, F. & Mikhailenko, B. G., 1981. Numerical modeling of nongeometrical effects by the Alekseev-Mikhailenko method. *Bull. Seism. Soc. Am.* **71**, 1011–1029.

Kennett, B. L. N., 1983. *Seismic wave propagation in stratified media*. Cambridge University Press.

Ma, C. C. & Huang, K. C., 1996. Exact transient solutions of buried dynamic point forces for elastic bimaterials. *Int. J. Solids Structures* **33**, 4511–4529.

Mellman, G. R. & Helmberger, D. V., 1974. High-frequency attenuation by a thin high-velocity

layer. *Bull. Seism. Soc. Am.* **64**, 1383–1388.

Miklowitz, J., 1978. *The theory of elastic waves and waveguides.* North-Holland.

Pao, Y. H. & Gajewski, R. R., 1977. The generalised ray theory and transient responses of layered elastic solids. In *Phys. Acoust. 13*, ed. by W. P. Mason & R. N. Thurston, 183-265, Academic Press, New York.

Pao, Y. H., Zeigler, F. & Wang, Y. S., 1989. Acoustic waves generated by a point source in a sloping fluid layer. *J. Acoust. Soc. Am.* **85**, 1414–1426.

Roever, W. L., Vining, T. F. & Strick, E., 1959. Propagation of elastic wave motion from an impulsive source along a fluid/solid interface. *Phil. Trans. R. Soc. Lond. A* **251**, 455–523.

Stephen, R. A. & Bolmer, S. T., 1985. The direct wave root in marine seismology. *Bull. Seism. Soc. Am.* **75**, 57–67.

Appendix 4.A. Quartic equation

The purpose of this appendix is to find an explicit expression for the Cagniard–de Hoop path. We would naturally assume that an explicit solution might be helpful for extracting the asymptotics. The path is the solution to a transcendental equation, namely,

$$c_d t = \pm(\zeta^2 + j^2)^{\frac{1}{2}} h \pm (\zeta^2 + k^2)^{\frac{1}{2}} y + \mathrm{i}\zeta x, \tag{4.A 1}$$

where $j(=1)$ and k are constants, chosen to satisfy the inversion contour. In the text, a Newton–Raphson algorithm is applied to find this path numerically. Here, we choose to formulate a quartic algebraic equation; the solution is standard. The notation follows Ma & Huang (1996), but crucially their equations contain some unfortunate typographic errors, that are corrected here.

Equation (4.A 1) may be rewritten as the following quartic equation for ζ,

$$\zeta^4 + I_1\zeta^3 + I_2\zeta^2 + I_3\zeta + I_4 = 0, \tag{4.A 2}$$

where

$$\begin{aligned} I_1 &= \frac{4\mathrm{i}c_d t x(x^2+y^2+h^2)}{(x^2+y^2+h^2)^2 - 4y^2h^2}, \\ I_2 &= -\frac{4c_d^2t^2x^2 + 4y^2h^2(j^2+k^2) + 2(x^2+y^2+h^2)(c_d^2t^2 - j^2h^2 - k^2y^2)}{(x^2+y^2+h^2)^2 - 4y^2h^2}, \\ I_3 &= -\frac{4\mathrm{i}c_d t x(c_d^2t^2 - j^2h^2 - k^2y^2)}{(x^2+y^2+h^2)^2 - 4y^2h^2}, \\ I_4 &= \frac{(c_d^2t^2 - j^2h^2 - k^2y^2)^2 - 4j^2k^2y^2h^2}{(x^2+y^2+h^2)^2 - 4y^2h^2}. \end{aligned} \tag{4.A 3}$$

The quartic equation (4.A 2) may now be solved, Abramowitz & Stegun (1972), and the analytical solution is expressed explicitly as

$$\zeta = \frac{1}{2}(P+Q), \tag{4.A 4}$$

where

$$
\begin{aligned}
P &= -\frac{1}{2}\left[I_1 - \left(I_1^2 - 4I_2 + 4R\right)^{\frac{1}{2}}\right], \qquad Q = \left\{P^2 - 2\left[R + \left(R^2 - 4I_4\right)^{\frac{1}{2}}\right]\right\}^{\frac{1}{2}}, \\
R &= S + T + \frac{I_2}{3}, \qquad S = \left[W + \left(V^3 + W^2\right)^{\frac{1}{2}}\right]^{\frac{1}{3}}, \\
T &= \left[W - \left(V^3 + W^2\right)^{\frac{1}{2}}\right]^{\frac{1}{3}}, \qquad V = \frac{1}{9}\left[3\left(I_1 I_3 - 4I_4\right) - I_2^2\right], \\
W &= \frac{1}{54}\left[-9I_2\left(I_1 I_3 - 4I_4\right) - 27\left(4I_2 I_4 - I_3^2 - I_1^2 I_4\right) + 2I_2^3\right].
\end{aligned}
\tag{4.A 5}
$$

This expression for the path is awkward to evaluate when $h \ll x, y$, but it compares favourably with the numerical solution to the path.

We now approximate the explicit solution with a view to comparing this representation with the perturbation approach used in Section 4.2.2. We may hope to get an asymptotic representation valid very close to t_{s^*}, that is, where our simple scheme breaks down. However, the behaviour of the branch points and cuts in the quartic, and the excess of algebraic terms makes this an arduous task, that is ultimately unrevealing. The part of this treatment that compares with the simple perturbation scheme we have adopted is outlined below.

Introduce $\tilde{I}_q = [(x^2 + y^2 + h^2)^2 - 4y^2h^2]I_q$, so that equations (4.A 3) may be rewritten as

$$
\begin{aligned}
\tilde{I}_1 &\sim 4\mathrm{i}c_d t x(x^2 + y^2) + h^2 4\mathrm{i}c_d t x, \\
\tilde{I}_2 &\sim -\left[4c_d^2 t^2 x^2 + 2(x^2 + y^2)(c_d^2 t^2 - k^2 y^2)\right] - h^2 2\left[c_d^2 t^2 + y^2(k^2 + 1) - x^2\right], \\
\tilde{I}_3 &\sim -4\mathrm{i}c_d t x(c_d^2 t^2 - k^2 y^2) + h^2 4\mathrm{i}c_d x, \\
\tilde{I}_4 &\sim (c_d^2 t^2 - k^2 y^2)^2 - h^2 2(c_d^2 t^2 + k^2 y^2).
\end{aligned}
\tag{4.A 6}
$$

Following a systematic expansion of the other equations (4.A 4-5) and crucially obtaining $Q^2 = h^2\mathcal{Z}^2$ we may find an asymptotic representation:

$$
\zeta = -\mathrm{i}c_d t x(x^2 + y^2)^{-1} + (c_d t^2 - k^2 x^2 - k^2 y^2)^{\frac{1}{2}} y(x^2 + y^2)^{-1} + h\mathcal{Z} + o(h^2). \tag{4.A 7}
$$

Note that when $h = 0$ we have regained the explicit zero path in equation (4.2.10). The explicit form of $\mathcal{Z}$ is lengthy and we exclude it here, but it can be shown numerically to compare favourably with the perturbation in equation (4.2.11).

Appendix 4.B. The zeros of $s(\zeta)$

The piece of the Cagniard path that gives the contribution leading to the compressional wavefront arrival is often close to a zero of the Schölte complement function $s(\zeta)$. The Schölte function is discussed in Appendix 3.B. The *migratory* behaviour of the zeros from the imaginary axis, Roever *et al.* (1959), is shown in Figure 4.13. For low values of the Poisson's ratio both zeros lie on the imaginary axis, the second zero lies close to the branch point at $-\mathrm{i}$. As the Poisson's ratio is increased the zeros approach each other, intersect, and, typically at $0.28 < \nu < 0.3$, migrate from imaginary axis and form conjugate pairs. The figure shows the position of the zeros for intervals $\nu = 0.02$ of the Poisson's ratio and $c_s = 60$ of the shear wavespeed. Typical results are that,

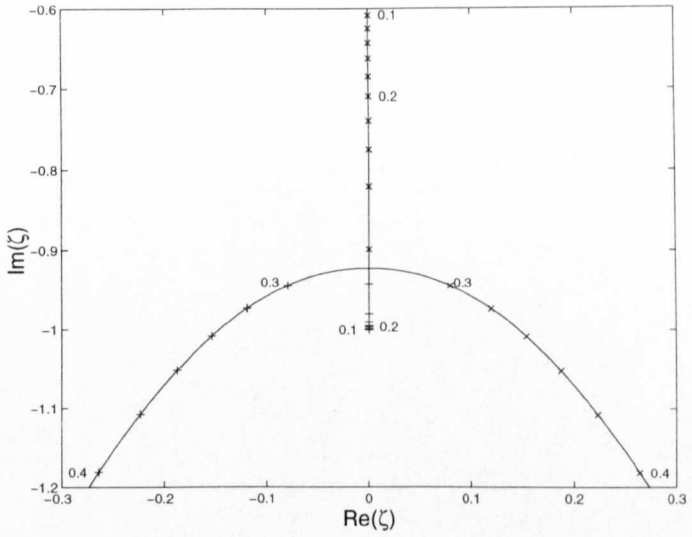

Figure 4.13. Part of the complex ζ plane showing the position of the zeros of $s(\zeta)$ as functions of the Poisson's ratio. The crosses show the pairs of zeros at intervals of $\nu = 0.02$ for the Poisson's ratio and $c_s = 60$ of the shear wavespeed; when $\nu = 0.1$, $c_s = 2271$. The behaviour of the zeros is discussed in the text.

for aluminium-water, $\pm \mathrm{i}k_p = \mp 0.15979 \pm \mathrm{i}1.01638$, and for sandstone-water, $\pm \mathrm{i}k_p = \pm \mathrm{i}0.99912$, $\pm \mathrm{i}0.638995$.

We have already observed that there is a square root singularity associated with the direct compressional wave that arrives at t_{pp} in the solid. The importance of the zeros is that

$$u_y^H(x, y, t_{pp}) \sim -\mathrm{sgn}\left[\mathrm{Re}\left(s(\zeta^{(P)}(t_{pp}))\right)\right] \frac{\mathrm{d}\zeta^{(P)}(t)}{\mathrm{d}t}\Big|_{t=t_{pp}}, \tag{4.B 1}$$

where $\zeta^{(P)}(t_{pp}) = -\mathrm{i}\sin\theta$, and the sign of the singularity associated with this response may change, see for instance Figure 4.4. Indeed we find that the path intersects the zero when the ratios x/h and y/h that determine the response, are chosen to satisfy $h + y = (k_p^{-2} - 1)^{\frac{1}{2}} x$.

Appendix 4.C. Reflection and transmission coefficients

The relevant reflection and transmission coefficients required in Section 4.3.1 are

$$\begin{aligned} T_{PP}(\zeta) &= \frac{2\gamma_1(\zeta)}{(\gamma_2(\zeta) + \rho\gamma_1(\zeta))}, \\ T^{PP}(\zeta) &= \frac{2\rho\gamma_2(\zeta)}{(\gamma_2(\zeta) + \rho\gamma_1(\zeta))}, \\ R_{PP}(\zeta) = R^{PP}(\zeta) &= \frac{\gamma_2(\zeta) - \rho\gamma_1(\zeta)}{\gamma_2(\zeta) + \rho\gamma_1(\zeta)}. \end{aligned} \tag{4.C 1}$$

The subscripts 1 and 2 are used to denote the fluids in $y < 0$, $y > h$, and in $0 < y < h$. In these formulae $\rho = \rho_2/\rho_1$ and the functions γ_1 and γ_2 are defined as $(\zeta^2 + k^2)^{\frac{1}{2}}$ $(k = c_2/c_1)$ and $(\zeta^2 + 1)^{\frac{1}{2}}$.

The relevant reflection and transmission coefficients required in Section 4.3.2 are

$$\begin{aligned}
T_{PP} &= 2\gamma_d(\zeta^2-\gamma_s^2)\left[\mu(\gamma_s\zeta^2+\gamma_s\gamma_s'^2-2\gamma_s'\zeta^2)+(\gamma_s'\zeta^2+\gamma_s'\gamma_s^2-2\gamma_s\zeta^2)\right]\mathcal{K},\\
T^{PP} &= 2\mu\gamma_d'(\zeta^2-\gamma_s'^2)\left[\mu(\gamma_s\zeta^2+\gamma_s\gamma_s'^2-2\gamma_s'\zeta^2)+(\gamma_s'\zeta^2+\gamma_s'\gamma_s^2-2\gamma_s\zeta^2)\right]\mathcal{K},\\
T_{PS} &= 2\mathrm{i}\gamma_d\zeta(\zeta^2-\gamma_s^2)\left[-\mu(\zeta^2+\gamma_s'^2-2\gamma_s\gamma_d')+(\zeta^2+\gamma_s^2-2\gamma_s\gamma_d')\right]\mathcal{K},\\
T^{SP} &= 2\mathrm{i}\mu\gamma_s'\zeta(\zeta^2-\gamma_s^2)\left[-\mu(\zeta^2+\gamma_s'^2-2\gamma_s\gamma_d')+(\zeta^2+\gamma_s^2-2\gamma_s\gamma_d')\right]\mathcal{K},
\end{aligned} \tag{4.C 2}$$

where

$$\begin{aligned}
&\mathcal{K}^{-1}=\delta_1+\delta_2+\delta_3,\qquad \delta_1=(\zeta^2-\gamma_d'\gamma_s')R_\gamma(\zeta),\qquad \delta_2=\mu^2(\zeta^2-\gamma_d\gamma_s)R_{\gamma'}(\zeta),\\
&\delta_3=-\mu\left[2\zeta^2(\zeta^2+\gamma_s'^2-2\gamma_d'\gamma_s')(\zeta^2+\gamma_s^2-2\gamma_s\gamma_d)+(\gamma_d\gamma_s'+\gamma_d'\gamma_s)(\zeta^2-\gamma_s^2)(\zeta^2-\gamma_s'^2)\right].
\end{aligned} \tag{4.C 3}$$

The primed letters are used to denote the elastic material in $0<y<h$ and the unprimed letters in $y<0$, $y>h$. In these formulae $\mu=c_s'^2\rho'/c_s^2\rho$ and the functions γ_d', γ_s', γ_d, and γ_s are defined as $\gamma_q'=(\zeta^2+k_q'^2)^{\frac{1}{2}}$, with $q=d$, s, and $\gamma_q=(\zeta^2+k_q^2)^{\frac{1}{2}}$, with $q=d$, s; $k_d'=1$, $k_s'=c_d'/c_s'$, $k_d=c_d'/c_d$, and $k_s=c_d'/c_s$.

The ratios for the transmitted waves to the incident wave at $y=h$ are labelled by the subscripts T_{PP}, T_{PS} (P wave transmits as P or S wave), and the transmitted waves at $y=0$ are labelled by the superscripts T^{PP}, T^{SP} (transmitted P or S wave transmits as P wave). In addition the ratios for the reflected waves in the layer are denoted by R where superscripts, PP, and subscripts, PP, again relate to the upper and lower interfaces respectively.

Chapter Five

Pulse scattering by a semi-infinite crack

5.1. Introduction

The dynamic stress loading of cracks, and the related fracture mechanics, is an area that has received much attention; for a detailed description see Freund (1990), Atkinson & Craster (1995b). There is particular interest in wave or pulse interactions with cracks that lie beneath surfaces or interfaces, as material failure or interfacial debonding is often caused by the subsequent growth of cracks. There has also been resurgent interest in the modelling of fracture in non-homogeneous solids (Craster & Atkinson, 1994; Choi, 1997; Ergüven & Gross, 1999), as modern fabrication methods and functionally graded materials become of more use, thus we also address some aspects of crack-wave interactions in non-homogeneous media.

Determining the stress fields, and crack tip stress intensity factors, generated by the interaction of stress waves with cracks, and boundaries, is of fundamental interest in fracture mechanics. It is also of great interest in the non–destructive evaluation of structures. The scattered field yields information for crack detection and characterisation, thereby enabling estimates to be made of the location and size of the crack. The presence of an interface or free surface is a complicating feature and analytical solutions are often difficult to obtain (Tsai & Ma, 1992, 1993). In these previous analyses for in-plane loadings the results are valid until the first wave scattered from the crack returns to the crack after having been reflected by the free surface. With the addition of an overlying fluid there are no current analyses. For anti-plane loadings the analysis becomes slightly simpler. One can utilise the method of images (Achenbach, 1973) for some rather special problems to extract the full solutions; however typically the situations are often somewhat more complicated.

The aim of this chapter is to develop approaches that generate the stress intensity factors and give the exact form of the wavefronts, up to a specified time, generated by the dynamic loading of a semi-infinite subsurface crack. For ease of exposition we consider cracks that are parallel to the interface, the results may be generalised to look at cracks arbitrarily orientated to the interface; these results are not presented here. A variety of different stress loadings may be considered and here we consider the crack to be subjected to a prescribed stress loading on the crack faces and if required this could be chosen to be that induced by an incident pulse and hence identical to a scattering problem. Unfortunately it turns out that the plane strain problem cannot currently

be solved conveniently and with this in mind we introduce an iterative (or *generalised* Wiener–Hopf) method in which successively the Cagniard–de Hoop (Cagniard, 1939; de Hoop, 1960) and Wiener–Hopf (*e.g.* Noble, 1958) techniques are applied to solve a matrix Wiener–Hopf equation. This follows the scheme presented by Haak & Kooij (1996) and Kooij & Quak (1988) for anti-plane problems. The application of the Cagniard–de Hoop technique follows Garvin (1956) and Harris (1980). The iterative scheme is illustrated in detail on an anti-plane crack problem and, in addition, we demonstrate how weight functions can be incorporated into the iterative scheme.

The analysis is performed using Fourier and Laplace transforms in space and time respectively. The Laplace transform in time, t, and its inverse, are defined as

$$\overline{f}(p) = \int_0^\infty f(t)e^{-pt}\mathrm{d}t, \quad f(t) = \frac{1}{2\pi\mathrm{i}}\int_{c-\mathrm{i}\infty}^{c+\mathrm{i}\infty}\overline{f}(p)e^{pt}\mathrm{d}p, \text{ for } \mathrm{Re}(c) > 0, \tag{5.1.1}$$

where the Laplace transform variable is p. The Fourier transform in one spatial direction, x, and its inverse, are defined as

$$\widetilde{f}(s) = \int_{-\infty}^\infty f(x)e^{\mathrm{i}sx}\mathrm{d}x, \quad f(x) = \frac{1}{2\pi}\int_{-\infty}^\infty \widetilde{f}(s)e^{-\mathrm{i}sx}\mathrm{d}s, \tag{5.1.2}$$

where s is the Fourier transform variable.

We also utilise the Cagniard–de Hoop technique, there is sometimes an element of mystery in the derivation used by some authors, in that p *must* be real and positive; this is unnecessary. The function ultimately occurring in the double transform inverse is, for the problems considered here, ultimately homogeneous in p and s. Thus in the analysis if we put $s = p\xi$ then p occurs only in the exponential and, depending upon the time dependence of the incident field, as an isolated factor. The resulting double transform pair is:

$$\begin{aligned} f(x,y,t) &= \frac{1}{4\pi^2\mathrm{i}}\int_{c-\mathrm{i}\infty}^{c+\mathrm{i}\infty}\int_{-\infty}^\infty \widetilde{\overline{f}}(s,y,p)e^{-\mathrm{i}sx+pt}\mathrm{d}s\ \mathrm{d}p \\ &= \frac{1}{4\pi^2\mathrm{i}}\int_{c-\mathrm{i}\infty}^{c+\mathrm{i}\infty}\int_{C_p} \widetilde{\overline{f}}(\xi,y,p)e^{-\mathrm{i}p\xi x}pe^{pt}\mathrm{d}\xi\ \mathrm{d}p. \end{aligned} \tag{5.1.3}$$

The change of variable in the inner integral rotates the integral path of that integral by $\arg(p)$, see for instance Hudson (1980); this does not cross any singularities, provided one defines the branch cuts that will arise in the appropriate manner. Thus by Cauchy's theorem, as we cross no singularities, we can take C_p to run along the real axis once again. Hence the rescaled Fourier transform pair,

$$\widetilde{f}(\xi) = \int_{-\infty}^\infty f(x)e^{\mathrm{i}\xi px}\mathrm{d}x, \quad f(x) = \frac{1}{2\pi}\int_{-\infty}^\infty \widetilde{f}(\xi)e^{-\mathrm{i}\xi px}\mathrm{d}\xi, \tag{5.1.4}$$

can be used at the outset with impunity. The technique itself is comprehensively discussed

by Achenbach (1973), Miklowitz (1978), and Hudson (1980). The double transform typically takes the form

$$\widetilde{\widetilde{f}}(\xi, y, p) = g(\xi)e^{-p\gamma(\xi)y},$$

for a function $g(\xi)$ that may contain branch cuts and poles, where $\gamma(\xi)$ is a function containing branch cuts, appropriately chosen. The aim of the Cagniard-de Hoop technique is, following Lamb (1904), to recast the inner integral as a Laplace transform via the substitution $t = \gamma(\xi)y + \mathrm{i}\xi x$, for t real and positive. This deforms the contour for the Fourier transform; the piece of this path in one quadrant is then related to the conjugate of the path in the other quadrant. This ultimately takes the inner integral to a Laplace transform and then inversion can be performed by inspection.

One of the most useful results found during any study of crack behaviour is the stress intensity factor; it is the stress intensity factor that characterises the near crack tip stress field. Here the results for the stress intensity factors are checked, and in some cases extended, using an invariant integral based on a pseudo energy momentum tensor (Atkinson, 1977; Atkinson & Craster, 1995a); which is a generalisation of the Eshelby (1951, 1970) energy momentum tensor. In particular, for a class of crack loadings, it enables us to investigate the effects of material inhomogeneity without any need for Wiener–Hopf analysis. This is motivated by the current interest in non-homogeneous or layered media.

For simplicity we treat a simple spatial form of stress loading on the crack faces. We then demonstrate how weight functions (Bueckner, 1970) can be deduced within this iterative procedure and this allows us to generalise the stress intensity factor results to deal with any stress loading.

The plan for the following five sections of this chapter is as follows: First, in Section 5.2, we consider the anti-plane problem of a semi-infinite crack in a layered elastic material. The exact solution is found as an inverse integral using the Wiener–Hopf technique. This integral could then be evaluated numerically; these results are not included. Instead, we employ an iterative *generalised* Wiener–Hopf method (*e.g.* Thau & Lu, 1971) that yields a series solution. The motivation for developing this approach is that the exact solution contains a triple integral to evaluate and this obscures the physical interpretation of the solution. Also the analogous problem of a subsurface crack in an elastic solid cannot currently be solved conveniently as one obtains a matrix Wiener–Hopf equation whose factorisation is awkward; we briefly consider this case in Section 5.5. An invariant integral is introduced in Section 5.3 which is then used to explore some model non-homogeneous materials, the aim is to illustrate the method as a useful analytical tool. Following this, in Section 5.4, we develop an iterative weight function method thus enabling us to use

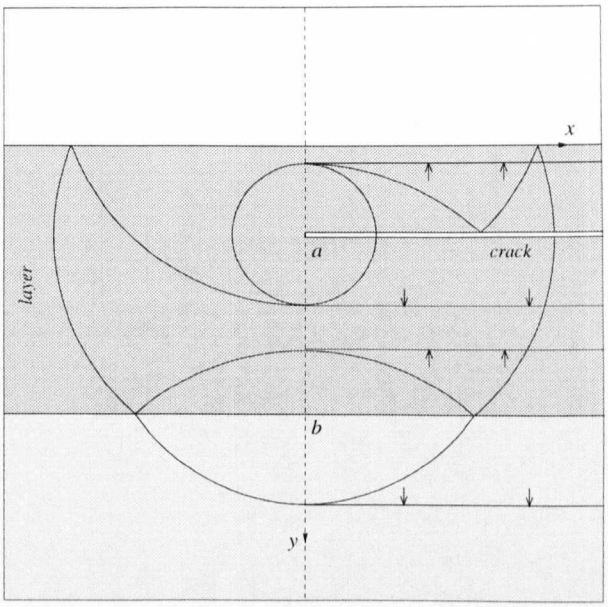

Figure 5.1. The geometry of the problem shown together with a schematic of the first reflected waves for $t < r_1 + 2a/c$ where $r_1^2 = x^2 + (y-a)^2$; $b - a > 2a$. This is after the wave from the crack that has been reflected from the surface strikes the crack, but before this wave returns to the surface, and before the wave reflected by the interface strikes the crack.

the generalised ray method to find formulae for the stress intensity factors exact up to a specified time.

The in-plane crack problems are substantially more complicated, involving mode coupling at both the crack tip and the interfaces. We briefly illustrate how the techniques developed in the simpler anti-plane case carry across to this harder situation in Section 5.5. Finally a summary of the results is given in Section 5.6.

5.2. Anti-plane loading

We consider an elastic layer in $0 < y < b$, bonded to a semi-infinite elastic material that occupies the half space $b < y < \infty$; along the interface, $y = b$, the stress and displacement fields of the two materials satisfy continuity conditions. Within the elastic layer a semi-infinite crack is present along $y = a$ $(a < b)$ for $x > 0$; this is shown in Figure 5.1.

A Cartesian coordinate system is adopted with x_1, x_2 corresponding to x and y. The problem is two-dimensional and the relevant stress components, $\sigma_{zj}(x, y, t)$, are related to the out-of-plane, that is, in the z-direction displacements $u_z(x, y, t)$ via

$$\sigma_{zj} = \mu u_{z,j} \tag{5.2.1}$$

where the comma denotes differentiation with respect to x_j and $\mu(x,y)$ is the elastic shear modulus. The governing equations are the equilibrium equations $\sigma_{zj,j} = \rho\ddot{u}_z$, where the notation $\ddot{}$ denotes partial double differentiation with respect to time and $\rho(x,y)$ is the material density. The displacement satisfies

$$\left[\frac{\partial}{\partial x}\left(\mu\frac{\partial}{\partial x}\right) + \frac{\partial}{\partial y}\left(\mu\frac{\partial}{\partial y}\right)\right] u_z = \rho\ddot{u}_z \tag{5.2.2}$$

which reduces to the wave equation $\nabla^2 u_z = \ddot{u}_z/c^2$ when the material parameters μ and ρ are constant; the wavespeed c is then defined as $c^2 = \mu/\rho$. To distinguish between the different materials in the layer and underlying half space a superscript (h) is adopted to denote the elastic half space $y > b$. In this section we henceforth assume that the material is homogeneous so μ and ρ are constant; we consider non-homogeneous materials in Section 5.3.

The surface $y = 0$ is taken to be rigid, hence $u_z = 0$ there; a very similar analysis can be performed if the surface is stress–free. The crack lies in undamaged material so the condition taken ahead of the crack, $y = a$ for $x < 0$, is that the displacement u_z is continuous there, and the stress σ_{zy} is continuous along $y = a$, $-\infty < x < \infty$. The loading taken on the crack $y = a$, $x > 0$ is that $\sigma_{zy} = F(t)H(x)$, where $F(t)$ is the time dependence of the pulse and $H(x)$ is the Heaviside function. Later, in Section 5.4, we utilise our solution in conjunction with weight functions to extend our final results to any spatial loading. Along the interface, $y = b$, both the displacement u_z and stress σ_{zy} are continuous, *i.e.* $u_z = u_z^{(h)}$ and $\sigma_{zy} = \sigma_{zy}^{(h)}$.

5.2.1. *Exact solution*

First we shall solve the problem exactly, and then using an iterative approach. To formulate a functional equation, we apply Fourier transforms in the spatial x coordinate and Laplace transforms in time, together with the following half-range Fourier transforms: the transform of the unknown stress σ_{zy} ahead of the crack $y = a$ for $x < 0$, and the transform of the unknown jump in the displacement, u_z, across $y = a$ for $x > 0$,

$$\sigma_-(\xi,p) = \int_{-\infty}^{0} \overline{\sigma}_{zy}(x,a,p)e^{i\xi x}\mathrm{d}x, \quad U_+(\xi,p) = \int_0^{\infty} \left[\overline{u}_z(x,a^+,p) - \overline{u}_z(x,a^-,p)\right] e^{i\xi x}\mathrm{d}x. \tag{5.2.3}$$

The subscripts $+$ and $-$ denote functions analytic in the 'plus' and 'minus' regions of the complex ξ-plane respectively; specifically in $\mathrm{Im}(\xi) > 0$ and in $\mathrm{Im}(\xi) < \min(p/c, p/c^h)$ respectively. In the following we loosely refer to these regions as the 'upper' and 'lower' halves of the complex ξ-plane. The superscripts $+$ $(-)$ for a^+ (a^-) denote the limit as we approach the crack faces $(y = a)$ from above (below).

The Wiener–Hopf technique generates a functional equation that connects the transforms of these unknown quantities. This equation is then disentangled to identify the unknowns, and hence it determines the full solution. Along the way we require, of course, to satisfy the edge conditions, that is in terms of polar coordinates (r,θ) based at the crack tip, the displacements are $O(r^{1/2})$ and the stresses are $O(r^{-1/2})$ at the crack tip. The functional equation emerges as

$$\mathcal{Q}(\xi,p)\,[\sigma_-(\xi,p)+\Upsilon_+(\xi,p)] = -\mu\gamma(\xi,p)U_+(\xi,p),\ \text{where}\ \Upsilon_+ = \frac{\overline{F}(p)}{\mathrm{i}\xi_+}; \tag{5.2.4}$$

the function Υ_+ has been introduced for convenience. To incorporate the specific loading adopted here, that is, the spatially constant stress loading we adopt the convention that the pole at zero is in the lower half of the complex ξ-plane; this is, it is a 'plus' function and we remind ourselves of this fact using the subscript + upon ξ and Υ. In (5.2.4) $\overline{F}(p)$ is the Laplace transform of the time dependence of the stress loading, $F(t)$, and the function $\gamma(\xi,p)$ $(\gamma(\xi,p)^{(h)})$ is defined as $\gamma(\xi,p) = [\xi^2+p^2/c^2]^{\frac{1}{2}}$ $(\gamma^{(h)}(\xi,p) = [\xi^2+p^2/c^{(h)^2}]^{\frac{1}{2}})$. The branch cuts for these functions, in the complex ξ-plane, are taken such that they run along the imaginary axis from $\pm\mathrm{i}p/c$ $(\pm\mathrm{i}p/c^{(h)})$ to $\pm\mathrm{i}\infty$.

A function $\mathcal{Q}(\xi,p)$ is introduced in (5.2.4) and is defined as

$$\mathcal{Q}(\xi,p)\cosh(\gamma\ a) = \frac{\mu^{(h)}\gamma^{(h)}\ \sinh(\gamma\ b)+\mu\gamma\cosh(\gamma\ b)}{\mu^{(h)}\gamma^{(h)}\cosh[\gamma\ (b-a)]+\mu\gamma\sinh[\gamma\ (b-a)]}, \tag{5.2.5}$$

where $\gamma \equiv \gamma(\xi,p)$ and $\gamma^{(h)} \equiv \gamma^{(h)}(\xi,p)$. This function captures all the essential physics of the wave reflections from the surface, crack faces and interface together with the waveguide nature of the geometry.

The next step in our Wiener–Hopf recipe involves separating the functional equation (5.2.4) into a piece that is analytic in the + region, and a piece that is analytic in the − region. These pieces have a common overlapping region in the ξ plane and thus are equal to the same analytic function within this strip. Hence, by analytic continuation, both sides *must* equal a function that is analytic everywhere. This must remain true even as $|\xi| \to \infty$, and so (by Liouville's Theorem) this function is a polynomial in ξ. This allows us to find the unknown transforms analytically. This polynomial is determined by applying the known edge behaviour at the crack tip, that is, the stresses are $O(r^{-1/2})$ there.

In order to make the split into the standard Wiener–Hopf form the function $\mathcal{Q}(\xi,p)$ is split into a product of $\pm$-functions: $\mathcal{Q}(\xi,p) = \mathcal{Q}_+(\xi,p)\mathcal{Q}_-(\xi,p)$; a related splitting is described in Appendix 5.B, here it is ultimately most easily performed in terms of some quadratures. We also require the product split $\gamma(\xi,p) = \gamma_+(\xi,p)\gamma_-(\xi,p)$ where $\gamma_\pm(\xi,p) = [\xi \pm \mathrm{i}p/c]^{\frac{1}{2}}_{\pm}$.

We now rearrange the functional equation (5.2.4) so that the left and right hand sides are analytic in the upper and lower halves of the complex ξ-plane respectively:

$$\mu\frac{\gamma_+(\xi,p)}{\mathcal{Q}_+(\xi,p)}U_+ + \Upsilon_+\frac{\mathcal{Q}_-(0,p)}{\gamma_-(0,p)} = -\frac{\mathcal{Q}_-(\xi,p)}{\gamma_-(\xi,p)}\sigma_- - \Upsilon_+\left[\frac{\mathcal{Q}_-(\xi,p)}{\gamma_-(\xi,p)} - \frac{\mathcal{Q}_-(0,p)}{\gamma_-(0,p)}\right]. \quad (5.2.6)$$

The regions of analyticity overlap on $0 < \mathrm{Im}(\xi) < \min(p/c, p/c^{(h)})$; this is enough to invoke analytic continuation and to determine that both sides of the functional equation can be extended to the full complex ξ-plane, and hence are equal to the same analytic function everywhere. Using the edge conditions (the stresses in the limit as $r \to 0$ are $O(r^{-1/2})$) this function is determined to be zero.

One of the most immediate results that can be deduced from the functional equation is the behaviour of the stress near the tip of the crack. The limit as $|\xi| \to \infty$ in the transform space corresponds to the limit as $x \to 0$ in the physical domain. The stress ahead of the tip of the crack is $\sigma_-(\xi,p)$ from which

$$\overline{\sigma}_{zy}(x,a,p) \sim \overline{F}(p)\left(\frac{c\mathcal{Q}(0,p)}{2p\pi}\right)^{\frac{1}{2}}(-x)^{-\frac{1}{2}} \equiv \overline{K}_{\mathrm{III}}(p)(-2\pi x)^{-\frac{1}{2}} \text{ for } x < 0. \quad (5.2.7)$$

To obtain this result we have employed the inverse Fourier transform given in Appendix 5.A and the result $\mathcal{Q}_-(\xi,p) \to 2^{1/2}$ as $|\xi| \to \infty$. The mode III Laplace transformed stress intensity factor $\overline{K}_{\mathrm{III}}(p) \equiv \overline{K}(p)$ is also defined by (5.2.7) and hence can be explicitly extracted; that result is also extracted using an invariant integral in Section 5.3. The full solution for the stresses in the elastic layer is identified from equation (5.2.6) as,

$$\sigma_{zy}(x,y,p) = \frac{1}{2\pi\mathrm{i}}\int_{c-\mathrm{i}\infty}^{c+\mathrm{i}\infty}\frac{1}{2\pi}\int_{-\infty}^{\infty}\frac{\overline{F}(p)\gamma_-(\xi,p)\mathcal{Q}_-(0,p)\cosh(\gamma\, y)}{\mathrm{i}\xi_+\gamma_-(0,p)\mathcal{Q}_-(\xi,p)\cosh(\gamma\, a)}e^{-\mathrm{i}\xi x}\mathrm{d}\xi\; e^{pt}\mathrm{d}p \quad (5.2.8)$$

for $0 < y < a$. A similar expression may be deduced in $a < y < b$ and in $y < 0$; these results are not included here. So far we have taken the stress loadings to be uniform along the crack faces, however, we may routinely generalise this to any loading of the form $\sigma_{zy} = F(t)G(x)$. For ease of presentation, we restrict ourselves to the stress intensity factors. The stress ahead of the crack tip is now asymptotically

$$\overline{\sigma}_{zy}(x,a,p) \sim -\overline{F}(p)\frac{1}{(2\pi\mathrm{i})^{\frac{1}{2}}}\left(\frac{1}{2\pi\mathrm{i}}\int_{-\infty}^{\infty}\frac{\mathcal{Q}_-(\chi,p)\widetilde{G}(\chi)}{\gamma_-(\chi,p)}\mathrm{d}\chi\right)(-x)^{-\frac{1}{2}}H(-x), \quad (5.2.9)$$

where $\widetilde{G}(\chi)$ is the Fourier transform of $G(x)$ (with Fourier transform variable χ). We also note that $\mathcal{Q}_-(\chi,p) \sim 2^{1/2} + O(e^{-2\gamma(\chi,p)a})$ to deduce the solution for a single crack in an infinite homogeneous material. This general formula is useful in comparison with one obtained later using weight functions.

These formulae formally solve the canonical problem. A direct numerical evaluation

of the integrals above can be performed, but this is not overly revealing. In cases when we expect the first few arrivals to completely characterise the solution it proves to be more straightforward to proceed iteratively. Hence we choose to develop a method that iteratively solves equation (5.2.4) rather than formally expand the integral in (5.2.8).

In this section we have made a direct product split $Q = Q_+ Q_-$. The essence of a generalised ray approach is rather than digest Q in its entirety, we swallow it as smaller more manageable portions, that is,

$$\frac{1}{Q} \sim \frac{1}{2}\left[1 + \exp[-2\gamma\ a] + \left(\frac{\mu(h)\gamma^{(h)} - \mu\gamma}{\mu(h)\gamma^{(h)} + \mu\gamma}\right)\exp[-2\gamma\ (b-a)] + \ldots\right] \tag{5.2.10}$$

and each term of Q now contains all the physics up to a specific time; the terms involving $\mu^{(h)}$, $\gamma^{(h)}$, μ, and γ can be identified with reflection coefficients from the interface or surface, and thus each term has physical significance. Each term of Q is ultimately split into a product $Q_+^j Q_-^j$ of + and − functions; however, the 'sum of products' that we construct does not, as a whole, have an obvious factorisation into a product of + and − functions so that Q_+ (or Q_-) is not easily recovered from its smaller portions as we may, at first, expect.

5.2.2. *Iterative solution*

In this section we utilise an iterative scheme similar to that described by Kooij & Quak (1988) and Haak & Kooij (1996) to solve the problem we formulated in the previous section. This places the physical language of various superpositions, see for instance Tsai & Ma (1993), in a more rigorous setting. This approach lends itself well to further generalisations.

To formulate the current problem the original functional equation (5.2.4) is split into a series of less complicated subsidiary equations. Each equation then corresponds to the wavefield due to successive reflections from the crack, the interface and the surface. In the following we drop the tilde and overline decoration on u_z and write $\bar{\tilde{u}}_z(\xi, y, p)$ as u_z to shorten the notation; the same convention applies to σ_{zy}. In order to use generalised ray theory we first expand u_z as

$$u_z = \sum_{m=0}^{\infty}\sum_{n=0}^{\infty} u_z^{(m,n)} \quad \text{in} \quad 0 < y < a, \tag{5.2.11}$$

with a similar expression for u_z in $y > b$ and for σ_{zy}. Similarly we expand the unknown quantities in the transform domain $\sigma_- \equiv \sigma_-(\xi, p)$ and $U_+ \equiv U_+(\xi, p)$; the arguments ξ and p are again omitted here and in $\gamma(\xi, p)$. The superscripts (m, n) correspond to m reflections against the interface, $y = b$, and the crack, and n reflections against the

surface of the elastic layer, $y = 0$, and the crack. The functional equation (5.2.4) is rewritten as

$$2\left(\sigma_- + \Upsilon_+\right)\left(\frac{1+\mathcal{R}e^{-2\gamma b}}{1-\mathcal{R}e^{-2\gamma(b-a)}}\right) = -\mu\gamma\left(1+e^{-2\gamma a}\right)U_+, \tag{5.2.12}$$

where $\mathcal{R}$ is the reflection coefficient at the interface of two dissimilar half spaces:

$$\mathcal{R} = \frac{\mu\gamma - \mu^{(h)}\gamma^{(h)}}{\mu^{(h)}\gamma^{(h)} + \mu\gamma}. \tag{5.2.13}$$

The reflection coefficient at a rigid surface is, of course, -1; so there is no need to introduce any extra notation for that reflection coefficient, although one can envisage having yet another elastic material in $y < 0$ and then requiring a reflection coefficient for reflected waves from $y = 0$. Using the expansion in equation (5.2.11) we split the functional equation (5.2.12) into a series of simple functional equations each of which is order $\exp[-2m\gamma(b-a) - 2n\gamma a]$. Doing so, we arrive at the following explicit functional equations:

$$\begin{aligned}
s_-^{(0,0)} &= -\frac{1}{2}\mu\gamma U_+^{(0,0)} \\
s_-^{(0,n)} &= -\frac{1}{2}\mu\gamma\left(U_+^{(0,n)} + U_+^{(0,n-1)}e^{-2\gamma a}\right) \quad \text{for } n \geq 1 \\
s_-^{(m,0)} + \sum_{q=0}^{m-1}\mathcal{R}^{m-q}e^{-2(m-q)\gamma(b-a)}s_-^{(q,0)} &= -\frac{1}{2}\mu\gamma U_+^{(u,0)} \quad \text{for } m \geq 1 \\
s_-^{(m,n)} + \sum_{q=0}^{m-1}\mathcal{R}^{m-q}\left(s_-^{(q,n)} + \sigma_-^{(q,n-1)}e^{-2\gamma a}\right)e^{-2(m-q)\gamma(b-a)} & \\
= -\frac{1}{2}\mu\gamma\left(U_+^{(m,n)} + U_+^{(m,n-1)}e^{-2\gamma a}\right) & \quad \text{for } m,n \geq 1.
\end{aligned} \tag{5.2.14}$$

In these formulae $s_-^{(0,0)} = \sigma_-^{(0,0)} + \Upsilon_+$ and otherwise $s_-^{(m,n)} = \sigma_-^{(m,n)}$. To recover the stresses in $0 < y < a$ we require a further expansion that has the following form

$$\sigma_{zy}^{(m,n)} = \left[\sum_{q=0}^{n}(-1)^q s_-^{(m,n-q)}e^{-2q\gamma a}\right]e^{-\gamma a}\left(e^{\gamma y} + e^{-\gamma y}\right); \tag{5.2.15}$$

recall that $\sigma_{zy} = \sum_{m=0}^{\infty}\sum_{n=0}^{\infty}\sigma_{zy}^{(m,n)}$. The stresses in $a < y < b$ and $b < y$ are not included here, but may be found in a similar way. Note that each successive solution in equation (5.2.15) includes both forward and backward going waves to $+\infty$ and $-\infty$ respectively, *i.e.* both the waves diffracted by the crack and reflected by the free surface at $y = 0$ and the interface at $y = b$ are described by a single iteration. A more physical approach that we could choose to exploit relies on a superposition of three separate problems. This approach is briefly described in Section 5.2.3.

5.2.2.1. *First loading*

The zero order functional equation from the first equation of (5.2.14) is

$$2\left(\sigma_-^{(0,0)} + \Upsilon_+\right) = -\mu\gamma U_+^{(0,0)}. \tag{5.2.16}$$

This is equivalent to the standard infinite medium problem (Freund, 1990) as the crack is initially unaware of either the surface or interface, and the unknown transforms emerge as

$$U_+^{(0,0)} = -\frac{2\Upsilon_+}{\mu\gamma_+(\xi,p)\gamma_-(0,p)} \quad \text{and} \quad \sigma_-^{(0,0)} = \Upsilon_+\left[\frac{\gamma_-(\xi,p)}{\gamma_-(0,p)} - 1\right], \tag{5.2.17}$$

from which we may deduce the zero order diffracted stress field explicitly. A more striking result that falls out of the analysis is the behaviour at the tip of the crack; we can extract the leading behaviour (using inverse Fourier results from Appendix 5.A) as

$$\sigma_{zy}^{(0,0)}(x,a,t) \sim L^{-1}\left[\overline{F}(p)\left(\frac{2c}{p}\right)^{\frac{1}{2}}(-2\pi x)^{-\frac{1}{2}}\right], \tag{5.2.18}$$

where L denotes the Laplace transform operator. This result verifies, in part, the near stress field evaluated in equation (5.2.7).

It is straightforward to find the zero order solution utilising the Cagniard–de Hoop method, a detailed description of the method may be found in Miklowitz (1978) and others. In this case it transpires that we require two different inversion contours, chosen so that $cT = (\zeta^2+1)^{\frac{1}{2}}(a-y) + \mathrm{i}\zeta x$ and $cT = (\zeta^2+1)^{\frac{1}{2}}(a+y) + \mathrm{i}\zeta x$, for time T real and positive. This is equivalent to constructing a generalised ray path; the path describes the vertical distance travelled by each wave, the total horizontal distance, and the direction of propagation. This device places the inverse Fourier integral in the form of a Laplace transform; in further iterations this is not enough and we are required to formulate further Cagniard paths. We now require the inverse Laplace transform of this integral and as a result the solution in real time is found immediately by inspection. The explicit solution, for a general time dependence, is

$$\begin{aligned}\sigma_{zy}^{(0,0)}(x,y,t) = \int_0^t F(t-\tau)\frac{1}{\pi}\Bigg[&H(\tau - r_1/c)\mathrm{Re}\left(\frac{\gamma_-(\zeta_1(\tau))}{\mathrm{i}\zeta_1(\tau)\gamma_-(0)}\frac{\mathrm{d}\zeta_1(\tau)}{\mathrm{d}\tau}\right)\\ &+(H(\tau - r_2/c)\mathrm{Re}\left(\frac{\gamma_-(\zeta_2(\tau))}{\mathrm{i}\zeta_2(\tau)\gamma_-(0)}\frac{\mathrm{d}\zeta_2(\tau)}{\mathrm{d}\tau}\right)\Bigg]\mathrm{d}\tau.\end{aligned} \tag{5.2.19}$$

In this formula $r_{1,2}^2 = x^2 + (y \mp a)^2$ and $\tan\theta_{1,2} = \mp x/(y \mp a)$. We have also added some further decoration on the Cagniard paths: $cT = \gamma(\zeta_{1,2}(T))(a \mp y) + \mathrm{i}\zeta_{1,2}(T)x$, and a rescaling $\gamma(\zeta) = [\zeta^2+1]^{\frac{1}{2}}$. This solution corresponds to the cylindrical wavefields in $x < 0$ generated by the crack and subsequently reflected by the surface $y = 0$. It is formally valid in the interval $0 < t < (r_1 + 2a)/c$. In addition in $x > 0$ waves parallel

to the crack faces are generated and in this case are given, by a residue calculation, in the form $F(t-(a-y)/c)+F(t-(a+y)/c)$. In further iterations it is necessary to formulate the integral in terms of 'plus' and 'minus' functions in $x<0$ and $x>0$ respectively as a result of shifting the integration path in the upper and lower halves of the complex ξ-plane. In (5.2.19) this distinction is not necessary. This result is plotted later in Figure 5.2 for the case $F(t)=\delta(t)$.

5.2.2.2. *Reloading by the surface*

To proceed we utilise the zero order solution we have determined in Section 5.2.2.1 to reload the crack and find the waves diffracted by the crack in this case. The Wiener–Hopf equation of exponential order $\exp[-2\gamma\, a]$ is given by (5.2.14) as

$$2\sigma_-^{(0,1)} = -\mu\gamma\left(U_+^{(0,1)} + e^{-2\gamma a}U_+^{(0,0)}\right). \tag{5.2.20}$$

In order to utilise the Wiener–Hopf equation we define $Q^{(0,1)}=e^{-2\gamma a}$ and this function is split into the sum of $\pm$-functions, *i.e.* $Q^{(0,1)}=Q_+^{(0,1)}+Q_-^{(0,1)}$ where

$$Q_\pm^{(0,1)}(\xi,p) = \pm\frac{1}{2\pi \mathrm{i}}\int_{C_\pm}\frac{Q^{(0,1)}(\eta_1,p)}{\eta_1-\xi}\mathrm{d}\eta_1 = \pm\frac{1}{2\pi \mathrm{i}}\int_{C_\pm}\frac{e^{-2\gamma(\eta_1,p)a}}{\eta_1-\xi}\mathrm{d}\eta_1, \tag{5.2.21}$$

and $Q_+^{(0,1)}(\xi,p)=Q_-^{(0,1)}(-\xi,p)$; C_+ (C_-) is the contour from $-\infty$ to ∞ indented below (above) the real axis. After some Wiener–Hopf analysis we arrive at the following expressions for the unknown transforms

$$\begin{aligned}\sigma_-^{(0,1)} &= \frac{\gamma_-(\xi,p)\Upsilon_+}{\gamma_-(0,p)}\left[Q_-^{(0,1)}(\xi,p)-Q_-^{(0,1)}(0,p)\right]\\ \text{and}\quad U_+^{(0,1)} &= \frac{2\Upsilon_+}{\mu\gamma_+(\xi,p)\gamma_-(0,p)}\left[Q_+^{(0,1)}(\xi,p)+Q_-^{(0,1)}(0,p)\right].\end{aligned} \tag{5.2.22}$$

(i) Stress intensity factors for $O(e^{-2\gamma a})$

We can again obtain the near tip behaviour either via taking the limit $|\xi|\to\infty$, that corresponds to $x\to 0$, in the inverse Fourier integral and evaluating the remaining integral in η_1, or equivalently utilising expression (5.2.22) directly. In the limit as $|\xi|\to\infty$ then $Q_+^{(0,1)}(\xi,p)\to 0$, and the near crack tip behaviour may now be extracted by evaluating $Q_-^{(0,1)}(0,p)$ only. This is obtained by collapsing the integral around the branch cut that runs from $\mathrm{i}p/c$ to $\mathrm{i}\infty$ in the upper half plane and then evaluating the resulting definite integral using 3.7166 of Gradshteyn & Ryzhik (1980). That is

$$Q_-^{(0,1)}(0,p) = \frac{1}{\pi}\int_0^{\frac{\pi}{2}}\sin(2pa\tan\psi/c)\tan\psi\mathrm{d}\psi = \frac{1}{2}e^{-2pa/c} = \frac{1}{2}Q^{(0,1)}(0,p), \tag{5.2.23}$$

so that we obtain

$$\sigma_{zy}^{(0,1)}(x,a,t) \sim -L^{-1}\left[\overline{F}(p)\left(\frac{2c}{p}\right)^{\frac{1}{2}}\frac{1}{2}e^{-2ap/c}(-2\pi x)^{-\frac{1}{2}},\right]. \tag{5.2.24}$$

The results for the stress intensity factor presented here using an iterative approach are again consistent with those obtained by expanding equation (5.2.7). We provide a further check on this analysis using an invariant integral in Section 5.3.

(ii) Stress intensity factors for $O(e^{-4\gamma a})$

Before we proceed to compute the stress field in this case, we briefly focus our attention on determining a further stress intensity factor. It is observed that the evaluation of further wavefields needs only the solution of a finite set of Wiener–Hopf equations. To evaluate this next reflection we require

$$Q^{(0,2)}(\xi,p) = Q^{(0,1)}(\xi,p)\left[Q_+^{(0,1)}(\xi,p) + Q_-^{(0,1)}(0,p)\right] = Q_+^{(0,2)}(\xi,p) + Q_-^{(0,2)}(\xi,p) \tag{5.2.25}$$

where

$$Q_-^{(0,2)}(\xi,p) = -\frac{1}{2\pi i}\int_{C_-}\frac{e^{-2\gamma(\eta_2,p)a}}{\eta_2-\xi}\left[Q_+^{(0,1)}(\eta_2,p) + Q_-^{(0,1)}(0,p)\right]d\eta_2, \tag{5.2.26}$$

and $Q_+^{(0,2)}(\xi,p)$ is similarly defined. As before, the near crack tip behaviour may now be extracted by evaluating $Q_-^{(0,2)}(0,p) = I_Q + \left[Q_-^{(0,1)}(0,p)\right]^2$. This is obtained by collapsing the integral I_Q around the branch cut that runs from ip/c to $i\infty$ in the upper half plane and in this case evaluating the resulting double definite integral numerically:

$$I_Q = \frac{1}{\pi^2}\int_{p/c}^{\infty}\int_{p/c}^{\infty}\frac{\sin\left[2\left(\psi^2-\frac{p^2}{c^2}\right)^{\frac{1}{2}}a\right]\sin\left[2\left(\chi^2-\frac{p^2}{c^2}\right)^{\frac{1}{2}}a\right]}{\psi(\chi+\psi)}d\chi\,d\psi = \frac{1}{8}e^{-4pa/c}. \tag{5.2.27}$$

Using this result we have found $Q_+^{(0,2)}$ and hence the near crack tip behaviour:

$$\sigma_{zy}^{(0,2)}(x,a,t) \sim L^{-1}\left[\overline{F}(p)\left(\frac{2c}{p}\right)^{\frac{1}{2}}\frac{3}{8}e^{-4ap/c}(-2\pi x)^{-\frac{1}{2}}\right]. \tag{5.2.28}$$

The stress intensity factors are discussed in detail in Section 5.3.

Following our short aside, writing $Q_+^{(0,1)}(\xi,p)$ and $Q_-^{(0,1)}(0,p)$ explicitly, the stress field is

$$\sigma_{zy}^{(0,1)}(\xi,y,p) = -\overline{F}(p)\frac{\gamma_-(\xi,p)}{\gamma_-(0,p)}\left[\frac{1}{2\pi i}\int_{-\infty}^{\infty}\frac{e^{-2\gamma(\eta_1,p)a}}{i\eta_1(\eta_1-\xi)}d\eta_1\right]\left(e^{\gamma(y-a)}+e^{-\gamma(y+a)}\right). \tag{5.2.29}$$

In the present case we wish to invert a transformed field quantity that already contains an integration over the variable η_1. Following Harris (1980) we introduce Cagniard contours in both the ζ-plane, as described above, and the η_1-plane,

$$ct_1 = 2(\eta_1^2 + 1)^{\frac{1}{2}}a. \tag{5.2.30}$$

We shift the ζ- and η_1- integrations onto contours along which T and t_1 are real. The η_1 path is defined by

$$\eta_1^{\pm}(t_1) = \pm\left[\left(\frac{ct_1}{2a}\right)^2 - 1\right]^{\frac{1}{2}}, \quad \text{for } \frac{2a}{c} < t_1, \tag{5.2.31}$$

and the $\zeta_{1,2}(T)$ path employed in the first iteration is here expressed explicitly as

$$\zeta_{1,2}(T) = -\mathrm{i}\frac{cT}{r_{1,2}}\sin\theta_{1,2} + \left[\left(\frac{cT}{r_{1,2}}\right)^2 - 1\right]^{\frac{1}{2}}\cos\theta_{1,2}, \quad \text{for } \frac{r_{1,2}}{c} < T; \tag{5.2.32}$$

we have taken the branch of the path with positive square root.

The modified Cagniard method (Harris, 1980) relies on a change of order of integration and the result $t = t_1 + T$ to rewrite the integral in the usual Cagniard form. Then the time transform is of such a form that the inverse transform can be identified for any general loading, $F(t)$, in $0 < y < a$ as

$$\sigma_{zy}^{(0,1)}(x,y,t) = \int_0^t F(t-\tau)\frac{1}{2\pi^2}\left[H(\tau-(r_1+2a)/c)\int_{r_1/c}^{\tau-2a/c}\mathcal{G}^{(0,1)}(\zeta_1(T),\eta_1(\tau-T))\mathrm{d}T\right.$$
$$\left.+H(\tau-(r_2+2a)/c)\int_{r_2/c}^{\tau-2a/c}\mathcal{G}^{(0,1)}(\zeta_2(T),\eta_1(\tau-T))\mathrm{d}T\right]\mathrm{d}\tau, \tag{5.2.33}$$

where the function $\mathcal{G}^{(0,1)}$ is defined by

$$\mathcal{G}^{(0,1)}(\zeta(T),\eta_1(t_1)) = -\mathrm{Im}\left[\frac{\partial\zeta}{\partial T}\frac{\gamma_-(\zeta)}{\gamma_-(0)}\left(\frac{1}{\mathrm{i}\eta_1^+(\eta_1^+-\zeta)}\frac{\partial\eta_1^+}{\partial t_1} - \frac{1}{\mathrm{i}\eta_1^-(\eta_1^--\zeta)}\frac{\partial\eta_1^-}{\partial t_1}\right)\right]. \tag{5.2.34}$$

In Figure 5.2 the wavefield valid in time $0 < t < r_1 + 4a/c$, that is $\sigma_{zy} = \sigma_{zy}^{(0,0)} + \sigma_{zy}^{(0,1)} + O(e^{-6\gamma a}, e^{-2\gamma(b-a)})$, until the second wave reflected by the surface returns to the crack, is shown in $x < 0$ and $0 < y < a$ for the loading $F(t) = \delta(t)$. In addition in $x > 0$ waves parallel to the crack faces are generated and proceed to be reflected by the surface in a similar way. Further reflections are mainly distinguished by the singularity associated with their arrival; this is partly seen in Figure 5.2.

As x/a is increased the sharp peak that occurs close to the wave arrival is smoothed out. When $y/a \ll 1$ and the observer is near to the interface then the amplitude of the reflected wave is increased and arrives near to the wave incident on the surface. Similarly

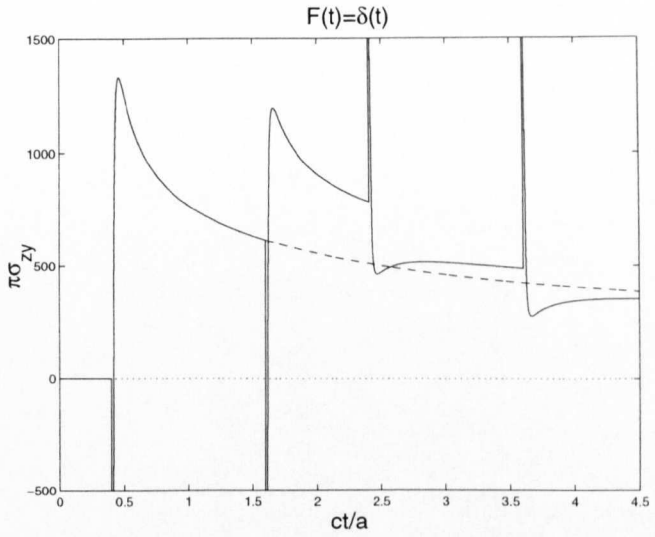

Figure 5.2. The stress field for the case $F(t) = \delta(t)$ is shown by the solid line for $t < r_1 + 4a/c$ for $x = -0.04$, $y = 1.2$, and $a = 2$. The dotted line shows the equivalent result in an infinite body. There is a one-sided singularity associated with each cylindrical wavefront, and these can be seen in the figure.

when $y/a \sim 1$ and the observer is now near the crack then the diffracted wave and the wave incident on the crack arrive close together. These observations may be predicted by physical considerations.

So far the formulation and analysis has been for a crack in a semi-infinite half space $0 < y < \infty$; that is the crack is unaware that it is in a layer above a half space. In $0 < y < a$ the effect of the interface between the fluid layer and half space is first seen after time $t > r_1 + 2(b-a)/c$, that is, after the first wave reflected by the interface returns to the crack. The previous analysis and Figure 5.2 have assumed that $b - a > 2a$. This problem is considered briefly in the next section.

5.2.2.3. *Reloading by the interface*

In this case the Wiener–Hopf equation of exponential order $\exp[-2\gamma\ (b-a)]$ is given by (5.2.14) as

$$-2\left[\sigma_-^{(1,0)} + \mathcal{R}\left(\sigma_-^{(0,0)} + \Upsilon_+\right) e^{-2\gamma(\xi,p)(b-a)}\right] = \mu\gamma U_+^{(1,0)}. \tag{5.2.35}$$

Following the approach used in Section (5.2.2.2) we define $Q^{(1,0)}(\xi,p) = e^{-2\gamma(b-a)}$, split this into $\pm$-functions, $Q^{(1,0)} = Q_+^{(1,0)} + Q_-^{(1,0)}$, and extract the expressions for the unknown transforms

$$\begin{aligned} \sigma_-^{(1,0)} &= -\frac{\Upsilon_+\gamma_-(\xi,p)}{\gamma_-(0,p)}\mathcal{R}\left[Q_-^{(1,0)}(\xi,p) - Q_-^{(1,0)}(0,p)\right] \\ \text{and}\quad U_+^{(1,0)} &= -\frac{2\Upsilon_+}{\mu\gamma_+(\xi,p)\gamma_-(0,p)}\mathcal{R}\left[Q_+^{(1,0)}(\xi,p) + Q_-^{(1,0)}(0,p)\right]. \end{aligned} \tag{5.2.36}$$

(i) Stress intensity factors for $O(e^{-2\gamma(b-a)})$

In the same way that we evaluated the near crack tip behaviour in Section 5.2.2.2 in this case it may be extracted by evaluating $Q_-^{(1,0)}(0,p)$. Again using integral 3.7166 in Gradshteyn & Ryzhik (1980) (or evenness of function $Q^{(1,0)}(\xi,p)$) we find that

$$\sigma_{zy}^{(1,0)}(x,a,t) \sim -L^{-1}\left[\overline{F}(p)\left(\frac{c}{p\pi}\right)^{\frac{1}{2}}\frac{1}{2}\Delta e^{-2p(b-a)/c}(-x)^{-\frac{1}{2}}\right] \tag{5.2.37}$$

where $\Delta = (\mu c^{(h)} - \mu^{(h)}c)/(\mu^{(h)}c + \mu c^{(h)})$ and this result is consistent with the solution in (5.2.7). Out of completeness, the stress field in this case is

$$\sigma_{zy}^{(1,0)}(\xi,y,p) = -\frac{\Upsilon_+\gamma_-(\xi,p)}{\gamma_-(0,p)}\mathcal{R}\left[Q_-^{(1,0)}(\xi,p) - Q_-^{(1,0)}(0,p)\right]\left(e^{\gamma(y-a)} - e^{-\gamma(y+a)}\right); \tag{5.2.38}$$

this expression may be routinely inverted using the Cagniard-de Hoop method described in Section 5.2.2.2.

5.2.3. *Comment on fundamental solutions*

An alternative approach of generating an iterative solution is to treat as separate problems the loading of the crack, the surface of the elastic layer, and the interface between the elastic layer and the underlying half space; each of these successive iterations takes the negative of the previous solution as its loading. This can be shown to be completely consistent with the analysis presented in the earlier sections and it has been used as a consistency check; the details are not included. Physically, this approach has some advantages over the iterative scheme used in Section 5.2.2 and in Haak & Kooij (1996); in a more complicated coupled situation, such as the in-plane scattering problem of Section 5.5 where identifying the wavefields is less elementary, it is sometimes more convenient to adopt this separation approach and extract each scattered field independently.

5.3. Invariant integral

In this section attention is given to the field near the crack tip, which is completely characterised by the stress intensity factor, and in particular we focus upon non-homogeneous materials. The results for the near crack tip stresses for a homogeneous material have been presented in Sections 5.2.1 and 5.2.2; these results are also recovered using a path-independent integral. The basic method was first used in dynamic elasticity by Nilsson (1973). Following the approach initiated in elastostatics by Eshelby (1970), a Lagrangian is deduced in the Laplace transform domain in each material such that the Euler-Lagrange

relations recover the governing equations; the Lagrangian L, is

$$L = -\frac{1}{2}\left(\overline{\sigma}_{zj}\overline{u}_{z,j} + \rho p^2 \overline{u}_z \overline{u}_z\right). \tag{5.3.1}$$

As this is defined in the transform domain this Lagrangian does not have an immediately obvious physical interpretation. When we consider the layer-half space configuration of Section 5.2 this Lagrangian is defined in $0 < y < b$ and we also need to define a Lagrangian $L^{(h)}$ in $b < y$ by (5.3.1) with appropriate changes to material parameters. Initially we treat a non-homogeneous half space and only need the first of these Lagrangians. The corresponding pseudo energy momentum tensor is

$$P_{lj} = \frac{\partial L}{\partial \overline{u}_{z,j}}\overline{u}_{z,l} - L\delta_{lj}; \tag{5.3.2}$$

again, unlike Eshelby's elastostatic energy momentum tensor the pseudo energy momentum tensor in the Laplace transform domain does not have any obvious physical interpretation. The Lagrangian does not depend explicitly on the space variable, and thus the integral, F_1, defined as

$$F_1 = \int_S P_{1j} n_j dS \tag{5.3.3}$$

is zero provided that the path S does not enclose any singularities; n_j is the unit vector normal to S (Figure 5.3). This integral is analogous to Rice's J-integral (Rice, 1968) but is now also incorporating dynamic effects and the non-homogeneous material variation.

For anti-plane strain the stress intensity factor can be rapidly evaluated using this invariant integral. Although it is important to realise that the technique only works neatly as a computational tool for spatially constant applied stress or displacement boundary conditions along the horizontal (x) boundaries and for material variation in the y coordinate. In the more complicated situations found for in-plane elastic problems mode-coupling occurs at the crack tip and the method often leads to a representation for the sum of the squares of the stress intensity factors (Section 5.5). In static elasticity theory this all reduces to the energy release rate, however we are currently in the Laplace transform domain and it is unclear what physical significance, if any, these results have apart from neatly capturing the transformed stress intensity factors.

In essence the information near to the crack tip can be obtained by studying the far away field; we evaluate the integrals far from the crack tip and relate this to the stress intensity factors. The behaviour near the tip of the crack is determined in terms of cylindrical polar coordinates (r, θ) centred on the tip with $\theta = 0$ ahead of the crack and the elastic material is in $-\pi \leq \theta \leq \pi$; the stress is locally $\overline{\sigma}_{zy} \sim \overline{K}(p)/(2\pi r)^{-1/2}\cos(\theta/2)$, and the related displacements are given in Appendix 5.C. The coefficient $\overline{K}(p)$, the stress

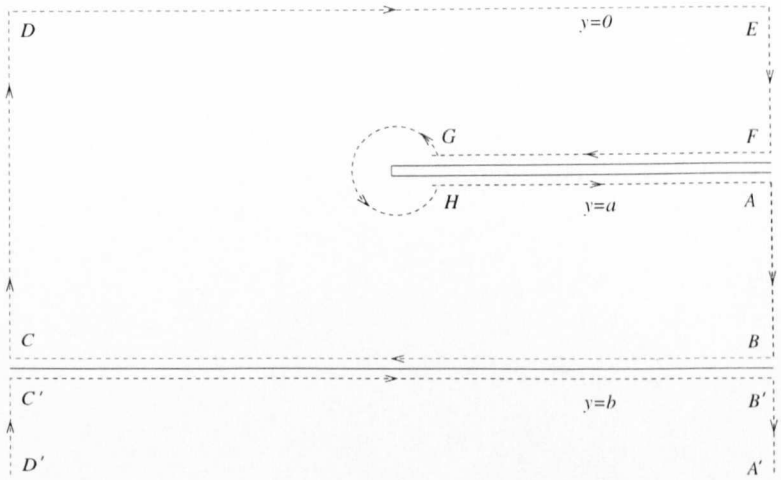

Figure 5.3. The path, S, required for the application of the invariant integral in Section 5.3.

intensity factor (in Laplace transform space), characterises the near tip singularity and here we shall extract it using the invariant integral. These near tip fields are used to evaluate the integral around GH (in path S).

To evaluate the stresses we note that the derivatives with respect to x tend to zero as $x \to \pm\infty$, see Nilsson (1973). As a result the governing equations become

$$\frac{\mathrm{d}\overline{\sigma}_{zy}}{\mathrm{d}y} = p^2\rho(y)\overline{u}_z \text{ where } \overline{\sigma}_{zy} = \mu(y)\frac{\mathrm{d}\overline{u}_z}{\mathrm{d}y}. \tag{5.3.4}$$

When treating spatial variations in the shear modulus or density the application of the Wiener–Hopf method or numerical methods, to a semi-infinite crack problem, may be difficult. Currently much of the non-homogeneous fracture mechanics literature concentrates upon static situations, for example, Ergüven & Gross (1999). However, the path independent integral is ideally suited to dealing with special situations (spatially constant loadings and material variation normal to the crack), and in fact the method gives results for any variation of modulus. Some related static problems are considered for general $\mu(y)$ in Atkinson & Craster (1995b).

For analytic simplicity, as in Atkinson (1975), we make the further restriction that the density ρ varies in such a way that $\rho(y)/\mu(y) = c^{-1}$ a constant. Introducing the substitution $v(y) = \mu^{1/2}(y)u_z(y)$ then enables the governing equation (5.3.4) to be rewritten as

$$\frac{\mathrm{d}^2 v}{\mathrm{d}y^2} = v\left[\frac{p^2}{c^2} + a(y)\right] \text{ where } a(y) = \frac{1}{4\mu}\left[2\frac{\mathrm{d}^2\mu}{\mathrm{d}y^2} - \frac{1}{\mu}\left(\frac{\mathrm{d}\mu}{\mathrm{d}y}\right)^2\right]. \tag{5.3.5}$$

We now make some specific choices for the material variation. The first choice, $\mu(y) = \alpha^2\exp(2\beta y)$, where β, α are constant, has the advantage that the resulting function $a(y)$ is equal to β^2. This results in the simple solutions $v(y) = A\exp(-\Gamma y) + B\exp(\Gamma y)$, where

$\Gamma = [(p/c)^2 + \beta^2]^{1/2}$, for constants A, B determined by the boundary conditions on $y = 0$ and $y = a$.

We now proceed to relate the integral around the crack tip to the known integrals around the body; the only integrals that contribute to the invariant are along EF, AB, (and $B'A'$ in an elastic layer), and the points at F and A along the crack faces. Performing the integrals we obtain

$$\overline{K}(p) = \overline{F}(p)\left[\frac{\Gamma(\sinh\Gamma a + \cosh\Gamma a)}{(\Gamma+\beta)(\Gamma\cosh\Gamma a - \beta\sinh\Gamma a)} + \frac{\beta}{2(\Gamma\cosh\Gamma a - \beta\sinh\Gamma a)^2}\right]^{\frac{1}{2}}. \quad (5.3.6)$$

In addition the solution in an infinite body with this modulus variation is found as

$$\overline{K}(p) = \overline{F}(p)\left(\frac{2\Gamma}{\Gamma^2 - \beta^2}\right)^{\frac{1}{2}}, \quad (5.3.7)$$

and we may invert the Laplace transform exactly, for example when $F(t) = H(t)$:

$$K(t) = 2\left(\frac{2c}{\pi}\right)^{\frac{1}{2}} t^{\frac{1}{2}}\,{}_1\mathrm{F}_2\left(-\frac{1}{4}; \frac{3}{4}, \frac{5}{4}; -\frac{1}{4}\beta^2c^2t^2\right), \quad (5.3.8)$$

where ${}_1\mathrm{F}_2$ is the generalised hypergeometric function. It is perhaps surprising that the stress intensity factor is independent of the choice of α for this specific loading. A related choice of $\mu(y)$ in an infinite body is $\alpha^2\exp(2\beta|y - a|)$ which is a symmetric modulus variation about the fracture plane, in this case the Laplace transform of the stress intensity factor for an infinite body is

$$\overline{K}(p) = \overline{F}(p)\left(\frac{2}{\Gamma+\beta}\right)^{\frac{1}{2}}. \quad (5.3.9)$$

The stress intensity factors are shown in Figure 5.4; the Laplace transform (5.3.6) is inverted using an adaptation of the Fourier inversion routine described in Atkinson & Craster (1992a). The rather striking changes in the stress intensity factor in Figure 5.4(a) are caused by the waves reflected from the surface reloading the crack; the reflections occur at equal values of ct/a since we have taken c to be constant. The result in an infinite body (5.3.8) is shown by the dashed line in this figure. Figure 5.4(b) compares this with the variation chosen to be symmetric about the crack and with $\beta = 0$ (constant μ).

Increasing the value of β in these results leads to larger peaks in the stress intensity factor as the material has decreasing rigidity in the layer between the crack and the surface; the net effect of which is to concentrate the wave energy near the surface and leads to a stronger reloading effect for waves reflected from the surface. The sharp reloadings become less evident, and this can already be partly seen in Figure 5.4(a).

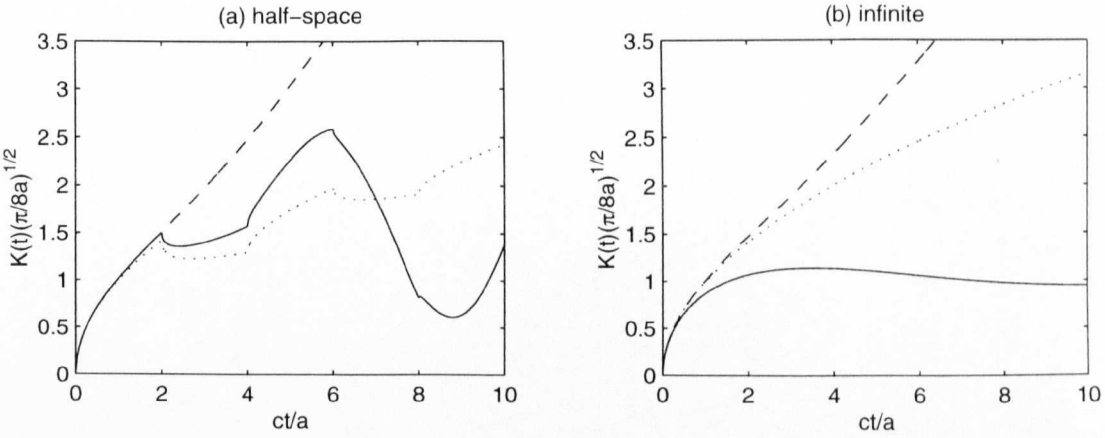

Figure 5.4. The stress intensity factor rescaled as $K(t)(\pi/8a)^{\frac{1}{2}}$ versus non-dimensional time ct/a. In panel (a) we show the intensity factors for a subsurface crack with parameters $\beta = 0.5/a$, $\alpha = 1$ for the modulus variation $\mu(y) = \alpha^2 \exp(2\beta y)$ (—); the corresponding result for a crack in an infinite material is shown by (– –). For comparison the dotted line $(\cdots)$ shows the results for constant μ. In panel (b) the effect of a modulus variation, symmetric about the fracture plane, on the intensity factor is shown for a crack in an infinite material with $\beta = 0.4/a$, $\alpha = 1$ and modulus variation $\mu(y) = \alpha^2 \exp(2\beta|y - a|)$ (—), and otherwise as in panel (a).

In contrast in Figure 5.4(b) the symmetric modulus variation is crudely speaking analogous to a rigid boundary above and below the crack, we no longer obtain the sharp peaks due to the distinct reloadings caused by the reflections from a rigid boundary, but rather we get a continual and gradual reloading which causes the stress intensity factor to level off to a constant value $\beta^{-1/2}$.

To contrast with the earlier choice of an exponential variation we now choose a variation with algebraic growth, $\mu(y) = (\beta y + \alpha)^2$, which is also analytically rewarding. The stress intensity factor is shown in Figure 5.5; this modulus variation leads to $a(y) = 0$ so that the solutions take the form $v(y) = A\sinh(py/c) + B\cosh(py/c)$. In general for $\mu(y) = (\beta y + \alpha)^n$ then $a(y) = n(n-2)\beta^2/4(\beta y + \alpha)^2$ and, therefore, in general we have to proceed numerically; this is not the case for $n = 2$. Evaluating the integrals and relating the non-zero contribution to the integral around the crack tip gives

$$\overline{K}(p) = \overline{F}(p)\left(\frac{p}{c}\right)^{\frac{1}{2}}\left[\frac{\sinh(pa/c) + \cosh(pa/c)}{\left(\frac{p}{c} + \frac{\beta}{(\beta a + \alpha)}\right)\left(\frac{p}{c}\cosh(pa/c) - \frac{\beta}{(\beta a + \alpha)}\sinh(pa/c)\right)}\right]^{\frac{1}{2}}. \tag{5.3.10}$$

where the solution in an infinite body is

$$\overline{K}(p) = \overline{F}(p)\left(\frac{2p}{c}\right)^{\frac{1}{2}}\left[\frac{p^2}{c^2} - \frac{\beta^2}{(\beta a + \alpha)^2}\right]^{-\frac{1}{2}}, \tag{5.3.11}$$

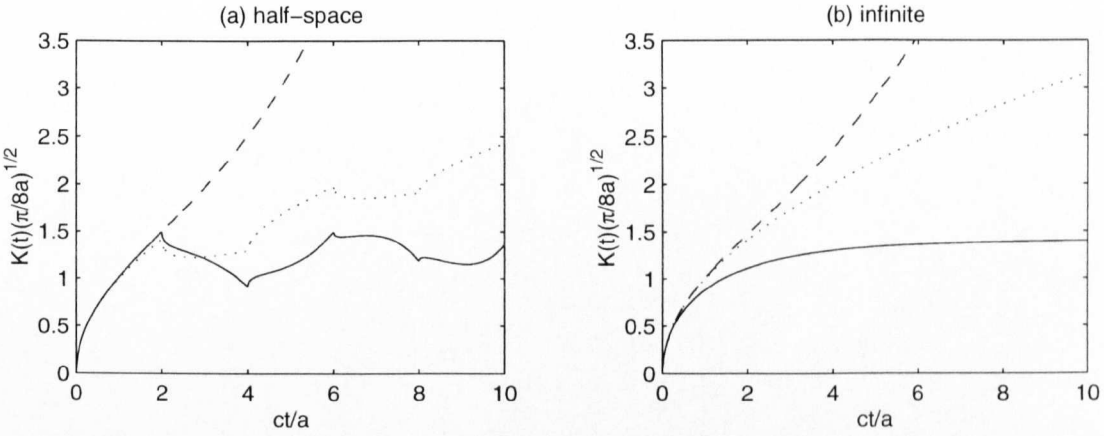

Figure 5.5. The stress intensity factor rescaled as $K(t)(\pi/8a)^{\frac{1}{2}}$ versus non-dimensional time ct/a. The modulus variation is $\mu(y) = (\beta y + \alpha)^2$ and the presentation of the results is as in Figure 5.4.

and the Laplace transform (5.3.11) is inverted for $F(t) = H(t)$ as

$$K(t) = 2\left(\frac{2c}{\pi}\right)^{\frac{1}{2}} t^{\frac{1}{2}}{}_1\mathrm{F}_2\left(\frac{1}{2}; \frac{5}{4}, \frac{3}{4}; \frac{1}{4}\frac{\beta^2 c^2}{(\beta a + \alpha)^2}t^2\right). \tag{5.3.12}$$

A related result in an infinite material for a symmetric variation about the crack $\mu(y) = (\beta|y - a| + \alpha)^2$ is $\overline{K}(p) = \overline{F}(p)[2/(p/c + \beta/\alpha)]^{1/2}$. Under Heaviside loading $F(t) = H(t)$ this can be inverted to give an error function $K(t) = (2\alpha/\beta)^{1/2}\mathrm{erf}\sqrt{\beta ct/\alpha}$. A comparison between this result and the result in an infinite body (5.3.12) is made in Figure 5.5(b), the symmetric modulus variation which have increasing shear moduli as one moves away from the crack, have lower stress intensity factors as waves return to reload the crack from the regions with higher rigidity. In contrast to the symmetric exponential loading, the stress intensity factor approaches a constant value, $(2\alpha/\beta)^{1/2}$, monotonically from below.

These solutions provide useful benchmark examples upon which numerical solutions can be tested. In addition they demonstrate the effect of inhomogeneity can be to substantially amplify the stress intensity factors after successive reflections reload the crack. Note that when $\beta = 0$ in both the cases we have considered in detail then the shear modulus is constant, $\mu = \alpha^2$, and we just recover the stress intensity factor for a cracked half space. For small β (or y) then for both cases, provided $\alpha = 1$, we find $\mu(y) \sim 1 + 2\beta y$ and we are in a position to compare algebraic and exponential variations and as we might expect the exponential growth leads to a stronger response with more noticeable peaks.

We now return to the layer-half space configuration of Sections 5.2.1 and 5.2.2, we can generalise the stress intensity factor results we have already obtained by using the

invariant integral with a Lagrangian in the half-space and layer: For convenience assume that both the layer and half space are homogeneous, then applying the invariant around the contour shown in Figure 5.3 and evaluating the integrals along the sides of the strip, one deduces that

$$\overline{K}(p) = \overline{F}(p)\left(\frac{c}{p\cosh(pa/c)}\right)^{\frac{1}{2}}\left[\frac{\mu^{(h)}c\sinh(pb/c) + \mu c^{(h)}\cosh(pb/c)}{\mu^{(h)}c\cosh(p(b-a)/c) + \mu c^{(h)}\sinh(p(b-a)/c)}\right]^{\frac{1}{2}}. \tag{5.3.13}$$

Some representative numerical results are shown in Figure 5.6(a) where we have chosen some typical values for the two free parameters b/a and $\mu c^{(h)}/\mu^{(h)}c$.

As an aside, the treatment of a layered-inhomogeneous material may, in certain considerations, be approximated by the suitably adjusted treatment of an n-layered material. The full solution of the n-layered problem is an arduous algebraic task since we are required to solve continuity conditions at each interface, however, the invariant integral yields the stress intensity factors very rapidly by utilising simplified continuity conditions and only the integrals over the layers as $x \to \infty$. The following result is for two layers above a half space, but may be routinely extended to several layers. The elastic layer in $0 < y < b_1$ ($\equiv b$) is now labelled by a subscript 1, and the second elastic layer in $b_1 < y < b_2$ is denoted by 2; the half space is in $b_2 < y < \infty$,

$$\overline{K}(p) = \overline{F}(p)\left(\frac{c_1}{p\cosh(pa/c_1)}\right)^{\frac{1}{2}}\left[\frac{\mu_2 c_1\kappa_1\sinh(pb_1/c_1) + \mu_1 c_2\kappa_2\cosh(pb_1/c_1)}{\mu_2 c_1\kappa_1\cosh(p(b_1-a)/c_1) + \mu_1 c_2\kappa_2\sinh(p(b_1-a)/c_1)}\right]^{\frac{1}{2}} \tag{5.3.14}$$

where $\bar{b} = b_2 - b_1$,

$$\kappa_1 = \frac{\mu_2}{c_2}\sinh\left(\frac{p\bar{b}}{c_2}\right) + \frac{\mu^{(h)}}{c^{(h)}}\cosh\left(\frac{p\bar{b}}{c_2}\right), \quad \kappa_2 = \frac{\mu_2}{c_2}\cosh\left(\frac{p\bar{b}}{c_2}\right) + \frac{\mu^{(h)}}{c^{(h)}}\sinh\left(\frac{p\bar{b}}{c_2}\right). \tag{5.3.15}$$

In this case we have five free parameters, b_1/a and $\mu_1 c^{(h)}/\mu^{(h)}c_1$, as before, and also b_2/a, c_1/c_2, and $\mu_1 c_2/\mu_2 c_1$.

The Laplace transforms (5.3.13) and (5.3.14) are again inverted numerically for the case $F(t) = H(t)$, and the stress intensity factors are shown in Figures 5.6. The rather striking changes in the stress intensity factor are, again, caused by the waves reflected from the surface, and this time also interface(s), reloading the crack. In Figure 5.6(a) the solid and dashed lines show the stress intensity factor for positive and negative values of Δ (when $b-a > a$) respectively; the layer wavespeed is slower, or faster than the wavespeed in the half space. (The dotted line shows the result for $\Delta = 0$ that corresponds to a crack in an infinite homogeneous body; the case $\rho = \rho^{(h)}$ and $c = c^{(h)}$.) This illustrates how, if we fix the material properties of the layer, changes in the half space contribute to the near field. In each case the first reflection, that from the surface $y = 0$ is identical,

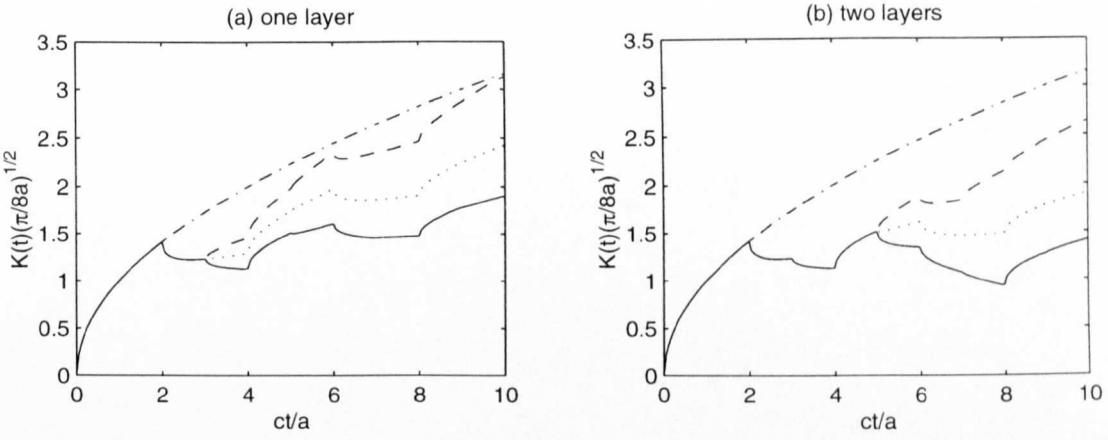

Figure 5.6. The stress intensity factor rescaled as $K(t)(\pi/8a)^{\frac{1}{2}}$ versus non-dimensional time ct/a under loading $F(t) = H(t)$. In panel (a) either the waves in the layer travel faster than those in the half space (—) (the specific parameter values are that $b/a = 5/2$, $\mu = \mu^{(h)}$, and $c = 2c^{(h)}$) or the wavespeed in the layer is slower than that of the half space (– –) ($\mu = \mu^{(h)}$ and $2c = c^{(h)}$). The dotted line (· · ·) shows the result when $\Delta = 0$ (the half space and layer parameters are identical) and the result for a crack in an infinite homogeneous body is given by the dotted-dashed line (· –). In panel (b) $b_1/a = 5/2$, $b_2/a = 4$, $c_1/c_2 = 2/3$, and $\mu_1 c^{(h)}/\mu^{(h)} c_1 = 1/2$. Either $\mu_1 c_2/\mu_2 c_1 = 4$ (—) or $\mu_1 c_2/\mu_2 c_1 = 1/4$ (– –) and the dotted line (· · ·) shows the result when materials 1 and 2 are identical. The semi-infinite result (in an infinite body) is given by the dotted-dashed line (· –).

thereafter if the wavespeed of the half space is slower less energy is reflected towards the crack and the stress intensity factor lies below the dotted (identical materials) line and vice-versa if the half space is faster then it lies above. It is worth noting, that changing the boundary conditions on the crack and on the free surface, may significantly alter the properties of the stress intensity factor.

Finally, in Figure 5.6(b), waves are reflected from the surface ($y = 0$) and the interfaces, $y = b_1$, $y = b_2$ at intervals $c_1 t/a = 2$, $c_1 t/a = 2(b_1/a - 1)$, and $c_1 t/a = 2(b_2/a - b_1/a)c_1/c_2 + 2(b_1/a - 1)$ respectively, and combine to generate reflections at all intervals of $c_1 t/a$. In the figure b_2/a and c_1/c_2 are chosen so that the lower layer first contributes at $c_1 t/a = 5$ and, for ease of presentation, so that the reflections occur at integer values of $c_1 t/a$. In this figure we compare the ratios of the moduli in the layers for a fixed ratio of their wavespeeds and demonstrate how similar energy distributions take place.

To explicitly identify the reflections that contribute to the near field expression (5.3.13) may be first rewritten as

$$\overline{K}(p) = \overline{F}(p)\left(\frac{2c}{p}\right)^{\frac{1}{2}}\left(1 + \Delta e^{-2pb/c}\right)^{\frac{1}{2}}\left(1 - \Delta e^{-2pb/c+2pa/c}\right)^{-\frac{1}{2}}\left(1 + e^{-2pa/c}\right)^{-\frac{1}{2}}, \tag{5.3.16}$$

where Δ is given following equation (5.2.37), and now by taking a Taylor expansion of each part in turn:

$$\overline{K}(p) = \overline{F}(p)\left(\frac{2c}{p}\right)^{\frac{1}{2}} \sum_{i=0}^{\infty} \frac{(2i)!\Delta^i e^{-2p(b-a)i/c}}{2^{2i}(i!)^2} \sum_{j=0}^{\infty} \frac{(-1)^{j+1}(2j)!\Delta^j e^{-2pbj/c}}{(2j-1)2^{2j}(j!)^2} \times \sum_{k=0}^{\infty} \frac{(-1)^k(2k)!e^{-2pak/c}}{2^{2k}(k!)^2}, \tag{5.3.17}$$

which corresponds to the value of K^2 that is deduced from equation (5.2.7). Note that the sign of K cannot be determined without additional information; nonetheless this provides a useful independent check upon one part of the analysis.

We can expand expression (5.3.17) in orders of the exponential, and this enables us to perform each Laplace inversion term by term to reconstruct the solution in real time explicitly as an infinite series; in particular when $F(t) = H(t)$ and $\Delta = 0$ we obtain

$$K(t) = 2\left(\frac{2c}{\pi}\right)^{\frac{1}{2}} \sum_{k=0}^{\infty} \frac{(-1)^k(2k)!(t-2ka/c)^{\frac{1}{2}}H(t-2ka/c)}{2^{2k}(k!)^2}. \tag{5.3.18}$$

This is consistent with the solution found numerically. In addition writing the first terms in the series,

$$K(t) = 2\left(\frac{2}{\pi}\right)^{\frac{1}{2}}\left[(ct)^{\frac{1}{2}}H(ct) - \frac{1}{2}(ct-2a)^{\frac{1}{2}}H(ct-2a) + \frac{3}{8}(ct-4a)^{\frac{1}{2}}H(ct-4a) + \cdots\right] \tag{5.3.19}$$

we can identify these with the coefficients of the singular fields found iteratively in equations (5.2.18,5.2.24,5.2.28) *i.e.* $K(t) = K^{(0,0)}(t) + K^{(0,1)}(t) + K^{(0,2)}(t) + \ldots$ In Figure 5.6(a), the dotted line for $K(t)$ in the interval $0 < ct < 6a$ is given by the first three terms in equation (5.3.19).

5.4. Weight functions

We have the explicit solution for our model problem of Section 5.2.1 when the stress loading on the crack is of a simple form; the purpose of this section is to identify the stress intensity factor for any loading using weight functions either for the exact solution, or for the iterative method. Other authors (*e.g* Thau & Lu, 1971) have utilised iterative methods for related problems; the weight function method carries across to those problems too.

The reciprocal theorem, assuming no body forces are present, is:

$$\int_S (\sigma^\star_{ij}u_i - \sigma_{ij}u^\star_i)n_j \mathrm{d}S = 0, \tag{5.4.1}$$

with n_j the outward pointing normal to the closed surface S. The starred and unstarred fields are independent solutions of the governing equations in the chosen geometry; the starred field is a specially chosen field typically more singular at the crack tip than the physically relevant solution and satisfying zero boundary conditions, that is, it is an eigensolution. Each term in (5.4.1) is taken to be in the Laplace transform domain.

For the eigensolution we consider stresses that are unphysically singular, $O(r^{-3/2})$, at the crack tip so that in Fourier transform space $\sigma_-^\star \sim O(\xi_-^{1/2})$ as $|\xi| \to \infty$:

$$\sigma_-^\star \sim 2^{\frac{1}{2}} \mathrm{i}_-^{-\frac{1}{2}} \xi_-^{\frac{1}{2}} K^\star, \quad U_+^\star \sim \frac{2^{\frac{3}{2}}}{\mu} \mathrm{i}_+^{\frac{1}{2}} \xi_+^{-\frac{1}{2}} K^\star. \tag{5.4.2}$$

In our exact formulation of Section 5.2.1 the functional equation for the eigensolutions is

$$\mu \frac{\gamma_+ U_+^\star}{\mathcal{Q}_+} = -\frac{\mathcal{Q}_- \sigma_-^\star}{\gamma_-} = C = 2\mathrm{i}_+^{\frac{1}{2}} K^\star; \tag{5.4.3}$$

C is an arbitrary constant which is determined by Liouville's theorem. The value of C is found by comparison with the known asymptotic form of the near crack tip stresses in (5.4.2). Using the reciprocal theorem along a contour applied around the crack tip; the contour then goes along the crack faces and is closed in a large circular arc at infinity,

$$\overline{K}^\star(p)\overline{K}(p) = \mu \int_0^\infty \sigma_{zy}(x, a, p) u_z^\star(x, a, p) \mathrm{d}x. \tag{5.4.4}$$

As $u_z^\star$ emerges from (5.4.3) we have a formula for $\overline{K}(p)$:

$$\overline{K}(p) = \frac{1}{2\pi} \mathrm{i}_+^{\frac{1}{2}} \int_0^\infty \sigma_{zy}(x, a, p) \int_{-\infty}^\infty \frac{\mathcal{Q}_+ e^{-\mathrm{i}\xi x}}{\gamma_+} \mathrm{d}\xi \, \mathrm{d}x. \tag{5.4.5}$$

The application of this formula to the full solution involving product splits of $\mathcal{Q}$ is not a trivial calculation. None the less one can do so and recover the general formula found earlier (5.2.9).

We can again proceed in an iterative manner and as a first step this reduces to

$$\frac{\mu}{2^{\frac{1}{2}}} \gamma_+ U_+^{\star(0,0)} = -2^{\frac{1}{2}} \frac{\sigma_-^{\star(0,0)}}{\gamma_-} = C = 2\mathrm{i}_+^{\frac{1}{2}} K^\star; \tag{5.4.6}$$

the formula for the stress intensity factor in this case is given by

$$\overline{K}^{(0,0)}(p) = \frac{1}{2\pi} (2\mathrm{i})_+^{\frac{1}{2}} \int_0^\infty \sigma_{zy}(x, a, p) \int_{-\infty}^\infty \frac{e^{-\mathrm{i}\xi x}}{\gamma_+} \mathrm{d}\xi \, \mathrm{d}x \tag{5.4.7}$$

The particular (Heaviside) loading chosen in the earlier analysis may be recovered using the Fourier transform results given in Appendix 5.A; namely $\overline{K}^{(0,0)} = \overline{F}(p)(2c/p)^{1/2}$. The point of the weight function is that having obtained the solution once for a specific

loading, we can utilise the same method to generate eigensolutions; the primary effort in any solution is the factorisation of the 'kernel' function Q. We now choose a loading that is no longer 'uniform' along the crack faces, for instance an exponential loading like $\sigma_{zy} = F(t)\exp(-\lambda x)$, that decays with distance along the crack for positive λ, in which case

$$\overline{K}^{(0,0)}(p) = \overline{F}(p)\left(\frac{2}{p/c+\lambda}\right)^{\frac{1}{2}} \tag{5.4.8}$$

and when $F(t) = H(t)$ we can find $K^{(0,0)}(t) = (2/\lambda)^{1/2}\mathrm{erf}\sqrt{\lambda ct}$. The uniform loading treated in the previous sections is a special case of this for $\lambda = 0$ and we can recover the earlier stress intensity factors.

So far the results have effectively been for a crack in an infinite body; that is the crack is unaware of either the surface or the interface. Next the solutions we have just derived are used to drive the 'reloading' of the unphysically singular crack,

$$\frac{\mu}{2^{\frac{1}{2}}}\gamma_+ U_+^{\star(0,1)} + 2\mathrm{i}_+^{\frac{1}{2}} Q_+^{(0,1)} K^\star = -2^{\frac{1}{2}}\frac{\sigma_-^{\star(0,1)}}{\gamma_-} - 2\mathrm{i}_-^{\frac{1}{2}} Q_-^{(0,1)} K^\star = 0 \tag{5.4.9}$$

using $Q_\pm^{(0,1)} \sim O(1/\xi) \to 0$ as $|\xi| \to \infty$. At first sight it is unclear that the stress or displacement field has the correct *too* singular behaviour. However if, for instance, we consider the stresses, $\sigma^\star = \sigma^{\star(0,0)} + \sigma^{\star(0,1)} + \ldots$, then this expression is still $O(\xi^{1/2})$ and thus after inversion to the physical domain is still too singular. The stress intensity factor taking into account the first reflection can be found again from applying the reciprocal theorem, and is

$$\overline{K}^{(0,1)}(p) = -\frac{1}{2\pi}(2\mathrm{i})_+^{\frac{1}{2}}\int_0^\infty \sigma_{zy}(x,a,p)\int_{-\infty}^\infty Q_+^{(0,1)}\frac{e^{-\mathrm{i}\xi x}}{\gamma_+}\mathrm{d}\xi\,\mathrm{d}x; \tag{5.4.10}$$

this formula reduces to equation (5.2.24) under a Heaviside loading, making a change of order of integration and then capturing the residue at $\xi = 0$ by closing in the upper half plane.

For further illustration we again take an exponential loading, $\exp(-\lambda x)$ along the crack faces in which case

$$\overline{K}^{(0,1)}(p) = -\overline{F}(p)\left(\frac{2}{p/c+\lambda}\right)^{\frac{1}{2}}\frac{1}{2}e^{-2pa/c} \tag{5.4.11}$$

and whose inversion for $F(t) = H(t)$ is $K^{(0,1)}(t) = -1/2(2/\lambda)^{1/2}\mathrm{erf}\sqrt{\lambda(ct-2a)}H(ct-2a)$. In Figure 5.7 a comparison is made between a uniform and an illustrative non-uniform (exponential) loading for the stress intensity factor. As λ increases the loading decays more rapidly with distance from the crack tip, and the resultant effects on the crack tip stresses are reduced; this is reflected in the reduced stress intensity factor values.

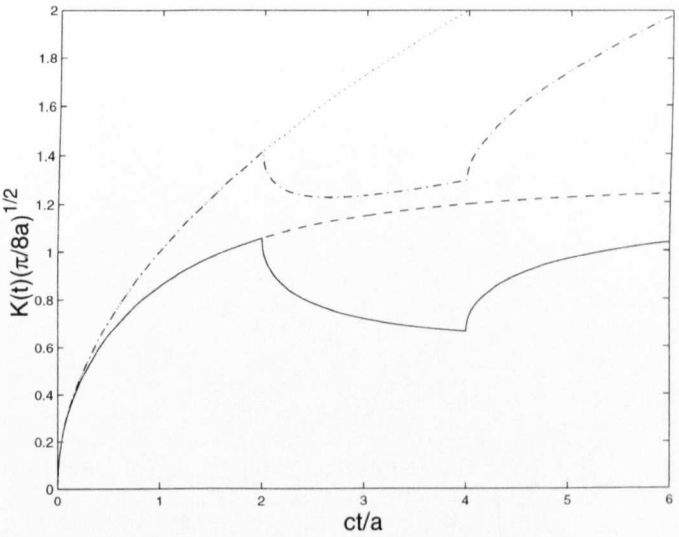

Figure 5.7. The stress intensity factor (—) for an exponential loading $\exp(-\lambda x)$ when $\lambda = 0.5/a$. This is compared with the intensity factor for a uniform loading (– ·); the equivalent solutions for a crack in an infinite body are also shown in each case.

The next solution is given in terms of $Q^{\star(0,2)} = Q_+^{(0,1)}Q^{(0,1)} = Q^{(0,2)} - Q_-^{(0,1)}(0)Q^{(0,1)}$, where $Q^{(0,2)}$ is given in equation (5.2.25),

$$\overline{K}^{(0,2)}(p) = -\frac{1}{2\pi}(2\mathrm{i})_+^{\frac{1}{2}} \int_0^\infty \sigma_{zy}(x,a,p) \int_{-\infty}^\infty Q_+^{\star(0,2)} \frac{e^{-\mathrm{i}\xi x}}{\gamma_+} \mathrm{d}\xi \; \mathrm{d}x; \tag{5.4.12}$$

for a uniform loading a single residue calculation again recovers our earlier solution. The stress intensity factor for an exponential loading after inversion ($F(t) = H(t)$), shown in Figure 5.7, is $K^{(0,2)}(t) = 3/8(2/\lambda)^{1/2}\mathrm{erf}\sqrt{\lambda(ct-4a)}H(ct-4a)$. The combination of formulae $K^{(0,0)}(t)+K^{(0,1)}(t)+K^{(0,2)}(t)+\ldots$ gives a representation for the stress intensity factors which is exact within the time window for which the last of these is valid. The weight function for waves reflected from the interface between the layer and half space also follows in a similar fashion.

5.5. In-plane loading

Despite the anti-plane problem of the previous sections being of some independent interest, we are usually more interested in the analogous in-plane problems which we outline in this section. Here there is little success to be had from tackling the problem head-on, unless one wishes to proceed numerically, because of the matrix Wiener–Hopf equation that emerges, however the iterative approach, that we have been advocating so far, is still applicable. There the application of the Cagniard–de Hoop method again avoids any potentially difficult or awkward evaluation of a Fourier and Laplace inverse integral that

typically contains a Wiener–Hopf split function. Although the continual reloading of the crack becomes progressively harder to describe.

5.5.1. *Formulation*

The problem is already complicated enough without an elastic layer so we only treat a single homogeneous medium with an overlying fluid: In the region $y > 0$ is an isotropic linear elastic material and in $y < 0$ is a compressible fluid. The responses of the two half spaces are coupled together through the continuity boundary conditions along the interface $y = 0$, these are discussed following (5.5.2). A Cartesian coordinate system is again adopted with x_1, x_2 corresponding to x, y.

The elastic material has (constant) Lamé constants λ, μ, and density ρ. The stresses σ_{ij} in the material are related to the displacements u_i via

$$\sigma_{ij} = \lambda \epsilon_{kk} \delta_{ij} + 2\mu \epsilon_{ij} \text{ where } \epsilon_{ij} = \frac{1}{2}(u_{i,j} + u_{j,i}), \tag{5.5.1}$$

the comma denoting differentiation with respect to x_i. The governing equations are the equilibrium equations $\sigma_{ij,j} = \rho \ddot{u}_i$, where the notation $\ddot{}$ denotes double partial differentiation with respect to time. In this case the analysis is most easily performed by utilising the displacement potentials ϕ and ψ where the displacement $\mathbf{u}$ is $\mathbf{u} = \nabla\phi + \nabla \times \psi\hat{z}$, where $\hat{z}$ is the unit vector in the z direction. The wave speeds c_d, c_s are defined in terms of the material parameters as $c_d^2 = \lambda + 2\mu/\rho$, $c_s^2 = \mu/\rho$. The subscripts d and s denote the variables associated with the dilatational and shear waves respectively.

The compressible fluid in $y < 0$ is effectively an elastic material that supports no shear stresses, thus $\sigma_{ij} = \lambda_f \epsilon_{kk} \delta_{ij}$, where the fluid has density ρ_f and compressional modulus λ_f. The governing equations are $\sigma_{ij,j} = \rho \ddot{u}_i$ again, and we introduce a third displacement potential χ such that the displacement $\mathbf{u}$ is $\mathbf{u} = \nabla\chi$. The compressional wavespeed of the fluid is defined as $c_o^2 = \lambda_f/\rho_f$.

It is useful to define the following γ-functions that occur throughout the analysis: $\gamma_q(\xi, p) = (\xi^2 + p^2/c_q^2)^{\frac{1}{2}}$ for $q = d, s, o, r$ where c_r is the Rayleigh wavespeed. A coupling parameter ϵ occurs throughout the analysis and is defined as $\epsilon = \rho_f c_o / \rho c_d$. The assumption that the compressional wavespeed of the fluid is less than the shear wavespeed of the solid is taken so that $c_d > c_s > c_o$.

The following boundary conditions are taken on $y = a$, ahead of, and on, the crack $x > 0$

$$[\![u_x]\!] = [\![u_y]\!] = 0, \ x < 0, \text{ and } \sigma_{xy} = 0, \ \sigma_{yy} = F(t)H(x), \ x > 0, \tag{5.5.2}$$

and the stresses σ_{xy}, σ_{yy} are continuous across $y = a$: $[\![\sigma_{xy}]\!] = [\![\sigma_{yy}]\!] = 0$. In addition,

the continuity boundary conditions

$$[\![\sigma_{yy}]\!] = 0, \ \sigma_{xy} = 0, \ [\![u_y]\!] = 0 \tag{5.5.3}$$

are taken on the interface $y = 0$, where the braces $[\![\ ]\!]$ denote the jump in a quantity across the interface; both the stresses σ_{yy} and the normal displacement u_y are continuous across $y = 0$. The fluid supports no shear stresses, thus $\sigma_{xy} = 0$ on $y = 0$. For convenience we have, again, taken a spatially uniform loading of the crack faces.

5.5.2. *Transform solution*

Once again we apply Fourier and Laplace transforms, this time with the following half-range Fourier transforms: the transform of the unknown stresses, σ_{xy} and σ_{yy}, on $y = a$, $x < 0$,

$$\tau_-(\xi, a, p) = \int_{-\infty}^{0} \overline{\sigma}_{xy}(x, a, p) e^{\mathrm{i}\xi x} \mathrm{d}x, \quad \sigma_-(\xi, a, p) = \int_{-\infty}^{0} \overline{\sigma}_{yy}(x, a, p) e^{\mathrm{i}\xi x} \mathrm{d}x, \tag{5.5.4}$$

and the transform of the unknown jump in the displacements, u_x and u_y, across $y = a$, $x > 0$,

$$\begin{aligned} V_+(\xi, a, p) &= \int_0^{\infty} \left[\overline{u}_x(x, a^+, p) - \overline{u}_x(x, a^-, p)\right] e^{\mathrm{i}\xi x} \mathrm{d}x, \\ U_+(\xi, a, p) &= \int_0^{\infty} \left[\overline{u}_y(x, a^+, p) - \overline{u}_y(x, a^-, p)\right] e^{\mathrm{i}\xi x} \mathrm{d}x. \end{aligned} \tag{5.5.5}$$

So far the problems treated have resulted in a single Wiener–Hopf equation like

$$P(\zeta)\Omega_+(\zeta) + Q(\zeta) = \Omega'_-(\zeta) \tag{5.5.6}$$

and in order to rearrange this equation into the standard Wiener–Hopf form we require only the product factorisation of $P(\zeta) = P_+(\zeta)P_-(\zeta)$. In the present case we obtain a coupled system of two Wiener–Hopf equations and to proceed we need a matrix factorisation. Unfortunately, the components of the matrix do not fall into any of the classes amenable to exact factorisation, and we require some numerical, approximate, or asymptotic method to provide it.

The resulting Wiener–Hopf matrix is

$$\begin{pmatrix} U_+ \\ V_+ \end{pmatrix} = \begin{pmatrix} a_{11} & a_{21} \\ a_{12} & a_{22} \end{pmatrix} \begin{pmatrix} \sigma_- + \Upsilon_+ \\ \tau_- \end{pmatrix} \quad \text{where } \Upsilon_+ = \frac{\overline{F}(p)}{\mathrm{i}\xi_+}; \tag{5.5.7}$$

much of the analysis is relegated to the appendices. The expressions for a_{ij} are lengthy and are omitted here; they are written in Appendix 5.D, alternatively we can use the language of generalised ray theory to piece together the matrix. It is our aim to split this equation into a series of elementary Wiener–Hopf equations each of exponential order

$\exp[-2m\gamma_d a - 2n\gamma_s a]$. This corresponds to m compressional and n shear reflections against the crack and the fluid-solid interface. The properties of a_{ij} in a Taylor expansion, required to formulate a series of Wiener–Hopf equations are given in Appendix 5.D.

An alternative to approaching the matrix problem head-on is to interpret each reloading separately (Section 2.3). If we do so here, and use displacement potentials, then the potentials that are generated by the first compressional wave that is reflected from the interface are

$$\phi = (\mathcal{R}_{pp}e^{\gamma_d a} + \mathcal{R}_{sp}e^{\gamma_s a})\, e^{-\gamma_d y}, \quad \psi = (\mathcal{R}_{ps}e^{\gamma_d a} + \mathcal{R}_{ss}e^{\gamma_s a})\, e^{-\gamma_s y}; \tag{5.5.8}$$

by iteratively constructing those potentials that arise after each reflection one can construct the matrix. In addition if one has, say, a crack obliquely aligned to an interface this method by-passes the necessity of constructing a formal Wiener–Hopf matrix equation. These potentials neatly encapsulate the reflection coefficients ($\mathcal{R}_{pp}$ *etc.*) that one expects to emerge from generalised ray theory and the same functional equations ultimately emerge; this is both algebraically and conceptually easier than dealing with a matrix.

The notation employed in Section 5.2 is again adopted; the arguments ξ and p are dropped whenever possible. The zero order Wiener–Hopf equation is equivalent to the symmetric problem for a semi-infinite crack in an infinite elastic material, and the corresponding anti-symmetric equation yields $\tau_-^{(0,0)} = 0$:

$$\mu R U_+^{(0,0)} = -2\gamma_d \frac{p^2}{c_s^2}(\sigma_-^{(0,0)} + \Upsilon_+), \quad \mu R V_+^{(0,0)} = -2\gamma_s \frac{p^2}{c_s^2}\tau_-^{(0,0)}. \tag{5.5.9}$$

In these formulae R is the standard Rayleigh function, $R(\xi,p) = (\xi^2+\gamma_s^2)^2 - 4\xi^2\gamma_d\gamma_s$. In order to rearrange the symmetric equation into the usual Wiener–Hopf form this function is split into the product of $\pm$-functions. To this end we introduce the function $\mathcal{L}(\xi,p) = \mathcal{L}_+(\xi,p)\mathcal{L}_-(\xi,p)$ defined by (5.B 5); the relevant details and expressions are given in Appendix 5.B. Rearranging this functional equation so that the left and right hand sides are analytic in the + and − regions (defined following (5.2.3)), equation (5.5.9) becomes

$$\begin{aligned} &-\frac{\gamma_{d-}(\xi,p)}{\gamma_{r-}^2(\xi,p)\mathcal{L}_-(\xi,p)}\sigma_-^{(0,0)} - \Upsilon_+\left[\frac{\gamma_{d-}(\xi,p)}{\gamma_{r-}^2(\xi,p)\mathcal{L}_-(\xi,p)} - \frac{\gamma_{d-}(0,p)}{\gamma_{r-}^2(0,p)\mathcal{L}_-(0,p)}\right] \\ &\quad = \mu\left(1-\frac{c_s^2}{c_d^2}\right)\frac{\gamma_{r+}^2(\xi,p)\mathcal{L}_+(\xi,p)}{\gamma_{d+}(\xi,p)}U_+^{(0,0)} + \Upsilon_+\frac{\gamma_{d-}(0,p)}{\gamma_{r-}^2(0,p)\mathcal{L}_-(0,p)} = \Sigma(\xi,p). \end{aligned} \tag{5.5.10}$$

Analytic continuation may now be invoked to determine that both sides of the functional equation are everywhere equal to the same analytic function, $\Sigma(\xi,p)$. The known edge conditions (that is, again, the stresses are $O(r^{-1/2})$ there) are now used to determine that

this function is in fact zero. This now yields the following expression for the unknown half-range transforms

$$\sigma_-^{(0,0)} = \Upsilon_+ \left[\frac{\gamma_{d-}(0,p)\gamma_{r-}^2(\xi,p)\mathcal{L}_-(\xi,p)}{\gamma_{d-}(\xi,p)\gamma_{r-}^2(0,p)\mathcal{L}_-(0,p)} - 1 \right]$$
$$\text{and } U_+^{(0,0)} = \Upsilon_+ \frac{\gamma_{d-}(0,p)\gamma_{d+}(\xi,p)}{\mu\gamma_{r-}^2(0,p)\gamma_{r+}^2(\xi,p)\mathcal{L}_-(0,p)\mathcal{L}_+(\xi,p)} \left(\frac{c_s^2}{c_d^2} - 1 \right)^{-1}, \tag{5.5.11}$$

where $\Upsilon_+ = \overline{F}(p)/\mathrm{i}\xi_+$.

The behaviour of the stresses near the crack tip may be extracted (using asymptotic results in Appendix 5.B) from (5.5.11) as $|\xi| \to \infty$, for $x < 0$:

$$\sigma_{yy}^{(0,0)}(x,a,t) \sim L^{-1}\left[\overline{F}(p) \left(\frac{c_s}{c_d} \right) \left[\frac{2\,(c_d^2 - c_s^2)}{p\pi c_d} \right]^{\frac{1}{2}} (-x)^{-\frac{1}{2}} \right], \quad \sigma_{xy}^{(0,0)}(x,a,t) \sim 0; \tag{5.5.12}$$

this result is checked using an invariant integral for the mode I and mode II stress intensity factors K_{I} and K_{II} in Section 5.5.3.

The Fourier and Laplace transform of the stress $\sigma_{yy}^{(0,0)}$ may be extracted from the expressions for $\sigma_-^{(0,0)}$ and the Cagniard–de Hoop method. In order to do this we need the six Cagniard paths that can be constructed from

$$c_d t = \gamma_q(\zeta)a \mp \gamma_q(\zeta)y + \mathrm{i}\zeta x, \text{ for } q = d,\ s \tag{5.5.13}$$

so that these paths place the inverse Fourier integrals in the form of a Laplace transform. This is almost equivalent to a generalised ray theory approach using the reflection and transmission coefficients given in Appendix 5.D. In the following we have introduced the rescaled γ-functions, $\gamma_q(\zeta) = (\zeta^2 + k_q)^{1/2}$ for $q = d,\ s,\ o,\ r$, where $k_d = 1$, $k_s = k = c_d/c_s$, $k_o = k' = c_d/c_o$, $k_r = c_d/c_r$. The explicit solution is

$$\begin{aligned}\sigma_{yy}^{(0,0)}(x,y,t) = \frac{1}{\pi}\mathrm{Re}\Bigg(& \left[\zeta_p^2 + \gamma_s^2(\zeta_p)\right]^2 \mathcal{Z}(\zeta_p)\frac{\mathrm{d}\zeta_p(t)}{\mathrm{d}t} - 4\zeta_s^2\gamma_s(\zeta_s)\gamma_d(\zeta_s)\mathcal{Z}(\zeta_s)\frac{\mathrm{d}\zeta_s(t)}{\mathrm{d}t} \\ & - 2\mathrm{i}\zeta_{ps}\gamma_s(\zeta_{ps})\left[\zeta_{ps}^2 + \gamma_s^2(\zeta_{ps})\right]\mathcal{R}_{ps}\mathcal{Z}(\zeta_{ps})\frac{\mathrm{d}\zeta_{ps}(t)}{\mathrm{d}t} \\ & + \left[\zeta_{pp}^2 + \gamma_s^2(\zeta_{pp})\right]^2 \mathcal{R}_{pp}\mathcal{Z}(\zeta_{pp})\frac{\mathrm{d}\zeta_{pp}(t)}{\mathrm{d}t} \\ & + 2\mathrm{i}\zeta_{sp}\gamma_d(\zeta_{sp})\left[\zeta_{sp}^2 + \gamma_s^2(\zeta_{sp})\right]\mathcal{R}_{sp}\mathcal{Z}(\zeta_{sp})\frac{\mathrm{d}\zeta_{sp}(t)}{\mathrm{d}t} \\ & + 4\zeta_{ss}^2\gamma_s(\zeta_{ss})\gamma_d(\zeta_{ss})\mathcal{R}_{ss}\mathcal{Z}(\zeta_{ss})\frac{\mathrm{d}\zeta_{ss}(t)}{\mathrm{d}t}\Bigg)\end{aligned} \tag{5.5.14}$$

where we have defined $\mathcal{Z}(\zeta)$ as

$$\mathcal{Z}(\zeta) = \frac{1}{\mathrm{i}\zeta_+ R(\zeta)}\left(\frac{\gamma_{d-}(0)\gamma_{r-}^2(\zeta)\mathcal{L}_-(\zeta)}{\gamma_{d-}(\zeta)\gamma_{r-}^2(0)\mathcal{L}_-(0)} \right). \tag{5.5.15}$$

5.5.2.1. *Reloading by the compressional wave*

In this section we consider the reloading of the crack by the compressional wave reflected by the interface. The same procedure may be followed, with some careful attention to the analysis, in extracting the successive Wiener–Hopf equations, to find both the compressional and shear wavefields up to the next arrival. For now we will *only* consider the first reloading of the crack, which for some practical purposes may be thought to be sufficient; further reloadings are briefly examined in Section 5.5.2.2. An interesting and unexpected result near the crack tip falls out of this analysis and is more rigorously explored in Section 5.5.3. In order to make use of the Wiener-Hopf equation of exponential order $\exp[-2\gamma_d a]$ we recall that $\tau_-^{(0,0)} = 0$ and therefore from the matrix (5.5.7), or using the displacement potentials (5.5.8),

$$\mu R U_+^{(1,0)} = -2\gamma_d \frac{p^2}{c_s^2}\left[\sigma_-^{(1,0)} - \frac{1}{2}\mathcal{R}_{pp}\left(1-\mathcal{R}_{pp}^N\right)e^{-2\gamma_d a}\left(\sigma_-^{(0,0)} + \Upsilon_+\right)\right]. \tag{5.5.16}$$

The coefficients $\mathcal{R}$ and $\mathcal{R}^N$ are related to the reflection coefficients for an incident P or S wave on an interface and a surface in the absence of the fluid respectively, and naturally occur in the equations. Their precise form is given in Appendix 5.D.

The corresponding 'anti-symmetric' Wiener–Hopf equation this times yields a non-zero $\tau_-^{(1,0)}$ (that we expect to contribute in the next iteration) from

$$\mu R V_+^{(1,0)} = -2\gamma_s \frac{p^2}{c_s^2}\left[\tau_-^{(1,0)} - \frac{1}{2}\mathcal{R}_{pp}\mathcal{R}_{ps}^N\left(\sigma_-^{(0,0)} + \Upsilon_+\right)\right]. \tag{5.5.17}$$

Our game plan now requires us to split equation (5.5.16) into the usual Wiener–Hopf form:

$$\begin{aligned} -\frac{\gamma_{d-}(\xi,p)}{\gamma_{r-}^2(\xi,p)\mathcal{L}_-(\xi,p)}\sigma_-^{(1,0)} - \Upsilon_+\Theta(\xi,p)\frac{\gamma_{d-}(0,p)}{\gamma_{r-}^2(0,p)\mathcal{L}_-(0,p)} \\ = \mu\left(1-\frac{c_s^2}{c_d^2}\right)\frac{\gamma_{r+}^2(\xi,p)\mathcal{L}_+(\xi,p)}{\gamma_{d+}(\xi,p)}U_+^{(1,0)}. \end{aligned} \tag{5.5.18}$$

We have taken in hand the sum split of $\Theta(\xi,p)$ into a + function and a − function:

$$\Theta(\xi,p) = -\frac{1}{2}\mathcal{R}_{pp}(1-\mathcal{R}_{pp}^N)e^{-2\gamma_d(\xi,p)a} = \Theta_+(\xi,p) + \Theta_-(\xi,p); \tag{5.5.19}$$

some consideration of the function reveals that $\Theta_+(\xi,p) = \Theta_-(-\xi,p)$ and therefore $2\Theta_\pm(0,p) = \Theta(0,p) = [(1-\epsilon)/(1+\epsilon)]e^{-2pa/c_d}$, which will be seen to be useful later. The resulting functional equation yields the unknown stress transform

$$\sigma_-^{(1,0)} = -\Upsilon_+\frac{\gamma_{d-}(0,p)\gamma_{r-}^2(\xi,p)\mathcal{L}_-(\xi,p)}{\gamma_{d-}(\xi,p)\gamma_{r-}^2(0,p)\mathcal{L}_-(0,p)}\left[\Theta_-(\xi,p) - \Theta_-(0,p)\right] \tag{5.5.20}$$

and we extract the stress intensity factor by employing asymptotic result $\Theta_-(\xi,p) \to O(1/\xi)$ as $\xi \to \infty$, *i.e.*

$$\sigma_{yy}^{(1,0)}(x,a,t) \sim L^{-1}\left[\overline{F}(p)\left(\frac{c_s}{c_d}\right)\left[\frac{2\left(c_d^2-c_s^2\right)}{p\pi c_d}\right]^{\frac{1}{2}}\Theta_-(0,p)(-x)^{-\frac{1}{2}}\right]; \tag{5.5.21}$$

where

$$\Theta_-(0,p) = \frac{1}{2\pi \mathrm{i}}\int_{-\infty+\mathrm{i}d}^{\infty+\mathrm{i}d}\frac{1}{2}\mathcal{R}_{pp}(1-\mathcal{R}_{pp}^N)e^{-2\gamma_d(u,p)a}\frac{\mathrm{d}u}{u} = \frac{1}{2}\frac{(1-\epsilon)}{(1+\epsilon)}e^{-2pa/c_d}; \tag{5.5.22}$$

d is some small, positive, real number. We may now use this result to find the mode I stress intensity factor, $\overline{K}_{\mathrm{I}}(p)$. In addition the mode II stress intensity factor may be found, in a similar manner, by first setting

$$\Phi(\xi,p) = -\frac{\gamma_{s-}}{2\gamma_{d-}}\mathcal{R}_{pp}\mathcal{R}_{ps}^N e^{-2\gamma_d(\xi,p)a} = \Phi_+(\xi,p)+\Phi_-(\xi,p). \tag{5.5.23}$$

The functional equation then yields

$$\tau_-^{(1,0)} = -\Upsilon_+\frac{\gamma_{d-}(0,p)\gamma_{r-}^2(\xi,p)L_-(\xi,p)}{\gamma_{s-}(\xi,p)\gamma_{r-}^2(0,p)L_-(0,p)}\left[\Phi_-(\xi,p)-\Phi_-(0,p)\right], \tag{5.5.24}$$

and we may extract the stress intensity factor utilising $\Phi_-(\xi,p) \sim O(1/\xi)$ as

$$\sigma_{xy}^{(1,0)}(x,a,t) \sim L^{-1}\left[\overline{F}(p)\left(\frac{c_s}{c_d}\right)\left[\frac{2\left(c_d^2-c_s^2\right)}{p\pi c_d}\right]^{\frac{1}{2}}\Phi_-(0,p)(-x)^{-\frac{1}{2}}\right], \tag{5.5.25}$$

where

$$\Phi_-(0,p) = \frac{1}{2\pi i}\int_{-\infty+\mathrm{i}d}^{\infty+\mathrm{i}d}\frac{\gamma_{s-}}{2\gamma_{d-}}\mathcal{R}_{pp}\mathcal{R}_{ps}^N e^{-2\gamma_d(u,p)a}\frac{\mathrm{d}u}{u} = 0, \tag{5.5.26}$$

as $\Phi(0,p) = \Phi_\pm(0,p) = 0$. As a consequence of this result the mode II stress intensity factor is zero, at least until the next wave reloads the crack; without the fluid loading and for a stationary crack a similar result is found by Tsai & Ma (1997). This is consistent with the invariant integral that we use in Section 5.5.3; there we conclude that the zero mode II intensity factor is a result of the specific stress loading we have taken on the crack faces.

We may pursue a modified Cagniard method again to explicitly determine the stress fields anywhere in the fluid or solid, using these results for unknown transforms and closely following the analysis in Section 5.2.2. Alternatively, as is this case here, we may further investigate the stress intensity factors. We have seen, when treating the anti-plane example, that this is often best achieved using an invariant integral. First, we briefly examine the effect near the crack tip, of some other waves reloading the crack using our iterative approach.

5.5.2.2. *Reloadings by other waves*

The crack is also reloaded by mode-converted and shear waves reflected by the interface whose contributions to the stress field may be found from the following functional equations:

- *SP* wave:

$$\begin{aligned}\mu R U_+^{(1,1)a} &= -2\gamma_d \frac{p^2}{c_s^2}\left[\sigma_-^{(1,1)a} - \frac{1}{2}\mathcal{R}_{ps}\mathcal{R}_{sp}^N e^{-\gamma_d a-\gamma_s a}\left(\sigma_-^{(0,0)}+\Upsilon_+\right)\right],\\ \mu R V_+^{(1,1)a} &= -2\gamma_s \frac{p^2}{c_s^2}\left[\tau_-^{(1,1)a} + \frac{1}{2}\mathcal{R}_{ps}\left(1+\mathcal{R}_{ss}^N\right)e^{-\gamma_d a-\gamma_s a}\left(\sigma_-^{(0,0)}+\Upsilon_+\right)\right];\end{aligned} \tag{5.5.27}$$

- *PS* wave:

$$\begin{aligned}\mu R U_+^{(1,1)b} &= -2\gamma_d \frac{p^2}{c_s^2}\left[\sigma_-^{(1,1)b} - \frac{1}{2}\mathcal{R}_{sp}\mathcal{R}_{ps}^N e^{-\gamma_d a-\gamma_s a}\left(\sigma_-^{(0,0)}+\Upsilon_+\right)\right],\\ \mu R V_+^{(1,1)b} &= -2\gamma_s \frac{p^2}{c_s^2}\left[\tau_-^{(1,1)b} - \frac{1}{2}\mathcal{R}_{ps}\left(1-\mathcal{R}_{ss}^N\right)e^{-\gamma_d a-\gamma_s a}\left(\sigma_-^{(0,0)}+\Upsilon_+\right)\right];\end{aligned} \tag{5.5.28}$$

- *SS* wave:

$$\begin{aligned}\mu R U_+^{(0,1)} &= -2\gamma_d \frac{p^2}{c_s^2}\left[\sigma_-^{(0,1)} + \frac{1}{2}\mathcal{R}_{ss}\left(1+\mathcal{R}_{ss}^N\right)e^{-2\gamma_s a}\left(\sigma_-^{(0,0)}+\Upsilon_+\right)\right],\\ \mu R V_+^{(0,1)} &= -2\gamma_s \frac{p^2}{c_s^2}\left[\tau_-^{(0,1)} - \frac{1}{2}\mathcal{R}_{ss}\mathcal{R}_{ps}^N e^{-2\gamma_s a}\left(\sigma_-^{(0,0)}+\Upsilon_+\right)\right].\end{aligned} \tag{5.5.29}$$

There are two mode-coverted waves (*SP* and *PS*) that reload the crack and some physical considerations are required to extract these equations separately from the matrix expansion (5.D 8–5.D 10) in Appendix 5.D. In each of these equations (5.5.27–5.5.29) the function to be split in order to make the correct combination of + and − functions is somewhat akin to Φ defined in equation (5.5.23) in that it is zero at the pole situated at $\xi_+ = 0_+$. Then, as in that case, some consideration of the the $\pm$-functions implies that they too are zero. Ultimately this means that both the mode I and mode II stress intensity factors are zero for each of these successive reloadings.

A more complete picture for the stress intensity factors is given in Section 5.5.3. That section suggests that we *only* expect to find a non-zero contribution near the crack tip from purely compressional reloadings on the crack. This multiply reflected wave becomes increasingly difficult to describe in our iterative language. However, there are simplifications that occur in the limit as $\xi \to \infty$ that we can take advantage of to find $\overline{K}_{\mathrm{I}}(p)$ directly. The functional equation in this case is

$$\begin{aligned}\mu R U_+^{(2,0)} = -2\gamma_d \frac{p^2}{c_s^2}\Big[&\sigma_-^{(2,0)} - \frac{1}{2}\mathcal{R}_{pp}\left(1-\mathcal{R}_{pp}^N\right)e^{-2\gamma_d a}\sigma_-^{(1,0)}\\ &- \frac{1}{2}\mathcal{R}_{pp}\mathcal{R}_{sp}^N e^{-2\gamma_s a}\tau_-^{(1,0)} - \frac{1}{2}\mathcal{R}_{pp}\mathcal{R}_{pp}^N\mathcal{R}_{pp}\left(1-\mathcal{R}_{pp}^N\right)e^{-4\gamma_d a}\left(\sigma_-^{(0,0)}+\Upsilon_+\right)\Big],\end{aligned} \tag{5.5.30}$$

so that the equality of a + and − function is ultimately given in terms of the sum split of Ψ:

$$\Psi(\xi,p) = \frac{1}{2}\mathcal{R}_{pp}\left(1-\mathcal{R}_{pp}^{N}\right)e^{-2\gamma_d a}\left[\Theta_-(\xi,p)-\Theta_-(0,p)\right]$$
$$+\frac{\gamma_{d-}}{2\gamma_{s-}}\mathcal{R}_{pp}\mathcal{R}_{sp}^{N}e^{-2\gamma_s a}\left[\Phi_-(\xi,p)-\Phi_-(0,p)\right]-\frac{1}{2}\mathcal{R}_{pp}\mathcal{R}_{pp}^{N}\mathcal{R}_{pp}\left(1-\mathcal{R}_{pp}^{N}\right)e^{-4\gamma_d a} \quad (5.5.31)$$
$$= \Psi_+(\xi,p)+\Psi_-(\xi,p);$$

the stress intensity factor is found by evaluating $\Psi_-(0,p) = I_\Psi + [\Theta_-(0,p)]^2$, the other pieces of Ψ do not contribute. The integral I_Ψ is found numerically:

$$I_\Psi = \frac{1}{2\pi \mathrm{i}}\int_{-\infty+\mathrm{i}d}^{\infty+\mathrm{i}d}\Theta(\eta,p)\Theta_-(\eta,p)\frac{\mathrm{d}\eta}{\eta} = \frac{1}{8}\left(\frac{1-\epsilon}{1+\epsilon}\right)^2 e^{-4pa/c_d}, \quad (5.5.32)$$

and this result gives the value of K_I, also found in the following section.

5.5.3. *Invariant integral*

In the previous section we observed that the mode II intensity factor for this specific loading is zero to $O(e^{-2\gamma_d a})$. This is perhaps unexpected and is verified in this section using an invariant integral, together with some extensions to non-homogeneous media. More general loadings, using a weight function, are not considered here but could be treated as in Section 5.4.

Following the approach used in Section 5.3 a Lagrangian is, this time, deduced in each half space (fluid and solid) such that the Euler–Lagrange relations recover the governing equations. In the elastic material the Lagrangian L is defined as

$$L = -\frac{1}{2}\left(\overline{\sigma}_{ij}\overline{u}_{i,j} + \rho p^2 \overline{u}_i\overline{u}_i\right) \quad (5.5.33)$$

and in the fluid half space $L^{(f)}$ is the same expression with superscripts (f) used to denote displacements and stresses in the fluid and ρ replaced by ρ_f. The pseudo energy momentum tensor P_{lj} is formed in the usual manner, *i.e.*

$$P_{lj} = \frac{\partial L}{\partial \overline{u}_{i,j}}\overline{u}_{i,l} - L\delta_{lj}. \quad (5.5.34)$$

This pseudo energy momentum tensor has $P_{lj,j} = 0$ so that the integrals defined by F_l are invariant. We should note, see Atkinson & Craster (1995a), that closing a contour around a crack tip gives a term involving $\overline{K}_\mathrm{I}^2(p) + \overline{K}_\mathrm{II}^2(p)$ and the physical significance of this result is not clear. Nevertheless, this is a valuable check on our, or further, numerical work. The designation I or II indicates the independent contribution due to crack extension in mode I or mode II.

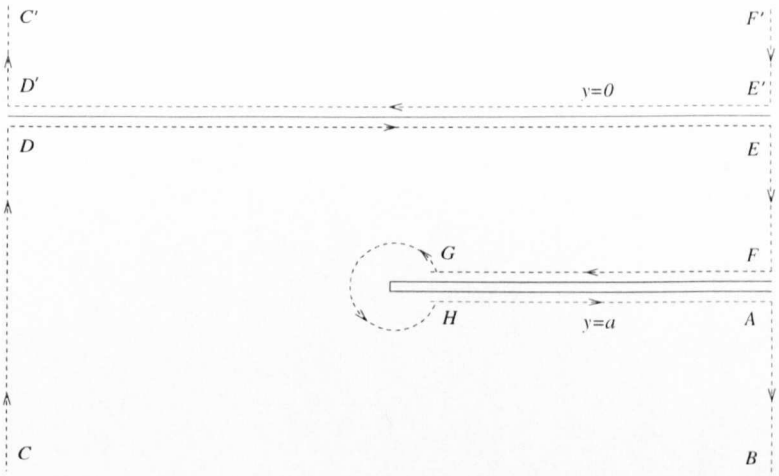

Figure 5.8. The path, S, required for the application of the invariant integral in Section 5.5.

The integrals defined as

$$F_1 = \int_S P_{1j} n_j \mathrm{d}S = \int_S -\overline{\sigma}_{ij} n_j \overline{u}_{i,1} + \frac{1}{2}\left(\overline{\sigma}_{ij}\overline{u}_{i,j} + \rho p^2 \overline{u}_i \overline{u}_i\right) n_1 \mathrm{d}S \tag{5.5.35}$$

are zero provided the path S (Figure 5.8) does not enclose any singularities and the path remains in the material for which P_{1j} is defined. In this formula n_j is the unit vector normal to S. The integral $F_1 = F_1 + F_1^{(f)}$ is considered around the contour shown in Figure 5.8; the paths in the fluid and the solid have the interface in common. Near edge fields are used to evaluate the integral around GH in Figure 5.8. The only other integrals that contribute to the invariant are along EF, AB, and $F'E'$ (in the fluid), and the points at F and A along the crack faces. The stresses at a crack tip are singular, *i.e.* $\sigma \sim KG(\theta) r^{-\frac{1}{2}}$ where r and θ are polar coordinates based at the crack tip; see Appendix 5.C.

Performing the integrals gives

$$\begin{aligned}\frac{(1-\nu^2)}{E}(\overline{K}_{\mathrm{I}}^2 + \overline{K}_{\mathrm{II}}^2)(p) + \int_{F'E'} \frac{1}{2}\left(\overline{\sigma}_{22}^{(f)}\overline{u}_{2,2}^{(f)} + \rho_f p^2 \overline{u}_2^{(f)}\overline{u}_2^{(f)}\right) \mathrm{d}y \\ + \int_{EF+AB} \frac{1}{2}\left(\overline{\sigma}_{22}\overline{u}_{2,2} + \rho p^2 \overline{u}_2 \overline{u}_2\right) \mathrm{d}y + \int_{FG+HA} \overline{\sigma}_{22}\overline{u}_{2,1} \mathrm{d}x = 0,\end{aligned} \tag{5.5.36}$$

where E is Young's modulus and ν is the Poisson's ratio; E and ν are related to the shear modulus μ and the wavespeeds c_d, c_s by $(1-\nu^2)/E = c_d^2/4\mu(c_d^2 - c_s^2)$. When we evaluate the integrals we obtain

$$\frac{(1-\nu^2)}{E}\left[\overline{K}_{\mathrm{I}}^2(p) + \overline{K}_{\mathrm{II}}^2(p)\right] = \frac{\overline{F}^2(p)}{p}\frac{1}{2\rho c_d}(\epsilon+1)\frac{\left(\cosh\dfrac{pa}{c_d} + \sinh\dfrac{pa}{c_d}\right)}{\left(\epsilon\cosh\dfrac{pa}{c_d} + \sinh\dfrac{pa}{c_d}\right)}. \tag{5.5.37}$$

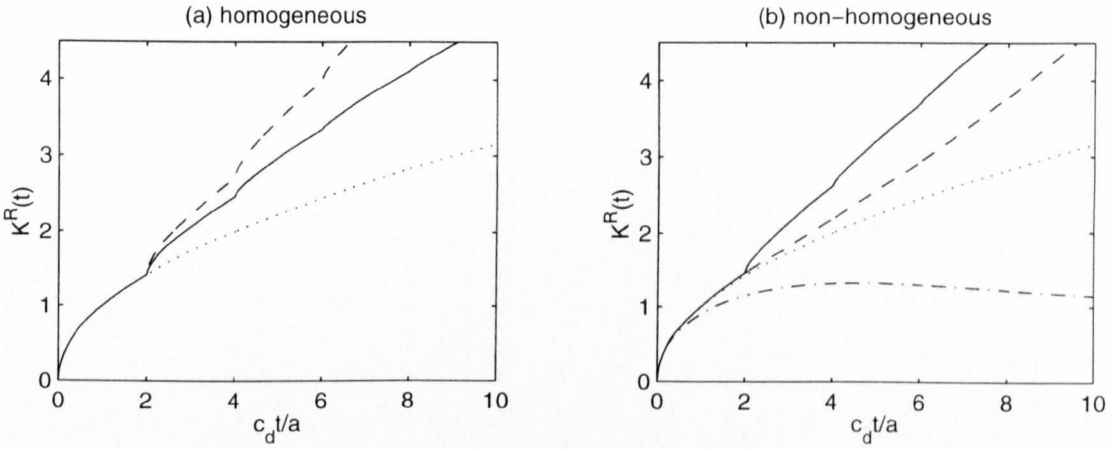

Figure 5.9. The stress intensity factor $(c_s/c_d)(1-c_s^2/c_d^2)^{1/2}K^R(t) = [K_{\rm I}^2(t)+K_{\rm II}^2(t)]^{1/2}(\pi/16a)^{1/2}$ versus non-dimensional time c_dt/a under loading $F(t) = H(t)$. In panel (a) we compare the two cases of moderate, $\epsilon = 0.2$ (—), and zero, $\epsilon = 0$ (– –), fluid loading on the stress intensity factor for a subsurface crack lying in a homogeneous elastic material; the corresponding result for a crack in an infinite elastic material is given by the dotted line $(\cdots)$. In panel (b) we show equation (5.5.40) by the solid line (—) when $\beta = 0.3/a$, $\beta_0 = 0.1c_d/c_oa$, and $\epsilon = \lambda_{f0}c_d/(\lambda_0+2\mu_0)c_o = 0.2$. The results in an infinite body are also compared for this inhomogeneity (– –) and replacing the y dependence of each parameter by $|y-a|$ to make it symmetric about the crack (– ·); the dotted line is when the material is homogeneous as in panel (a).

The stress intensity factor in $0 < c_dt/a < 2$ is the first term in the expansion,

$$\overline{K}_{\rm I}(p) = 2\overline{F}(p)\left(\frac{c_s}{c_d}\right)\left(\frac{c_d^2-c_s^2}{pc_d}\right)^{\frac{1}{2}}\left[1+\frac{1}{2}\left(\frac{1-\epsilon}{1+\epsilon}\right)e^{-2pa/c_d}+\frac{3}{8}\left(\frac{1-\epsilon}{1+\epsilon}\right)^2 e^{-4pa/c_d}+\ldots\right]. \tag{5.5.38}$$

This result corresponds to the value of $K_{\rm I}$ that is deduced from (5.5.12). The second term is also consistent with (5.5.21). This provides a useful independent check upon one part of our analysis. It is noteworthy that these results are the same as those we would obtain if we had 'pre-fractured' the plane $y = a$, and therefore $\sigma_{xy} = 0$ for all x along $y = a$. In that case, one only extracts a mode I stress intensity factor $\overline{K}_{\rm I}$ using the invariant rather than the sum of the squares of both intensity factors. Apart from a term which comes from the time dependence of the crack loading, the result in (5.5.37) only includes the compressional wavespeed suggesting that no shear waves reload the crack in such a way as to induce singular shear stresses at the crack tip. Hence we conjecture that for the specific 'opening' loading on the crack then, in fact, $K_{\rm II}$ is zero for all time. Further inspection of the iterative scheme confirms this.

Similarly for a 'shearing' loading on the crack, like $\sigma_{yy} = 0$, $\sigma_{xy} = F(t)$ on $y = a$,

$x > 0$, then we find the combination of stress intensity factors to be

$$\frac{(1-\nu^2)}{E}\left[\overline{K}_{\rm I}^2(p)+\overline{K}_{\rm II}^2(p)\right]=\frac{\overline{F}^2(p)}{p}\frac{1}{2\rho c_s}\frac{\left(\cosh\dfrac{pa}{c_s}+\sinh\dfrac{pa}{c_s}\right)}{\sinh\dfrac{pa}{c_s}}. \tag{5.5.39}$$

and this time $K_{\rm I}$ is zero.

In Figure 5.9(a) we compare the stress intensity factors under moderate and zero fluid loading, and we can see that the effect of the fluid is to draw energy away leading to less reflected back towards the crack. In contrast to the anti-plane results in Figures 5.4, 5.6 which were for a crack beneath a rigid surface, the stress continuity conditions on the interface have reloaded the crack in such a way as to increase the stress intensity factor with each successive reloading.

The organisation of this section has primarily been to investigate the stress intensity factors of the previous section, and hence, a homogeneous cracked elastic half-space coupled to an overlying fluid. But there is nothing to stop us, bar some unpleasant algebra, from looking at non-homogeneous materials; for simple analytical results the moduli variations in the y direction are best given specific forms. For example, if we choose $\lambda(y)=\lambda_0 e^{2\beta y}$, $\mu(y)=\mu_0 e^{2\beta y}$, and $\lambda_f(y)=\lambda_{f0}e^{2\beta_f y}$ to vary in such a way that c_d, c_s, and c_o are all constant, then the square of the stress intensity factors is

$$\begin{aligned}&\frac{(1-\nu^2)}{E}\left[\overline{K}_{\rm I}^2(p)+\overline{K}_{\rm II}^2(p)\right]\\&=\frac{\overline{F}^2(p)}{2(\lambda+2\mu)(a)}\left[\frac{1}{(\Gamma_d+\beta)}-\left(\frac{(\beta+\mathcal{E}\Gamma_d)\sinh\Gamma_d a+\Gamma_d\cosh\Gamma_d a}{(\beta^2+\mathcal{E}\beta\Gamma_d-\Gamma_d^2)\sinh\Gamma_d a-\mathcal{E}\Gamma_d^2\cosh\Gamma_d a}\right)\right]\end{aligned} \tag{5.5.40}$$

where

$$\mathcal{E}=\frac{\lambda_{f0}(\Gamma_0-\beta_f)}{(\lambda_0+2\mu_0)\Gamma_d}\quad(=\epsilon\ \text{ when }\beta=\beta_f=0) \tag{5.5.41}$$

and we have defined $\Gamma_d=(p^2/c_d^2+\beta^2)$ and $\Gamma_0=(p^2/c_o^2+\beta_f^2)$. As in Section 5.3 if we now choose $\lambda(y)=\lambda_0 e^{2\beta|y-a|}$ and $\mu(y)=\mu_0 e^{2\beta|y-a|}$ in an infinite elastic body then we find for such a symmetric variation

$$\overline{K}_{\rm I}(p)=2\overline{F}(p)\left(\frac{c_s}{c_d}\right)\left[\frac{c_d^2-c_s^2}{(\Gamma_d+\beta)c_d^2}\right]^{\frac{1}{2}}. \tag{5.5.42}$$

This result (Figure 5.9(b)) again demonstrates how the effect of inhomogeneity can be to increase or decrease the stress intensity factors. In the latter case, when the material variation is such that the crack, in effect, appears to be within a strip bounded by rigid walls. It is worth noting that the special situation of a crack centred in a strip (Atkinson & Craster, 1992b) with either symmetric, or anti-symmetric, loadings applied to the strip walls is a special case, here the invariant extracts the stress intensity factor (and there is

now only one factor due to the complete symmetry or anti-symmetry of the problem) in a particularly neat and concise manner.

5.6. Conclusion

An efficient method based on both physical considerations and an iterative approach to the underlying Wiener–Hopf equation(s) for scattering by a crack is demonstrated in this study. In essence, the equation is broken into smaller pieces, using generalised ray theory, that capture the wavefield within a finite time window. Of course it is necessary to pose and solve a series of Wiener–Hopf equations, and this procedure can become progressively more involved.

To illustrate the scope of the method we have applied it to both anti-plane and in-plane loadings of a crack, and extracted the stress fields and the stress intensity factors. It is noted that for a specific class of in-plane loadings on the crack, namely a spatially constant pure 'opening' or 'shearing', there is no complementary 'shearing' or 'opening' piece of the stress intensity factors.

A second route taken in this chapter is to use an invariant integral to extract the stress intensity factors directly. This is, in part, an independent check on the results. It also permits some extensions to non-homogeneous media, where our other approach is less feasible. Some illustrative results are given and it is anticipated that the general methodology will carry over to problems of a harder nature. The effect of the inhomogeneity is, of course, dependent on the precise nature of the variation as one moves away from the crack, and we demonstrate some contrasting behaviour in the stress intensity factors dependent upon whether the modulus decreases or increases with distance away from the fracture plane.

Specifically, for either stress free or rigid boundary conditions the reloading on the crack faces reinforces the initial opening stress or it stifles the opening. The non-homogeneous moduli do this in a 'continuous' way rather than via the discrete reflections of a layered material.

References

Achenbach, J. D., 1973. *Wave Propagation in Elastic Solids*. Amsterdam, North-Holland.

Atkinson, C., 1975. Some results on crack propagation in media with spatially varying elastic moduli. *Int. J. Fracture* **21**, 619–628.

Atkinson, C., 1977. On quasi-static problems of cracks in a non-homogeneous elastic layer. *Acta Mech.* **26**, 103–113.

Atkinson, C. & Craster, R. V., 1992a. The application of invariant integrals in diffusive elastic solids. *Phil. Trans. R. Soc. Lond. A* **339**, 231–263.

Atkinson, C. & Craster, R. V., 1992b. Fracture in fully coupled dynamic thermoelasticity. *J. Mech. Phys. Solids* **40**, 1415–1432.

Atkinson, C. & Craster, R. V., 1995a. Invariant integrals, stress concentrations and energy release rates. In *Fracture; a topical encyclopedia of current knowledge dedicated to Alan Arnold Griffith*, ed. by C. Cherepanov, 496-517, Krieger, New York.

Atkinson, C. & Craster, R. V., 1995b. Theoretical aspects of fracture mechanics. *Prog. Aerospace Sci.* **31**, 1–83.

Bueckner, H. F., 1970. A novel principle for the computation of stress intensity factors. *J. Appl. Math. Mech. (ZAMM)* **50**, 529–546.

Cagniard, L., 1939. *Réflection et réfraction des ondes séismique progressives*. Gauthiers-Villars, Paris. Trans. and rev. by E. A. Flinn & C. H. Dix, 1962. *Reflection and refraction of progressive seismic waves.* McGraw-Hill, New York.

Choi, H. J., 1997. A periodic array of cracks in a functionally graded nonhomogeneous medium loaded under in-plane normal and shear. *Int. J. Fracture* **88**, 107–128.

Craster, R. V. & Atkinson, C., 1994. Mixed boundary value problems for non-homogeneous elastic materials. *Quart. J. Mech. Appl. Math.* **47**, 183–206.

de Hoop, A. T., 1960. A modification of Cagniard's method for solving seismic pulse problems. *Appl. sci. Res. B* **8**, 349–356.

Erdogan, F., 1983. Stress intensity factors. *J. Appl. Mech.* **50**, 992–1002.

Ergüven, M. E. & Gross, D., 1999. On the penny-shaped crack in inhomogeneous elastic materials under normal extension. *Int. J. Solids Structures* **36**, 1869–1882.

Eshelby, J. D., 1951. The force on an elastic singularity. *Phil. Trans. R. Soc. Lond. A* **244**, 87–112.

Eshelby, J. D., 1970. Energy relations and the energy-momentum tensor in continuum mechanics. In *Inelastic behaviour of solids*, ed. by M. F. Kanninen *et. al*, 77-115, McGraw-Hill, New York.

Freund, L. B., 1990. *Dynamic fracture mechanics*. Cambridge University Press.

Garvin, W. W., 1956. Exact transient solution of the buried line source problem. *Proc. R. Soc. Lond. A* **234**, 528–541.

Gradshteyn, I. S. & Ryzhik, I. M., 1980. *Table of integrals, series, and products (Corrected and enlarged edition)*. London: Academic Press.

Haak, K. F. I. & Kooij, B. J., 1996. Transient acoustic diffraction in a fluid layer. *Wave Motion* **23**, 139–164.

Harris, J. G., 1980. Diffraction of a crack by a cylindrical longitudinal pulse. *J. Appl. Math. Phys. (ZAMP)* **31**, 367–381.

Hudson, J. A., 1980. *The excitation and propagation of elastic waves*. Cambridge University Press.

Kooij, B. J. & Quak, D., 1988. Three-dimensional scattering of impulsive acoustic waves by a semi-infinite crack in the plane interface of a half-space and a layer. *J. Math. Phys.* **29**, 1712–1721.

Lamb, H., 1904. On the propagation of tremors over the surface of an elastic solid. *Phil. Trans. R. Soc. Lond. A* **203**, 1–42.

Miklowitz, J., 1978. *The theory of elastic waves and waveguides*. North-Holland.

Nilsson, F., 1973. A path-independent integral for transient crack problems. *Int. J. Solids Struct.* **9**, 1107–1115.

Noble, B., 1958. *Methods based on the Wiener-Hopf technique*. Pergamon Press.

Rice, J. R., 1968. A path independent integral and the approximate analysis of strain concentration by notches and cracks. *J. Appl. Mech.* **35**, 379–386.

Thau, A. & Lu, T. H., 1971. Transient stress intensity factors for a finite crack in an elastic solid caused by a dilatational wave. *Int. J. Solids Structures* **7**, 731–750.

Tsai, C. H. & Ma, C. C., 1992. Transient analysis of a semi-infinite crack subjected to dynamic concentrated forces. *J. Appl. Mech.* **59**, 804–811.

Tsai, C. H. & Ma, C. C., 1993. The stress intensity factor of a subsurface inclined crack subjected to dynamic impact loading. *Int. J. Solids Structures* **30**, 2163–2175.

Tsai, C. H. & Ma, C. C., 1997. Theoretical transient analysis of the interaction between a dynamically propagating in-plane crack and traction-free boundaries. *J. Appl. Mech.* **64**, 819–827.

Appendix 5.A. Fourier transform results

If F denotes the Fourier transform operator, then

$$F^{-1}\left(\frac{1}{\xi_+^{n+1/2}}\right) = \frac{(x)^{n-1/2}H(x)}{\mathrm{i}_+^{n+1/2}\Gamma(n+1/2)}, \tag{5.A 1}$$

where n is an integer, and $\Gamma(z)$ is the Gamma function defined to be

$$\Gamma(n+1) = \int_0^\infty t^n e^{-t}\mathrm{d}t. \tag{5.A 2}$$

Appendix 5.B. Product splits

In Section 5.2.1 we have taken in hand the the product split of $Q(\xi,p)$ (see equation (5.2.5)). This function is split into + and − functions that are analytic and non-zero in the upper and lower complex ξ-planes: $Q(\xi,p) = Q_+(\xi,p)Q_-(\xi,p)$,

$$\log Q_-(\xi,p) = -\frac{1}{2\pi\mathrm{i}}\int_{-\infty+\mathrm{i}d}^{\infty+\mathrm{i}d}\frac{\log Q(\eta,p)}{\eta-\xi}\mathrm{d}\eta \quad \text{and} \quad \log Q_+(\xi,p) = \frac{1}{2\pi\mathrm{i}}\int_{-\infty-\mathrm{i}d}^{\infty-\mathrm{i}d}\frac{\log Q(\eta,p)}{\eta-\xi}\mathrm{d}\eta \tag{5.B 1}$$

for $-d < \mathrm{Im}(\xi) < d$, where d is some small, positive, real number. It is adequate, in most cases, to compute this product split numerically, and this is most easily performed using quadratures.

There is a useful limit as $b \to \infty$ that permits some explicit formulae to be derived. In this case, the function to be split into a product of $\pm$-functions is $Q^*(\xi,p) = e^{\gamma(\xi,p)a}/\cosh(\gamma(\xi,p)a)$, and

these be constructed analytically. The factorisation can be achieved by considering separately the factorisations of $e^{-\gamma a}$ and $\cosh \gamma a$, and has the familiar form, Noble (1958),

$$\frac{1}{Q_+^\star}(\xi,p) = e^{-\chi(\xi,p)-\psi_+(\xi,p)} \prod_{n=0}^{\infty} \left[(1+p^2 a_{n-\frac{1}{2}}^2 c^{-2})^{\frac{1}{2}} - \mathrm{i}\xi a_{n-\frac{1}{2}}\right] e^{\mathrm{i}\xi a_{n-\frac{1}{2}}} \tag{5.B 2}$$

where $a_{n-\frac{1}{2}} = a/(n-\frac{1}{2})\pi$, $Q_-^\star(\xi,p) = Q_+^\star(-\xi,p)$ and

$$\psi_+(\xi,p) = \frac{a}{\pi}\left(\xi^2 + \frac{p^2}{c^2}\right)^{\frac{1}{2}} \cos^{-1}\left(-\mathrm{i}\frac{\xi c}{p}\right), \quad \psi_-(\xi,p) = \psi_+(-\xi,p). \tag{5.B 3}$$

In equation (5.B 2) $\chi(\xi,p)$ is an arbitrary function chosen so that $Q_+^\star$ and $Q_-^\star$ have polynomial behaviour at infinity. Thus, using well known properties of the gamma function we choose

$$\chi(\xi,p) = -\mathrm{i}\frac{\xi a}{\pi}\left[1-\gamma+\log\left(-\mathrm{i}\frac{\pi c}{2ap}\right)\right] + \frac{\xi a}{2}, \tag{5.B 4}$$

where in (5.B 4) γ is Euler's constant. In practice, we can avoid these splits be using the modified Cagniard method.

The Wiener–Hopf method in Section 5.5 requires the product split of the Rayleigh function, $R(\zeta)$, suitably rescaled. To split this Rayleigh function first consider a new function $\mathcal{L}(\zeta)$ (that appears in Section 5.5),

$$\mathcal{L}(\zeta) = \frac{(2\zeta^2+k^2)^2 - 4\zeta^2(\zeta^2+1)^{\frac{1}{2}}(\zeta^2+k^2)^{\frac{1}{2}}}{2(k^2-1)(\zeta^2+k_r^2)}; \tag{5.B 5}$$

the product splits for $R(\zeta)$ follow directly from those of $\mathcal{L}(\zeta)$: $\mathcal{L}(\zeta) = \mathcal{L}_+(\zeta)\mathcal{L}_-(\zeta)$. By introducing the branch cuts $\mathrm{Re}(\zeta) = 0$, $1 < |\mathrm{Im}(\zeta)| < k$, $\mathcal{L}(\zeta)$ is made analytic everywhere in this cut ζ plane. The following asymptotic property is useful: in the limit as $|\zeta| \to \infty$, $\mathcal{L}(\zeta) \to 1 + O(\zeta^{-2})$. These properties of $\mathcal{L}(\zeta)$ make the logarithmic function $\log \mathcal{L}(\zeta)$ analytic everywhere in the same cut ζ plane as $\mathcal{L}(\zeta)$ and ensures that the Cauchy integrals converge. Using Cauchy's theorem $\mathcal{L}_-(\zeta)$ is determined explicitly as

$$\log \mathcal{L}_-(\zeta) = -\frac{1}{\pi}\int_1^k \tan^{-1}\left[\frac{4\tau^2(\tau^2-1)^{\frac{1}{2}}(k^2-\tau^2)^{\frac{1}{2}}}{(k^2-2\tau^2)^2}\right]\frac{\mathrm{d}\tau}{\tau+\mathrm{i}\zeta}, \tag{5.B 6}$$

where $\mathcal{L}_+(\zeta) = \mathcal{L}_-(-\zeta)$ and the branch of the inverse tangent is chosen so that $0 \le \tan^{-1}\phi \le \pi/2$. Some further asymptotic properties of $\mathcal{L}_+(\zeta)$ are useful when we come to consider the stress intensity factors: as $|\zeta| \to \infty$ then $\mathcal{L}_+(\zeta) \to 1$, and $\mathcal{L}_+(0) = k^2/[2^{\frac{1}{2}}(k^2-1)^{\frac{1}{2}}k_r]$. Then we have

$$R_-(\zeta) = 2^{\frac{1}{2}}(k^2-1)^{\frac{1}{2}}\gamma_{r-}^2(\xi,p)\mathcal{L}_-(\xi,p); \tag{5.B 7}$$

a rescaling by $\xi = p\zeta/c$ and $k = c_d/c_s$ is required in the main text.

In more general diffraction problems the kernel function is split similar to the above fundamental procedure, although often explicit formulae are not forthcoming.

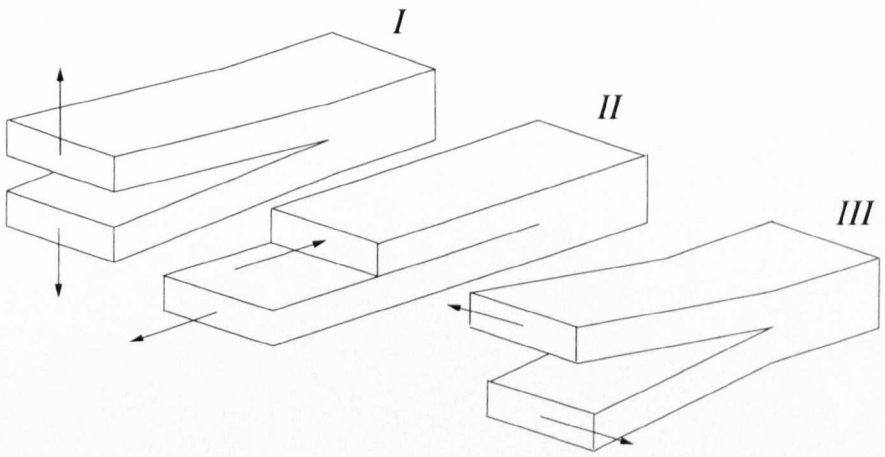

Figure 5.10. An illustration of the three types of crack opening modes: pure opening I, in-plane shearing II, and anti-plane shearing III (Erdogan, 1983).

Appendix 5.C. Near crack fields

The relations between the stresses, σ_{ij}, and displacements, u_j, are defined for anti-plane and in-plane in equations (5.2.1) and (5.5.1) respectively. One of the most important results that we extract concerns the stress intensity factors and this arises as the stresses at a crack tip are singular, *i.e.*

$$\sigma \sim KG(\theta)r^{-\frac{1}{2}} \tag{5.C 1}$$

where r and θ are polar coordinates based at the crack tip. The stress intensity factor characterises the interaction between the applied stress field and the crack tip. The following results are standard for isotropic bodies in plane strain (Atkinson & Craster, 1995b) where $\kappa = 3 - 4\nu$ (plane strain), and are illustrated in Figure 5.10.

- Mode I

$$\left.\begin{matrix}\sigma_{xx}\\ \sigma_{xy}\\ \sigma_{yy}\end{matrix}\right\} = \frac{K_{\mathrm{I}}}{(2\pi r)^{\frac{1}{2}}}\cos\frac{\theta}{2}\begin{Bmatrix}1-\sin\frac{\theta}{2}\sin\frac{3\theta}{2}\\ \sin\frac{\theta}{2}\cos\frac{3\theta}{2}\\ 1+\sin\frac{\theta}{2}\sin\frac{3\theta}{2}\end{Bmatrix}, \tag{5.C 2}$$

$$\left.\begin{matrix}u_x\\ u_y\end{matrix}\right\} = \frac{K_{\mathrm{I}}}{2\mu(2\pi)^{\frac{1}{2}}}r^{\frac{1}{2}}\begin{Bmatrix}\cos\frac{\theta}{2}\left(\kappa-1+2\sin^2\frac{\theta}{2}\right)\\ \sin\frac{\theta}{2}\left(\kappa+1-2\cos^2\frac{\theta}{2}\right)\end{Bmatrix}, \tag{5.C 3}$$

- Mode II

$$\left.\begin{matrix}\sigma_{xx}\\ \sigma_{xy}\\ \sigma_{yy}\end{matrix}\right\} = \frac{K_{\mathrm{II}}}{(2\pi r)^{\frac{1}{2}}}\begin{Bmatrix}1-\sin\frac{\theta}{2}\left(2+\cos\frac{\theta}{2}\cos\frac{3\theta}{2}\right)\\ \cos\frac{\theta}{2}\left(1-\sin\frac{\theta}{2}\sin\frac{3\theta}{2}\right)\\ \sin\frac{\theta}{2}\cos\frac{\theta}{2}\cos\frac{3\theta}{2}\end{Bmatrix}, \tag{5.C 4}$$

$$\left.\begin{matrix} u_x \\ u_y \end{matrix}\right\} = \frac{K_{\mathrm{II}}}{2\mu(2\pi)^{\frac{1}{2}}} r^{\frac{1}{2}} \begin{cases} \sin\frac{\theta}{2}\left(\kappa + 1 + 2\cos^2\frac{\theta}{2}\right) \\ -\cos\frac{\theta}{2}\left(\kappa - 1 - 2\sin^2\frac{\theta}{2}\right) \end{cases}, \tag{5.C 5}$$

- Mode III

$$\left.\begin{matrix} \sigma_{xz} \\ \sigma_{yz} \end{matrix}\right\} = \frac{K_{\mathrm{III}}}{(2\pi r)^{\frac{1}{2}}} \begin{cases} -\sin\frac{\theta}{2} \\ \cos\frac{\theta}{2} \end{cases}, \tag{5.C 6}$$

$$u_z = \frac{2K_{\mathrm{III}}}{\mu(2\pi)^{\frac{1}{2}}} r^{\frac{1}{2}} \sin\frac{\theta}{2}. \tag{5.C 7}$$

Appendix 5.D. Reflection coefficients and Wiener-Hopf notation

In this first part to this appendix the coefficients $\mathcal{R}$ and $\mathcal{R}^N$ are related to the reflection coefficients for an incident P or S wave on an interface and a surface in the absence of the fluid respectively (the superscript N denotes no fluid). The subscripts on $\mathcal{R}$ and $\mathcal{R}^N$ follow the convention that the first denotes the type of incident wave and the second denotes the type of reflected wave.

There are related transmission coefficients, and coefficients given by incident waves from the fluid, but these are not required in the application considered in the text.

In the following the usual notation is used for the Rayleigh, $R(\xi)$, and Schölte, $S(\xi)$, functions and also their complements $r(\xi)$ and $s(\xi)$. The Laplace transform parameter, p, dependence has been omitted for ease of presentation.

- Incident P wave:

$$\mathcal{R}_{pp} = -\frac{s(\xi)}{S(\xi)}, \quad \mathcal{R}_{ps} = \frac{4\mathrm{i}\xi\gamma_d(\xi)[\xi^2 + \gamma_s^2(\xi)]}{S(\xi)}, \quad \mathcal{R}^N_{pp} = -\frac{r(\xi)}{R(\xi)}, \quad \mathcal{R}^N_{ps} = \frac{4\mathrm{i}\xi\gamma_d(\xi)[\xi^2 + \gamma_s^2(\xi)]}{R(\xi)}. \tag{5.D 1}$$

- Incident S wave:

$$\mathcal{R}_{sp} = -\frac{4\mathrm{i}\xi\gamma_s(\xi)[\xi^2 + \gamma_s^2(\xi)]}{S(\xi)}, \qquad \mathcal{R}_{ss} = -\frac{S(\xi) + 8\xi^2\gamma_s(\xi)\gamma_d(\xi)}{S(\xi)},$$
$$\mathcal{R}^N_{sp} = -\frac{4\mathrm{i}\xi\gamma_s(\xi)[\xi^2 + \gamma_s^2(\xi)]}{R(\xi)}, \qquad \mathcal{R}^N_{ss} = -\frac{r(\xi)}{R(\xi)}. \tag{5.D 2}$$

In Section 5.5 the problem reduces to the solution of a Wiener–Hopf matrix (5.5.7)

$$\begin{pmatrix} U_+ \\ V_+ \end{pmatrix} = \begin{pmatrix} a_{11} & a_{12} \\ a_{21} & a_{22} \end{pmatrix} \begin{pmatrix} \sigma_- + \Upsilon_+ \\ \tau_- \end{pmatrix}. \tag{5.D 3}$$

It is unfortunately the case that the matrix terms a_{ij} become rather ugly, and as noted in the text we can piece together the matrix in orders of the exponential using generalised ray theory. Alternatively we can deal with the matrix and perform a series of expansions. The latter route is taken here:

$$\mu a_{11} = -\gamma_d \frac{p^2}{c_s^2}\left[\frac{1}{R} + \frac{1}{\mathcal{K}}\left(S + s e^{-2\gamma_d a} - (S + 8\xi^2\gamma_s^2\gamma_d^2)e^{-2\gamma_s a} - (s - 8\xi^2\gamma_s\gamma_d)e^{-2(\gamma_d+\gamma_s)a}\right)\right] \tag{5.D 4}$$

where

$$\mathcal{K}=SR-sre^{-2\gamma_d a}-(S+8\xi^2\gamma_s^2\gamma_d^2)re^{-2\gamma_s a}+(s-8\xi^2\gamma_s\gamma_d)Re^{-2(\gamma_d+\gamma_s)a}+32\xi^2\gamma_s\gamma_d(\xi^2+\gamma_s^2)^2e^{-(\gamma_d+\gamma_s)a}. \tag{5.D 5}$$

Note that in the case of a pre-fractured crack where the boundary condition ahead of the crack is $\sigma_{xy} = 0$ so that the shear stresses are zero all along $y = a$, then the Wiener–Hopf equation (5.5.7) reduces to $U_+ = a_{11}(\sigma_- + \Upsilon_+)$. The remaining components are as follows:

$$\mu a_{12} = -\mu a_{21} = \mathrm{i}\xi\left[\frac{q_2}{R}-\frac{1}{\mathcal{K}}\left(q_2S-sq_1e^{-2\gamma_d a}-(S+8\xi^2\gamma_s\gamma_d)q_1e^{-2\gamma_s a}\right.\right. \\ \left.\left.+(s-8\xi^2\gamma_s\gamma_d)q_2e^{-2(\gamma_d+\gamma_s)a}+8\gamma_s\gamma_d(\gamma_s^2+\xi^2)(\gamma_2+3\xi^2)e^{-(\gamma_d+\gamma_s)a}\right)\right], \tag{5.D 6}$$

$$\mu a_{22}=-\gamma_s\frac{p^2}{c_s^2}\left[\frac{1}{R}+\frac{1}{\mathcal{K}}\left(S-se^{-2\gamma_d a}+(S+8\xi^2\gamma_s\gamma_d)e^{-2\gamma_s a}-(s-8\xi^2\gamma_s\gamma_d)e^{-2(\gamma_d+\gamma_s)a}\right)\right]; \tag{5.D 7}$$

we have introduced $q_1 = (\xi^2 + \gamma_s^2 + 2\gamma_s\gamma_d)$ and $q_2 = (\xi^2 + \gamma_s^2 - 2\gamma_s\gamma_d)$ for convenience.

The leading exponential terms required in the text and relevant to the present chapter are given by a Taylor's expansion. They are intricately connected with the reflection and transmission coefficients but this is, often, not transparent when each component is taken in turn.

$$\mu R a_{11} = -\gamma_d\frac{p^2}{c_s^2}\left\{2+\frac{s}{S}\left(1+\frac{r}{R}\right)e^{-2\gamma_d a}-\frac{S+8\xi^2\gamma_s\gamma_d}{S}\left(1-\frac{r}{R}\right)e^{-2\gamma_s a}\right. \\ +2\left(1+\frac{s}{S}\right)\left(1-\frac{r}{R}\right)e^{-(\gamma_d+\gamma_s)a} \\ +\frac{s^2r}{S^2R}\left(1+\frac{r}{R}\right)e^{-4\gamma_d a}-\frac{(S+8\xi^2\gamma_s\gamma_d)^2r}{S^2R}\left(1-\frac{r}{R}\right)e^{-4\gamma_s a} \\ \left.+O(e^{-(3\gamma_d+\gamma_s)a})+O(e^{-2(\gamma_d+\gamma_s)a})+O(e^{-(\gamma_d+3\gamma_s)a})\right\}, \tag{5.D 8}$$

$$\mu R^2 a_{12} = -\mu R^2 a_{21} = 4\mathrm{i}\xi\gamma_s\gamma_d(\xi^2+\gamma_s^2)\frac{p^2}{c_s^2}\left[\frac{s}{S}e^{-2\gamma_d a}+\frac{S+8\xi^2\gamma_s\gamma_d}{S}e^{-2\gamma_s a}\right. \\ -\frac{s+S+8\xi^2\gamma_s\gamma_d}{S}e^{-(\gamma_d+\gamma_s)a}+\frac{s^2r}{S^2R}e^{-4\gamma_d a}+\frac{(S+8\xi^2\gamma_s\gamma_d)^2r}{S^2R}e^{-4\gamma_s a} \\ \left.+O(e^{-(3\gamma_d+\gamma_s)a})+O(e^{-2(\gamma_d+\gamma_s)a})+O(e^{-(\gamma_d+3\gamma_s)a})\right], \tag{5.D 9}$$

$$\mu R a_{22} = -\gamma_s\frac{p^2}{c_s^2}\left\{2-\frac{s}{S}\left(1-\frac{r}{R}\right)e^{-2\gamma_d a}+\frac{S+8\xi^2\gamma_s\gamma_d}{S}\left(1+\frac{r}{R}\right)e^{-2\gamma_s a}\right. \\ +2\left(1+\frac{s}{S}\right)\left(1-\frac{r}{R}\right)e^{-(\gamma_d+\gamma_s)a} \\ -\frac{s^2r}{S^2R}\left(1-\frac{r}{R}\right)e^{-4\gamma_d a}+\frac{(S+8\xi^2\gamma_s\gamma_s)^2r}{S^2R}\left(1+\frac{r}{R}\right)e^{-4\gamma_s a} \\ \left.+O(e^{-(3\gamma_d+\gamma_s)a})+O(e^{-2(\gamma_d+\gamma_s)a})+O(e^{-(\gamma_d+3\gamma_s)a})\right\}. \tag{5.D 10}$$

Similarly the expressions for the stresses and displacements are recovered from an expansion in terms of the displacement potentials.

Chapter Six

Diffraction at plate junctions by flexural plate waves

6.1. Introduction

The scattering of structure-borne waves from material inhomogeneities is a key ingredient in sound generation by fluid-loaded structures: vibrational energy is often carried by flexural plate waves and significant acoustic energy can only be radiated into the fluid when the flexural waves scatter off structural changes. The diffraction of acoustic and structure-borne waves at plate junctions is particularly important in many engineering contexts. For example, in marine engineering there is interest in the acoustic fields of ships, submarines, and submerged structures such as pipelines. There are further examples in mechanical and nuclear engineering, as described by Crighton (1989).

One of the simplest ways to model sharp structural changes occurring at plate junctions is as material discontinuities or defects (Crighton, 1989; Junger & Feit, 1986). For defects, wave scattering can lead to some interesting physical effects, such as beam formation and resonance phenomena. For example, the problem of wave scattering from an isolated line defect, such as a rib, can be solved exactly in terms of a Fourier integral (Leppington, 1978; Howe, 1994b). Adding more ribs leads to the possibility of multiple scatterings and acoustic resonances (Leppington, 1976; Crighton & Innes, 1983). These responses can dominate the scattered acoustic field, and often occur in the limit of light or heavy fluid loading, where a single inhomogeneity can reflect an incoming flexural plate wave almost perfectly, except for a phase change. For obliquely incident flexural plate waves, this reflection property can occur over the full frequency spectrum subject to a constraint, discussed later, on the angle of incidence.

Here we consider the scattering of flexural plate waves from the junction of two semi-infinite and co-planar, elastic plates. Scattering problems of this type are often tackled using Fourier transforms and the Wiener–Hopf technique, and we shall follow that route here. Most previous authors have dealt exclusively with normally incident plate waves, line sources or incoming plane waves from the fluid. Moreover, they have typically assumed that one elastic plate is attached to a rigid baffle, or is unbaffled (Cannell, 1975, 1976). When treating realistic underwater structures, materials cannot realistically be considered to be rigid. This led Brazier-Smith (1987) to provide a comprehensive study that generalises many of the previous analyses to differing kinds of plates; that study has recently been reworked by Norris & Wickham (1995). Both papers specialise to giving

numerical results for plates of identical material properties, but differing thicknesses at a latter stage. Here, we will consider the general problem of scattering from plates with different composition and thickness, that are joined in various ways, and we will allow the incident waves to have arbitrary angle of incidence.

The reason why most previous studies have concentrated on normal incidence is that the analysis becomes apparently rather awkward for oblique incidence. For example, the analysis of flexural waves incident obliquely along a baffled, heavily fluid-loaded membrane appears in Crighton & Innes (1984); from that analysis it appears that concise results may not be forthcoming. Analogous incident acoustic wave problems for line defects have been modelled using phased line sources (Crighton & Maidanik, 1981; Rogoff & Tew, 1997). But in many physical situations we have to deal with three dimensional problems and oblique incidence becomes important. In particular, for incoming plate waves, oblique incidence introduces a critical angle above which transmission of flexural waves is no longer possible. Moreover, the locations of peaks in the angular distribution of scattered acoustic waves (the directivity) are dependent upon incidence angle. It is our aim here to describe these effects within a formulation that neatly connects with the simpler, limiting cases of heavy fluid loading (Abrahams, 1981; Cannell, 1976; Crighton & Innes, 1984) and light fluid loading.

The plan of the chapter is as follows: in Section 6.2 we formulate the scattering problem, non-dimensionalise, and discuss the critical angles. The solution and a power flow result are described in Section 6.3. Results are provided in Section 6.4, showing the partition of power converted into the reflected, transmitted or acoustic far field, together with representative directivity patterns, concentrating primarily upon clamped and welded edge conditions. Section 6.5 is split into subsections that describe various limiting cases, where one plate is rigid, acoustically soft, or where both plates are identical. Later subsections in Section 6.5 concentrate upon heavy or light fluid loading. Some concluding remarks are compiled in Section 6.6. Much of the mathematical details are subsumed into appendices.

6.2. Formulation

We consider the geometrical configuration sketched in Figure 6.1; the junction of two elastic plates with fluid loading to one side. We assume time-harmonic vibrations of frequency ω, and so all physical variables have an $e^{-i\omega t}$ dependence; this dependence is considered understood, and is henceforth suppressed.

The two plates that occupy the plane $z = 0$ are taken to be of different material and thickness; they occupy the half-planes, $x < 0$ and $x > 0$, and so the junction is the line

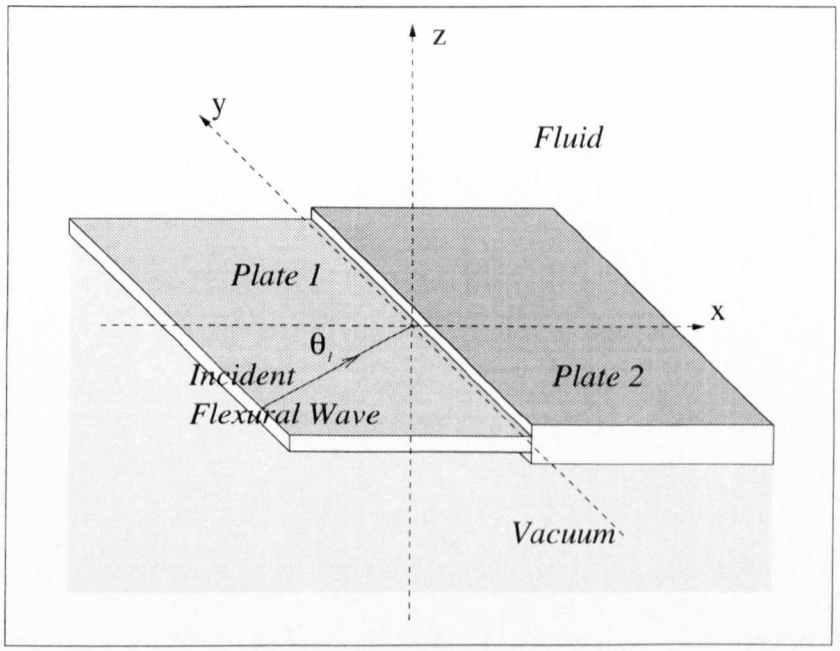

Figure 6.1. The geometry of the problem. The angle of incidence, θ_1, is the angle made between the wavenumber vector and the (horizontal) normal to the plate junction (which lies along the line $x = z = 0$).

$x = z = 0$. These plates are assumed to separate the fluid in the region $z > 0$ from a vacuum lying in $z < 0$. The fluid lies in the half space, $z > 0$ and $-\infty < x, y < \infty$; we assume it to be compressible and inviscid.

With the assumed time dependence, the fluid pressure $\hat{p}(x, y, z)$ satisfies the Helmholtz equation in $z > 0$,

$$(\nabla^2 + k_0^2)\hat{p}(x, y, z) = 0, \tag{6.2.1}$$

and k_0, the acoustic wavenumber, is related to the sound speed of the fluid, c_0: $k_0 = \omega/c_0$. The displacement in the z direction on the plate, $\hat{\eta}(x, y)$, is related to the fluid pressure:

$$\rho\omega^2\hat{\eta}(x, y) = \hat{p}_z(x, y, 0). \tag{6.2.2}$$

To model the elastic plates we adopt the thin plate equation (Junger & Feit, 1986) in the form,

$$B_j\nabla_h^4\hat{\eta}(x, y) - m_j\omega^2\hat{\eta}(x, y) = -\hat{p}(x, y, 0), \tag{6.2.3}$$

where ∇_h^2 is the horizontal Laplacian,

$$\nabla_h^2 \equiv \frac{\partial^2}{\partial x^2} + \frac{\partial^2}{\partial y^2}, \tag{6.2.4}$$

and with $j = 1$ for $x < 0$ and $j = 2$ for $x > 0$. Here B_j and m_j are material parameters. Apart from a membrane, this is the simplest model for a wave-bearing structure.

Crucially it neglects transverse shear and rotary inertia effects, which introduces a loss of accuracy for frequencies near to and above the coincidence frequency (the frequency when the *in vacuo* flexural and fluid wavespeeds are equal). Nevertheless the thin plate equation is widely used, and often gives useful insights into phenomena associated with scattering by elastic plates.

We must supplement these two plate equations with edge conditions that must be imposed at the junction. These edge conditions reflect the detailed way in which the two plates are joined. The most commonly encountered edge conditions are clamped, welded, free, and hinged. Each of these can be described by mathematical relations that translate to conditions on the plate displacement and its derivatives as we limit into the joint from either side (Timoshenko & Woinowsky-Kreiger, 1959). We leave the precise form of the edge conditions open for the moment, but later on, we consider explicitly the cases of clamped or welded edges. However, there is no pressing reason to quote the formulae at this stage. We write the form of the edge conditions in the four cases in Appendix 6.B.

The bending stiffness B_j and mass per unit area m_j of each plate are related to the physical properties of the elastic plate through

$$B_j = \frac{E_j h_j^3}{12(1-\nu_j^2)} \quad \text{and } m_j = \rho_j h_j, \tag{6.2.5}$$

where E_j, h_j, ν_j, and ρ_j denote the Young's modulus, thickness, Poisson ratio and mass density of the elastic material, respectively. In order to minimise the number of parameters that occur later, we introduce the quantities,

$$\kappa_j^4 \equiv \frac{\omega^2 m_j}{B_j}, \quad \epsilon_j = \frac{\rho}{m_j}\left(\frac{B_j}{m_j c_0^2}\right)^{\frac{1}{2}} \quad \text{and } \Omega_j = \left(\frac{k_0}{\kappa_j}\right)^2 = \frac{\omega}{c_0\rho} m_j \epsilon_j \text{ for } j = 1,2. \tag{6.2.6}$$

Here, κ_j represents the *in vacuo* flexural wavenumbers. Also, Ω_j is the square of the ratio of the *in vacuo* plate wave speed to that of the fluid, and provides a dimensionless measure of frequency. Lastly, ϵ_j, provides a frequency-independent measure of fluid loading. Thus, for each plate there are two parameters that we vary by adjusting the dimensional frequency and material combinations: Ω_j and ϵ_j. We take fluid loading to be 'heavy' when $\Omega_j \ll \epsilon_j$ and $\epsilon_j \ll 1$. The loading is 'light' when $\Omega_j > 1$ and $\epsilon_j \ll 1$.

In this chapter, all results are presented for elastic plates beneath water. Typically the plates have thicknesses of order 10^{-2} m (Junger & Feit, 1986), and we show illustrative values of the main elastic constants for aluminium and steel in Table 6.1. From these values we observe that ϵ_j is usually small. However, Ω_j, ranges through all values. Note that, for aluminium and steel, $\Omega_2/\Omega_1 = 0.996 h_2/h_1$; thus the main effect of material differences is through the changes in the fluid loading parameter.

Constants	Aluminium	Steel
E	70.3 GPa	211.9 GPa
ν	0.345	0.291
ρ	2700 kg/m^3	7900 kg/m^3
ϵ (water)	0.393	0.134

Table 6.1. Physical constants (Bradfield, 1964).

6.2.1. *Non-dimensionalisation*

To proceed we first non-dimensionalise the equations. There is no need to non-dimensionalise $\hat{p}$, however it is convenient to scale $\hat{p}$ so that the incident wave amplitude on the plate is unity. We adopt the dimensionless space variable $\tilde{\mathbf{x}} = k_0\mathbf{x}$ derived from the acoustic wavenumber. (Alternatively, we could rescale using, say, either of the *in vacuo* wavenumbers κ_1 or κ_2.)

On dropping the tilde and hat decoration, the governing equation becomes

$$\left(\frac{\partial^2}{\partial x^2} + \frac{\partial^2}{\partial y^2} + \frac{\partial^2}{\partial z^2} + 1\right) p(x,y,z) = 0, \tag{6.2.7}$$

subject to the thin plate equations (boundary conditions),

$$\left[\Omega_j^2 \left(\frac{\partial^2}{\partial x^2} + \frac{\partial^2}{\partial y^2}\right)^2 - 1\right] \frac{\partial p}{\partial z}(x,y,0) + \frac{\epsilon_j}{\Omega_j} p(x,y,0) = 0 \quad \text{for } j = 1,2, \tag{6.2.8}$$

and $p \to 0$ as $z \to \infty$.

6.2.2. *Flexural waves and critical angles*

Each plate can support a flexural wave that, in the fluid, takes the form,

$$p(x,y,z) = \exp[-(\Gamma_j^2 - 1)^{\frac{1}{2}} z + \mathrm{i}\xi_j x + \mathrm{i}\kappa y], \tag{6.2.9}$$

where the total plate wavenumbers, Γ_j, are defined by $\Gamma_j^2 = \xi_j^2 + \kappa^2$. These wavenumbers are found from substituting the solution into the plate equations. Then we find the dispersion functions,

$$\mathcal{K}_j(\xi) = \left[\Gamma^4(\xi) - \frac{1}{\Omega_j^2}\right] - \frac{\epsilon_j}{\Omega_j^3} \frac{1}{[\Gamma^2(\xi) - 1]^{\frac{1}{2}}} \qquad (j = 1,2). \tag{6.2.10}$$

Note that, formally, $\mathcal{K}_j$ is a function of only the total flexural wavenumber, $\Gamma_j = \Gamma(\xi_j)$, which is, in turn, a function of ξ_j. The total flexural wavenumber is given by the real, positive value of Γ that produces a zero of the dispersion functions, $\mathcal{K}_j = 0$. The total flexural wavenumber is real, positive and always greater than unity, which signifies that these waves are subsonic relative to the acoustic wavespeed. Given, Γ_j, we may then construct the transverse (to the junction) flexural wavenumbers, ξ_j (this wavenumber is not necessarily real; see below).

Depending upon the precise choice of branch cuts for $(\Gamma^2(\xi) - 1)^{\frac{1}{2}}$ the dispersion functions (6.2.10) also have zeros for complex Γ; these roots and their significance are discussed further in Appendix 6.A.

The flexural waves in each plate are associated with an angle of propagation θ_j, see Figure 6.1, such that $\xi_j = \Gamma_j \cos\theta_j$ and $\kappa = \Gamma_j \sin\theta_j$. In the scattering problem, both plates support such waves, but they may have different total wavenumbers. However, the wavenumber along the junction, κ, cannot change as a result of scattering. Hence we deduce a version of Snell's law:

$$\kappa \equiv \Gamma_1 \sin\theta_1 = \Gamma_2 \sin\theta_2. \tag{6.2.11}$$

Now, in the formulation of the problem, the angle of incidence, θ_1, is prescribed ($0 \leq \theta_1 \leq \pi/2$), and so

$$\sin\theta_2 = \frac{\Gamma_1}{\Gamma_2} \sin\theta_1. \tag{6.2.12}$$

Thus, if $\Gamma_2 < \Gamma_1$ there can be incident angles for which the right-hand side of (6.2.12) is greater than unity and, therefore, θ_2 does not exist as a real angle. In other words, there is a possibility of total internal reflection for angles of incidence above a critical threshold. This critical angle, θ_c, is given by the ray for which the transmitted wave emerges with $\theta_2 = \pi/2$: $\theta_c = \sin^{-1}(\Gamma_2/\Gamma_1)$.

The critical angle is plotted against Ω_1 (a non-dimensional frequency) in Figure 6.2. Both material contrast and variations in plate thickness can lead to cut-off frequencies below which transmission of flexural waves ceases. Above the threshold, the incident flexural wave excites an edge wave which decays spatially with distance into the plate (ξ_2 is complex). The minimum values of the critical angle decrease on increasing the material contrast, or relative plate thicknesses. These minimum values of the critical angle occur in the heavy loading limit, for which $\Gamma_j \sim \epsilon_j^{1/5} \Omega_j^{-3/5}$.

6.2.3. *Radiated acoustic waves*

In the scattering problem, the incident flexural wave can also excite acoustic waves that propagate in the fluid. In the far field these are cylindrical waves, and are better described

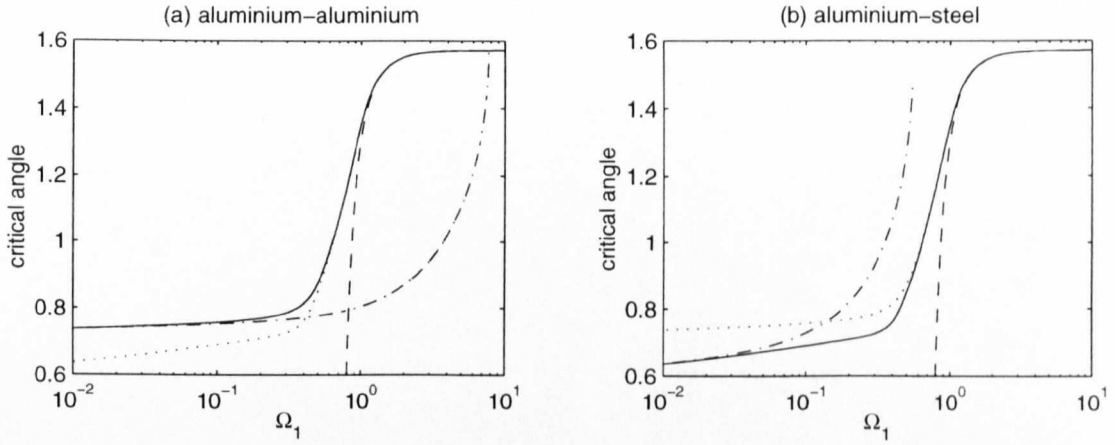

Figure 6.2. The critical angles versus dimensionless frequency with the thickness of plate two, $x > 0$, double that of plate one, $x < 0$. In panel (a) both plates are aluminium, and in panel (b) there is material contrast with aluminium-steel plates. The dashed lines are approximations to the critical angle θ_c using $\Gamma_j \sim 1 + \frac{1}{2}(\epsilon_j/\Omega_j(\Omega_j^2 - 1))^2$ for $\Omega_j \gg 1$ and $\Gamma_j \sim \epsilon_j^{1/5}\Omega_j^{-3/5}\left(2 - (1 + \frac{1}{5}(\Omega_j/\epsilon_j^2)^{2/5})^{-1}\right)$ for $\Omega_j \ll \epsilon_j$ and $\Omega_j \ll 1$. The dotted line in each panel compares the two cases.

in a cylindrical polar coordinate system (r, ϑ, y) whose axis lies along the junction ($x = r\cos\vartheta, z = r\sin\vartheta$). These waves have the far-field form,

$$p(r, \vartheta, y) \propto \sqrt{\frac{2}{\pi\lambda r}} G(\vartheta) e^{\mathrm{i}\lambda r - \mathrm{i}\frac{\pi}{4} + \mathrm{i}\kappa y}, \tag{6.2.13}$$

characterised by an angular directivity $G(\vartheta)$, where $\lambda = \sqrt{1 - \kappa^2}$ is the radial wavenumber of the acoustic wave.

When the incident flexural wavenumber has $\kappa < 1$, the scattering off the junction will excite acoustic waves in the fluid. But if $\kappa > 1$, these waves are evanescent and there are no scattered acoustic waves in the far field. Equivalently, in order to excite acoustic waves, the component of the flexural wave in the y direction must travel super-sonically.

In other words, there is a second critical angle, $\theta_a = \sin^{-1}(1/\Gamma_1)$, for scattered acoustic waves. This cut-off angle is always smaller than that arising from flexural waves associated with the material contrast. The situation is illustrated in Figure 6.3.

6.3. Transform solution

We now move on to the full scattering problem. As sketched in Figure 1, we consider incoming flexural waves from $x < 0$ with an angle of incidence θ_1. The case $\theta_1 = 0$ corresponds to normal incidence, and was treated by Brazier-Smith (1987) and Norris &

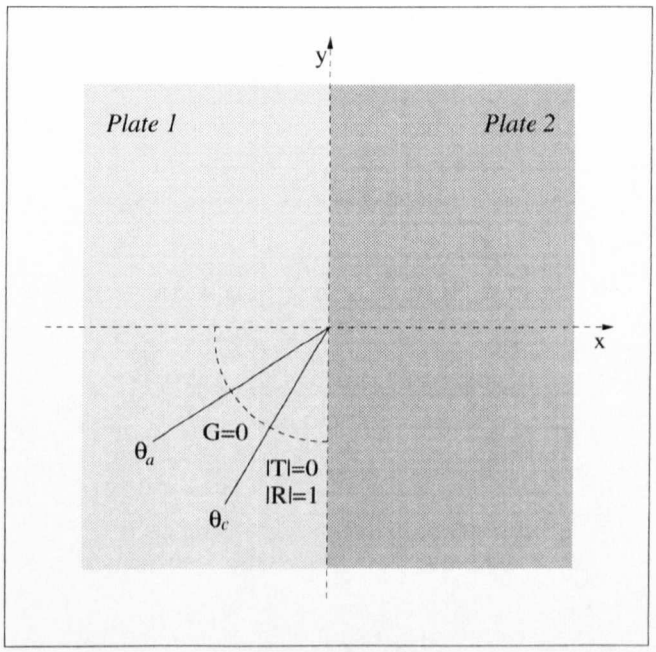

Figure 6.3. An illustration showing the critical angles beyond which, first $G \equiv 0$ (no scattered acoustic waves), and then both $G \equiv 0$ and $|T| \equiv 0$ (no scattered acoustic wave nor transmitted flexural waves).

Wickham (1995); the latter authors give some explicit results for the limit of heavy fluid loading. (More complicated incoming wave behaviour can be considered, but here we are concerned with the essential details of scattering and so we take incoming plate waves for simplicity.)

The incident field has the form,

$$p^{inc}(x, y, z) = \exp(-\gamma_1 z + \mathrm{i}\xi_1 x + \mathrm{i}\kappa y) \tag{6.3.1}$$

where $\gamma_1^2 = \Gamma_1^2 - 1$ and $\Gamma_1^2 = (\xi_1^2 + \kappa^2)$; equivalently $\xi_1 = \Gamma_1 \cos\theta_1$ and $\kappa = \Gamma_1 \sin\theta_1$. We next write

$$p(x, y, z) = p^{inc}(x, y, z) + p^{sc}(x, z)e^{\mathrm{i}\kappa y}, \tag{6.3.2}$$

thereby introducing the scattered field $p^{sc}(x, z)$; $p^{inc}(x, y, z)$ has the same exponential y dependence. We now formulate a boundary value problem for the scattered field $p^{sc}(x, z)$, and drop the superscript sc hereon.

In terms of the scattered field we have

$$\left(\frac{\partial^2}{\partial x^2} + \frac{\partial^2}{\partial z^2} - \kappa^2 + 1\right) p(x, z) = 0 \tag{6.3.3}$$

in $-\infty < x < \infty$ and $z > 0$, subject to the plate boundary conditions on $z = 0$ that

$$\left\{\left[\Omega_j^2\left(\frac{\partial^2}{\partial x^2} - \kappa^2\right)^2 - 1\right]\frac{\partial}{\partial z} + \frac{\epsilon_j}{\Omega_j}\right\} p(x,0) = \begin{cases} \Omega_2^2(\Gamma_1^2 - 1)^{\frac{1}{2}}\mathcal{K}_2(\xi_1)e^{i\xi_1 x} \text{ for } x > 0 \\ 0 \text{ otherwise} \end{cases}. \tag{6.3.4}$$

The scattering problem falls into a class of mixed boundary value problems that can be solved via the Wiener–Hopf technique (*e.g.* Noble, 1958).

6.3.1. *The functional equation*

To proceed we apply Fourier transforms in the spatial x direction. First, we define the transform of the pressure

$$P(\xi, z) = \int_{-\infty}^{\infty} p(x,z)e^{i\xi x}\mathrm{d}x = P_+(\xi, z) + P_-(\xi, z), \tag{6.3.5}$$

where $P_\pm$ denote the half-range transforms of $p(x,z)$:

$$P_+(\xi, z) = \int_0^{\infty} p(x,z)e^{i\xi x}\mathrm{d}x, \quad P_-(\xi, z) = \int_{-\infty}^{0} p(x,z)e^{i\xi x}\mathrm{d}x. \tag{6.3.6}$$

Note that the scattered flexural wave field may have finite amplitude as $x \to \pm\infty$ and the transforms must be interpreted in a generalised sense (*e.g.* Lighthill, 1958).

The inverse transform is defined by

$$p(x,z) = \frac{1}{2\pi}\int_C P(\xi, z)e^{-i\xi x}\mathrm{d}\xi, \tag{6.3.7}$$

where the path C runs from $-\infty$ to $+\infty$ and is indented above (below) any singularities occurring on the negative (positive) real axis. The region above (below) C is the 'plus' ('minus') region; in what follows, we loosely refer to these two regions as the 'upper' and 'lower' halves of the complex ξ plane. This definition of C avoids the unnecessary introduction of artificial dissipation and then later limiting this to zero. We may evaluate the inversion integral by closing the contour C on adding arcs enclosing either the entire lower or upper half planes. In these half planes the functions to be inverted may have poles that in the physical domain correspond to reflected or transmitted waves, and branch point singularities that give rise to scattered acoustic waves. Oblique incidence distorts the familiar pattern of singularities found in normal incidence as, for example, the branch points may no longer lie on the real axis, but upon the imaginary axis instead.

On applying the half-range transforms to the governing equation we find

$$P_{zz}(\xi, z) - [\Gamma^2(\xi) - 1]P(\xi, z) = 0, \quad \text{with } \Gamma^2(\xi) - 1 = \xi^2 + \kappa^2 - 1. \tag{6.3.8}$$

The relevant solution is

$$P(\xi,z) = I(\xi)\exp[-\sqrt{\Gamma^2(\xi)-1}\;z], \tag{6.3.9}$$

where the function $I(\xi)$ is currently unknown. Also, we choose the branch cuts of $(\Gamma^2 - 1)^{1/2}$ so that this function becomes $-i(1-\Gamma^2)^{\frac{1}{2}}$ for Γ real and less than unity; this ensures that (6.3.9) then becomes the correct, out-going wave solution. The aim is to find $I(\xi)$ by using the plate conditions. Once this function is determined, the far field behaviour of $p(x,z)$ and other quantities of interest follow from the inverse transform.

Following Balmforth & Craster (1999), we next consider the quantities

$$\Delta_{j\pm} = \left[\Gamma^4(\xi) - \frac{1}{\Omega_j^2}\right] P_{\pm z}(\xi,0) + \frac{\epsilon_j}{\Omega_j^3} P_{\pm}(\xi,0) + \mathcal{R}^{\pm}(\xi). \tag{6.3.10}$$

These functions capture the edge behaviour of the plates within the terms,

$$\mathcal{R}^{\pm}(\xi) = \mp\left[p_{zxxx}(0^{\pm},0) - \mathrm{i}\xi p_{zxx}(0^{\pm},0) - (2\kappa^2+\xi^2)p_{zx}(0^{\pm},0) + \mathrm{i}\xi(2\kappa^2+\xi^2)p_z(0^{\pm},0)\right]. \tag{6.3.11}$$

In the following we mainly encounter half-range transforms on $z = 0$. To shorten the notation, we write $P_+(\xi,0)$ as $P_+(\xi)$, and similarly for the other transform, unless explicitly denoted otherwise.

The sum of the two half-range transforms in (6.3.10) provides the relation,

$$\Delta_{j+} + \Delta_{j-} = \left[\Gamma^4(\xi) - \frac{1}{\Omega_j^2}\right] P_z(\xi,0) + \frac{\epsilon_j}{\Omega_j^3} P(\xi,0) + \mathcal{R}^{+}(\xi) + \mathcal{R}^{-}(\xi). \tag{6.3.12}$$

Also, from the transformed boundary conditions,

$$\Delta_{1-} = \left[\Gamma^4(\xi) - \frac{1}{\Omega_1^2}\right] P_{-z}(\xi) + \frac{\epsilon_1}{\Omega_1^3} P_{-}(\xi) + \mathcal{R}^{-}(\xi) = 0, \tag{6.3.13}$$

and

$$\Delta_{2+} = \left[\Gamma^4(\xi) - \frac{1}{\Omega_2^2}\right] P_{+z}(\xi) + \frac{\epsilon_2}{\Omega_2^3} P_{+}(\xi) + \mathcal{R}^{+}(\xi) = -\frac{\gamma_1 \mathcal{K}_2(\xi_1)}{\mathrm{i}(\xi+\xi_1)_+}. \tag{6.3.14}$$

The + subscript on the final term in (6.3.14) reminds us that this pole on the real axis is to be interpreted as lying in the minus region, that is, the final term is analytic in the plus region.

Some algebraic manipulations (including the use of the solution in (6.3.9)) then allow us to eliminate $P_z(\xi,0)$, $P(\xi,0)$, and the $\Delta_{j\pm}$'s:

$$\begin{aligned}&\left[\Gamma^4(\xi) - \frac{1}{\Omega_2^2}\right] P_{-z}(\xi) + \frac{\epsilon_2}{\Omega_2^3} P_{-}(\xi) - \mathcal{R}^{+}(\xi) - \frac{\gamma_1 \mathcal{K}_2(\xi_1)}{\mathrm{i}(\xi+\xi_1)_+} \\ &= \frac{\mathcal{K}_2(\xi)}{\mathcal{K}_1(\xi)}\left\{\left[\Gamma^4(\xi) - \frac{1}{\Omega_1^2}\right] P_{+z}(\xi) + \frac{\epsilon_1}{\Omega_1^3} P_{+}(\xi) - \mathcal{R}^{-}(\xi)\right\}.\end{aligned} \tag{6.3.15}$$

This relation is nearly in the form suitable to use the Wiener-Hopf technique; we need only split the functions $K_j(\xi)$ into products of $\pm$−functions: $K_j(\xi) = K_{j+}(\xi)K_{j-}(\xi)$. These minus and plus functions analytic and non-zero in the lower and upper complex ξ planes (or, more properly, the regions above and below the contour of integration of the inverse transform), respectively. We describe how to accomplish the splitting in Appendix 6.A.

With the splitting in hand, we may write the basic *functional equation*,

$$\frac{K_{1-}(\xi)}{K_{2-}(\xi)}\left\{\left[\Gamma^4(\xi)-\frac{1}{\Omega_2^2}\right]P_{-z}(\xi)+\frac{\epsilon_2}{\Omega_2^3}P_-(\xi)-\mathcal{R}^+(\xi)-\frac{\gamma_1 K_2(\xi_1)}{\mathrm{i}(\xi+\xi_1)_+}\right\}+\frac{\gamma_1 K_{2-}(\xi_1)K_{1+}(\xi_1)}{\mathrm{i}(\xi+\xi_1)_+}$$
$$=\frac{K_{2+}(\xi)}{K_{1+}(\xi)}\left\{\left[\Gamma^4(\xi)-\frac{1}{\Omega_1^2}\right]P_{+z}(\xi)+\frac{\epsilon_1}{\Omega_1^3}P_+(\xi)-\mathcal{R}^-(\xi)\right\}+\frac{\gamma_1 K_{2-}(\xi_1)K_{1+}(\xi_1)}{\mathrm{i}(\xi+\xi_1)_+}=-E(\xi), \tag{6.3.16}$$

which expresses the equality of a + function to a − function, and therefore both are equal to an entire function, $E(\xi)$. Strictly speaking the + and − functions are equal to the entire function along a common line of analyticity, and analytic continuation is then used to extend this relation to the full complex ξ plane. We may deduce what this entire function must be by considering the behaviour of the $\pm$−functions for $|\xi| \to \infty$: In this limit, $K_{j\pm}(\xi) \sim O(\xi^2)$ and $P_z \sim O(1/\xi)$. Thus, using Liouville's theorem, $E(\xi)$ is a cubic polynomial: $E(\xi) = E_3\xi^3 + E_2\xi^2 + E_1\xi + E_0$.

To reduce the length of the following expressions we define

$$\frac{1}{\Omega^2}=\left(\frac{\Omega_2}{\epsilon_2}-\frac{\Omega_1}{\epsilon_1}\right)\left(\frac{\Omega_2^3}{\epsilon_2}-\frac{\Omega_1^3}{\epsilon_1}\right)^{-1},\quad \Pi(\xi)=\frac{\gamma_1 K_{1+}(\xi_1)K_{2-}(\xi_1)}{\mathrm{i}(\xi+\xi_1)_+}, \tag{6.3.17}$$

and

$$\Phi(\xi)=\frac{\Omega_2^3}{\epsilon_2}\mathcal{R}^+(\xi)+\frac{\Omega_1^3}{\epsilon_1}\mathcal{R}^-(\xi)+\frac{\Omega_2^3}{\epsilon_2}\frac{\gamma_1 K_2(\xi_1)}{\mathrm{i}(\xi+\xi_1)}. \tag{6.3.18}$$

Hence,

$$\left(\frac{\Omega_2^3}{\epsilon_2}-\frac{\Omega_1^3}{\epsilon_1}\right)\left[\Gamma^4(\xi)-\frac{1}{\Omega^2}\right]P_{+z}(\xi)=\frac{\Omega_1^3 K_{1+}(\xi)}{\epsilon_1 K_{2+}(\xi)}[E(\xi)+\Pi(\xi)]-\Phi(\xi), \tag{6.3.19}$$

and

$$\left(\frac{\Omega_2^3}{\epsilon_2}-\frac{\Omega_1^3}{\epsilon_1}\right)\left[\Gamma^4(\xi)-\frac{1}{\Omega^2}\right]P_{-z}(\xi)=-\frac{\Omega_2^3 K_{2-}(\xi)}{\epsilon_2 K_{1-}(\xi)}[E(\xi)+\Pi(\xi)]+\Phi(\xi). \tag{6.3.20}$$

It is important to note that both sides of (6.3.19) and (6.3.20) are analytic in the correct pieces of the complex ξ planes. However, the transforms, $P_{\pm z}(\xi)$, are themselves *not* analytic unless we satisfy the four simultaneous equations,

$$\frac{\Omega_1^3 K_{1+}(\xi)}{\epsilon_1 K_{2+}(\xi)}\left[E(\xi)+\frac{\gamma_1 K_{1+}(\xi_1)K_{2-}(\xi_1)}{\mathrm{i}(\xi+\xi_1)_+}\right]=\frac{\Omega_2^3}{\epsilon_2}\mathcal{R}^+(\xi)+\frac{\Omega_1^3}{\epsilon_1}\mathcal{R}^-(\xi)+\frac{\Omega_2^3\gamma_1 K_2(\xi_1)}{\epsilon_2\mathrm{i}(\xi+\xi_1)_+}, \tag{6.3.21}$$

for $\xi = \chi_j$, $j = 1,\ldots,4$, where

$$\chi_{1,2} = \pm i\left(\kappa^2 + \frac{1}{\Omega}\right)^{\frac{1}{2}}_{\mp} \text{ and } \chi_{3,4} = \begin{cases} \pm i\left(\kappa^2 - \frac{1}{\Omega}\right)^{\frac{1}{2}}_{\mp} & \text{for } \kappa^2 > \frac{1}{\Omega} \\ \pm\left(\frac{1}{\Omega} - \kappa^2\right)^{\frac{1}{2}}_{\mp} & \text{for } \kappa^2 < \frac{1}{\Omega} \end{cases}, \tag{6.3.22}$$

are the four roots of $\Gamma^4(\xi) - 1/\Omega^2 = 0$. The zeros in the plus (minus) region are χ_1 and χ_3 (χ_2 and χ_4). In physical terms, this set of constraints ensures that the scattered field consists only of outgoing waves.

In order to satisfy these constraints, we must fix some of the free parameters that are hidden in (6.3.19)-(6.3.20). These free parameters are the coefficients, E_l with $l = 0,...,3$, of our cubic polynomial $E(\xi)$, and the displacement and its derivatives at the edge, which are contained in $\mathcal{R}^{\pm}$: $p_z(0^{\pm},0)$, $p_{zx}(0^{\pm},0)$, $p_{zxx}(0^{\pm},0)$, and $p_{zxxx}(0^{\pm},0)$. In total, this makes twelve unknown parameters. However, the coefficients of the cubic and quadratic terms in $E(\xi)$ are simply related to the jumps in the displacement and its first derivative across the joint or edge:

$$E_3 = p_z(0^+,0) - p_z(0^-,0), \quad \text{and} \quad E_2 = p_{xz}(0^+,0) - p_{xz}(0^-,0) + \text{constant} \times E_3; \tag{6.3.23}$$

the constant in the last term of (6.3.23) requires an asymptotic expansion of the split functions $\mathcal{K}_{j+}(\xi)$ as $\xi \to \infty$. Moreover, it is only the combination $\Omega_2^3\mathcal{R}_+/\epsilon_2 + \Omega_1^3\mathcal{R}_-/\epsilon_1$ that appears in (6.3.19)-(6.3.20). This signifies that our unknown variables enter only through combinations of the form, $\Omega_2^3\partial_x^l p_z(0^+,0)/\epsilon_2 - \Omega_1^3\partial_x^l p_z(0^-,0)/\epsilon_1$ for $l = 0,...,3$. In other words, we have only eight unknown variables. Explicitly, these are

$$\begin{aligned} E_0, &\quad E_1, \\ p_z(0^+,0), &\quad p_z(0^-,0), \\ p_{xz}(0^+,0), &\quad p_{xz}(0^-,0), \\ \Omega_2^3 p_{xxz}(0^+,0)/\epsilon_2 &- \Omega_1^3 p_{xxz}(0^-,0)/\epsilon_1, \\ \Omega_2^3 p_{xxxz}(0^+,0)/\epsilon_2 &- \Omega_1^3 p_{xxxz}(0^-,0)/\epsilon_1. \end{aligned} \tag{6.3.24}$$

Lastly we recall the edge conditions. These provide four more relations between the unknowns (see Appendix 6.B). Hence, there are, in total, eight equations for eight unknowns, and as a prelude to evaluating the full solution, we must solve these simultaneous equations. In practice, we adopt either clamped or welded edges. There is a simplification that occurs in this case because $p_z(0^+,0) = p_z(0^-,0)$ and $p_{xz}(0^+,0) = p_{xz}(0^-,0)$ are both prescribed. Hence, in this case, we need only solve the four simultaneous equations (6.3.21).

Finally, from $P_z(\xi) = P_{+z}(\xi) + P_{-z}(\xi) = -I(\xi)(\Gamma^2 - 1)^{\frac{1}{2}}$, and the inverse transform,

$$p(x,z) = \frac{1}{2\pi}\int_C \frac{E(\xi) + \Pi(\xi)}{[\Gamma^2(\xi) - 1]^{\frac{1}{2}}\mathcal{K}_{1-}(\xi)\mathcal{K}_{2+}(\xi)} \exp(-i\xi x - [\Gamma^2(\xi) - 1]^{\frac{1}{2}} z)\mathrm{d}\xi. \tag{6.3.25}$$

The far-field form of $p(x,z)$ is extracted from this integral using asymptotic means. We quote the results next.

6.3.2. *Reflection, transmission, and diffraction coefficients*

The far-field behaviour consists of different contributions. First, we may identify the scattered flexural waves; these arise from poles in the transform lying on the real axis (the zero of $\mathcal{K}_{1-}(\xi)$ on the positive real axis lead to the reflected wave, and any zero of $\mathcal{K}_{2+}(\xi)$ on the negative real axis generates a transmitted wave). In addition, the integrand in (6.3.25) contains a factor $[\Gamma(\xi)^2-1]^{-1/2}$ which possesses a branch cut. This leads to a second contribution that, if the branch point is on the real axis, provides the scattered cylindrical waves in the fluid. In addition, for light fluid loading, one can (if desired) identify a piece of the wave spectrum with a 'leaky' wave (Crighton, 1979).

The scattered flexural wave amplitude is given explicitly in terms of reflection and transmission coefficients, R and T:

$$p(x,z) \sim R\ \exp(-\mathrm{i}\xi_1 x - \gamma_1 z) \quad \text{as} \quad x \to -\infty, \tag{6.3.26}$$

and provided $\theta_1 < \theta_c$,

$$p(x,z) \sim T\ \exp(+\mathrm{i}\xi_2 x - \gamma_2 z) \quad \text{as} \quad x \to +\infty, \tag{6.3.27}$$

with $\gamma_2^2 = \Gamma_2^2 - 1$ and $\Gamma_2 = \Gamma(\xi_2)$. If $\theta_1 > \theta_c$, on the other hand, there is no transmission.

If $\kappa < 1$, we define $\lambda = (1-\kappa^2)^{1/2}$ and the form of the far-field scattered cylindrical wave can be extracted using either stationary phase or saddle point arguments. This cylindrical wave is characterised by the directivity, $G(\vartheta)$, and the pressure field is given by

$$p(r,\vartheta) \sim G(\vartheta)\left(\frac{2}{\pi\lambda r}\right)^{\frac{1}{2}} e^{\mathrm{i}\lambda r - \mathrm{i}\frac{\pi}{4}}, \tag{6.3.28}$$

as $r \to \infty$ and $0 \le \vartheta \le \pi$. If $\kappa > 1$, the pressure field is $O(\exp[-\sqrt{\kappa^2-1}\ r])$ in the far field, and there is no scattered cylindrical wave.

By using the explicit form of the transform solution for $p(x,z)$, it follows that

$$R = \mathrm{i}\frac{[E(\xi_1)+\Pi(\xi_1)]}{(\Gamma_1^2-1)^{\frac{1}{2}}}\frac{\mathcal{K}_{1+}(\xi_1)}{\mathcal{K}_{2+}(\xi_1)\mathcal{K}_1'(\xi_1)},\quad T = \mathrm{i}\frac{[E(-\xi_2)+\Pi(-\xi_2)]}{(\Gamma_2^2-1)^{\frac{1}{2}}}\frac{\mathcal{K}_{2+}(\xi_2)}{\mathcal{K}_{1+}(\xi_2)\mathcal{K}_2'(\xi_2)}, \tag{6.3.29}$$

and

$$G(\vartheta) = -\mathrm{i}\frac{[E(-\lambda\cos\vartheta)+\Pi(-\lambda\cos\vartheta)]}{2\mathcal{K}_{1+}(\lambda\cos\vartheta)\mathcal{K}_{2-}(\lambda\cos\vartheta)}. \tag{6.3.30}$$

6.3.3. *Power flow*

We may also extract a 'power flow theorem' that gives a relation among $|R|^2$, $|T|^2$, and $G(\vartheta)$. This relation derives from the identity

$$\mathrm{Im}\left(\int_S p^\star \frac{\partial p}{\partial x_j} n_j \mathrm{d}S\right) = 0, \tag{6.3.31}$$

where * denotes the complex conjugate and S is a closed surface enclosing the plate joint and the plates themselves. The integral may be evaluated in terms of the far-field behaviour of $p(x,z)$, leading to the relation,

$$\mathrm{Re}\left[\frac{\Omega_1^3}{2\epsilon_1}(\Gamma_1^2-1)\mathcal{K}_1'(\xi_1)(|R|^2-1) + \frac{\Omega_2^3}{2\epsilon_2}(\Gamma_2^2-1)\mathcal{K}_2'(\xi_2)|T|^2 + \frac{2}{\pi}\int_0^\pi |G(\vartheta)|^2 \mathrm{d}\vartheta\right] = 0. \tag{6.3.32}$$

This relation holds for all edge conditions that do not introduce energy into the system. Equation (6.3.32) is used to verify all results presented within this chapter.

The proportion of the scattered power converted to flexural waves is given by the sum of the reflected power, P_R, and the transmitted power, P_T. The remainder comprises that converted into the diffracted acoustic far field, P_A. From (6.3.32) we deduce that

$$P_R = |R|^2, \quad P_T = \frac{\Omega_2^3\epsilon_1(\Gamma_2^2-1)\mathcal{K}_2'(\xi_2)}{\Omega_1^3\epsilon_2(\Gamma_1^2-1)\mathcal{K}_1'(\xi_1)}|T|^2, \quad P_A = \frac{4\epsilon_1\int_0^\pi |G(\vartheta)|^2\mathrm{d}\vartheta}{\pi\Omega_1^3(\Gamma_1^2-1)\mathcal{K}_1'(\xi_1)}. \tag{6.3.33}$$

The power-flow relation is simpler in some limiting cases. For example, in the limit of heavy fluid loading, the fluid is effectively incompressible, and so the diffracted acoustic power is negligible. Hence, to leading order, the power flow result becomes a relation between the flexural reflection and transmission coefficients

$$1 - |R|^2 = |T|^2 \frac{\cos\theta_2}{\cos\theta_1} \tag{6.3.34}$$

provided $\theta_1 < \theta_c$; otherwise $|R|^2 = 1$.

6.4. Numerical results for clamped or welded edges

We now specialise to the specific cases of clamped or welded edges and present some numerical results. Even though we have explicit formulae for the solution, numerical computations are needed because the splitting of the functions $\mathcal{K}_j$ is most easily performed in terms of some quadratures (see Appendix 6.A).

In Figures 6.5–6.9, we display the partitioned energy distributions for clamped and welded junctions of aluminium ($x < 0$) and steel ($x > 0$) plates beneath water. One

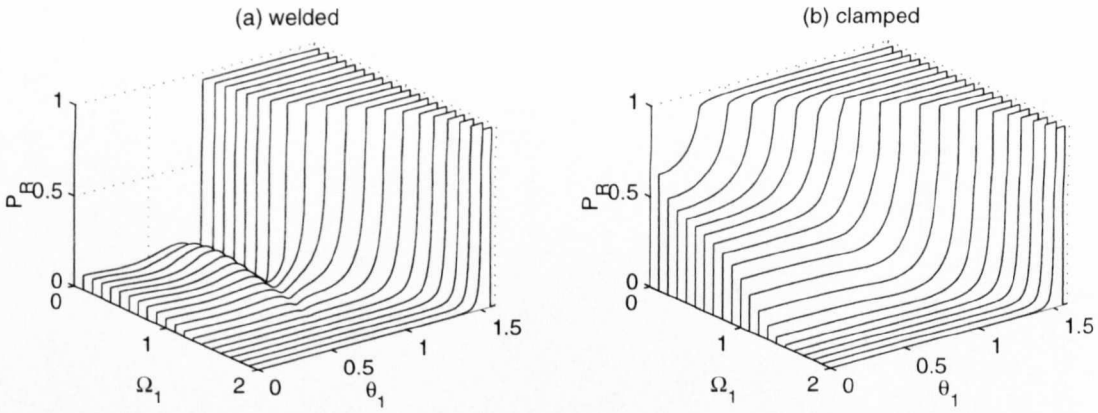

Figure 6.4. The distribution of reflected power, P_R, as a function of the dimensionless frequency, Ω_1, and incident angle, θ_1, caused by diffraction at the welded or clamped junctions of aluminium-steel plates. The relative plate thicknesses are $h_2 = 1.6h_1$.

of the most important effects of oblique incidence is the introduction of the two critical angles (Figure 6.3). On raising θ_1 from zero (normal incidence), the first critical angle we encounter is associated with the 'Mach' number of the longitudinal (with respect to the junction) flexural wavespeed, θ_a. For $\theta_1 > \theta_a$, the scattering of power into the acoustic far field is zero, $G(\vartheta) \equiv 0$. Then, under the conditions discussed earlier, there may exist a second angle, θ_c, beyond which no flexural waves are transmitted into the plate in $x > 0$; here both $|T|$ and $G(\vartheta)$ are zero.

The critical angles are both important and distinctive; below these critical angles the welded and clamped plates have very different behaviour. Figure 6.4 compares the reflected power and Figure 6.5 contrasts the transmitted flexural and diffracted acoustic power in the two cases for various values of frequency Ω_1 and incident angle θ_1. For incident angles below the cut-offs, a welded plate reflects very little power, and the majority of the wave energy is transmitted as flexural waves in $x > 0$, with some scattering into the acoustic far field.

In Figure 6.5 one sees that beyond the first cut-off, the far-field acoustic power vanishes, and the transmitted power increases. However, on passing above the second cut-off, all power is reflected. Clamped plates show qualitatively similar details regarding the cut-offs, but the clamped joint typically scatters far more energy into both the reflected and scattered acoustic fields, with an attendant reduction in transmitted flexural power. Although both welded and clamped plates have $|R| = 1$ above the two cut-off angles, phase change associated with reflection is markedly different (this is not shown in these figures).

But, in any event, a striking result for oblique incidence is that we can have total

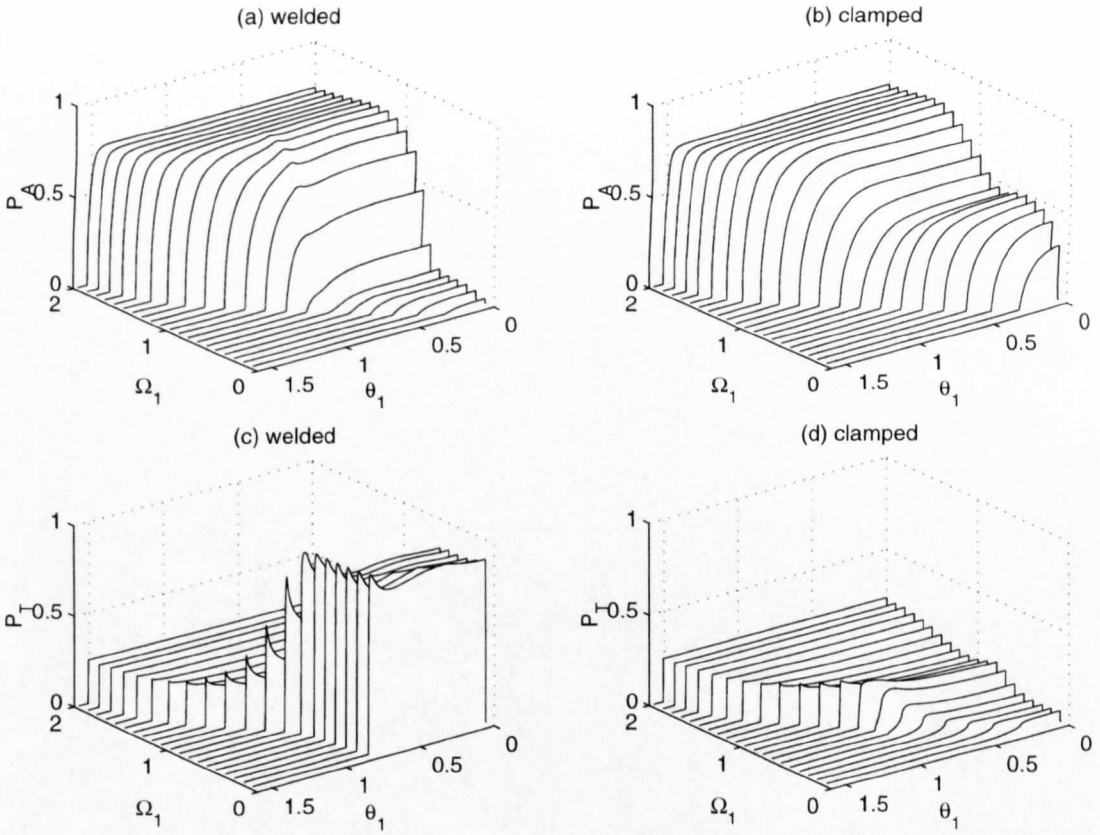

Figure 6.5. The distribution of power scattered into the acoustic far-field, P_A, and transmitted as flexural waves into the plate along $x > 0$, P_T. These are shown as a function of the dimensionless frequency, Ω_1, and incident angle, θ_1, caused by diffraction at either welded or clamped junctions of aluminium-steel plates. The relative plate thicknesses are $h_2 = 1.6h_1$. For ease of visualisation the orientation of the frequency and incident angle axes have been reversed from that used in Figure 6.4.

reflection (with an associated phase shift) for situations away from the limits of heavy or light fluid loading. This is significant because it implies that resonant behaviour may occur over wider physical regimes in plates with multiple junctions.

In Figures 6.6, 6.7 the partitions of scattered energy are directly compared for a fixed incident angle.

In Figure 6.8, we show the modulus of the directivity, $|G(\vartheta)|$, for the incident angle $\theta_1 = \pi/12$. The figure shows $|G(\vartheta)|$ as a function of the polar angle ϑ; the axes in the figure are cartesian (so each curve shows the angular distribution of $|G|$ at various values of Ω_1). In both cases, there is a substantial amount of scatter in the forward direction; this leads to the large lobes near $\vartheta \sim 0$. But, there are also differences in the two

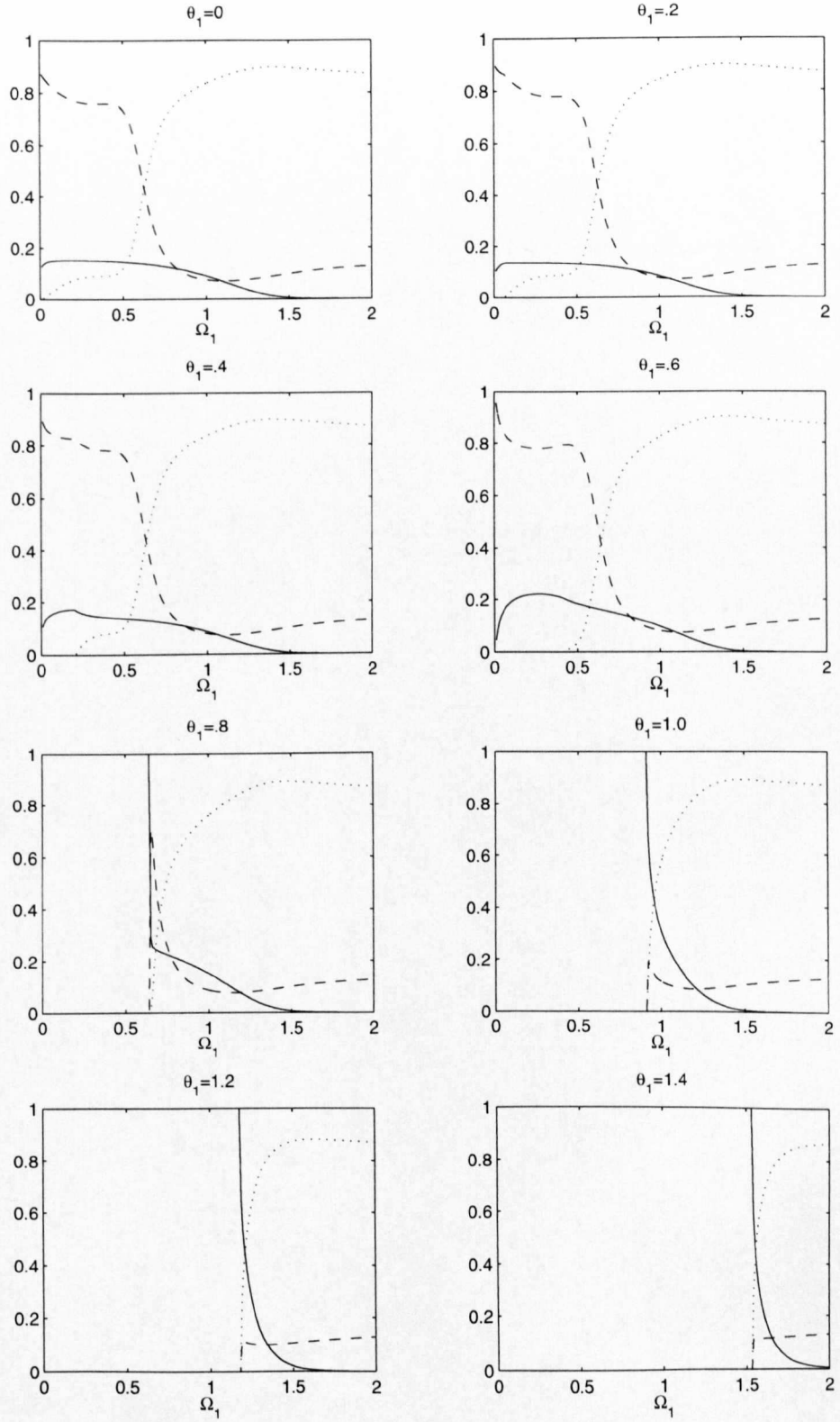

Figure 6.6. The power distribution at the welded junction of aluminium-steel plates; $h_2 = 2h_1$. $P_R(—)$, $P_T(- -)$, $P_A(\cdots)$.

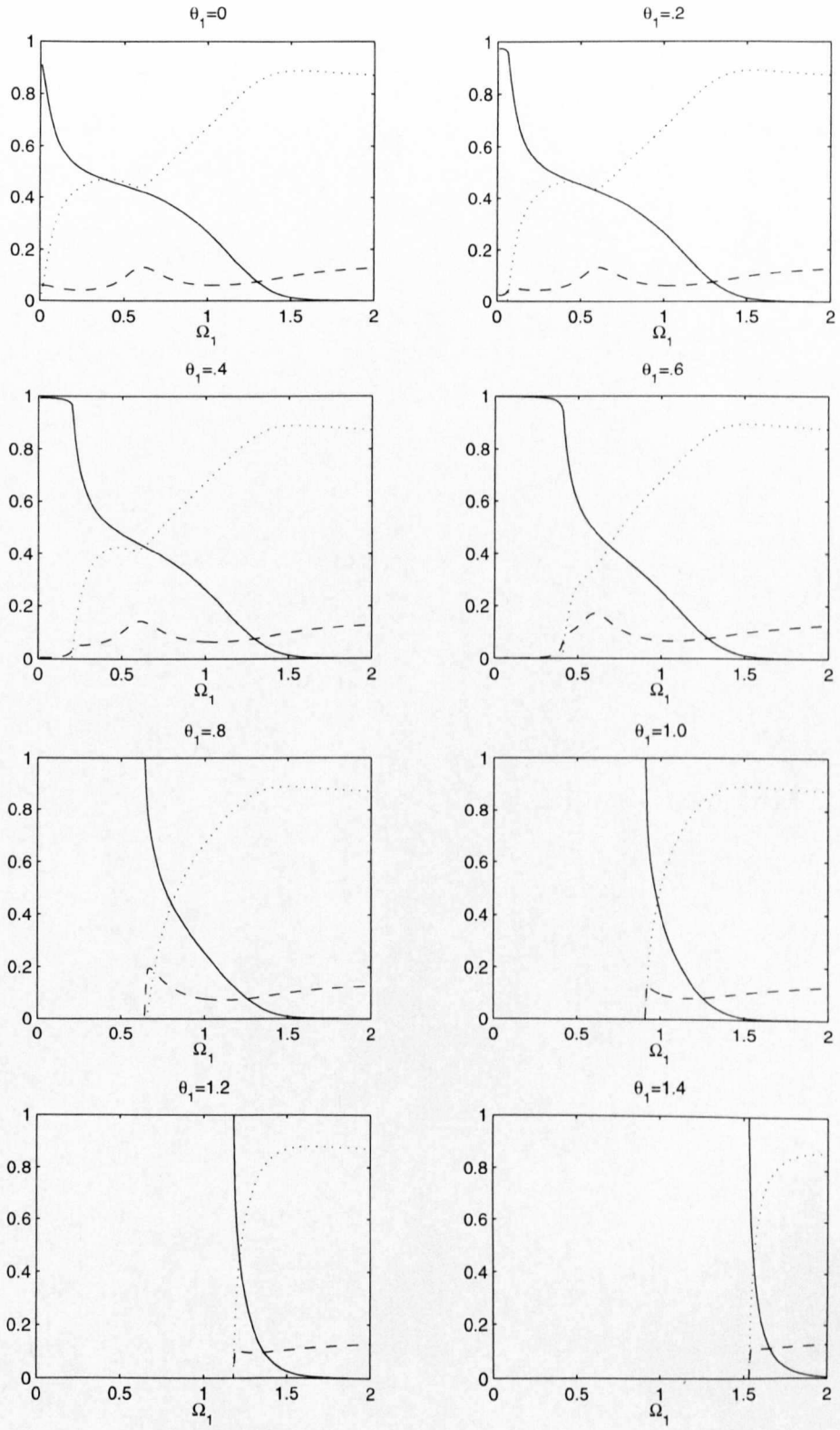

Figure 6.7. The power distribution at the clamped junction of aluminium-steel plates; $h_2 = 2h_1$. $P_R(—)$, $P_T(- -)$, $P_A(\cdots)$.

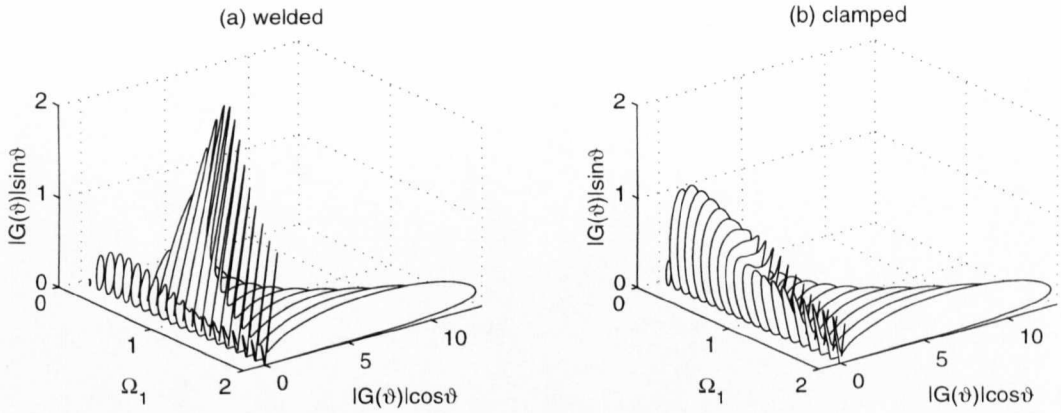

Figure 6.8. The directivity $|G(\vartheta)|$ shown as a function of the dimensionless frequency Ω_1. The specific choice of incident angle $\theta_1 = \pi/12$ has been taken.

directivity patterns, because the amount of scattering into the acoustic field is different for welded and clamped joints (see Figure 6.5).

In addition, there are also two distinctive, sharp peaks that occur in both plots along specific angles determined by the frequency and incident angle. The occurrence of these special angles can be understood in terms of the appearance of 'leaky waves' (that is, a disturbance that can be thought of as the remnant of the flexural wave that exists only provided the plate is *in vacuo* – see Crighton, 1979). Provided the wavespeed of the *in vacuo* flexural wave is greater than the acoustic wavespeed then the leaky wave sheds energy into the fluid along precise angles (this is further described in Section 6.5.4); the two peaks which appear in the directivities form along these angles.

As we increase the frequency, a peak develops first in the forward direction, $0 < \vartheta < \pi/2$. This arises because, for the choice of materials here, the plate in $x > 0$ is close to the limit of light fluid loading (where leaky waves typically occur), but the plate in $x < 0$ is not. Further increasing the frequency places both plates in the light fluid loading limit, and a peak also emerges in $\pi/2 < \vartheta < \pi$.

The results can also be seen for a particular choice of the dimensionless frequency in Figure 6.9.

In the cases shown in the figures , the aluminium plate in $x > 0$ is either 8/5 times the thickness of the steel one in $x < 0$ (6.4,6.5,6.8,6.9) or twice the thickness (6.6,6.7). Further increasing the plate thickness in $x > 0$ has the main effect of reducing the amount of energy transmitted to $x > 0$; some further examples are shown in later figures. If we specialise to plates of identical material, but different thicknesses, and then consider only normal incidence, we recover the numerical results presented by Norris & Wickham (1995) and Brazier-Smith (1987); these results are shown in Figure 6.10. The effect of

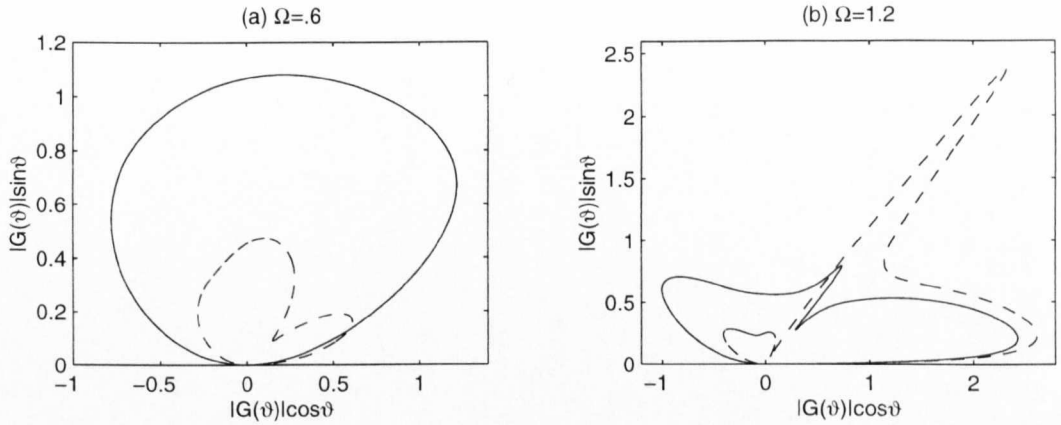

Figure 6.9. A comparison of the directivity $|G(\vartheta)|$ with either clamped (—) or welded (– –) edges is shown for dimensionless frequency (a) $\Omega_1 = .6$ and (b) $\Omega_1 = 1.2$. The specific choice of incident angle $\theta_1 = \pi/12$ has been taken.

increasing the material contrast (that is, having a material in $x > 0$ that supports slower flexural waves than that in $x < 0$) is very similar to increasing the plate thickness in $x > 0$.

6.5. Special cases

There are some special, limiting cases in which the scattering problem is more accessible, and we devote this section to a discussion of these simpler cases. The special cases are of three flavours. First, simplifications occur when the plate lying along $x > 0$ is either completely rigid or acoustically soft. This case corresponds to the distinguished limits, $\Omega_2, \epsilon_2/\Omega_2 \to 0$ (a rigid plate) or $\epsilon_2/\Omega_2 \to \infty$ (an acoustically soft plate). Second, the formulae gain symmetries and can be reduced further when we consider two identical plates with a joint. Thirdly, there are simplifications when the fluid loading is either light or heavy; here, $\epsilon_j \ll 1$ and $\Omega_j > 1$, or $\epsilon_j \ll 1$ and $\Omega_j \ll \epsilon_j$, respectively. These cases all limit neatly from the formulae of the full analysis.

6.5.1. *Rigid plate*

For an elastic plate in $x < 0$ connected to a co-planar rigid plate on $x > 0$, we have the relation, $P_{+z}(\xi) = \mathrm{i}(\Gamma_1^2 - 1)^{1/2}/(\xi + \xi_1)$. The functional equation then becomes

$$\mathcal{K}_1(\xi)\left[P_{-z}(\xi) - \frac{(\Gamma_1^2 - 1)^{1/2}}{\mathrm{i}(\xi_1 + \xi)_+}\right] = \left[\Gamma^4(\xi) - \frac{1}{\Omega_1^2}\right] P_{+z}(\xi) + \frac{\epsilon_1}{\Omega_1^3} P_+(\xi) - \mathcal{R}^-(\xi). \qquad (6.5.1)$$

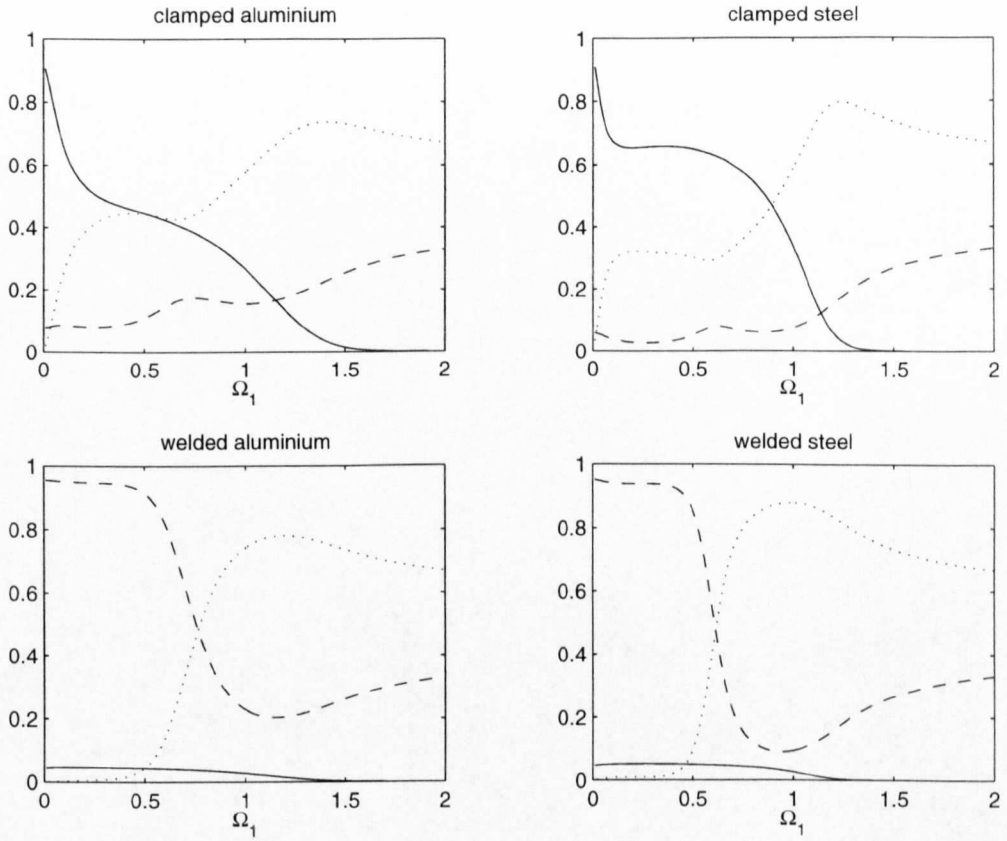

Figure 6.10. The energy distribution at the clamped and welded junction of aluminium-aluminium and steel-steel plates (Norris & Wickham, 1995; Brazier–Smith, 1987); $h_2 = 2h_1$. $P_R(—)$, $P_T(- -)$, $P_A(\cdots)$.

In this case, our entire function, $E(\xi)$, is $O(\xi)$ when $|\xi| \to \infty$, for *all* edge conditions in Appendix 6.B. Hence,

$$P_{-z}(\xi) = \frac{E_1\xi + E_0}{\mathcal{K}_{1-}(\xi)} + \frac{(\Gamma_1^2 - 1)^{1/2}}{\mathrm{i}(\xi_1 + \xi)_+}\left[1 - \frac{\mathcal{K}_{1+}(\xi_1)}{\mathcal{K}_{1-}(\xi)}\right] \tag{6.5.2}$$

and

$$\frac{\epsilon_1}{\Omega_1^3}P_+(\xi) = \mathcal{K}_{1+}(\xi)(E_1\xi + E_0) - \frac{(\Gamma_1^2 - 1)^{1/2}}{\mathrm{i}(\xi_1 + \xi)_+}\left[\mathcal{K}_{1+}(\xi)\mathcal{K}_{1+}(\xi_1) - \Gamma^4(\xi) + \frac{1}{\Omega_1^2}\right] + \mathcal{R}^-(\xi). \tag{6.5.3}$$

If we take the edge to be clamped, it transpires that $E_1 = E_0 = 0$, and so

$$P(\xi, z) = \frac{(\Gamma_1^2 - 1)^{1/2}}{[\Gamma^2(\xi) - 1]^{1/2}} \frac{\mathcal{K}_{1+}(\xi_1)}{\mathrm{i}(\xi + \xi_1)_+ \mathcal{K}_{1-}(\xi)} \exp\left[-\left(\Gamma^2(\xi) - 1\right)^{1/2} z\right]. \tag{6.5.4}$$

In the construction of the inverse transform, the residue contribution at $\xi = \xi_1$ then gives

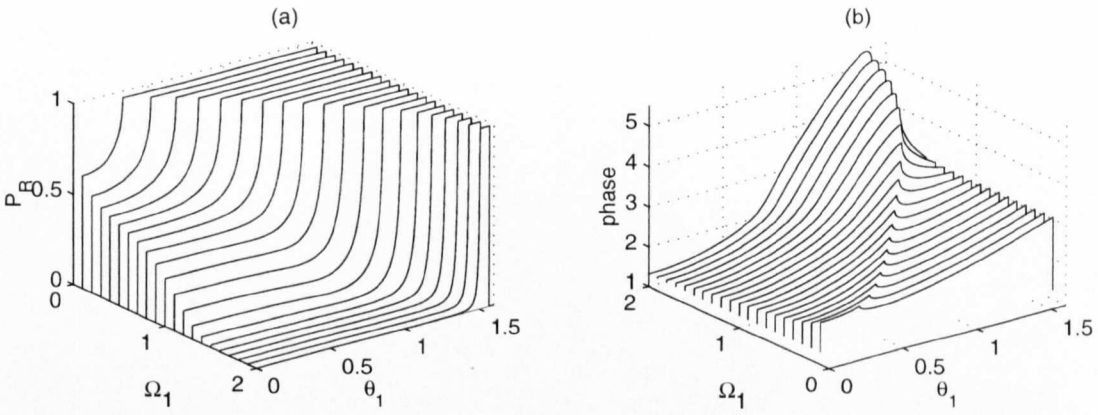

Figure 6.11. The reflected power $P_R \equiv |R|^2$, panel (a), and the phase, panel (b), versus angle of incidence and frequency for an elastic aluminium plate clamped to a rigid plate.

the reflected wave:

$$p(x,z) = \frac{\mathcal{K}_{1+}^2(\xi_1)}{2\xi_1 \mathcal{K}_1'(\xi_1)} \exp\left[-(\Gamma_1^2 - 1)^{1/2} z - \mathrm{i}\xi_1 x\right]. \tag{6.5.5}$$

Consequently, the reflection coefficient, R, is

$$R = \frac{\mathcal{K}_{1+}^2(\xi_1)}{2\xi_1 \mathcal{K}_1'(\xi_1)} = |R| \exp(\mathrm{i}\psi). \tag{6.5.6}$$

Some results contained in Appendix 6.A (equation (6.A 7)) indicate that $|R| = 1$ for $\kappa > 1$. Thus, when the component of the flexural wavespeed in the longitudinal direction is subsonic relative to the acoustic wave speed, all the scattered energy is reflected back along the plate. But there is scattering into acoustic waves when $\kappa < 1$.

The reflected power and phase shift ψ are shown in Figure 6.11 for various values of the angle of incidence θ_1 (hence κ) and Ω_1 (the non-dimensional frequency). It is worth noting the similarity between the reflected power in Figure 6.11 and that in panel (b) of Figure 6.4 for the aluminium-steel plates. This suggests that changing the type of plate in $x > 0$ can alter the distribution of power scattered into the transmitted and acoustic fields, but leaves the reflected power largely unchanged.

As Ω_1 increases, θ_a also increases, and so the range of θ_1 over which total reflection occurs becomes smaller. Indeed, for large Ω_1, the scattered wave energy is primarily concentrated in the fluid, leading to the large forward lobe in the directivity (Figure 6.12). As we approach higher frequencies, another peak emerges in the backward direction along the critical angle linked to the leaky zero of the plate dispersion relation (see Section 6.5.4). The peak is 'sharpest' for normal incidence; this is also seen later in Figure 6.17.

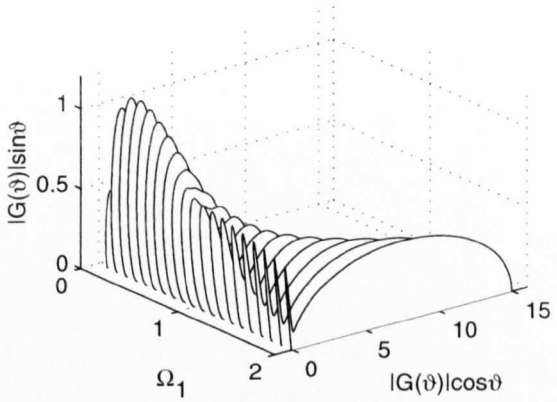

Figure 6.12. The modulus of the directivity $|G(\vartheta)|$ for an elastic aluminium plate clamped to a rigid plate as a function of the dimensionless frequency, Ω_1, which ranges from 0.1 to 2.0 in steps of 0.1. The angle of incidence is $\theta_1 = \pi/12$.

6.5.2. *Soft plate*

If the plate on $x > 0$ is now taken to be acoustically soft, then the boundary condition for $x > 0$ on $z = 0$ becomes $p(x,0) = -p^{inc}(x,0)$. In this limiting case, $\mathcal{K}_2(\xi) \sim -\epsilon_2/\mathcal{G}(\xi)\Omega_2^3$ with $\mathcal{G}(\xi) = (\xi^2+\kappa^2-1)^{\frac{1}{2}} = (\xi+\sqrt{\kappa^2-1})^{\frac{1}{2}}(\xi-\sqrt{\kappa^2-1})^{\frac{1}{2}} \equiv \mathcal{G}_+(\xi)\mathcal{G}_-(\xi)$; and $\mathcal{G}_-(\xi) = -\mathrm{i}\mathcal{G}_+(-\xi)$. Moreover, $P_+(\xi)$ is defined by $P_+(\xi) = -\mathrm{i}/(\xi+\xi_1)$ and the functional equation reduces to

$$E_1\xi + E_0 = \mathcal{G}_-(\xi)\mathcal{K}_{1-}(\xi)P_-(\xi) + \frac{[-\mathrm{i}\mathcal{G}_-(\xi)\mathcal{K}_{1-}(\xi) + \mathcal{G}_+(\xi_1)\mathcal{K}_{1+}(\xi_1)]}{(\xi+\xi_1)_+}$$

$$= \frac{1}{\mathcal{K}_{1+}(\xi)\mathcal{G}_+(\xi)}\left\{\mathcal{R}^-(\xi) - \frac{\epsilon_1}{\Omega_1^3\mathrm{i}(\xi+\xi_1)_+} - \left[\Gamma^4(\xi) - \frac{1}{\Omega_1^2}\right]P_{+z}(\xi)\right\} + \frac{\mathcal{G}_+(\xi_1)\mathcal{K}_{1+}(\xi_1)}{(\xi+\xi_1)_+}, \tag{6.5.7}$$

where the entire function $E(\xi)$ is again linear for all edge conditions, and we remind the reader that

$$\mathcal{R}^-(\xi) = p_{zxxx}(0^-,0) - \mathrm{i}\xi p_{zxx}(0^-,0) - (2\kappa^2+\xi^2)p_{zx}(0^-,0) + \mathrm{i}\xi(2\kappa^2+\xi^2)p_z(0^-,0). \tag{6.5.8}$$

Thus $P_{\pm z}(\xi)$ can again be isolated from the functional equation. But, as in the full problem described above, these functions are only analytic in the respective regions of the complex plane if we satisfy some simultaneous equations. In the case at hand, these equations are

$$\mathcal{R}^-(\chi) - \frac{\epsilon_1}{\Omega_1^3\mathrm{i}(\chi+\xi_1)_+} - \mathcal{K}_{1+}(\chi)\mathcal{G}_+(\chi)\left[E_1\chi + E_0 - \frac{\mathcal{G}_+(\xi_1)\mathcal{K}_{1+}(\xi_1)}{(\chi+\xi_1)_+}\right] = 0 \tag{6.5.9}$$

where χ takes each of the four values satisfying, $\Gamma^4(\chi) - 1/\Omega_1^2 = 0$. By solving these equations, we determine E_0 and E_1 and the two free constants in $\mathcal{R}^-$ that remain after applying edge conditions.

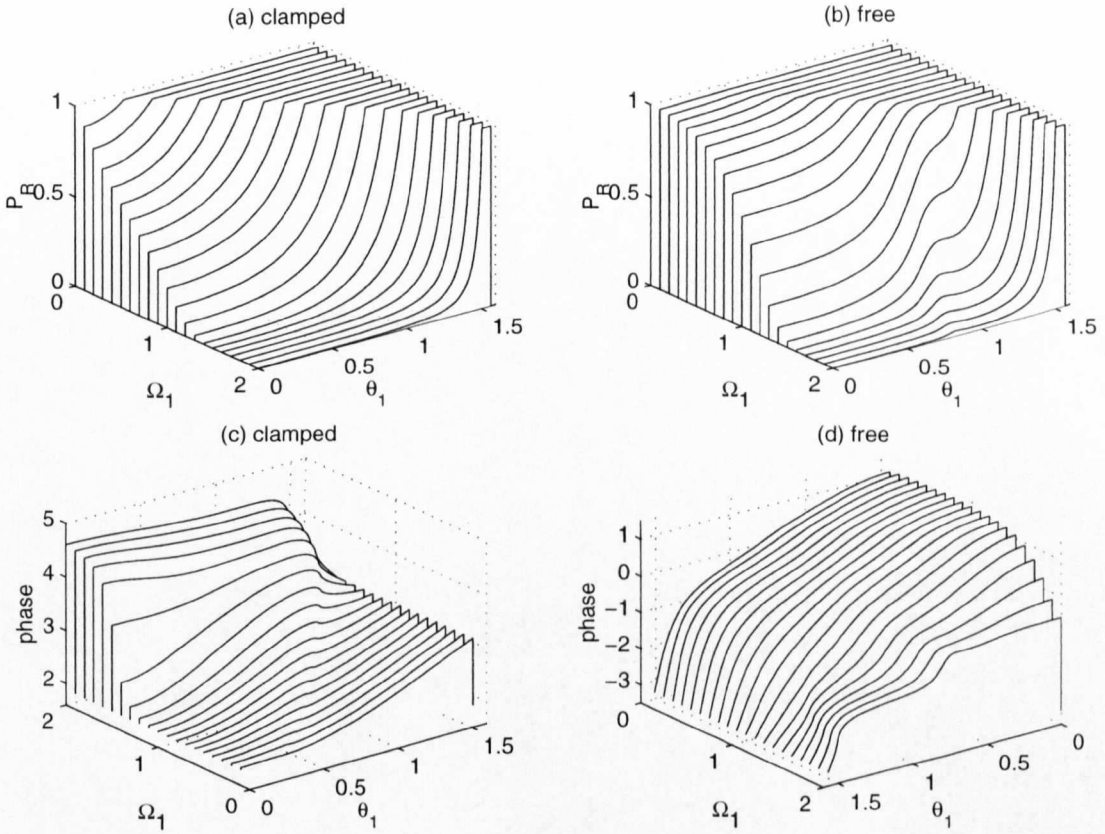

Figure 6.13. The modulus and phase of the reflection coefficient for an elastic aluminium plate either freely attached or clamped to an acoustically soft plate. The reflected power P_R is shown in panels (a) and (b) and the phase in panels (c) and (d) versus angle of incidence and frequency.

Finally, the reflection coefficient is

$$R = \frac{\mathrm{i}\mathcal{K}_{1+}(\xi_1)}{\mathcal{G}_-(\xi_1)\mathcal{K}_1'(\xi_1)}\left[E_1\xi_1 + E_0 - \frac{\mathcal{G}_+(\xi_1)\mathcal{K}_{1+}(\xi_1)}{2\xi_1}\right]; \tag{6.5.10}$$

the plate in $x > 0$ does not support flexural waves, thus $T = 0$.

The reflected power, phase shift, and directivity are plotted in Figures 6.13–6.14 for clamped and free junctions. It is striking that even in this special case, the condition of the junction greatly influences the scattering properties. The free edge radiates less energy in the fluid, but the peaks in the directivity (Figure 6.14b), are much more pronounced than for the clamped edges (Figure 6.14a).

Note that in the two extremes of rigid and acoustically soft plates, the distributions of power converted into reflected waves are similar, although the phases on reflection are not. The acoustic directivity patterns are also quite different; in the acoustically soft case there is no scatter in the direction of the plate and the orientation of the lobe in $0 < \vartheta < \pi/2$ largely obscures the other, sharper peaks.

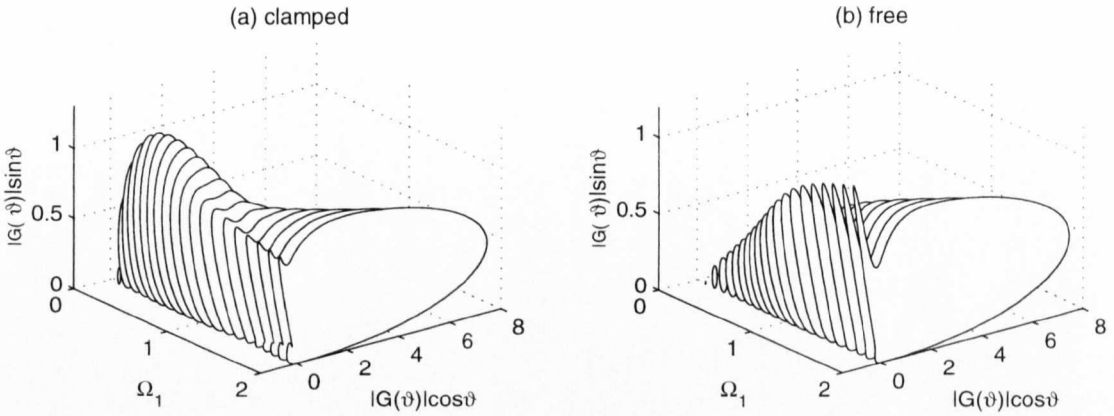

Figure 6.14. Representative directivities for $|G(\vartheta)|$ with $\theta_1 = \pi/12$ versus Ω_1 for an elastic aluminium plate freely attached or clamped to an acoustically soft plate.

6.5.3. *Identical plates*

We now take the two plates to be constructed of identical material, but retain a junction at $x = 0$. This makes our problem equivalent to scattering in an infinite plate with a line constraint or gap. For normal incidence, such examples have been treated by Howe (1986, 1994b). For oblique incidence, we take the appropriate limits of the formulae above. Then

$$P_z(\xi) = -\frac{[E(\xi) + \mathrm{i}\gamma_1 \mathcal{K}_1'(\xi_1)]}{\mathcal{K}_1(\xi)}, \tag{6.5.11}$$

and there is no longer any need for a Wiener–Hopf analysis. For brevity we give the results in the clamped case when $E(\xi)$ is linear in ξ; E_0 and E_1 emerge explicitly as

$$E_1 = \xi_1\gamma_1 \left[\frac{1}{2\pi}\int_C \frac{\xi^2}{\mathcal{K}_1(\xi)}\mathrm{d}\xi\right]^{-1}, \quad E_0 = -\mathrm{i}\gamma_1\mathcal{K}_1'(\xi_1) - \gamma_1\left[\frac{1}{2\pi}\int_C \frac{\mathrm{d}\xi}{\mathcal{K}_1(\xi)}\right]^{-1}, \tag{6.5.12}$$

from which it is straightforward to determine that

$$\begin{aligned} R &= \mathrm{i}\frac{(E_1\xi_1 + E_0)}{\gamma_1\mathcal{K}_1'(\xi_1)} - 1, \quad T = -\mathrm{i}\frac{(E_1\xi_1 - E_0)}{\gamma_1\mathcal{K}_1'(\xi_1)}, \\ G(\vartheta) &= -\mathrm{i}\left[\frac{-E_1\lambda\cos\vartheta + E_0 + i\gamma_1\mathcal{K}_1'(\xi_1)}{2\mathcal{K}_1(\lambda\cos\vartheta)}\right]. \end{aligned} \tag{6.5.13}$$

In this example, because the two plates are identical, only the acoustic cut-off angle, θ_a is present; $G(\vartheta) = 0$ for $\kappa > 1$, and then $|R|^2 + |T|^2 = 1$. However, there is also a second type of cut-off angle that is associated with the leaky waves that give rise to the sharp peaks in acoustic directivity, when $\kappa < 1$. We describe this second angular cut-off in more detail in Section 6.5.4.

The proportion of power converted to reflected waves, as shown in Figure 6.15, is very similar to previous figures for clamped plates. The main consequence of the identical

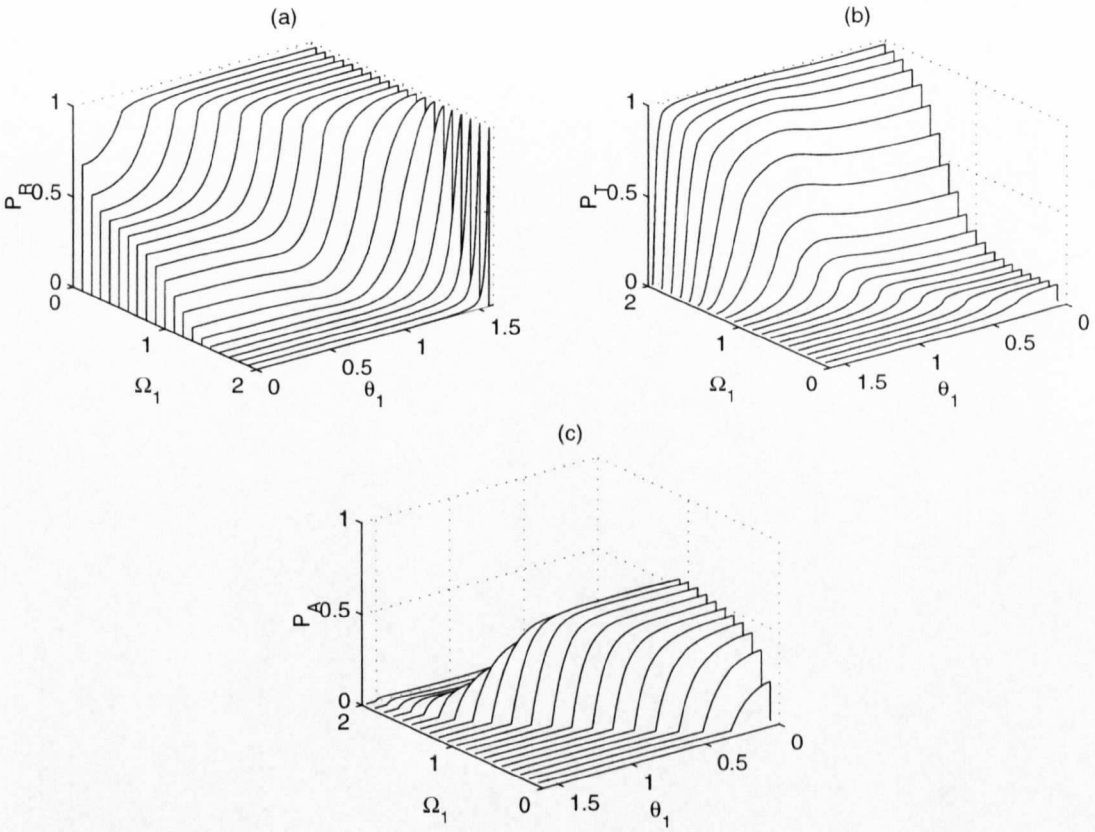

Figure 6.15. The partition of scattered powers P_R, P_T and P_A for an infinite elastic aluminium plate with a clamped joint. The non-dimensional frequency Ω_1 ranges from 0.1 to 2.0 in steps of 0.1.

plate in $x > 0$ is that, as the frequency increases, the majority of the scattered power is converted to the transmitted flexural plate waves.

Figure 6.16 compares directivities for a clamped junction in aluminium and steel plates. The distributions are similar, but as ϵ is smaller for steel plates, there are more prominent sharp peaks associated with leaky waves. Also, the large forward scatter prominent in previous examples is absent in this figure because of the lack of material contrast.

The results described above are for a closed gap. Open gaps with normal incidence are treated by Howe (1994b) and one can generalise that analysis to oblique incidence in a straightforward manner using the methodology outlined above.

6.5.4. *Light fluid loading*

In the light fluid loading limit, $\epsilon_j \ll 1$ and $\Omega_j > 1$, two complex zeros of the dispersion relation $\mathcal{K}_j(\xi)$, at $\pm k_j^l$, are associated with leaky waves. These disturbances (which are

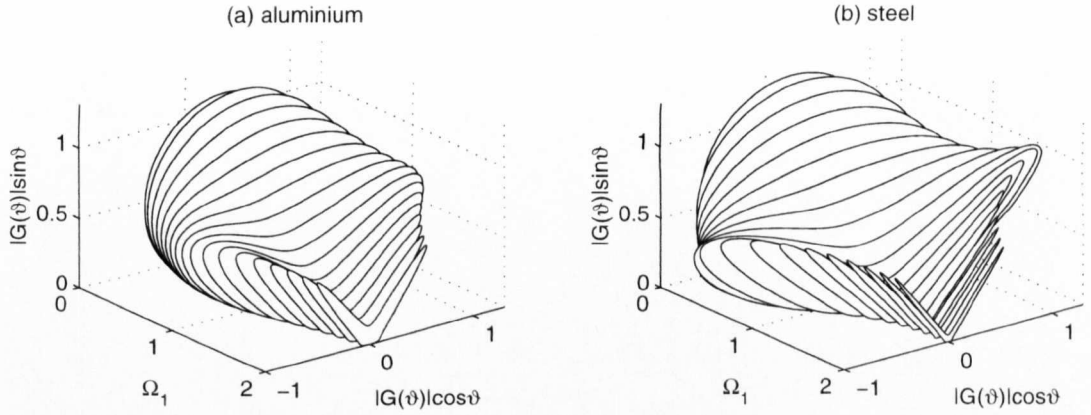

Figure 6.16. The modulus of the directivity $|G(\vartheta)|$ for an elastic aluminium plate, panel (a), and a steel plate, panel (b), with a clamped joint.

not strictly individual waves in their own right) are related to certain flexural waves of the plate if it were *in vacuo*. These waves disappear on the addition of fluid loading, but they nevertheless leave behind a remnant signal, commonly referred to as leaky waves. Moreover, provided the *in vacuo* flexural wavespeed is greater than the acoustic wavespeed, then energy is shed into the fluid along a certain angle (Crighton, 1979). This leads to distinctive beaming along that angle, and the directivity develops sharp peaks.

In the case of oblique incidence,

$$k_j^l = \left(\Omega_j^{-1} - \kappa^2\right)^{\frac{1}{2}} + \frac{\mathrm{i}\epsilon_j}{4\Omega_j^2}\left(\Omega_j^{-1} - \kappa^2\right)^{-\frac{1}{2}}\left(1 - \Omega_j^{-1}\right)^{-\frac{1}{2}}, \tag{6.5.14}$$

and by modifying the analysis of Crighton (1979), one finds the special angles to be

$$\vartheta_{Bj} \sim \cos^{-1}\left[\left(\Omega_j^{-1} - \kappa^2\right)/(1 - \kappa^2)\right]^{\frac{1}{2}} \tag{6.5.15}$$

(as measured in the cylindrical polar coordinates based at the plate junction).

This angle exists only if $1/\Omega_j > \kappa^2$ and $\kappa < 1$, which is not automatic. Indeed, as we increase the angle of incidence, the beam of leaky waves eventually cuts off. In other words, oblique incidence introduces a second kind of critical angle associated with the disappearance of peaks in the directivity corresponding to leaky waves. We illustrate this cut off in Figure 6.17: As one varies the angle of incidence past $\theta_B \sim 0.7833$ the leaky-wave peaks disappear and the directivity becomes a featureless lobe.

This example shows a case in which there are both forward and backward peaks in directivity, which transpires because the plates are identical. In Figure 6.18, we show a case with material contrast. In this second example, the plate along $x < 0$ has $\Omega_1 < 1$ and does not radiate energy in leaky waves, but there are forward peaks in the acoustic

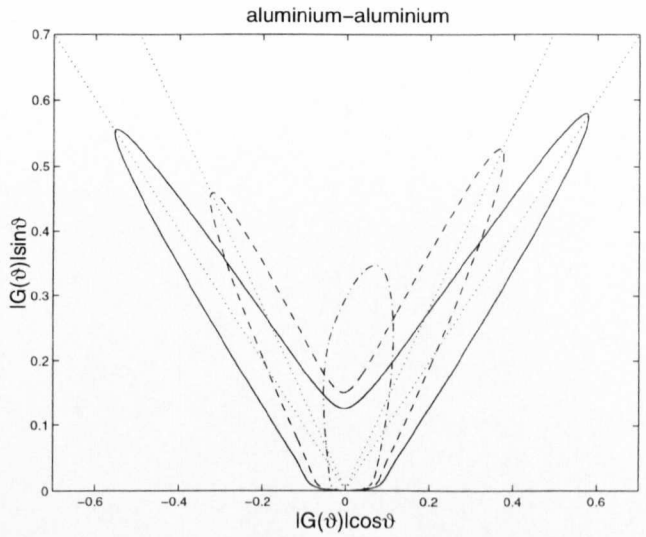

Figure 6.17. The modulus of the directivity $|G(\vartheta)|$ in the light fluid loading limit. The directivity is shown for the clamped joint of identical (aluminium) plates for angles of incidence $\theta_1 = 0(—)$, $\pi/6(- -)$, and $\pi/4(- \cdot)$ with $\Omega_1 = 2.0$. The angles from (6.5.15) are shown as dotted lines.

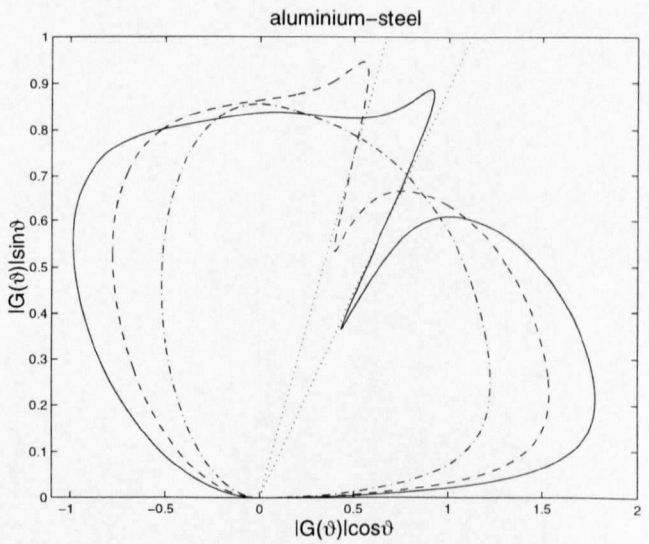

Figure 6.18. The modulus of the directivity $|G(\vartheta)|$ in the light fluid loading limit. The directivity is shown for the clamped joint of aluminium-steel plates ($h_2 = 2.0h_1$) for angles of incidence $\theta_1 = 0(—)$, $\pi/6(- -)$, and $\pi/4(- \cdot)$ with $\Omega_1 = 0.9$. The angles from (6.5.15) are shown as dotted lines.

directivity associated with leaky waves in the other plate. But these peaks disappear as we increase the angle of incidence. With a suitable choice of materials we could also find cases in which there are only backward peaks in directivity (that are again removable by changing θ_1).

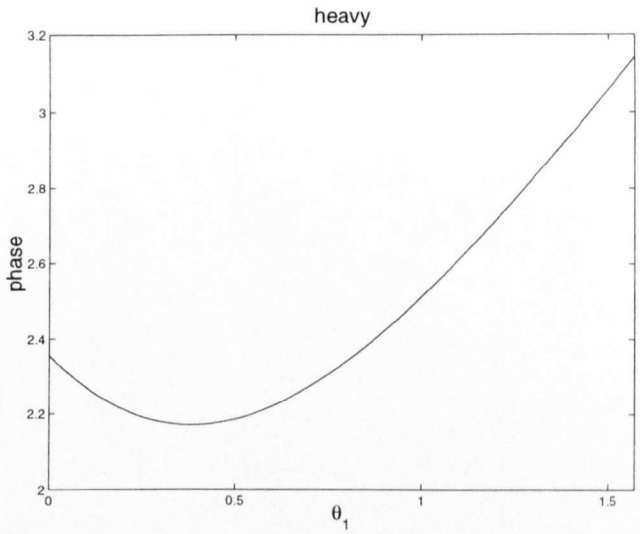

Figure 6.19. The phase change in R as the angle of incidence changes for an aluminium plate clamped to a rigid plate.

6.5.5. *Heavy fluid loading*

The heavy fluid loading limit, $\epsilon_j \ll 1$ and $\Omega_j^2 \ll \epsilon$, can be approached either directly from the governing equations (Crighton & Innes, 1984), or from a reduction of our non-dimensional equations. The main feature this limit is that structural inertia terms disappear and the fluid becomes effectively incompressible. The governing and plate equations in this limit reduce to:

$$\nabla^2 p(x, y, z) = 0 \tag{6.5.16}$$

in $z > 0$, and

$$\left(\frac{\partial^2}{\partial x^2} - \kappa^2\right)^2 \frac{\partial p}{\partial z}(x, 0) + N_j p(x, 0) = \begin{cases} 0 & \text{for } x < 0 \\ (N_1 - N_2) \exp(\mathrm{i}\xi_1 x) & \text{for } x > 0 \end{cases}, \tag{6.5.17}$$

with $N_j = \epsilon_j / \Omega_j^3 \equiv \rho\omega^2 / B_j k_0^5$.

For the analysis in the main text, when one approaches this limit, one can make considerable progress using simpler factorisations of the functions $\mathcal{K}_j(\xi)$, as described in Appendix 6.A. However the range of validity is restrictive, as Figure 6.20 demonstrates. This figure is for scattering from the welded junction of aluminium and steel plates when $\theta_i = \pi/6$; for this angle of incidence, $\kappa > 1$ and so the power scattered into the acoustic far field is zero.

If the plate is attached to a rigid baffle, then in this limit, all the incident power is reflected, regardless of incident angle. The only distinguishing feature between different edge conditions is an associated phase change; this is important for resonance behaviour.

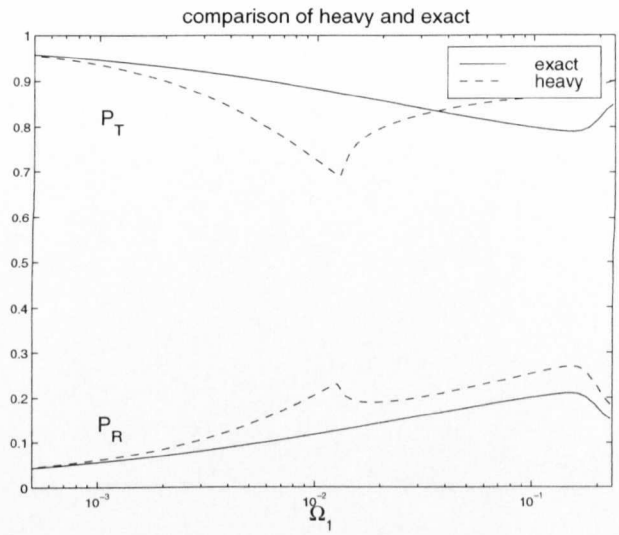

Figure 6.20. A comparison between results deduced using the heavy limit and the full analysis; this is for scattering at a welded aluminium-steel joint (steel plate double the thickness of the aluminium plate) and incident angle $\pi/6$.

Crighton & Innes (1984) detail the phase changes for normal incidence. In Figure 6.19 we show the phase change as the angle of incidence varies for an elastic plate clamped to a rigid plate; the purpose of this is to demonstrate that oblique incidence changes the phase quite dramatically from the value $3\pi/8$ found for normal incidence.

6.6. Concluding remarks

In this chapter, we have provided a general solution for oblique scattering of flexural plate waves upon a plate junction; this general solution encompasses many limiting cases. Although we have concentrated upon clamped and welded edge conditions, the analysis carries through, with minor changes, to other edge conditions. Our main thrust has been to investigate the effect of non-normal flexural wave incidence, as this has been largely ignored in previous studies.

The general trend illustrated by our results is that the reflected power is very similar for all cases involving one kind of joint. The chief effect of altering the properties of the plate in $x > 0$ is to redistribute the proportion of scattered power transmitted into plate waves, or into the scattered acoustic field. As one increases the frequency so that the power is concentrated in the fluid then for identical materials the power is totally converted into the transmitted flexural wave, whereas with a rigid, or soft, plate in $x > 0$ the power is totally converted into the acoustic far field.

Perhaps the most important effect of oblique incidence is the introduction of two types of cut-off angle. The first type is of a geometrical flavour: when the angle of incidence exceeds one threshold, the scattered acoustic power vanishes. There is also sometimes a second threshold beyond which flexural waves are not transmitted. The second type of cut-off is in peaks in the directivity of scattered acoustic power that are associated with leaky waves. By raising the angle of incidence we can also eliminate these peaks.

The occurrence of these cut offs implies that conclusions based upon results for normal incidence may be a little misleading. For example, for welded junctions under normal incidence, there is negligible reflected power. However, for some angles of incidence, perfect reflection can occur; this may lead to resonances developing for several joined plates. Other details, such as the phase change on reflection in the heavy fluid loading limit are also highly dependent upon the angle of incidence.

References

Abrahams, I. D., 1981. Scattering of sound by a heavily loaded finite elastic plate. *Proc. R. Soc. Lond. A* **378**, 89–117.

Balmforth, N. J. & Craster, R. V., 1999. Ocean waves and ice sheets. To appear in *J. Fluid Mech.*

Bradfield, G., 1964. Notes on applied science No. 30 *Use in industry of elasticity measurements in metals with the help of mechanical vibrations*. H.M.S.O, London.

Brazier-Smith, P. R., 1987. The acoustic properties of two co-planar half-plane plates. *Proc. R. Soc. Lond.* A **409**, 115–139.

Cannell, P. A., 1975. Edge scattering of aerodynamic sound by a lightly loaded elastic half-plane. *Proc. R. Soc. Lond.* A **347**, 213–238.

Cannell, P. A., 1976. Acoustic edge scattering by a heavily loaded elastic half-plane. *Proc. R. Soc. Lond.* A **350**, 71–89.

Crighton, D. G., 1979. The free and forced waves on a fluid–loaded elastic plate. *J. Sound Vib.* **63**, 225–235.

Crighton, D. G., 1989. The 1988 Rayleigh medal lecture: fluid loading – the interaction between sound and vibration. *J. Sound Vib.* **133**, 1–27.

Crighton, D. G. & Innes, D., 1983. Low frequency acoustic radiation and vibration response of locally excited fluid-loaded structures. *J. Sound Vib.* **91**, 293–314.

Crighton, D. G. & Innes, D., 1984. The modes, resonances and forced response of elastic structures under heavy fluid loading. *Phil. Trans. R. Soc. Lond.* A **312**, 295–342.

Crighton, D. G. & Maidanik, G., 1981. Acoustic and vibration fields generated by ribs on a fluid-loaded panel, 1: Plane-wave problems for a single rib. *J. Sound Vib.* **75**, 437–452.

Howe, M. S., 1986. Attenuation and diffraction of bending waves at gaps in fluid loaded plates. *IMA J. Appl. Math.* **36**, 247–262.

Howe, M. S., 1994b. Scattering of bending waves by open and closed cracks and joints in a fluid-loaded elastic plate. *Proc. R. Soc. Lond. A* **444**, 555–571.

Junger, M. C. & Feit, D., 1986. *Sound, structures and their interaction*. Acoustical Society of America. Second edition.

Leppington, F. G., 1976. Scattering of sound waves by finite membranes and plates near resonance. *Quart. J. Mech. Appl. Math.* **24**, 527–546.

Leppington, F. G., 1978. Acoustic scattering by membranes and plates with line constraints. *J. Sound Vib.* **58**, 319–332.

Lighthill, M. J., 1958. *Introduction to Fourier analysis and generalised functions*. Cambridge University Press.

Llewellyn–Smith, S. G. & Craster, R. V., 1999. Numerical and asymptotic approaches to scattering problems involving finite elastic plates in structural acoustics. *Wave Motion* **30**, 17–41.

Noble, B., 1958. *Methods based on the Wiener-Hopf technique*.

Norris, A. N. & Wickham, G. R., 1995. Acoustic diffraction from the junction of two plates. *Proc. R. Soc. Lond. A* **451**, 631–655.

Rogoff, Z. M. & Tew, R. H., 1997. Acoustic radiation from a phased line source at a fluid-solid boundary. *IMA J. Appl. Math* **58**, 93–110.

Timoshenko, S. & Woinowsky-Kreiger, S., 1959. *Theory of Plates and Shells*. McGraw-Hill.

Appendix 6.A. Factorisation: for $\mathcal{K}(\xi)$

The purpose of this appendix is to describe the factorisation of the functions $\mathcal{K}_j(\xi)$ (see equation (6.2.10)) required by the Wiener–Hopf method. Because both functions have a similar mathematical form we split both in the same way. Hence we drop the subscript and consider

$$\mathcal{K}(\xi) = \left(\xi^2 + \kappa^2\right)^2 - \frac{1}{\Omega^2} - \frac{\epsilon}{\Omega^3}\left(\xi^2 + \kappa^2 - 1\right)^{-1/2}. \tag{6.A 1}$$

This function must be split into a product of functions that are analytic and non-zero in the upper and lower complex ξ-planes: $\mathcal{K}(\xi) = \mathcal{K}_+(\xi)\mathcal{K}_-(\xi)$. (This terminology is a little loose; strictly speaking, the two regions are the areas above and below the contour of integration of the inverse Fourier transform - see Section 6.3.1.)

We proceed in two complementary ways, first we generate a general formula for the splits that is convenient numerically. Then we deduce some explicit formulae.

The function $\mathcal{K}(\xi)$ typically has two zeros at $\pm\alpha$ that correspond to flexural waves (or edge waves if α is complex), and, depending upon the choice of branch cuts for the function $(\xi^2 + \kappa^2 - 1)^{1/2}$, additional complex roots. The first stage of the factorisation is to take the zeros at $\pm\alpha$ explicitly into account. We also need to make a choice for the branch cuts of $(\xi^2 + \kappa^2 - 1)^{1/2}$. First of all, we take these cuts to be $\pm[\mathrm{i}\sqrt{\kappa^2 - 1}, \mathrm{i}\infty)$ if $\kappa > 1$, or $\pm[\sqrt{1 - \kappa^2} + \mathrm{i}0, \sqrt{1 - \kappa^2} + \mathrm{i}\infty)$ if $\kappa < 1$,

To split the functions in a numerically convenient fashion, consider a new function,

$$\mathcal{R}(\xi) = \frac{\mathcal{K}(\xi)}{(\xi^2 - \alpha^2)(\xi^2 + 1)}. \tag{6.A 2}$$

The product splits for $\mathcal{K}(\xi)$ follow directly from those of $\mathcal{R}(\xi)$. Importantly, this function tends to unity as $|\xi| \to \infty$, and has no zeros on the real axis. Thus we take

$$\log \mathcal{R}_-(\xi) = -\frac{1}{2\pi i}\int_{-\infty+ia}^{\infty+ia} \frac{\log \mathcal{R}(\eta)}{\eta - \xi} d\eta \quad \text{and} \quad \log \mathcal{R}_+(\xi) = \frac{1}{2\pi i}\int_{-\infty-ia}^{\infty-ia} \frac{\log \mathcal{R}(\eta)}{\eta - \xi} d\eta \qquad (6.A\,3)$$

for $-a < \mathrm{Im}(\xi) < a$, where a is some small, real number ($0 < a \ll 1$). Then $\log \mathcal{R}_+ + \log \mathcal{R}_- = \log \mathcal{R}$, provided there are no singularities of $\mathcal{R}(\xi)$ in $-a < \mathrm{Im}(\xi) < a$. This may always be achieved for $\kappa > 1$ by taking a to be sufficiently small. When $\kappa < 1$, we must be careful about the branch cuts of $(\xi^2 + \kappa^2 - 1)^{1/2}$, and we then indent the path of integration in (6.A 3) beneath the branch point on the positive real axis and above that on the negative real axis. Then we may define $\log \mathcal{R}_+ + \log \mathcal{R}_- = \log \mathcal{R}$ in both cases.

We may evaluate the contour integral rather easily by changing the contour of integration. First, we take advantage of the even nature of $\mathcal{R}(\xi)$, to write

$$\log \mathcal{R}_+(\xi) = \frac{1}{\pi i}\int_0^{\infty} \frac{\log \mathcal{R}(\eta)\ \xi}{\eta^2 - \xi^2} d\eta \qquad (6.A\,4)$$

for $\mathrm{Im}(\xi) > 0$ (and similarly for $\log \mathcal{R}_-$). Then, we deform the contour of integration such that it runs from the origin to infinity along a line of slope $-\pi/4$. This is permissible as the wedge shaped region between this line and the real axis encloses no zeros, and one can use Cauchy's residue theorem and the known behaviour at infinity. Finally, we map this semi-infinite line onto a finite interval $[0, 1]$ and the resulting quadrature is then simply and rapidly achieved; this is equivalent to a change of variable $\eta = e^{-i\pi/4} q/(1-q)$ where $0 \le q \le 1$ in (6.A 4). A similar change of variable can be used to enable us to evaluate $\log \mathcal{R}_-$ just as easily.

This numerical construction of the product split is adequate for most purposes. However in some particular parameter regimes, and for limiting or asymptotic cases it is convenient to have more explicit formulae. We derive these formulae differently in the two cases, $\kappa < 1$ and $\kappa > 1$.

(i) $\kappa > 1$

With our current choice of branch cuts for $(\xi^2 + \kappa^2 - 1)^{1/2}$, the function $\mathcal{K}(\xi)$ has two real zeros at $\pm\alpha$ (for some values of Ω and ϵ the continuation of these real roots are purely imaginary and have modulus $< (\kappa^2 - 1)^{1/2}$) and a quartet of complex zeros at $\pm\delta, \pm\delta^*$. Thus we define a function,

$$\mathcal{Q}(\xi) = \frac{(\xi^2 + \kappa^2 - 1)\mathcal{K}(\xi)}{(\xi^2 - \alpha^2)(\xi^2 - \delta^2)(\xi^2 - \delta^{*2})}. \qquad (6.A\,5)$$

Now $\mathcal{Q}(\xi)$ has no zeros in the cut plane and $\mathcal{Q}(\xi) \to 1$ as $|\xi| \to \infty$. It is now straightforward to show that

$$\mathcal{Q}_\pm(\xi) = \exp\left[-\frac{1}{\pi}\int_{\sqrt{\kappa^2-1}}^{\infty} \cot^{-1}\left(\frac{\Omega^3}{\epsilon}(\eta^2 - \kappa^2 + 1)^{\frac{1}{2}}[(\eta^2 - \kappa^2)^2 - 1/\Omega^2]\right) \frac{d\eta}{\eta \mp i\xi}\right]. \qquad (6.A\,6)$$

Note that for real ξ,

$$|\mathcal{K}_+(\xi)| = \left|\frac{\mathcal{K}(\xi)(\xi + \alpha)}{(\xi - \alpha)}\right|^{\frac{1}{2}}, \qquad (6.A\,7)$$

which emerges by using the following observation: $\mathcal{Q}(\xi)$ is even in ξ, and so $\mathcal{Q}_+(\xi) = \mathcal{Q}_-(-\xi)$. Thus, for real ξ, $|\mathcal{Q}_+(\xi)|^2 = |\mathcal{Q}(\xi)|$; the result then follows. This result is useful as it proves that $|R| = 1$ for certain of the cases in the text, and because it allows explicit results to be deduced in the limits of light and heavy fluid loading.

In the heavy fluid-loading limit, we rescale, $\zeta = \xi/N^{1/5}$ ($N = \epsilon/\Omega^3$) and then

$$\mathcal{K}(\xi) = \Gamma^4(\xi) - N/\Gamma(\xi) = N^{4/5}K(\zeta), \tag{6.A 8}$$

with $K(\zeta) = \gamma^4(\zeta) - 1/\gamma(\zeta)$, and $\gamma^2(\zeta) = \zeta^2 + \sin^2\theta_1$. The splits for this function are expedited by explicit formulae for the roots of the dispersion relation: $\pm\cos\theta_1$, $\pm\delta$, and $\pm\delta^*$ where $\delta = (e^{4\pi i/5} - \sin^2\theta_1)^{1/2} = q^{1/2} = |q|^{1/2}e^{i\psi/2}$ (with the branch taken such that $\mathrm{Re}(\delta) > 0$). Then, the rescaled $Q(\xi)$ ($= N^{-4/5}\mathcal{Q}(\xi)$) has simple product splits in the form

$$Q_\pm(\zeta) = \exp\left\{-\frac{1}{\pi}\int_{\sin\theta_1}^{\infty} \cot^{-1}\left[(\eta^2 - \sin^2\theta_1)^{\frac{5}{2}}\right]\frac{\mathrm{d}\eta}{\eta \mp \mathrm{i}\zeta}\right\}. \tag{6.A 9}$$

In the text, we require the split functions to be evaluated at specific points. In particular it is useful to note that, if $\zeta = \cos\theta_1$, then, from (6.A 7),

$$|K_+(\cos\theta_1)| = 10^{\frac{1}{2}}\cos\theta_1, \tag{6.A 10}$$

and

$$\begin{aligned}\arg[K_+(\cos\theta_1)] = \frac{1}{\pi}\int_{\sin\theta_1}^{\infty} \frac{5p(p^2 - \sin^2\theta_1)^{\frac{3}{2}}}{(p^2 - \sin^2\theta_1)^5 + 1}\tan^{-1}\left(\frac{\sin\theta_1}{p}\right)\mathrm{d}p \\ + \tan^{-1}\left(\frac{2\cos\theta_1 \sin\frac{\psi}{2}|q|^{\frac{1}{2}}}{\cos^2\theta_1 - |q|}\right) - \frac{\theta_1}{2} + \frac{3\pi}{4}.\end{aligned} \tag{6.A 11}$$

This last formula is useful for computations of phase and can be approximated for $\theta_1 \ll 1$ or $\theta_1 \sim \pi/2$. Explicitly, if $\theta_1 = 0$ then the argument is $3\pi/8$, and if $\theta_1 = \pi/2$, the argument is $\pi/2$. Also

$$|K_+(\beta^{1/5}\cos\theta)| = \left[\beta^{-\frac{1}{5}}(\beta - 1)\frac{(\beta^{\frac{1}{5}}\cos\theta + \cos\theta_1)}{(\beta^{\frac{1}{5}}\cos\theta - \cos\theta_1)}\right]^{\frac{1}{2}}, \tag{6.A 12}$$

where $\beta^{1/5}\cos\theta$ is the positive real root of $\Gamma^5(\xi) = \beta$ with $\kappa = \beta^{1/5}\sin\theta$.

(ii) $\kappa < 1$

In a similar manner we can extract an explicit factorisation for $\kappa < 1$. But this time it is more convenient to take the branch cuts of $(\xi^2 + \kappa^2 - 1)^{1/2}$ to lie along the real axis. The function $\mathcal{K}(\xi)$ then has two real zeros at $\pm\alpha$ which now lie on the branch cuts. In addition there are four complex zeros. Two of these zeros, $\pm k_l$ are associated with leaky waves. The remaining two zeros, at $\pm\mu$ lie close to the imaginary axis. We take

$$\mathcal{Q}(\xi) = \frac{(\xi^2 + \kappa^2 - 1)\mathcal{K}(\xi)}{(\xi^2 - \alpha^2)(\xi^2 - k_l^2)(\xi^2 - \mu^2)}. \tag{6.A 13}$$

Now $\mathcal{Q}(\xi)$ has no zeros in the cut plane and $\mathcal{Q}(\xi) \to 1$ as $|\xi| \to \infty$. Using Cauchy's integral

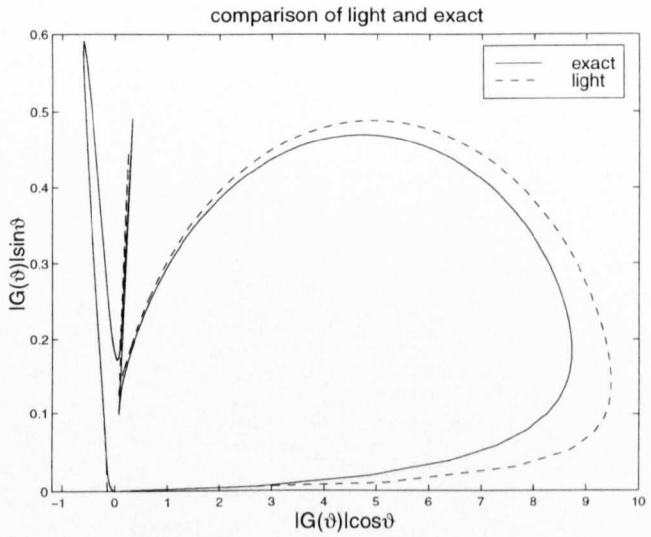

Figure 6.21. A comparison between results deduced for the directivity using an approximate factorisation in the light limit and the full analysis; this is for scattering at a clamped aluminium-steel joint (steel plate double the thickness of the aluminium plate), incident angle $\pi/12$, and non-dimensional frequency $\Omega_1 = 1.8$.

formula it is straightforward to show that

$$\mathcal{Q}_-(\xi) = \left[\frac{\xi - (1-\kappa^2)^{1/2}}{\xi - \alpha}\right]^{\frac{1}{2}} \times \exp\left[-\frac{1}{2\pi i}\int_{\sqrt{1-\kappa^2}}^{\infty} \log\left|\frac{\left(\eta^2+\kappa^2\right)^2 - \frac{1}{\Omega^2} - \frac{\epsilon}{\Omega^3}\left(\eta^2+\kappa^2-1\right)^{-1/2}}{\left(\eta^2+\kappa^2\right)^2 - \frac{1}{\Omega^2} + \frac{\epsilon}{\Omega^3}\left(\eta^2+\kappa^2-1\right)^{-1/2}}\right| \frac{\mathrm{d}\eta}{\eta - \xi}\right]. \tag{6.A 14}$$

In the light fluid-loading limit, $\epsilon/\Omega \ll 1$ and so $\mathcal{Q}_\pm(\xi) \sim 1$. Hence, an asymptotic factorisation is simply achieved using the zeros of the dispersion relation:

$$\mathcal{K}_+(\xi) \sim (\xi + k_l)(\xi + \mu). \tag{6.A 15}$$

Note that $\alpha \sim (1-\kappa^2)^{\frac{1}{2}} + O(\epsilon)$ in this limit.

The details of the full Wiener–Hopf factorisation described above are admittedly a little technical. However, there are also some approximate formulae available that can provide adequate results (Llewellyn–Smith & Craster 1999). These approximations contain no contour integrals and involve only finding the roots of the dispersion relation, in the light fluid loading limit. A brief comparison between these results and the full analysis is shown in Figure 6.21.

Appendix 6.B. Edge conditions

In the text, we outline a general solution to the scattering problem that is independent of the precise edge conditions that we impose at the junction. But in any illustration, we must use explicit conditions (Timoshenko & Woinowsky-Kreiger, 1959). If we define $0_j = 0^\pm$ for $j = 1, 2,$

and use $[\![X(\xi)]\!]$ to denote the jump in $X(\xi)$ across the edge from $\xi = 0^+$ to $\xi = 0^-$, then the following are four commonly applied edge conditions.

- *Clamped edges* Both the displacement and rotation vanish on either side of $x = 0$:

$$p_z(0^-,0) = p_z(0^+,0) = \gamma_1, \quad p_{zx}(0^-,0) = p_{zx}(0^+,0) = \mathrm{i}\xi_1\gamma_1. \tag{6.B 1}$$

- *Welded edges* Continuity of the displacement, rotation, bending moment, and shear force at $x = 0$:

$$p_z(0^-,0) = p_z(0^+,0), \quad \left[\!\!\left[\frac{\Omega_j^3}{\epsilon_j}\left(\partial_x^2 - (2-\nu_j)\kappa^2\right) p_{zx}(0_j,0)\right]\!\!\right] = -\mathrm{i}\xi_1\gamma_1 \left[\!\!\left[\frac{\Omega_j^3}{\epsilon_j}[\xi_1^2 + (2-\nu_j)\kappa^2]\right]\!\!\right], \tag{6.B 2}$$

$$p_{zx}(0^-,0) = p_{zx}(0^+,0), \quad \left[\!\!\left[\frac{\Omega_j^3}{\epsilon_j}\left(\partial_x^2 - \nu_j\kappa^2\right) p_z(0_j,0)\right]\!\!\right] = -\gamma_1 \left[\!\!\left[\frac{\Omega_j^3}{\epsilon_j}[\xi_1^2 + \nu_j\kappa^2]\right]\!\!\right]. \tag{6.B 3}$$

- *Free edges* The bending moment and force are zero at either side of $x = 0$:

$$(\partial_x^2 - \nu_j\kappa^2)p_z(0_j,0) = -\gamma_1(\xi_1^2 + \nu_j\kappa^2), \; [\partial_x^2 - (2-\nu_j)\kappa^2]p_{zx}(0_j,0) = -\mathrm{i}\xi_1\gamma_1[\xi_1^2 + (2-\nu_j)\kappa^2]. \tag{6.B 4}$$

- *Hinged edges* The displacement and force are continuous across $x = 0$ and the bending moments are zero either side of $x = 0$:

$$p_z(0^-,0) = p_z(0^+,0), \quad (\partial_x^2 - \nu_j\kappa^2)p_z(0_j,0) = -\gamma_1(\xi_1^2 + \nu_j\kappa^2), \tag{6.B 5}$$

$$\left[\!\!\left[\frac{\Omega_j^3}{\epsilon_j}\left[\partial_x^2 - (2-\nu_j)\kappa^2\right] p_{zx}(0_j,0)\right]\!\!\right] = -\mathrm{i}\xi_1\gamma_1 \left[\!\!\left[\frac{\Omega_j^3}{\epsilon_j}[\xi_1^2 + (2-\nu_j)\kappa^2]\right]\!\!\right]. \tag{6.B 6}$$

Chapter Seven

A reciprocity relation between plane and flexural plate waves scattered by rigid defects

7.1. Introduction

The diffraction of acoustic, flexural or leaky waves from inhomogeneities embedded in elastic plates or shells is important in any description of scattering by a fluid-loaded structure. The waves scattered from these defects generate sound in the fluid, and scattered flexural plate or leaky waves are also responsible for further sound generation via interaction with other material inhomogeneities. Numerical and analytical studies of these problems are often complicated by geometrical considerations and edge conditions that are required at sharp structural changes. Our aim here is to derive, and apply, a reciprocity relation that should be a useful tool for both checking results, and for reducing computational effort in parametric studies.

Reciprocity theorems have a long history in acoustics, electromagnetism and elasticity notably initiated by Helmholtz and Rayleigh amongst others. Many of these reciprocity theorems involve two scattering problems found by interchanging the position of a source and receiver; thus relations between the two states are deduced, and these are particularly useful in structural acoustics, say, scattering from an elastic sphere or cylinder (Junger & Feit, 1986, pp. 376).

A closely related reciprocity result is often used in acoustics, and in a more complicated guise in elasticity. In the latter case several different body waves (both shear and compression), surface waves and mode conversion at interfaces often lead to complicated analysis; it is well-worth having subsidiary results to act as check. If one is interested in scattering by an obstacle, of arbitrary shape or cross section, say, a crack or void, then reciprocity relations have been deduced for obstacles in an infinite isotropic elastic domain (Tan, 1977; Varatharajulu, 1977), an elastic half space (Mei, 1978; Neerhoff, 1980; Rogoff, 1993) or coupled fluid-solid media (Craster, 1998). Typically these reciprocity theorems are concerned with relating one aspect of the solution of one problem to another aspect of a second problem. It is usual to explore how one relates the scattered far field angular coefficient (the directivity) associated with a scattered cylindrical wave, or the amplitude of a scattered surface wave, that is generated by one type of incident wave (the first problem) to the scattered far field coefficient generated by another incident wave (the second problem); the incident waves in isotropic elasticity could be either

plane compressional or shear body waves, surface Rayleigh waves or interfacial Stoneley waves.

A typical relation would emerge from analysing the scattered shear directivity, say, generated by an incident plane compressional wave upon a defect to the scattered compressional directivity generated by an incident plane shear wave. If we have a half space or joined elastic media then other relations occur with, and between, the other waves of interest, that is, surface or interfacial waves. One can construct several different interrelations each of which forms a useful non-trivial check upon any numerical or analytical work. The theorems are usually quite general and hold for obstacles of arbitrary number, orientation and shape, provided they are compact, that is, in so far as the far-field is concerned they are all clustered near to the origin. These results are particularly useful for checking numerical or analytical results that involve complicated subsidiary calculations, say, the evaluation of Green's functions and solution of coupled integral equations for scattering by sub-surface cracks. As the reciprocity formulae arise from finding equivalences between two different scattering problems, this can also substantially reduce the number of calculations in a parametric study.

In a similar vein we now consider a compressible fluid overlying a thin elastic plate; the plate contains embedded obstacles, cracks, or other scatterers. This is in many ways analogous to the elastic half space problems in that we now have both a compressional fluid wave (a body wave) and a flexural plate wave (a surface wave). Thin elastic plates coupled to an overlying compressible fluid support a subsonic flexural wave, and many problems in structural acoustics are concerned with the mechanisms whereby model defects scatter these waves; a substantial proportion of vibrational energy in a structure is transmitted into a fluid via such interactions. Our aim is to deduce the relation that exists between the scattered far field directivity associated with the scattered cylindrical wave in the fluid due to a flexural wave obliquely incident (in the plane occupied by the plate) upon this collection of defects to the amplitude of a scattered flexural wave created by an incoming fluid compressional plane wave also incident upon those defects. To demonstrate the manner in which the relation should be applied we briefly consider two model geometries for which analytical solutions can be derived and the reciprocity relation verified.

The present analysis is designed to complement so-called "optical theorems", these arise from power balance considerations and are also useful in scattering problems; recent work along these lines in structural acoustics and fluid-solid coupled media are contained in Guo (1995), Craster (1998) and Andronov & Belinskiy (1998).

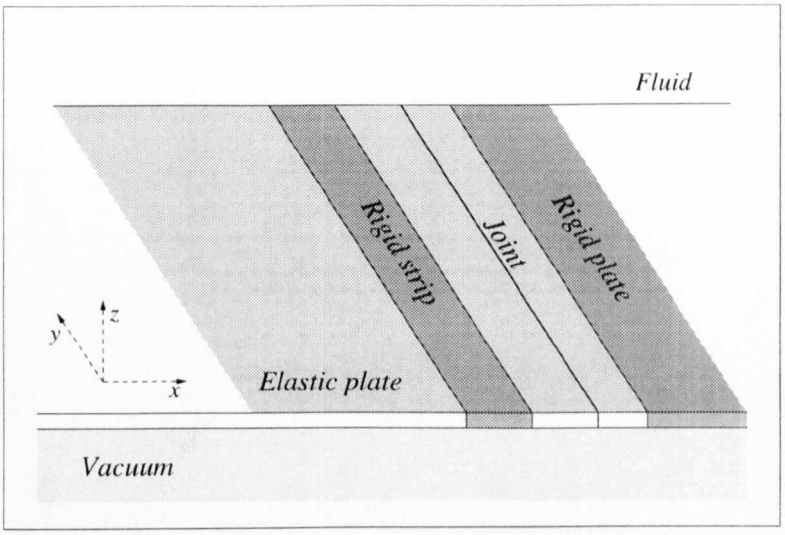

Figure 7.1. The geometry of a general problem showing typical rigid defects, involving rigid strips and plates, and line joints.

7.2. Basic equations

We consider a single elastic plate, with one-sided fluid loading, containing embedded rigid strips, or line defects and joints; a typical geometrical configuration shown in Figure 7.1.

Time-harmonic vibrations of frequency ω are assumed, thus all physical variables have an $e^{-\mathrm{i}\omega t}$ dependence; this is considered understood, and is henceforth suppressed. The problem is three dimensional with an inviscid, compressible fluid lying in the half space $z > 0$ and $-\infty < x, y < \infty$. With this assumed time dependence the fluid pressure $\hat{p}(x, y, z)$ satisfies the Helmholtz equation in $z > 0$,

$$(\nabla^2 + k_0^2)\hat{p}(x, y, z) = 0, \tag{7.2.1}$$

and k_0, the acoustic wavenumber, is related to the sound speed of the fluid, c_0, via $k_0 = \omega/c_0$. The displacement in the z direction on the plate, $\hat{\eta}(x, y)$, is related to the fluid pressure via $\rho\omega^2\hat{\eta}(x, y) = \hat{p}_z(x, y, 0)$.

The elastic plate lies in the plane $z = 0$ and is potentially separated by a number, j, of embedded rigid defects; these defects occupy domains $\mathcal{D}_j$ where $a_j \leq x \leq b_j$. To model the elastic plate we adopt the classical thin plate equation (Junger & Feit, 1986) in the form

$$B\nabla_h^4\hat{\eta}(x, y) - m\omega^2\hat{\eta}(x, y) = -\hat{p}(x, y, 0), \tag{7.2.2}$$

where ∇_h^2 is the horizontal Laplacian,

$$\nabla_h^2 \equiv \frac{\partial^2}{\partial x^2} + \frac{\partial^2}{\partial y^2}. \tag{7.2.3}$$

The plate separates fluid in the region $z > 0$ from a vacuum in $z < 0$. The bending stiffness, B, and mass per unit area, m, of the plate are related to the physical properties of the elastic plate through $B = Eh^3/12(1-\nu^2)$ and $m = \rho h$, with E, h, ν, and ρ the Young's modulus, plate thickness, Poisson ratio and mass density of the elastic material respectively. In order to minimise the number of parameters that occur later, we introduce the *in vacuo* flexural wavenumber κ_p, 'Mach' number Ω and fluid loading parameter ϵ as

$$\kappa_p^4 \equiv \frac{\omega^2 m}{B}, \quad \epsilon = \frac{\rho}{m}\left(\frac{B}{mc_0^2}\right)^{\frac{1}{2}} \quad \text{and } \Omega = \left(\frac{k_0}{\kappa_p}\right)^2 = \frac{\omega}{c_0\rho} m\epsilon. \tag{7.2.4}$$

Here Ω, the square of the ratio of the *in vacuo* plate wave speed to that of the fluid, provides a dimensionless frequency and the fluid loading parameter, ϵ, provides a frequency independent measure of fluid loading.

At plate edges, joints, or defects various edge conditions can be adopted (as the displacement is directly related to p_z we give the conditions in terms of the latter quantity); we take $x = 0$ to be the edge of a rigid plate extending along $0 < x < \infty$, say, and then $x = 0^-$ is the line along which the edge condition is to be applied, for instance:

- *Clamped edges*: Both the displacement and rotation vanish at $x = 0^-$, *i.e.*,

$$\hat{p}_z(0^-, y, 0) = \hat{p}_{zx}(0^-, y, 0) = 0. \tag{7.2.5}$$

- *Hinged edges*: The displacement and force are zero at $x = 0^-$, *i.e.*,

$$\hat{p}_z(0^-, y, 0) = 0, \quad \left(\frac{\partial^2}{\partial x^2} + \nu\frac{\partial^2}{\partial y^2}\right)\hat{p}_z(0^-, y, 0) = 0. \tag{7.2.6}$$

7.2.1. *Non-dimensionalisation*

To proceed we first non–dimensionalise the equations and adopt the non-dimensional space variable $\tilde{\mathbf{x}} = k_0\mathbf{x}$ based on the acoustic wavenumber; henceforth we drop the tilde and hat decoration. For convenience, the pressure is scaled so that the amplitude of the incident waves is unity.

The governing equation is now

$$\left(\frac{\partial^2}{\partial x^2} + \frac{\partial^2}{\partial y^2} + \frac{\partial^2}{\partial z^2} + 1\right) p(x, y, z) = 0, \tag{7.2.7}$$

subject to the non-dimensional thin plate equation

$$\left[\Omega^2\left(\frac{\partial^2}{\partial x^2} + \frac{\partial^2}{\partial y^2}\right)^2 - 1\right]\frac{\partial p}{\partial z}(x, y, 0) + \frac{\epsilon}{\Omega} p(x, y, 0) = 0, \tag{7.2.8}$$

for all x on $z = 0$ excluding $x \in \mathcal{D}_j$. In addition the scattered field decays as $z \to \infty$. For $x \in \mathcal{D}_j$ the rigid plate condition translates to $p_z = 0$.

7.2.2. *Incident wave structure*

Several different incident wavefields could be considered, incident flexural plate, leaky and acoustic waves are the more common, although we could also treat 'end-fire' waves (Brazier-Smith, 1987), and we briefly discuss the flexural, leaky and acoustic waves.

7.2.2.1. *Flexural waves*

An elastic plate can support a flexural wave, of unit amplitude on the plate, that takes the form

$$p^{(inc)}(x, y, z) = \exp[-(\Gamma_1^2 - 1)^{\frac{1}{2}} z + \mathrm{i}\xi_1 x + \mathrm{i}\kappa y]; \tag{7.2.9}$$

the superscript (inc) denotes that this is an incident wave. This surface wave decays exponentially with distance into the fluid and is localised close to the plate. The total plate wavenumber Γ_1, defined from $\Gamma_1^2 = \xi_1^2 + \kappa^2$, is found from the positive real root (for Γ) of the dispersion relation $\mathcal{K}(\xi)$:

$$\mathcal{K}(\xi) = \left(\Gamma^4(\xi) - \frac{1}{\Omega^2}\right) - \frac{\epsilon}{\Omega^3} \frac{1}{(\Gamma^2(\xi) - 1)^{\frac{1}{2}}}. \tag{7.2.10}$$

The total plate wavenumber Γ_1 is greater than unity and this indicates that the flexural plate waves are subsonic relative to the acoustic wavespeed. Associated with the flexural plate wave is an angle of propagation θ_1, see Figure 7.2, such that $\xi_1 = \Gamma_1 \cos\theta_1$ and $\kappa = \Gamma_1 \sin\theta_1$.

7.2.2.2. *Leaky waves*

Depending upon the precise choice of branch cuts for $(\Gamma^2(\xi) - 1)^{\frac{1}{2}}$ in equation (7.2.10) then the dispersion relation $\mathcal{K}(\xi)$ has, in addition to two real solutions at $\pm\xi_1$, complex roots that are also potentially important. In particular when the fluid loading is *light*, that is, the dimensionless frequency is large, $\Omega \gg 1$, and the fluid loading parameter is small, $\epsilon \ll 1$, then the *in-vacuo* flexural plate waves (which, as $\Omega > 1$, have supersonic velocities relative to the acoustic wavespeed) are perturbed by the presence of the overlying fluid and shed energy into the fluid along characteristic angles (Crighton, 1979). In terms of the dispersion relation these waves emerge from complex roots, with small imaginary part, at $\xi = \pm\xi_{leaky}$, where

$$\xi_{leaky} \sim \left(\Omega_j^{-1} - \kappa^2\right)^{\frac{1}{2}} + \frac{\mathrm{i}\epsilon_j}{4\Omega_j^2} \left(\Omega_j^{-1} - \kappa^2\right)^{-\frac{1}{2}} \left(1 - \Omega_j^{-1}\right)^{-\frac{1}{2}}. \tag{7.2.11}$$

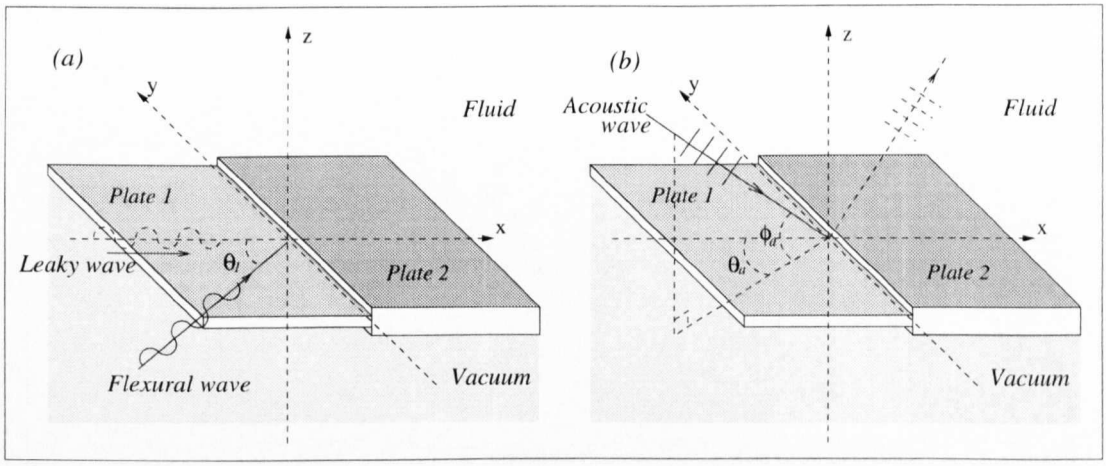

Figure 7.2. The geometry of the problem and the incident wave fields under consideration. In panel (a) the obliquely incident flexural wave of Section 7.2.2.1 is shown; the angle of incidence, θ_1, is the angle made between the wavenumber vector and the horizontal normal to the plate junction (which lies along the line $x = z = 0$). In addition an incident leaky wave Section 7.2.2.2 is also illustrated. In panel (b) an incident acoustic wave (Section 7.2.2.3) from the fluid, along an angle, θ_a, to the horizontal normal and an angle, ϕ_a, to the vertical normal of the plate junction is shown together with the wave that would be reflected from a defect-free elastic plate.

The incident field of a leaky wave is then

$$p^{(inc)}(x, y, z) = \exp[-(\Gamma^2_{leaky} - 1)^{\frac{1}{2}} z + \mathrm{i}\xi_{leaky} x + \mathrm{i}\kappa y]; \tag{7.2.12}$$

here we take κ real, and note that a leaky wave is a piece of the wave spectrum that can be identified explicitly, but cannot exist in isolation, the wave decays exponentially with both distance into the fluid and distance along the plate; they are discussed in Crighton (1979). In addition if $\Omega > 1/\kappa^2$ then the leaky wave root no longer has the imaginary component, and this can significantly affect the scattered far-field (Chapter 6).

7.2.2.3. *Acoustic plane wave*

Alternatively we could have incoming acoustic waves and associate angles of incidence with this wave; one angle in the $z = 0$ plane giving the angle of incidence on the plate relative to the joint, and the other giving the angle of incidence within the fluid relative to the $z = 0$ plane. Thus we define an angle of incidence θ_a in the $z = 0$ plane (on the plate) as the angle subtended between the projection of the incoming wave and the x axis and angle ϕ_a as the angle subtended between the incoming wave and the plate; see Figure 7.2.

Taking the incident field to have unit amplitude then that acoustic wave has the form

$$p^{(inc)}(x, y, z) = \exp[(\Gamma^2_a - 1)^{1/2} z + \mathrm{i}\xi_a x + \mathrm{i}\kappa y]. \tag{7.2.13}$$

In terms of the angles of incidence we define $\Gamma_a^2 = (\xi_a^2 + \kappa^2) = \cos^2\phi_a$ (so the square root term is $[\Gamma_a^2 - 1]^{1/2} \equiv -\mathrm{i}\sin\phi_a$), with $\xi_a = \cos\theta_a \cos\phi_a$ and $\kappa = \sin\theta_a \cos\phi_a$; note the wavenumber in the y direction, κ has $|\kappa| < 1$ always, this is in contrast to the case of incoming flexural plate waves, where κ due to the subsonic nature of the flexural wave can be greater than unity. In order to deduce a relation between the flexural and acoustic waves we shall require κ to be identical for both problems, thus we restrict our attention to $\kappa < 1$.

Later in this chapter we shall require the solution for a plane wave reflected from a defect-free elastic plate; this is shown in $x > 0$ in Figure 7.2. In this regard, we define a plate reflection coefficient, R, as

$$R = \frac{\tilde{\mathcal{K}}(\xi_a)}{\mathcal{K}(\xi_a)}, \quad \text{with} \quad \tilde{\mathcal{K}}(\xi) = \left(\Gamma^4(\xi) - \frac{1}{\Omega^2}\right) + \frac{\epsilon}{\Omega^3} \frac{1}{(\Gamma^2(\xi) - 1)^{\frac{1}{2}}} \tag{7.2.14}$$

and the reflected field, denoted by a superscript (ref), is

$$p^{(ref)}(x, y, z) = R \ \exp[-(\Gamma_a^2 - 1)^{1/2} z + \mathrm{i}\xi_a x + \mathrm{i}\kappa y]. \tag{7.2.15}$$

Thus, for an acoustic wave incident upon a defect-free plate, the full field is

$$p(x, y, z) = p^{(inc)}(x, y, z) + p^{(ref)}(x, y, z). \tag{7.2.16}$$

7.2.3. *Far-field wave structure*

We assume the defects, ribs, joints or plates are all clustered within a non-dimensional distance d of the origin, and that we observe the far-field such that $x, r \gg d$.

The scattered field, denoted by the superscript (sc), falls into two distinguishable pieces in the far field. Firstly, one generates scattered flexural plate waves that propagate to $x \to \pm\infty$, these are characterised by amplitude coefficients $H^{\pm}$:

$$p^{(sc)}(x, y, z) \sim H^{\pm} \exp[\pm \mathrm{i}\xi_1 x + \mathrm{i}\kappa y - (\Gamma_1^2 - 1)^{\frac{1}{2}} z]. \tag{7.2.17}$$

Secondly, we can also excite acoustic waves that propagate in the fluid. In the far field these are cylindrical waves, and are better described in a cylindrical polar coordinate system (r, ϑ, y) whose axis lies along the line $x = 0$ ($x = r\cos\vartheta, z = r\sin\vartheta$). These waves have the far-field form,

$$p^{(sc)}(r, \vartheta, y) \sim \sqrt{\frac{2}{\pi\lambda r}} G(\vartheta) e^{\mathrm{i}\lambda r - \mathrm{i}\pi/4 + \mathrm{i}\kappa y}, \tag{7.2.18}$$

characterised by an angular directivity $G(\vartheta)$, where $\lambda = \sqrt{1 - \kappa^2}$ is the radial wavenumber of the acoustic wave. For scattered cylindrical waves we require $\kappa < 1$; if $\kappa > 1$,

these waves are evanescent and there are no scattered acoustic waves in the far field; see Chapter 6 for further details. Equivalently, in order to excite acoustic waves, the component of the flexural wave in the y direction must travel supersonically. To deduce our reciprocity relation we restrict our attention to $\kappa < 1$. Additionally, if the fluid loading is light we can distinguish a response due to a leaky wave; we attach amplitude coefficients $L^{\pm}$ to this response and take

$$p^{(sc)}(x,y,z) \sim L^{\pm} \exp[\pm \mathrm{i}\xi_{leaky} x + \mathrm{i}\kappa y - (\Gamma^2_{leaky} - 1)^{\frac{1}{2}} z], \tag{7.2.19}$$

as $x \to \pm\infty$.

We assume that each defect does not vary spatially in the y direction, thus the wavenumber in the y direction is unaltered during the scattering from a defect and this $e^{\mathrm{i}\kappa y}$ dependence can be incorporated throughout. That is, we take

$$p^{(sc)}(x,y,z) = p^{(sc)}(x,z)e^{\mathrm{i}\kappa y} \tag{7.2.20}$$

with a similar form for the incident fields, and henceforth we omit the $e^{\mathrm{i}\kappa y}$ term and consider this exponential y dependence as understood.

Given a collection of defects on the plane $z = 0$ with $x \in \mathcal{D} = \bigcup_j D_j$ then the scattered field can, using an appropriate Green's function, be immediately written down as

$$p^{(sc)}(x,z) = \int_{\mathcal{D}} [\mathcal{L}(\partial_{x'}) p_z^{sc}(x',0) + \mathcal{M}(\partial_{x'}) p^{(sc)}(x',0)] p^G(x,z;x') \mathrm{d}x'. \tag{7.2.21}$$

Using $\partial_{x'}$ to denote the partial derivative with respect to x', the operators $\mathcal{L}(\partial_x)$ and $\mathcal{M}(\partial_x)$ are

$$\mathcal{L}(\partial_x) = (\partial_x^2 + \kappa^2)^2 - 1/\Omega^2, \qquad \mathcal{M}(\partial_x) = \epsilon/\Omega^3. \tag{7.2.22}$$

Each integral within (7.2.21) must be interpreted as an integral over $a_j < x < b_j$ together with a contribution from the edges a_j and b_j, that is,

$$\begin{aligned}
&\int_{D_j} [\mathcal{L}(\partial_{x'}) p_z^{(sc)}(x',0) + \mathcal{M}(\partial_{x'}) p^{(sc)}(x',0)] p^G(x,z;x') \mathrm{d}x' \\
&\equiv \int_{a_j}^{b_j} [\mathcal{L}(\partial_{x'}) p_z^{(sc)}(x',0) + \mathcal{M}(\partial_{x'}) p^{(sc)}(x',0)] p^G(x,z;x') \mathrm{d}x' \\
&+ p^G(x,z,x') \partial^3_{x'} p_z^{(sc)}(x',0)|_{a_j}^{b_j} - \partial_{x'} p^G(x,z,x') \partial^2_{x'} p_z^{(sc)}(x',0)|_{a_j}^{b_j} \\
&+ \partial^2_{x'} p^G(x,z,x') \partial_{x'} p_z^{(sc)}(x',0)|_{a_j}^{b_j} - \partial^3_{x'} p^G(x,z,x') p_z^{(sc)}(x',0)|_{a_j}^{b_j} \\
&+ 2\kappa^2 [\partial_{x'} p^G(x,z,x') p_z^{(sc)}(x',0)|_{a_j}^{b_j} - p^G(x,z,x') \partial_{x'} p_z^{(sc)}(x',0)|_{a_j}^{b_j}].
\end{aligned} \tag{7.2.23}$$

The scattered pressure field is given in terms of an unknown distribution of point forces along the elastic plate. The Green's function follows from solving the Helmholtz equation with boundary condition

$$\mathcal{L}(\partial_x) p_z^G(x,z;x') + \mathcal{M}(\partial_x) p^G(x,z;x') = \delta(x - x') \tag{7.2.24}$$

on $z = 0$. The resulting solution is found as the inverse Fourier transform

$$p^G(x,z;x') = -\frac{1}{2\pi}\int_C \frac{\exp[-\mathrm{i}\xi(x-x') - (\Gamma^2-1)^{\frac{1}{2}}z]}{(\Gamma^2-1)^{\frac{1}{2}}K(\xi)}\mathrm{d}\xi. \tag{7.2.25}$$

The path C in the inverse Fourier transform runs from $-\infty$ to $+\infty$ and is indented above (below) any singularities occurring on the negative (positive) real axis. We now substitute this Green's function into equation (7.2.21) to deduce the far-field scattered pressure. Analysing the asymptotic form of the Fourier integral using residues, or a saddle point analysis, we explicitly identify the characteristic far-field coefficients as:

$$\mathrm{i}(\Gamma_1^2-1)^{\frac{1}{2}}K'(\xi_1)H^{\pm} = \int_{\mathcal{D}}[\mathcal{L}(\partial_{x'})p_z^{(sc)}(x',0) + \mathcal{M}(\partial_{x'})p^{(sc)}(x',0)]e^{\mp\mathrm{i}\xi_1 x'}\mathrm{d}x'; \tag{7.2.26}$$

the prime on $K'(\xi)$ denotes the differential with respect to ξ,

$$\mathrm{i}(\Gamma_{leaky}^2-1)^{\frac{1}{2}}K'(\xi_{leaky})L^{\pm} = \int_{\mathcal{D}}[\mathcal{L}(\partial_{x'})p_z^{(sc)}(x',0) + \mathcal{M}(\partial_{x'})p^{(sc)}(x',0)]e^{\mp\mathrm{i}\xi_{leaky}x'}\mathrm{d}x' \tag{7.2.27}$$

and

$$2\mathrm{i}K(\lambda\cos\vartheta)G(\vartheta) = \int_{\mathcal{D}}[\mathcal{L}(\partial_{x'})p_z^{(sc)}(x',0) + \mathcal{M}(\partial_{x'})p^{(sc)}(x',0)]e^{-\mathrm{i}x'\lambda\cos\vartheta}\mathrm{d}x'. \tag{7.2.28}$$

The domain $\mathcal{D}$ incorporates the edge, and as in (7.2.23) the edge conditions are included in these expressions. This is illustrated for a single joint in Section 7.4.1.

7.3. The reciprocity relation

In this section we extract a reciprocity relation between the scattered fields generated by the different incident waves under consideration in this chapter. In order to achieve this we use the reciprocity relation

$$\int_S \left[p^{(f)}p_{n_i}^{(a)} - p^{(a)}p_{n_i}^{(f)}\right] n_i \mathrm{d}S = 0 \tag{7.3.1}$$

for two independent states (f) and (a) (the choice of superscript will become transparent) in a source-free domain bounded by a surface S (with outward pointing normal n_i), for which both states satisfy the Helmholtz equation. Taking the assumed y dependence and using this result in the x,z plane with S bounded by a semi-circular arc at infinity and running parallel to, and just above, the plate, then furthermore

$$\int_S \left([\mathcal{L}(\partial_{n_i})p_{n_i}^{(f)} + \mathcal{M}(\partial_{n_i})p^{(f)}]p_{n_i}^{(a)} - [\mathcal{L}(\partial_{n_i})p_{n_i}^{(a)} + \mathcal{M}(\partial_{n_i})p^{(a)}]p_{n_i}^{(f)}\right) n_i \mathrm{d}S = 0. \tag{7.3.2}$$

Provided, that is, $[\mathcal{L}(\partial_x)p_z^{(f,a)} + \mathcal{M}(\partial_x)p^{(f,a)}] = 0$ as $x \to \pm\infty$ and $p^{(f,a)}$ decays at infinity. Now we manipulate this.

Let state (f) be the scattered field due to an incoming flexural plate wave, (7.2.9),

$$p^{(f\ inc)}(x,z) = \exp[\mathrm{i}\xi_1 x - (\Gamma_1^2 - 1)^{\frac{1}{2}} z], \tag{7.3.3}$$

and state (a) is that due to an incident acoustic wave together with its reflection from an unblemished elastic plate (7.2.16), that is,

$$p^{(a\ inc)}(x,z) = \exp[\mathrm{i}\xi_a x + (\Gamma_a^2 - 1)^{\frac{1}{2}} z] + R\exp[\mathrm{i}\xi_a x - (\Gamma_a^2 - 1)^{\frac{1}{2}} z]. \tag{7.3.4}$$

Both incident fields have $\mathcal{L}(\partial_x)p_z^{(f,a\ inc)}(x,z) + \mathcal{M}(\partial_x)p^{(f,a\ inc)}(x,z) = 0$ on $z = 0$. Thus the relation (7.3.2) gives

$$\int_{\mathcal{D}} [\mathcal{L}(\partial_x)p_z^{(f\ sc)} + \mathcal{M}(\partial_x)p^{(f\ sc)}]p_z^{(a\ inc)}\mathrm{d}x = \int_{\mathcal{D}} [\mathcal{L}(\partial_x)p_z^{(a\ sc)} + \mathcal{M}(\partial_x)p^{(a\ sc)}]p_z^{(f\ inc)}\mathrm{d}x; \tag{7.3.5}$$

where we have used the rigid boundary condition $p_z^{(sc)} + p_z^{(inc)} = 0$ on $\mathcal{D}$. We have also exploited the edge conditions (7.2.5–7.2.6); taking into account the $\exp(\mathrm{i}\kappa y)$ dependence these translate to: clamped, $p_z(0^-,0) = 0, p_{zx}(0-,0) = 0$; hinged, $p_z(0-,0) = 0, p_{zxx}(0-,0) = 0$. The direct relations with p_z and its derivatives mean that these edge conditions can be easily incorporated.

Inserting the respective incident fields into equation (7.3.5), and furthermore noticing the similarity to the $H^{\pm}$ and G formulae, equations (7.2.26,7.2.28), yields

$$(\Gamma_1^2 - 1)\mathcal{K}'(\xi_1)H^{(a)-}(\theta_a,\phi_a) = \frac{4\epsilon}{\Omega^3}G^{(f)}(\vartheta,\theta_1). \tag{7.3.6}$$

We have now appended some further decoration to the flexural wave amplitude H^- and directivity G, this is to make it plain that this relation holds for specific angles of incidence, angles of observation and types of wave incidence.

- $H^{(a)-}(\theta_a,\phi_a)$ is the amplitude of the scattered flexural wave travelling to $x = -\infty$ due to an incoming plane wave, state (a), from θ_a, ϕ_a
- $G^{(f)}(\vartheta,\theta_1)$ is the directivity due to an incident flexural wave travelling, state (f), from $x = -\infty$. This travels along an angle θ_1 to the x axis; the directivity is evaluated at angle ϑ:

$$\vartheta = \pi - \cos^{-1}\left[\frac{1}{\lambda}\cos\theta_a\cos\phi_a\right]. \tag{7.3.7}$$

The wavenumber in the y direction, κ, is identical for both incident waves; this leads to the relation $\Gamma_1\sin\theta_1 = \sin\theta_a\cos\phi_a$, and we recall that $\lambda = \sqrt{1-\kappa^2}$; if $\kappa = 0$, that is, normal incidence then these formulae simplify with $\vartheta = \pi - \phi_a$. One then observes the directivity along the same angle, given the definitions of these angles, upon which the acoustic wave in state (a) is incoming; the effect of altering the angle of incidence (in the plate) of the flexural wave is to remove this simple relation.

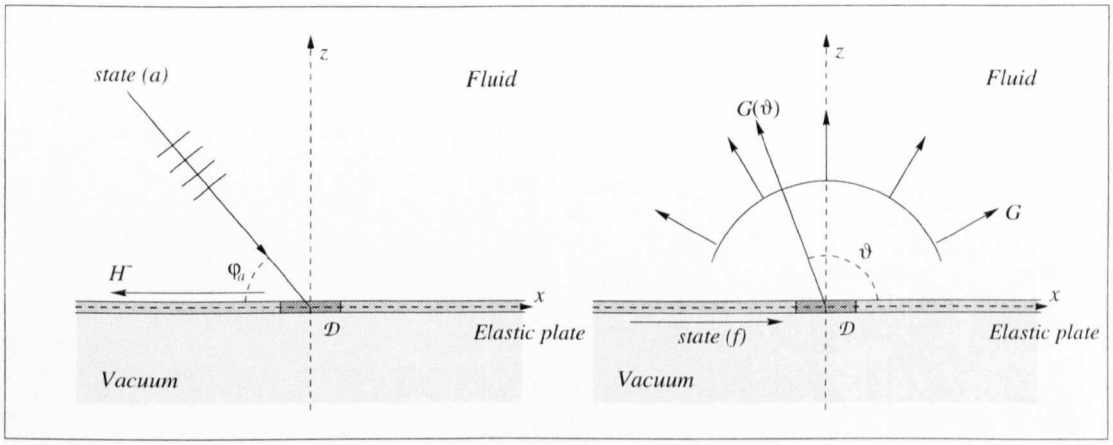

Figure 7.3. Illustration of the reciprocity relation for states (f) and (a). $\vartheta + \phi_a \leq \pi$.

At this point it is worthwhile to draw the readers attention to the precise angular behaviour in the x, z plane and a sketch of the two relations is shown in Figure 7.3.

7.4. Illustrative examples

The main application of the reciprocity relation is in numerical studies; it is also valuable for analytic work and we briefly demonstrate the manner in which it can be applied for a line joint or semi-infinite plate.

7.4.1. *A single line joint*

A single line joint is probably the simplest example upon which to illustrate the reciprocity relation as we have a single defect of vanishing width so that a_1 and b_1 are 0_- and 0_+ respectively.

The far-field coefficients then involve the jumps in scattered field across the joint (denoted by $[\![\ ]\!]$), for instance, the amplitude of the scattered flexural wave, H^- is

$$\mathrm{i}(\Gamma_1^2 - 1)^{\frac{1}{2}}\mathcal{K}'(\xi_1)H^- = [\![p^{(sc)}_{zxxx}(x',0)]\!] - \mathrm{i}\xi_1[\![p^{(sc)}_{zxx}(x',0)]\!] - \xi_1^2[\![p^{(sc)}_{zx}(x',0)]\!] + \mathrm{i}\xi_1^3[\![p^{(sc)}_{z}(x',0)]\!]. \tag{7.4.1}$$

This is crucially dependent upon the edge conditions, see for instance Howe (1986, 1994b). Following that analysis for a clamped joint

$$p^{(sc)}_z(x,z) = -\frac{1}{2\pi}\int_C \frac{(E_1\xi + E_0)}{\mathcal{K}(\xi)} \exp\left[-\mathrm{i}\xi x - (\Gamma^2 - 1)^{\frac{1}{2}}z\right] \mathrm{d}\xi, \tag{7.4.2}$$

with constants E_1 and E_0 determined from the incident field. We now consider two states (f) and (a) as those due to incoming flexural and acoustic waves respectively. The constants E_1 and E_0 take different forms in both cases and we distinguish them as $E_0^{(f,a)}$

and $E_1^{(f,a)}$. Applying the edge conditions which are that the jump in p_z and p_{zx} across the joint are zero one finds that

$$E_0^{(f,a)} = -\mathcal{A}^{(f,a)}\left[\frac{1}{2\pi}\int_C \frac{\mathrm{d}\xi}{\mathcal{K}(\xi)}\right]^{-1} = -\frac{\mathcal{A}^{(f,a)}}{I_0}, \tag{7.4.3}$$

$$E_1^{(f,a)} = \xi^{(f,a)}\mathcal{A}^{(f,a)}\left[\frac{1}{2\pi}\int_C \frac{\xi^2}{\mathcal{K}(\xi)}\mathrm{d}\xi\right]^{-1} = \frac{\xi^{(f,a)}\mathcal{A}^{(f,a)}}{I_1}. \tag{7.4.4}$$

The constants $\mathcal{A}^{(f,a)}$ are

$$\mathcal{A}^{(f)} = (\Gamma_1^2 - 1)^{\frac{1}{2}}, \qquad \mathcal{A}^{(a)} = (R-1)(\Gamma_a^2 - 1)^{\frac{1}{2}} \tag{7.4.5}$$

and the $\xi^{(f,a)}$ are $\xi^{(f)} = \xi_1$ and $\xi^{(a)} = \xi_a$. We have also defined I_q (Howe, 1986) as

$$I_q = \frac{1}{2\pi}\int_C \frac{\xi^{2q}}{\mathcal{K}(\xi)}\mathrm{d}\xi \tag{7.4.6}$$

where the path C is defined following equation (7.2.25).

Asymptotic considerations of the inverse Fourier transform for $p^{(sc)}(x,z)$ (which follows from (7.4.2)) give the far-field coefficients required for (7.3.6) as

$$H^{(a)-}(\theta_a,\phi_a) = \mathrm{i}\frac{[E_1^{(a)}\xi_1 + E_0^{(a)}]}{\mathcal{K}'(\xi)(\Gamma_1^2-1)^{\frac{1}{2}}} \equiv \mathrm{i}\frac{(R-1)(\Gamma_a^2-1)^{\frac{1}{2}}}{\mathcal{K}'(\xi_1)(\Gamma_1^2-1)^{\frac{1}{2}}}[\xi_a\xi_1 I_1^{-1} - I_0^{-1}], \tag{7.4.7}$$

$$G^{(f)}(\vartheta,\theta_1) = -\mathrm{i}\left[-E_1^{(f)}\lambda\cos\vartheta + E_0^{(f)}\right]\frac{(\Gamma_1^2-1)^{\frac{1}{2}}}{2\mathcal{K}(\lambda\cos\vartheta)} \equiv -\mathrm{i}\frac{(\Gamma_1^2-1)^{\frac{1}{2}}}{2\mathcal{K}(\lambda\cos\vartheta)}[\xi_a\xi_1 I_1^{-1} - I_0^{-1}] \tag{7.4.8}$$

for ϑ given by (7.3.7). After substitution into (7.3.6) one sees that the reciprocity relation holds.

Other edge conditions upon the joint can be considered, and the analysis is then more complicated as the integrals which appear in an analogous manner to those in (7.4.8) can be apparently divergent (Howe, 1986). None the less one can pursue the analysis and obtain similar results.

7.4.2. *A semi-infinite rigid plate*

The reciprocity relation is valid even when the rigid defect covers the half plane on $z = 0$ for $x > 0, -\infty < y < \infty$ and we now turn to this slightly more involved example, that is, an elastic plate on $z = 0$ in $x < 0$ connected to a co-planar rigid plate on $x > 0$. This can be solved using Fourier transforms and the Wiener–Hopf technique, see for instance Crighton & Innes (1984). One can approach this either by constructing an integral

equation manipulating (7.2.21) or directly from the governing equations and boundary conditions; we follow the latter route.

We define the Fourier transform of the scattered pressure

$$P(\xi,z)=\int_{-\infty}^{\infty}p^{(sc)}(x,z)e^{\mathrm{i}\xi x}\mathrm{d}x=P_{+}(\xi,z)+P_{-}(\xi,z), \tag{7.4.9}$$

where $P_{\pm}$ denote the half-range transforms of $p^{(sc)}(x,z)$;

$$P_{+}(\xi,z)=\int_{0}^{\infty}p^{(sc)}(x,z)e^{\mathrm{i}\xi x}\mathrm{d}x,\quad P_{-}(\xi,z)=\int_{-\infty}^{0}p^{(sc)}(x,z)e^{\mathrm{i}\xi x}\mathrm{d}x; \tag{7.4.10}$$

the same notation is used for the half range transforms of $p_z^{(sc)}(x,z)$ which are $P_{\pm z}$. The inverse transform is defined by

$$p^{(sc)}(x,z)=\frac{1}{2\pi}\int_{C}P(\xi,z)e^{-\mathrm{i}\xi x}\mathrm{d}\xi, \tag{7.4.11}$$

where the path C is defined after (7.2.25). The subscripts + and − attached to the half-range transforms denote that these functions are analytic in the + and − regions; these denote the regions of the complex ξ plane above and below C; we loosely refer to these two regions as the 'upper' and 'lower' halves of the complex ξ-plane. In what follows we shall mainly deal with the transforms along the plate, $z=0$, and we shall shorten $P_{+}(\xi,0)$ to $P_{+}(\xi)$ henceforth, and similarly for the other half range transforms on $z=0$.

We generate a functional relation between half-range transforms that are unknown. This relation is then unravelled using the Wiener–Hopf technique to identify the unknowns and deduce the full solution. Along the way we are required to satisfy the edge conditions; for problems in structural acoustics these edge conditions are slightly awkward to incorporate.

The incident flexural and acoustic waves can be treated simultaneously: we let state (f) be that associated with an incident flexural wave (7.2.9), and (a) be that associated with an incident acoustic wave (7.2.16). Using the rigid boundary condition $p_z^{(inc)}+p_z^{(sc)}=0$ on $z=0$ and $x>0$ then for the states (f) and (a) we have the relation, $P_{+z}^{(f,a)}(\xi)=\mathrm{i}\mathcal{A}^{(f,a)}/(\xi+\xi^{(f,a)})_{+}$. The terms involving the superscript (f,a) take different values depending upon whether we are dealing with state (f) or state (a). The representation of $P_{+z}^{(f,a)}(\xi)$ simply states that the transform of $p_z^{sc}(x,0)$ is known, and the subscript + we have attached to the last term is to remind us that the pole at $-\xi^{(f,a)}$ is taken to lie in the plus region, and we must indent the inversion contour, and take account of this in the analysis, accordingly.

The constants $\mathcal{A}^{(f,a)}$ are given in equation (7.4.5) and the $\xi^{(f,a)}$ are again $\xi^{(f)}=\xi_1$ and $\xi^{(a)}=\xi_a$.

We follow the usual Wiener–Hopf recipe (Noble, 1958) and the functional equation emerges as

$$\mathcal{K}(\xi)\left[P_{-z}^{(f,a)}(\xi)-\frac{\mathcal{A}^{(f,a)}}{\mathrm{i}(\xi^{(f,a)}+\xi)_+}\right]=\left[\Gamma^4(\xi)-\frac{1}{\Omega^2}\right]P_{+z}^{(f,a)}(\xi)+\frac{\epsilon}{\Omega^3}P_{+}^{(f,a)}(\xi)-\mathcal{R}^{-(f,a)}(\xi). \tag{7.4.12}$$

This relates the transform of the unknown pressure on the rigid plate, $P_+(\xi)$, to the transform of the unknown displacement of the elastic plate, effectively $P_{-z}(\xi)$; these are clearly different depending upon the incident field. The edge behaviour of the plates is completely captured in the term,

$$\mathcal{R}^-(\xi)=\left[p_{zxxx}^{(sc)}(0^-,0)-\mathrm{i}\xi p_{zxx}^{(sc)}(0^-,0)-(2\kappa^2+\xi^2)p_{-}^{(sc)}(0^{\pm},0)+\mathrm{i}\xi(2\kappa^2+\xi^2)p_{z}^{(sc)}(0^-,0)\right]. \tag{7.4.13}$$

Our most valuable player here is the Wiener–Hopf technique, in essence one separates the functional equation into a piece that is analytic in the + region and a piece that is analytic in the − region. These two pieces are equal along a common line and therefore both are equal to the same entire function $E(\xi)$, using analytic continuation this is extended to the whole complex ξ plane. Edge behaviour is then used with Liouville's theorem to fix the form of $E(\xi)$.

Technically we require the split of the function $\mathcal{K}(\xi)$ into a product of + and − functions. That is, we require $\mathcal{K}(\xi)=\mathcal{K}_+(\xi)\mathcal{K}_-(\xi)$; this is discussed in detail in Chapter 6 and is not repeated here, splitting is most easily performed in terms of some quadratures. (It is worth mentioning that $\mathcal{K}_-(+\xi)=\mathcal{K}_+(-\xi)$). For our purposes here it is only necessary to note that one can do the factorisation and we proceed formally.

This factorisation and subsequent rearrangement of the functional equation expresses the equality of a + and − function, and utilising Liouville's theorem and an estimate of the growth behaviour of the unknown transforms we may deduce that our entire function, $E^{(f,a)}(\xi)$, is $O(\xi)$ when $|\xi|\to\infty$, for all edge conditions; this leads to the transform of the unknown p_z along the plate as

$$P_{-z}^{(f,a)}(\xi)=\frac{E_1^{(f,a)}\xi+E_0^{(f,a)}}{\mathcal{K}_-(\xi)}+\frac{\mathcal{A}^{(f,a)}}{\mathrm{i}(\xi^{(f,a)}+\xi)_+}\left[1-\frac{\mathcal{K}_+(\xi^{(f,a)})}{\mathcal{K}_-(\xi)}\right]. \tag{7.4.14}$$

Both $E_{0,1}^{(f,a)}$ are unknown and must be determined from the edge conditions; we shall consider clamped and hinged cases. Hence, the scattered pressure field is ultimately

$$p^{(sc\ f,a)}(x,z)=-\frac{1}{2\pi}\int_C\left[E_1^{(f,a)}\xi+E_0^{(f,a)}-\frac{\mathcal{A}^{(f,a)}\mathcal{K}_+(\xi^{(f,a)})}{\mathrm{i}(\xi+\xi^{(f,a)})_+}\right]\times\frac{\exp\left[-\left(\Gamma^2(\xi)-1\right)^{1/2}z-\mathrm{i}\xi x\right]}{\mathcal{K}_-(\xi)\left[\Gamma^2(\xi)-1\right]^{1/2}}\mathrm{d}\xi \tag{7.4.15}$$

and the far-field coefficients follow from asymptotic considerations of this integral. Consequently, the coefficients for incident waves (f) (flexural) and (a) (acoustic), are

$$H^{(f,a)-} = \frac{-\mathrm{i}\mathcal{K}_+(\xi_1)}{(\Gamma_1^2-1)^{\frac{1}{2}}\mathcal{K}'(\xi_1)}\left[E_1^{(f,a)}\xi_1 + E_0^{(f,a)} - \frac{\mathcal{A}^{(f,a)}\mathcal{K}_+(\xi^{(f,a)})}{\mathrm{i}(\xi_1+\xi^{(f,a)})}\right], \tag{7.4.16}$$

$$L^{(f,a)-} = \frac{-\mathrm{i}\mathcal{K}_+(\xi_{leaky})}{(\Gamma_{leaky}^2-1)^{\frac{1}{2}}\mathcal{K}'(\xi_{leaky})}\left[E_1^{(f,a)}\xi_{leaky} + E_0^{(f,a)} - \frac{\mathcal{A}^{(f,a)}\mathcal{K}_+(\xi^{(f,a)})}{\mathrm{i}(\xi_{leaky}+\xi^{(f,a)})}\right], \tag{7.4.17}$$

and

$$G^{(f,a)}(\vartheta) = \frac{-\mathrm{i}}{2\mathcal{K}_+(\lambda\cos\vartheta)}\left[-E_1^{(f,a)}\lambda\cos\vartheta + E_0^{(f,a)} - \frac{\mathcal{A}^{(f,a)}\mathcal{K}_+(\xi^{(f,a)})}{\mathrm{i}(\xi^{(f,a)}-\lambda\cos\vartheta)}\right]. \tag{7.4.18}$$

If required, the coefficients for incident leaky waves may be similarly deduced; they are closely related to incident flexural waves replacing Γ_1 with Γ_{leaky} in $\mathcal{A}^{(f)}$ and $\xi^{(f)}$.

Clearly the terms $G^{(f)}(\vartheta,\theta_1)$ and $H^{(a)-}(\theta_a,\phi_a)$ required for the reciprocity result (7.3.6) appear similar, at least they have a similar structure, but we still have the edge conditions to incorporate; it is at first sight unclear that these components too are correctly related.

If we take the edge to be clamped, it transpires that $E_1^{(f,a)} = E_0^{(f,a)} \equiv 0$ and upon noting the choice of ϑ for the reciprocity relation is $\lambda\cos\vartheta = -\xi_a$ then the relation (7.3.6) is immediately satisfied. However, more complicated edge conditions have non-zero E's associated with them. In general, to satisfy relation (7.3.6) the constants must satisfy

$$\mathcal{A}^{(f)}\mathcal{K}_+(\xi^{(f)})\left[E_1^{(a)}\xi^{(f)} + E_0^{(a)}\right] = \mathcal{A}^{(a)}\mathcal{K}_+(\xi^{(a)})\left[E_1^{(f)}\xi^{(a)} + E_0^{(f)}\right]. \tag{7.4.19}$$

If we now take the edge to have the hinged conditions, (7.2.6), these edge conditions are incorporated by taking the limit in the Fourier transform $P_{-z}^{(f,a)}(\xi)$ that $\xi \to \infty$ which after inversion corresponds to $x \to 0^-$. That is, we explicitly determine p_z along the elastic plate and then enforce the edge conditions.

To enforce the chosen edge condition we require the expansion of the split function $\mathcal{K}_-(\xi)$ as $\xi \to \infty$ which is

$$\mathcal{K}_-(\xi) \sim \xi^2 + k_1\xi + \ldots. \tag{7.4.20}$$

where k_1 is independent of ξ, and for our purposes is a constant found using quadratures. Inserting this result into $P_{-z}^{(f,a)}$ and inverting term by term to obtain that

$$p_z(x,z) = p_0 + xp_1 + x^2p_2 + \ldots; \tag{7.4.21}$$

for constants p_0, p_1, and p_2. This result is for the total pressure now and not only the

scattered piece of the pressure. On applying the hinged conditions we find that $E_1^{(f,a)} = 0$ and use the equation

$$0 = 2p_2 - \nu\kappa^2 p_0 = -\mathrm{i}\left[-E_0^{(f,a)}k_1 + \mathrm{i}\mathcal{A}^{(f,a)}\mathcal{K}_+(\xi^{(f,a)})\right] \tag{7.4.22}$$

to determine that

$$E_0^{(f,a)} = \frac{\mathcal{A}^{(f,a)}\mathcal{K}_+(\xi^{(f,a)})}{\mathrm{i}k_1}, \tag{7.4.23}$$

and thus the constants are determined.

Substitution into the equations (7.4.16,7.4.18) leads to the far-field coefficients

$$H^{(a)-}(\theta_a,\phi_a) = -\frac{\mathcal{K}_+(\xi_1)\mathcal{K}_+(\xi_a)(R-1)(\Gamma_a^2-1)^{\frac{1}{2}}}{(\Gamma_1^2-1)^{\frac{1}{2}}\mathcal{K}'(\xi_1)}\left(\frac{1}{k_1} - \frac{1}{(\xi_1+\xi_a)}\right), \tag{7.4.24}$$

and

$$G^{(f)}(\vartheta,\theta_1) = -\frac{(\Gamma_1^2-1)^{\frac{1}{2}}\mathcal{K}_+(\xi_1)}{2K_+(\lambda\cos\vartheta)}\left(\frac{1}{k_1} - \frac{1}{(\xi_1-\lambda\cos\vartheta)}\right). \tag{7.4.25}$$

Noting that the choice of ϑ in (7.3.7) ensures that $\xi_a = -\lambda\cos\vartheta$, and some minor manipulations, these too satisfy the reciprocity relation (7.3.6) and (7.4.19).

7.5. Concluding remarks

A reciprocity relation has been identified for rigid plates lying upon an infinite elastic plate that should, besides being of independent interest, be of value in numerical studies involving, say, arrays of rigid ribs, plates and other rigid defects; it provides a non-trivial check. It therefore complements other results, such as extensions of the optical scattering theorem Guo (1995), Norris & Rebinsky (1995) and Andronov & Belinskiy (1998). The two analytic examples demonstrate how the result should be applied.

In addition, the reciprocity result we have given can be generalised in a straightforward manner to rigid plates on, say, a membrane, or rigid cylindrical shells on an elastic cylindrical shell; the general methodology outlined here should be useful in those contexts. However, the replacement of the rigid plate by an elastic plate (of differing material properties to the plate which extends to infinity) and higher order edge conditions leads to further difficulties, and this is currently under study.

There are two additional reciprocity results, that is, involving two incident waves of the same type, that is, both flexural waves or both acoustic, and then interrelating the scattering coefficients; the resulting relations are then obvious, so we have not given upon these cases. Relations between flexural (or acoustic) waves and incident, scattered leaky

waves can also be deduced. For instance, if we have an incident leaky wave with the form (7.2.12) then

$$(\Gamma_1^2 - 1)\mathcal{K}'(\xi_1)H^-(\theta_{leaky}) = (\Gamma_{leaky}^2 - 1)\mathcal{K}'(\xi_{leaky})L^-(\theta_1) \tag{7.5.1}$$

where we taken the two states to be

- $H^-(\theta_{leaky})$ is the amplitude of the flexural wave travelling to $x = -\infty$ due to an incoming leaky wave from θ_{leaky}
- $L^-(\theta_1)$ is the amplitude of the leaky wave travelling to $x = -\infty$ due to an incoming flexural wave from θ_1.

References

Andronov, I. V. & Belinskiy, B. P., 1998. Acoustic scattering on an elastic plate described by the Timoshenko model: Contact conditions and uniqueness of the solution. *J. Acoust. Soc. Am.* **103**, 673–682.

Brazier-Smith, P. R., 1987. The acoustic properties of two co-planar half-plane plates. *Proc. R. Soc. Lond.* A **409**, 115–139.

Craster, R. V., 1998. Scattering by cracks beneath fluid-solid interfaces. *J. Sound Vib.* **209**, 343–372.

Crighton, D. G., 1979. The free and forced waves on a fluid–loaded elastic plate. *J. Sound Vib.* **63**, 225–235.

Crighton, D. G. & Innes, D., 1984. The modes, resonances and forced response of elastic structures under heavy fluid loading. *Phil. Trans. R. Soc. Lond.* A **312**, 295–342.

Guo, Y. P., 1995. On sound energy scattered by a rigid body near a compliant surface. *Proc. R. Soc. Lond. A* **451**, 543–552.

Howe, M. S., 1986. Attenuation and diffraction of bending waves at gaps in fluid loaded plates. *IMA J. Appl. Math.* **36**, 247–262.

Howe, M. S., 1994b. Scattering of bending waves by open and closed cracks and joints in a fluid-loaded elastic plate. *Proc. R. Soc. Lond. A* **444**, 555–571.

Junger, M. C. & Feit, D., 1986. *Sound, structures and their interaction.* Acoustical Society of America. Second edition.

Mei, C. C., 1978. Extensions of some identities in elastodynamics with rigid inclusions. *J. Acoust. Soc. Am.* **64**, 1514–1522.

Neerhoff, F. L., 1980. Reciprocity and power-flow theorems for the scattering of plane elastic waves in a half space. *Wave Motion* **2**, 99–113.

Noble, B., 1958. *Methods based on the Wiener–Hopf technique.* Pergamon Press.

Norris, A. N. & Rebinsky, D. A., 1995. Acoustic and membrane wave interaction at plate junctions. *J. Acoust. Soc. Am.* **97**, 2063–2073.

Rogoff, Z. M., 1993. Reciprocity relations between the incident field and the mode-converted scattered far-field for compact obstacles in an elastic half-space. *M.Sc. Thesis (University of Manchester)*.

Tan, T. H., 1977. Reciprocity relations for scattering of plane, elastic waves. *J. Acoust. Soc. Am.* **61**, 928–931.

Varatharajulu, V., 1977. Reciprocity relations and forward amplitude theorems for rigid inclusions. *J. Math. Phys.* **18**, 537–543.

Chapter Eight

Concluding remarks

8.1. Summary of conclusions

This thesis investigates, in detail, various topics involving wave-bearing surfaces under fluid loading; the understanding of fluid loading effects and leaky waves has been furthered by the problems considered. The organisation and results in this thesis have already been described in the introduction and the proceeding chapters. Here attention is simply drawn to compiling some broader remarks. The problems described have been approached by mainly analytical routes involving integral transform techniques and related methods such as the Wiener–Hopf method and matched asymptotic expansions. This unearths many of the physical mechanisms involved, for instance the emergence of surface and leaky waves. It also allows us to identify physical approximations to tackle problems where an exact solution is not feasible. A direct numerical approach may fail to expose some of these, often subtle, details. A particular advantage of having the explicit solution is that limiting cases and useful approximations emerge.

For instance, in Chapter 2, matched asymptotic expansions were used to look at the scattering effects of low frequency waves by very small interfacial defects. We observed a natural separation that occurs in the inner problem into fluid and solid pieces. This enabled us, in each case, to give a useful physical interpretation of each defect in terms of a specific interfacial discontinuity.

Also in the second chapter, several directivity patterns were used to demonstrate the distinctive beaming that occurs along the Rayleigh angles (where energy is 'leaked' into the fluid) for light fluid loading.

When treating the scattering of flexural plate waves, in structural acoustics, in Chapter 6, we encountered similar peaks in the directivity of scattered acoustic power that were again associated with leaky waves, although these peaks now also depended upon the angle of incidence of the waves that are ultimately scattered. In this case, a critical angle for the transmission of flexural waves from one plate into another, and this is caused by non-normal flexural wave incidence; this aspect has been largely ignored in previous studies. In addition, two geometrical critical angles emerge that give us information about the energy distribution of the scattered field. That is, for some angles of incidence, all of the energy is reflected and there is then scope for resonances to occur for several joined plates. Related power flow and reciprocity relations have also been derived in Chapter 7.

In the third and fourth chapters we looked at the time dependent wave motion generated by sources in a fluid-elastic solid set-up. We were able to identify asymptotic representations for each wavefront arrival and in addition give an interpretation of the leaky Rayleigh and non-geometric waves that emerge in a broadly analogous way in regimes of 'light' fluid and 'shallow' source loading.

The interaction of waves multiply reflected from (fluid-solid) interfaces and surfaces with a crack under an initial 'opening' loading was our concern in Chapter 5. We chose to focus mainly on the wavefield close to the crack tip and not the multiples of 'leaky' waves that could emerge. However, along the way, we did observe that the effect of the fluid loading on the crack was broadly to draw energy away from it.

8.2. So what happens next ?

We now address possible extensions to the work presented here. Although a number of topics have been covered in this thesis there are some noteworthy omissions. For instance, scattering by defects upon a curved fluid-solid interface, or at the junction of two dissimilar, elastic, fluid-loaded shells; the analytical methods described here should be useful. When treating elastic shells, most previous authors have considered one shell that is either open-ended (Howe, 1994a) or closed (Skelton, 1999), or attached to a rigid baffle (Lawrie, 1986, 1987). The analysis of Chapter 6 with suitable additions should allow us to consider joined dissimilar shells. We may also generalise the problem of co-planar elastic plates to curved plates, recently Norris *et al.* (1998) looked at curved plates with normally incident plate waves. Much of the analysis contained in Chapter 6 also carries across to the curved plate situation. The reciprocity and power flow relations can also be generalised to these cases.

Finite elastic plates are often of more practical interest, an elastic plate embedded in a rigid baffle is looked at in Llewellyn–Smith & Craster (1999). The observations in Chapter 6 suggest that for some angles of incidence, for excitations of an elastic plate embedded in a second infinite elastic plate, there is scope for reverberant build up. That is, if the finite plate is excited then all the energy may be trapped in the plate. This too should be investigated.

The application of an invariant integral as a means to obtaining the stress intensity factors (Chapter 5) has also led to some interesting questions regarding other possible uses of this method in, say, structural acoustics. It is speculated that the non-singular behaviour at the junction of elastic or rigid plates, or at an opening in a plate could be investigated in this way.

Ultimately, we may be interested in a finite elastic plate under fluid loading lying on an elastic solid (that is, the vacuum-backing in Chapters 6 and 7 has been replaced with an elastic solid). By a physical analogy with the structural acoustics problems one could conjecture that for an obliquely incident surface Schölte wave at the open end of a plate, then the energy distribution in the fluid, solid, and plate would be governed by a similar physical mechanism as we found in Chapter 6. There are additional complications here due to the edge conditions of the plate.

Another aspect that has not been treated fully here is the asymptotics of very 'light' fluid loading, Craster (1997). The underlying idea is that a natural separation occurs into fluid and solid pieces (*c.f.* Chapter 2) from which we can piece together the solution without attempting the (often complicated) coupled fluid-solid problem. In a similar vein, the solutions we have found, together with their physics, provide useful building blocks for some related problems.

There are also a wealth of related problems involving fluid-layered elastic, anisotropic, and viscoelastic media. In the main, these are treated by various approximate methods; some of these methods are discussed in Aki & Richards (1980). Nevertheless we may generalise some of these problems, for example an infinite inhomogeneous material containing single (Ergüven & Gross, 1999) or multiple (Choi, 1997) cracks, to include the effects of fluid loading. Some aspects of non-homogeneous media under fluid loading were discussed in Chapter 5.

It is hoped that this thesis provides some insight into these, and many other related problems.

References

Aki, K. & Richards, P. G., 1980. *Quantitative seismology: theory and methods*. W.H. Freeman and Co., San Francisco.

Choi, H. J., 1997. A periodic array of cracks in a functionally graded nonhomogeneous medium loaded under in-plane normal and shear. *Int. J. Fracture* **88**, 107–128.

Craster, R. V., 1997. The light fluid loading limit for fluid/solid interactions. *Euro. J. Appl. Math* **8**, 485–505.

Ergüven, M. E. & Gross, D., 1999. On the penny-shaped crack in inhomogeneous elastic materials under normal extension. *Int. J. Solids Structures* **36**, 1869–1882.

Howe, M. S., 1994a. On the sound produced when flexural waves are reflected at the open end of a fluid-loaded cylinder. *J. Acoust. Soc. Am.* **96**, 265–276.

Lawrie, J. B., 1986. Vibrations of a heavily loaded, semi-infinite, cylindrical elastic shell. I. *Proc. R. Soc. Lond. A* **408**, 103–128.

Lawrie, J. B., 1987. Vibrations of a heavily loaded, semi-infinite, cylindrical elastic shell. II. *Proc.*

R. Soc. Lond. A **414**, 371–387.

Llewellyn–Smith, S. G. & Craster, R. V., 1999. Numerical and asymptotic approaches to scattering problems involving finite elastic plates in structural acoustics. *Wave Motion* **30**, 17–41.

Norris, A. N., Rebinsky, D. A. & Wickham, G. R., 1998. On wave interaction and diffraction from the junction of two curved plates under unilateral fluid loading. *Phil. Trans. R. Soc. Lond. A* **356**, 1421–1467.

Skelton, E. A., 1999. Acoustic scattering by a closed semi-infinite fluid-loaded elastic cylindrical shell. *Proc. R. Soc. Lond. A* **455**, 1637–1681.

References

Pages on which a reference is cited are indicated by numbers in square brackets at the end of the reference.

Abrahams, I. D., 1981. Scattering of sound by a heavily loaded finite elastic plate. *Proc. R. Soc. Lond. A* **378**, 89–117. [137]

Abrahams, I. D. & Wickham, G. R., 1992a. Scattering of elastic waves by a small inclined surface breaking crack. *J. Mech. Phys. Solids* **40**, 1707–1733. [10, 17, 29]

Abrahams, I. D. & Wickham, G. R., 1992b. Scattering of elastic waves by an arbitrary small imperfection in the surface of a half-space. *op. cit.* 1683–1706. [10, 17, 26, 29]

Abramovici, F., Lawrence, H. T. L. & Kanasewich, E. R., 1989. The evanescent wave in Cagniard's problem for a line source generating SH waves. *Bull. Seism. Soc. Am.* **79**, 1941–1955. [67]

Abramowitz, M. & Stegun, I. A., 1972. *Handbook of Mathematical Functions*. Dover. [88]

Achenbach, J. D., 1973. *Wave Propagation in Elastic Solids*. Amsterdam, North-Holland. [92, 94]

Aki, K. & Richards, P. G., 1980. *Quantitative seismology: theory and methods*. W.H. Freeman and Co., San Francisco. [65, 192]

Andronov, I. V. & Belinskiy, B. P., 1998. Acoustic scattering on an elastic plate described by the Timoshenko model: Contact conditions and uniqueness of the solution. *J. Acoust. Soc. Am.* **103**, 673–682. [173, 187]

Atkinson, C., 1975. Some results on crack propagation in media with spatially varying elastic moduli. *Int. J. Fracture* **21**, 619–628. [108]

Atkinson, C., 1977. On quasi-static problems of cracks in a non-homogeneous elastic layer. *Acta Mech.* **26**, 103–113. [94]

Atkinson, C. & Craster, R. V., 1992a. The application of invariant integrals in diffusive elastic solids. *Phil. Trans. R. Soc. Lond. A* **339**, 231–263. [109]

Atkinson, C. & Craster, R. V., 1992b. Fracture in fully coupled dynamic thermoelasticity. *J. Mech. Phys. Solids* **40**, 1415–1432. [128]

Atkinson, C. & Craster, R. V., 1995a. Invariant integrals, stress concentrations and energy release rates. In *Fracture; a topical encyclopedia of current knowledge dedicated to Alan Arnold Griffith*, ed. by C. Cherepanov, 496-517, Krieger, New York. [94, 125]

Atkinson, C. & Craster, R. V., 1995b. Theoretical aspects of fracture mechanics. *Prog. Aerospace Sci.* **31**, 1–83. [92, 108, 133]

Babich, V. M. & Kiselev, A. P., 1989. Non-geometrical waves - are there any? An asymptotic description of some 'non-geometrical' phenomena in seismic wave propagation. *Geophys. J. Int.* **99**, 415–420. [67]

Balmforth, N. J. & Craster, R. V., 1999. Ocean waves and ice sheets. To appear in *J. Fluid Mech.* [145]

Bradfield, G., 1964. Notes on applied science No. 30 *Use in industry of elasticity measurements in metals with the help of mechanical vibrations*. H.M.S.O, London. [85, 140]

Brazier-Smith, P. R., 1987. The acoustic properties of two co-planar half-plane plates. *Proc. R. Soc. Lond.* A **409**, 115–139. [136, 142, 154, 156, 176]

Brekhovskikh, L. M., 1980. *Waves in layered media*. Academic Press, New York, Second edition. [14, 21, 26, 67]

Briggs, G. A. D., 1985. *An introduction to scanning acoustic microcopy*. Oxford University Press: Royal Microscopical Society. [1]

Briggs, G. A. D., 1992. *Acoustic microscopy*. Monographs on the physics and chemistry of materials: 47, Oxford University Press. [1, 4, 10, 21, 35, 39, 40, 74, 85]

Briggs, G. A. D., Jenkins, P. J. & Hoppe, M., 1990. How fine a surface crack can you see in a scanning acoustic microscope? *J. Microsc.* **159**, 15–32. [1, 10]

Brind, R. J. & Wickham, G. R., 1991. Near-field behaviour of the fundamental elastodynamic solutions for a semi-infinite homogeneous isotropic elastic solid. *Proc. R. Soc. Lond. A* **433**, 101–120. [11]

Bueckner, H. F., 1970. A novel principle for the computation of stress intensity factors. *J. Appl. Math. Mech. (ZAMM)* **50**, 529–546. [94]

Cagniard, L., 1939. *Réflection et réfraction des ondes séismique progressives*. Gauthiers-Villars, Paris. Trans. and rev. by E. A. Flinn & C. H. Dix, 1962. *Reflection and refraction of progressive seismic waves*. McGraw-Hill, New York. [1, 3, 35, 65, 93]

Cannell, P. A., 1975. Edge scattering of aerodynamic sound by a lightly loaded elastic half-plane. *Proc. R. Soc. Lond.* A **347**, 213–238. [136]

Cannell, P. A., 1976. Acoustic edge scattering by a heavily loaded elastic half-plane. *Proc. R. Soc. Lond.* A **350**, 71–89. [136, 137]

Chapman, C. H., 1972. Lamb's problem and comments on the paper 'On Leaking Modes' by Usha Gupta. *Pure Appl. Geophys.* **94**, 233–247. [36, 51]

Choi, H. J., 1997. A periodic array of cracks in a functionally graded nonhomogeneous medium loaded under in-plane normal and shear. *Int. J. Fracture* **88**, 107–128. [92, 192]

Craster, R. V., 1996a. A canonical problem for fluid-solid interfacial wave coupling. *Proc. R. Soc. Lond. A* **452**, 1695–1711. [64]

Craster, R. V., 1996b. Wavefront expansions for pulse scattering by a surface inhomogeneity. *Quart. J. Mech. Appl. Math.* **49**, 657–674. [47, 59]

Craster, R. V., 1997. The light fluid loading limit for fluid/solid interactions. *Euro. J. Appl. Math* **8**, 485–505. [29, 62, 192]

Craster, R. V., 1998. Scattering by cracks beneath fluid-solid interfaces. *J. Sound Vib.* **209**, 343–372. [172, 173]

Craster, R. V. & Atkinson, C., 1994. Mixed boundary value problems for non-homogeneous elastic materials. *Quart. J. Mech. Appl. Math.* **47**, 183–206. [92]

Crighton, D. G., 1979. The free and forced waves on a fluid-loaded elastic plate. *J. Sound Vib.* **63**, 225–235. [2, 28, 148, 154, 162, 176, 177]

Crighton, D. G., 1989. The 1988 Rayleigh Medal lecture: fluid loading - the interaction between sound and vibration. *J. Sound Vib.* **133**, 1–27. [1, 3, 36, 136]

Crighton, D. G. & Innes, D., 1983. Low frequency acoustic radiation and vibration response of locally excited fluid-loaded structures. *J. Sound Vib.* **91**, 293–314. [136]

Crighton, D. G. & Innes, D., 1984. The modes, resonances and forced response of elastic structures under heavy fluid loading. *Phil. Trans. R. Soc. Lond.* A **312**, 295–342. [137, 164, 165, 183]

Crighton, D. G. & Leppington, F. G., 1973. Singular perturbation methods in acoustics: diffraction by a plate of finite thickness. *Proc. R. Soc. Lond. A* **335**, 313–339. [10, 27]

Crighton, D. G. & Maidanik, G., 1981. Acoustic and vibration fields generated by ribs on a fluid-loaded panel .1. Plane-wave problems for a single rib. *J. Sound Vib.* **75**, 437–452. [137]

Daley, P. F. & Hron, F., 1983. High-frequency approximation to the nongeometrical S^* arrival. *Bull. Seism. Soc. Am.* **73**, 109–123. [67]

Datta, S. K., 1979. Diffraction of SH-waves by an edge crack. *J. Appl. Mech.* **46**, 101–106. [16]

Datta, S. K. & El-Akily, N., 1978. Diffraction of elastic waves in a half-space I: Integral representation

and matched asymptotic expansions. In *Proc. IUTAM symposium on modern problems in elastic wave propagation*, ed. by J. Miklowitz & J. D. Achenbach, 197-218. [11, 28]

Datta, S. K. & Sabina, F. J., 1986. Matched asymptotic expansions applied to diffraction of elastic waves. In *Low and high frequency asymptotics*, ed. by V. K. Varadan & V. V. Varadan, 71-264. [10]

de Hoop, A. T., 1960. A modification of Cagniard's method for solving seismic pulse problems. *Appl. sci. Res. B* **8**, 349–356. [3, 35, 65, 93]

de Hoop, A. T. & van der Hijden, J. H. M. T., 1983. Generation of acoustic waves by an impulsive line source in a fluid/solid configuration with a plane boundary. *J. Acoust. Soc. Am.* **74**, 333–342. [36]

de Hoop, A. T. & van der Hijden, J. H. M. T., 1984. Generation of acoustic waves by an impulsive point source in a fluid/solid configuration with a plane boundary. *J. Acoust. Soc. Am.* **75**, 1709–1715. [36]

de Hoop, A. T. & van der Hijden, J. H. M. T., 1985. Seismic waves generated by an impulsive point source in a fluid/solid configuration with a plane boundary. *Geophysics* **50**, 1083–1090. [1, 35, 36, 60]

Drijkoningen, G. G., 1991. Tunneling and the generalized ray method in piecewise homogeneous media. *Geophysical Prospecting* **39**, 757–781. [67, 80]

Drijkoningen, G. G. & Chapman, C. H., 1988. Tunneling rays using the Cagniard–de Hoop method. *Bull. Seism. Soc. Am.* **78**, 898–907. [49, 67, 78]

Einziger, P. D. & Felsen, L. B., 1982. Evanescent waves and complex rays. *IEEE Trans. Antennas Propagat.* **AP-30**, 594–605. [67]

England, A. H., 1971. *Complex variable methods in elasticity*. Wiley. [26, 32]

Erdogan, F., 1983. Stress intensity factors. *J. Appl. Mech.* **50**, 992–1002. [133]

Ergüven, M. E. & Gross, D., 1999. On the penny-shaped crack in inhomogeneous elastic materials under normal extension. *Int. J. Solids Structures* **36**, 1869–1882. [92, 108, 192]

Eshelby, J. D., 1951. The force on an elastic singularity. *Phil. Trans. R. Soc. Lond. A* **244**, 87–112. [94]

Eshelby, J. D., 1970. Energy relations and the energy-momentum tensor in continuum mechanics. In *Inelastic behaviour of solids*, ed. by M. F. Kanninen *et. al*, 77-115, McGraw-Hill, New York. [94, 106]

Ewing, W. M., Jardetzky, W. S. & Press, F., 1957. *Elastic waves in layered media*. McGraw-Hill, New York. [1, 80]

Freund, L. B., 1990. *Dynamic fracture mechanics*. Cambridge University Press. [92, 101]

Garvin, W. W., 1956. Exact transient solution of the buried line source problem. *Proc. R. Soc. Lond. A* **234**, 528–541. [47, 93]

Gradshteyn, I. S. & Ryzhik, I. M., 1980. *Table of integrals, series, and products (Corrected and enlarged edition)*. London: Academic Press. [102, 106]

Guo, Y. P., 1995. On sound energy scattered by a rigid body near a compliant surface. *Proc. R. Soc. Lond. A* **451**, 543–552. [173, 187]

Gutowski, P. R., Hron, F., Wagner, D. E. & Treitel, S., 1984. S^*. *Bull. Seism. Soc. Am.* **74**, 61–78. [67]

Haak, K. F. I. & Kooij, B. J., 1996. Transient acoustic diffraction in a fluid layer. *Wave Motion* **23**, 139–164. [93, 99, 106]

Harris, F. J., 1978. On the use of windows for harmonic analysis with the discrete Fourier transform. *Proc. Inst. Elect. and Electron. Eng.* **66**, 51–83. [60]

Harris, J. G., 1980. Diffraction of a crack by a cylindrical longitudinal pulse. *J. Appl. Math. Phys. (ZAMP)* **31**, 367–381. [93, 104]

Hein, V. L. & Erdogan, F., 1971. Stress singularities in a two-material wedge. *Int. Journ. of Fracture Mech.* **7**, 317–330. [19]

Hildebrand, J. A. & Rugar, D., 1984. Measurement of cellular elastic properties by acoustic microscopy.

J. Microsc. **134**, 245–260. [1]

Hong, T. L. & Helmberger, D. V., 1977. Generalized ray theory for dipping structure. *Bull. Seism. Soc. Am.* **67**, 995–1008. [49, 86]

Howe, M. S., 1986. Attenuation and diffraction of bending waves at gaps in fluid loaded plates. *IMA J. Appl. Math.* **36**, 247–262. [160, 182, 183]

Howe, M. S., 1990. Diffraction of sound by a surface scratch on an elastic solid. *Euro. J. Appl. Math.* **1**, 353–369. [10]

Howe, M. S., 1994a. On the sound produced when flexural waves are reflected at the open end of a fluid-loaded cylinder. *J. Acoust. Soc. Am.* **96**, 265–276. [191]

Howe, M. S., 1994b. Scattering of bending waves by open and closed cracks and joints in a fluid-loaded elastic plate. *Proc. R. Soc. Lond. A* **444**, 555–571. [136, 160, 161, 182]

Hron, F. & Mikhailenko, B. G., 1981. Numerical modeling of nongeometrical effects by the Alekseev-Mikhailenko method. *Bull. Seism. Soc. Am.* **71**, 1011–1029. [66, 67, 75]

Hudson, J. A., 1980. *The excitation and propagation of elastic waves*. Cambridge University Press. [3, 93, 94]

Junger, M. C. & Feit, D., 1986. *Sound, structures and their interaction*. Acoustical Society of America. Second edition. [136, 138, 139, 172, 174]

Kennett, B. L. N., 1983. *Seismic wave propagation in stratified media*. Cambridge University Press. [83]

Knopoff, L. & Gilbert, F., 1959. First motion methods in theoretical seismology. *J. Acoust. Soc. Am.* **31**, 1161–1168. [51]

Kooij, B. J. & Quak, D., 1988. Three-dimensional scattering of impulsive acoustic waves by a semi-infinite crack in the plane interface of a half-space and a layer. *J. Math. Phys.* **29**, 1712–1721. [93, 99]

Lamb, H., 1904. On the propagation of tremors over the surface of an elastic solid. *Phil. Trans. R. Soc. Lond. A* **203**, 1–42. [3, 36, 94]

Lawrie, J. B., 1986. Vibrations of a heavily loaded, semi-infinite, cylindrical elastic shell. I. *Proc. R. Soc. Lond. A* **408**, 103–128. [191]

Lawrie, J. B., 1987. Vibrations of a heavily loaded, semi-infinite, cylindrical elastic shell. II. *Proc. R. Soc. Lond. A* **414**, 371–387. [191]

Leppington, F. G., 1972. On the radiation and scattering of short surface waves. Part 1. *J. Fluid Mech.* **56**, 101–119. [10]

Leppington, F. G., 1976. Scattering of sound waves by finite membranes and plates near resonance. *Quart. J. Mech. Appl. Math.* **24**, 527–546. [136]

Leppington, F. G., 1978. Acoustic scattering by membranes and plates with line constraints. *J. Sound Vib.* **58**, 319–332. [136]

Lighthill, M. J., 1958. *Introduction to Fourier analysis and generalised functions*. Cambridge University Press. [144]

Llewellyn–Smith, S. G. & Craster, R. V., 1999. Numerical and asymptotic approaches to scattering problems involving finite elastic plates in structural acoustics. *Wave Motion* **30**, 17–41. [170, 191]

Ma, C. C. & Huang, K. C., 1996. Exact transient solutions of buried dynamic point forces for elastic bimaterials. *Int. J. Solids Structures* **33**, 4511–4529. [88]

McIver, P. & Rawlins, A. D., 1993. Two-dimensional wave-scattering problems involving parallel-walled ducts. *Quart. J. Mech. Appl. Math.* **46**, 89–116. [10]

Mei, C. C., 1978. Extensions of some identities in elastodynamics with rigid inclusions. *J. Acoust. Soc. Am.* **64**, 1514–1522. [172]

Mellman, G. R. & Helmberger, D. V., 1974. High-frequency attenuation by a thin high-velocity layer.

Bull. Seism. Soc. Am. **64**, 1383–1388. [66, 78, 82]

Miklowitz, J., 1978. *The theory of elastic waves and waveguides.* North-Holland. [3, 43, 65, 72, 94, 101]

Muskhelishvili, N. I., 1953. *Some basic problems of the mathematical theory of elasticity.* P. Noordhoff Ltd., Groningen, Holland, Third edition. [25, 26, 32]

Neerhoff, F. L., 1980. Reciprocity and power-flow theorems for the scattering of plane elastic waves in a half space. *Wave Motion* **2**, 99–113. [172]

Nilsson, F., 1973. A path-independent integral for transient crack problems. *Int. J. Solids Struct.* **9**, 1107–1115. [106, 108]

Noble, B., 1958. *Methods based on the Wiener–Hopf technique.* Pergamon Press. [3, 93, 132, 144, 185]

Norris, A. N. & Rebinsky, D. A., 1995. Acoustic and membrane wave interaction at plate junctions. *J. Acoust. Soc. Am.* **97**, 2063–2073. [187]

Norris, A. N., Rebinsky, D. A. & Wickham, G. R., 1998. On wave interaction and diffraction from the junction of two curved plates under unilateral fluid loading. *Phil. Trans. R. Soc. Lond. A* **356**, 1421–1467. [191]

Norris, A. N. & Wickham, G. R., 1995. Acoustic diffraction from the junction of two plates. *Proc. R. Soc. Lond. A* **451**, 631–655. [136, 142, 154, 156]

Pao, Y. H. & Gajewski, R. R., 1977. The generalised ray theory and transient responses of layered elastic solids. In *Phys. Acoust. 13*, ed. by W. P. Mason & R. N. Thurston, 183-265, Academic Press, New York. [80, 84]

Pao, Y. H., Zeigler, F. & Wang, Y. S., 1989. Acoustic waves generated by a point source in a sloping fluid layer. *J. Acoust. Soc. Am.* **85**, 1414–1426. [86]

Pekeris, C. L., 1940. A pathological case in the numerical solution for integral equations. *Proc. Nat. Acad. Sci. USA* **26**, 433–437. [3]

Rice, J. R., 1968. A path independent integral and the approximate analysis of strain concentration by notches and cracks. *J. Appl. Mech.* **35**, 379–386. [107]

Roever, W. L., Vining, T. F. & Strick, E., 1959. Propagation of elastic wave motion from an impulsive source along a fluid/solid interface. *Phil. Trans. R. Soc. Lond. A* **251**, 455–523. [36, 42, 56, 72, 89]

Rogoff, Z. M., 1993. Reciprocity relations between the incident field and the mode-converted scattered far-field for compact obstacles in an elastic half-space. *M.Sc. Thesis (University of Manchester).* [172]

Rogoff, Z. M. & Tew, R. H., 1997. Acoustic radiation from a phased line source at a fluid-solid boundary. *IMA J. Appl. Math* **58**, 93–110. [137]

Sabina, F. J. & Willis, J. R., 1977. Scattering of Rayleigh waves by a ridge. *J. Geophys.* **43**, 401–419. [10, 17, 28]

Skelton, E. A., 1999. Acoustic scattering by a closed semi-infinite fluid-loaded elastic cylindrical shell. *Proc. R. Soc. Lond. A* **455**, 1637–1681. [191]

Stallybrass, M. P., 1970. A crack perpendicular to an elastic half-plane. *Int. J. Engng Sci.* **8**, 351–362. [22]

Stephen, R. A. & Bolmer, S. T., 1985. The direct wave root in marine seismology. *Bull. Seism. Soc. Am.* **75**, 57–67. [67]

Tan, T. H., 1977. Reciprocity relations for scattering of plane, elastic waves. *J. Acoust. Soc. Am.* **61**, 928–931. [172]

Tew, R. H., 1992. Diffraction of sound by a surface inhomogeneity at a fluid-solid interface. *Euro. J. Appl. Math.* **3**, 115–145. [28]

Thau, A. & Lu, T. H., 1971. Transient stress intensity factors for a finite crack in an elastic solid caused

by a dilatational wave. *Int. J. Solids Structures* **7**, 731–750. [94, 114]

Timoshenko, S. & Woinowsky-Kreiger, S., 1959. *Theory of Plates and Shells*. McGraw-Hill. [139, 170]

Tsai, C. H. & Ma, C. C., 1992. Transient analysis of a semi-infinite crack subjected to dynamic concentrated forces. *J. Appl. Mech.* **59**, 804–811. [92]

Tsai, C. H. & Ma, C. C., 1993. The stress intensity factor of a subsurface inclined crack subjected to dynamic impact loading. *Int. J. Solids Structures* **30**, 2163–2175. [92, 99]

Tsai, C. H. & Ma, C. C., 1997. Theoretical transient analysis of the interaction between a dynamically propagating in-plane crack and traction-free boundaries. *J. Appl. Mech.* **64**, 819–827. [123]

van der Hijden, J. H. M. T., 1987. *Propagation of transient elastic waves in stratified anisotropic media*. North-Holland series in applied mathematics and mechanics: vol. 32. [37]

Varatharajulu, V., 1977. Reciprocity relations and forward amplitude theorems for rigid inclusions. *J. Math. Phys.* **18**, 537–543. [172]

Wickham, G. R., 1977. The forced two dimensional oscillations of a rigid strip in smooth contact with a semi-infinite elastic solid. *Proc. Camb. Phil. Soc.* **81**, 291–311. [10, 27]